A Log-Periodic Focal-Plane Architecture for Cosmic Microwave Background Polarimetry

by

Roger Christopher O'Brient

B.S. (California Institute of Technology) 2001
M.A. (University of California at Berkeley) 2004

A dissertation submitted in partial satisfaction
of the requirements for the degree of

Doctor of Philosophy

in

Physics

in the

GRADUATE DIVISION

of the

UNIVERSITY OF CALIFORNIA, BERKELEY

Committee in charge:

Professor Adrian T. Lee, Chair
Professor Martin White
Professor William Welch

Fall 2010

The dissertation of Roger Christopher O'Brient is approved.

Chair Date

Date

Date

University of California, Berkeley

Aug 2010

A Log-Periodic Focal-Plane Architecture for Cosmic Microwave Background Polarimetry

by

Roger Christopher O'Brient

Abstract

A Log-Periodic Focal-Plane Architecture for Cosmic Microwave Background Polarimetry

by

Roger Christopher O'Brient

Doctor of Philosophy in Physics

University of California, Berkeley

Professor Adrian T. Lee, Chair

We describe the design, fabrication, and laboratory-demonstration of a novel dual-polarized multichroic antenna-coupled Transition Edge Sensor (TES) bolometer. Each pixel separates the incident millimeter radiation into two linear polarization channels as well as several frequency channels (bands). This technology enables us to realize bolometer arrays for Cosmic Microwave Background (CMB) polarimetry measurements that map the sky at multiple colors while simultaneously boosting the optical throughput over what would have been attained from arrays of single-frequency channel detectors. Observations at multiple frequency channels are important for differentiating polarized galactic foregrounds and atmospheric fluctuations from the CMB.

Each pixel couples free-traveling radiation onto lithographed microstrip transmission lines prior to the bolometers using a dual-polarized broadband antenna known as a sinuous antenna. The transmission lines are integrated onto the back of the antenna arms and the antennas are in direct contact with an extended-hemispherical lens. We show measurements of scale model (4-12GHz) and to-scale (80-240Hz) antennas to demonstrate high antenna-gain, low cross-polarization contamination, and efficient coupling over a 1-2 octave bandwidth.

We have developed microstrip circuits that divide the antenna's wide bandwidth into smaller channels. In one scheme, two or three frequency channels can be extracted from the antenna's received power using microstrip circuits known as diplexers and triplexers. These avoid atmospheric spectral lines and are well suited to terrestrial observations. We can also partition this bandwidth into contiguous bands using cochlear channelizers inspired by the physiology of the human ear; this design is most advantageous for satellite missions where there are no concerns about atmospheric contamination. We present design methodologies for these circuits and show measurements of prototypes coupled to TES bolometers to verify acceptable performance. We also describe the fabrication of a broadband anti-reflection coating for the contacting lenses and demonstrate that lens-coupled sinuous pixels receive more power with the coatings than without. Finally, we remark on the last un-resolved challenge of forming symmetric beams and balun designs that may help form patterns more useful for polarimetry.

This technology is a candidate for use in the Polarbear ground-based experiment. By packing more detectors into the focal-plane than can be done with monochromatic pixels, multichroic pixels will allow Polarbear to map the sky much faster. This technology is also candidate for future space-based missions as well, where multhchroic pixels will allow a less massive payload and hence a lower cost mission. Finally, we envision using arrays of similar pixels in sub-millimeter observations of high-redshift galaxy clusters as well (e.g.example Sunyaev-Zeldovich Effect measurements). However, we require more sophisticated lithography and etching techniques to shrink these pixels to a size suitable for such wavelengths.

Professor Adrian T. Lee
Dissertation Committee Chair

In memory of Huan Tran, who provided crucial early leadership on this project and dragged me out of complacency on a number of occasions. He missed seeing the final results from these efforts by a few weeks; I think he would have gotten a kick out of them.

Contents

List of Figures

List of Tables

Acknowledgements

The research described in this thesis is the result of several peoples' ideas coming together, so this section is important to give credit where it is due.

I owe a deep thanks to my advisor Adrian Lee who has been incredibly patient and allowed me an unusual degree of freedom to pursue some pretty wild detectors ideas. He is also unique in our field right now by training students in both microwave design and clean-room fabrication; I was delighted to recently learn that these skills are in high demand. I also am in debt to Paul Richards who always made himself available when troubleshooting his renowned "Sewer-pipe" interferometer. His astonishingly methodical knowledge of obscure material properties was also invaluable. Thanks to Bill Holzapfel for loaning some old ACBAR optical filters that are important parts of Dewar 576's filter stack; there's no way I could have done these measurements without those. Finally, Greg Engargiola worked with me on simulations of the sinuous as well as designs for the CPW-balun that is outlined in Chapter 9.

My fellow graduate students and post-docs have had an enormous impact on this work as well. I'm damn near certain that at least half of the ideas in here were originally from Mike Myers. And while he was always two or three conceptual steps ahead of me, he was classy enough to simply make suggestions and let me work out many of the details. Sherry Cho and Jared Mehl trained me in the Berkeley Microlab and I worked along-side Eric Shirokoff and Kam Arnold when actually fabricating devices; we were frequently all-night-long microlab partners allowing all parties to make rapid progress. Trevor Lanting taught me much of what I know about cryogenics and provided useful guidance on how to modify Dewar 576 after he handed it off to me. Ziggy Kermish also provided the crucial suggestion of using copious amounts of porous teflon to make my filter stack work on it's first try; it's not supposed to be that easy. Erin Quealy has made phenomenal progress on anti-reflection coatings for our lenses and her pioneering measurements of TMM's optical properties were the foundation for our efforts on a broadband coating described in chapter 7. I didn't really make it work as well as I'd like, so there's plenty of room for her to improve. Finally, it's

been a pleasure training Aritoki Suzuki as my replacement; if I have nothing but graduate students like him someday, I'm sure my career will be smooth sailing. This project is left in competant hands.

For the past three years, this project has been a collaboration with Gabriel Rebeiz's group at UC San Diego's Electrical Engineering Department and his graduate students have been also been enormously helpful. Chris Galbraith shared his trade-secrets on tuning up his elegant cochlear channelizer described in chapter 8. Jen Edwards and Gabriel were the first to think clearly about the impedance of the antenna and to point out that it was not truly self-complimentary and that the excitations of interest are not eigenmodes. We also developed ray-tracing algorithms in parallel with San Deigo (see Chapter 4), but Jen made her's work first. She generously helped trouble-shoot my code and pointed out that we need to consider image currents through the ground-plane when doing the diffraction integrals. Subtle, eh?

I also owe a debt of gratitude to people outside my group that made life enjoyable when I wasn't hunkered down in the lab. This includes other graduate students in the department who I'd share a beer with on Friday afternoons, fellow residents of"Casa del Physics," "Salad House" and "Prospect House," and of course Anne Takazawa and Donna Sakima for helping guide me and many others through Berkeley's notorious red tape. My folks, who live just over the hills, were always happy to have me over for dinner to escape from Berkeley for a few hours.

Lastly, I have to thank my wife Abby. She's been helping me through over half of this and has put up with a lot of crap from me! This includes the evenings when I'd stay in the lab until 3-4 AM with my cell-phone off to minimize noise and rf-interference, as well as the days when I'd try to set an alarm at similar times so I could sneak back into the lab. It also includes the last few months of grad school when I stayed in Berkeley to finish measurements after she had already moved to Southern California. I could not have remained a functional human being while doing this without her at my side.

This work was supported by NASA grant NNG06GJ08G. All devices were fabricated in the Berkeley Microlab

Chapter 1

Introduction

1.1 Overview

Cosmology has blossomed into a mature and precise scientific field over the past few decades. During this time, measurements of phenomena as diverse as Cosmic Microwave Background (CMB) anisotropies, large-scale galactic structure, high redshift Type Ia supernovae, and primordial nucleosynthesis abundances have produced a surprisingly consistent picture of our universe's dynamics and composition. We live in a universe that is composed of only 4% baryonic matter, with the remainder split between cold (non-relativistic) dark-matter (20%) and a poorly understood dark energy (76%) that is causing the expansion of our universe to accelerate. The geometry of space in our universe is flat on the largest observable scales and we hypothesize that this was fine-tuned by a period of rapid expansion in the first fraction of a second after the Big Bang. We also suspect that this rapid expansion amplified gravitational wells to cosmic scales and that matter later fell into them to form stars and galaxies. This model of our universe's structure and evolution is known as the inflationary Lambda-CDM (Cold Dark Matter) cosmology.

While this model enjoys consistent support from a wide variety of measurements, none of these observations have matched the CMB data set in terms of variety and precision of constrained cosmological parameters. The CMB is our most ancient optical image of the

universe, created a scant 300,000 years after the Big Bang when atoms first formed from the hot primordial plasma. Because it was created so early in our universe's history and has only been slightly perturbed since, the microwave background bears the signature of our universe's structure long before matter gravitationally collapsed into starts and galaxies. As a result, the features of the CMB can be compared against models where matter and energy have a sufficiently low density that their dynamics are described by linear equations. Such linear equations are significantly simpler than the full non-linear models relevant later in the universe's history. This relative simplicity has allowed cosmologists to make a deep comparison between theory and CMB observations and to constrain numerous cosmological parameters to unprecedented accuracy. Because of these successes, the cosmic microwave background has been referred to by some as a "Cosmic Rosetta Stone."

1.2 History

Despite the linear theory underlying the CMB's structure making it easy to interpret, its weak signal has made it one of the most technologically challenging astrophysical sources to measure. Historically, most experimental advances in this field have been linked to technological advances in the receivers. In fact, the sensitivities of bolometric receivers have followed a Moore's-Law-like growth, where the Noise Equivalent Powers (NEPs) have dropped in half roughly every 2 years for the past half-century (see Figure 1.1).

The CMB was first detected serendipitously by Bell Labs scientists Penzias and Wilson in 1964 as a 3.5K signal that was uniform across the sky. While they initially thought this to be simply "excess noise" generated within their microwave telescope, it was soon realized to be relic radiation from the Big Bang. Numerous follow-up experiments used similar heterodyne receivers to measure the CMB's spectrum in the Rayleigh Jean's limit, but they all suffered from limited sensitivity at higher frequencies (*Partridge* [1995]). This limitation was finally overcome with the Woody-Richards balloon-borne experiment that used a far more sensitive bolometer behind a Fourier-Transform Spectrometer (FTS) to provide spectral discrimination over nearly a decade of bandwidth (*Woody and Richards*

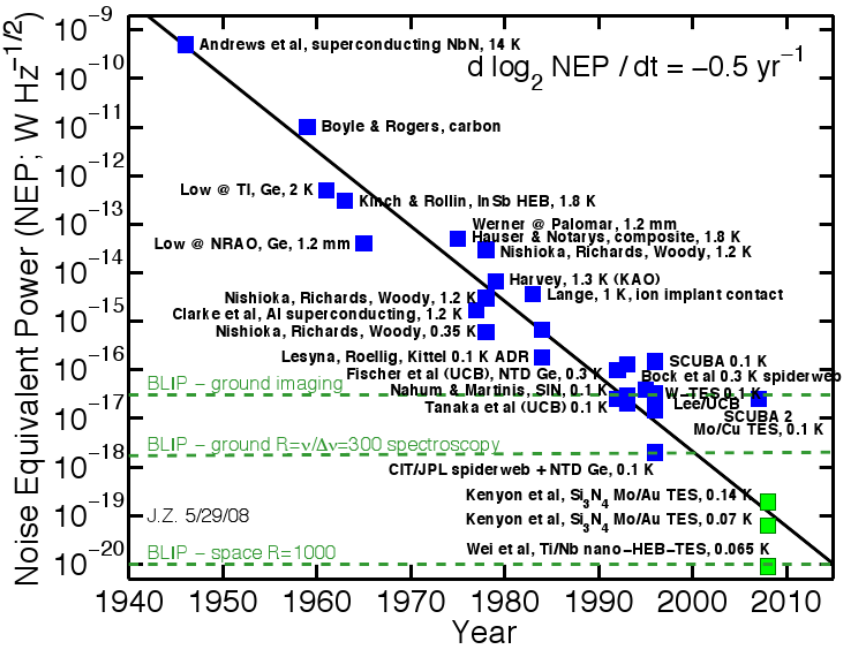

Figure 1.1. NEP of Bolometeric detectors vs publication date. NEP is defined as the source power that a detector would have to look at to attain a signal to noise ratio of unity for a half second of integration time. Figure courtesy *Zmuidzinas* [2010].

[1979]). This was the first experiment that measured the CMB's spectrum out into the Wein-tail and demonstrated it to be a true blackbody. These spectral measurements culminated in the late 1980s FIRAS (Far Infrared Absolute Spectrometer) experiment on the COBE (Cosmic Background Explorer) satellite which characterized the spectrum from 60 to 600 GHz and constrained it's temperature to 2.728 ± 0.004 K (*Fixsen et al.* [1996]).

Despite the CMB's remarkable uniformity across the sky, scientists made considerable efforts to detect anisotropies in temperature. George Smoot's team at LBNL first detected a $3.5mK$ dipole anisotropy in 1977 with a differential radiometer aboard a U-2 aircraft. They attributed this to a Doppler shift caused by the Earth's motion relative to the CMB (*Smoot et al.* [1977]). Anisotropies with cosmological origins were finally seen in 1992 with COBE's Differential Microwave Radiometer (DMR), detecting $16 \pm 4\mu K$ variations on scales larger than 7^o (*Smoot et al.* [1992]). This detection, as well as dramatic improvements in bolometric and HEMT receivers, triggered a race to see degree scale anisotropies generated by acoustic oscillations in the early primordial plasma. These anisotropies were finally

seen in the late 1990s by two balloon-borne bolometric experiments (BOOMERANG and MAXIMA, *de Bernardis et al.* [2000] and *Hanany et al.* [2000]), and terrestrial HEMT-based receivers (TOCO and DASI, *Miller et al.* [1999] and *Halverson et al.* [2002]), detecting a primary peak in the anisotropies at $l \sim 200$. Two other terrestrial bolometric receivers (CBI and ACBAR, *Pearson et al.* [2003] and *Reichardt et al.* [2009]) measured anisotropies during this time at even higher scales out to $l \sim 2000$. These efforts culminated in the well known WMAP satellite experiment that mapped the full sky (2003-present) out to $l \sim 1000$ with HEMT-based detectors (*Larson et al.* [2010b]). The Plank Satellite, with a mixed HEMT/ bolometer focal plane, will provide an even higher precision full sky map in the years to come.

Through the past decade, several teams, most-notably South Pole Telescope (SPT) Collaboration, have detected the Sunyaev-Zeldovich (SZ) Effect, a spectral distortion of the CMB on angular scales above $l = 2000$ that arises when when photons pass through hot ionized gas in galaxy clusters. They have successfully used this effect to discover numerous high-redshift galaxy clusters and are using them to constrain cosmology late in the universe (*Vieira et al.* [2009] and *Staniszewski et al.* [2009]). However, these measurements required much higher sensitivity than the previous-generation of CMB experiments. This was attained by switching to TES-bolometers that can be monolithically integrated into focal planes with hundreds to thousands of detectors. By contrast, the old-generation cameras had less than 100 detectors each.

Finally, the cosmic microwave background's E-mode partial polarization was first detected at the μK level by DASI in 2002 (*Kovac et al.* [2002]). Since then, the terrestrial experiments QUAD and BICEP-1 have both used focal planes with tens of detectors to map E-mode polarization and construct angular power spectra with features consistent with the temperature power spectrum (*Ade et al.* [2008] and *Chiang et al.* [2010]). Over the years following the writing of this thesis, several experiments, including Polarbear, SPT-pol, BICEP-2, SPIDER, and the Keck Array will deploy with TES-bolometer focal planes. These experiments will bring the level of sensitivity used for SZ measurements to polarization measurements in an attempt to detect B-mode polarization. These experiments'

detectors have lithographed transmission lines between the antennas and bolometers to integrate optical filtering into the chip. This design obviates some of the filters that can complicate beam systematics. All of these experiments will have focal planes with thousands of dual-polarized antenna-coupled bolometers.

Antenna-coupled bolometers can potentially integrate other high-frequency optics into the lines between bolometers and antenna. For example, researchers at NASA's Goddard Flight Center have investigating placing a MEMS switch in the lines to rapidly chop on-chip (*Kogut et al.* [2006]). Another new possibility is to place multiple filters behind a single antenna to partition its bandwidth between multiple bolometers. A detector with this design could be very advantagous for CMB measurements.

1.3 Motivation for Multi-color detectors

As is clear from the history of CMB measurements, the required increases in sensitivity have often come from gains in sensitivity of the focal plane. In fact, our field has witnessed more than seven orders of magnitude improvement over the past half century *Zmuidzinas* [2010]. These advancements have been achieved through either decreasing the internal noise of the detectors or increasing the optical throughput by expanding to ever larger arrays of pixels. A third way to increase sensitivity that has not been explored until recently is to increase the optical throughput of each pixel by expanding their bandwidth.

Most recent CMB experiments have used detectors that receive a relatively narrow spectral range(20%-40%) because it was not practical to receive a larger continuous bandwidth. However, the advent of lithographed antenna-coupled bolometers that integrate filtering onto the chip provides the possibility of coupling a very broadband planar antenna to a channelizer circuit. Such a circuit can partition that bandwidth into narrow frequency channels before terminating each at different bolometers. This architecture would provide a significant increase in throughput, but still allow for beams with narrow frequency channels and well controlled properties. Submillimeter astronomers are already exploring this possibility and it is not a huge leap to use these techniques in CMB measurements as well.

Future CMB-polarization measurements will likely need to remove polarized galactic foregrounds from their maps. In principle, this can be done by mapping the sky at multiple frequency channels. Most experiments plan to receive the different channels in different pixels or in separate receivers. In both cases, all but a narrow spectral range is reflected away or absorbed before the bolometer. Multi-color pixels naturally facilitate these systematic controls while maintaining a higher optical throughput.

Finally, terrestrial experiments must often contend with an unstable atmosphere that itself anisotropically absorbs and re-emits in the millimeter spectral range. To control for atmospheric fluctuations, some experiments have designed observing channels centered at 90GHz or 150GHz and then an additional channel at 200-300GHz that receives stronger loading from water than the others. While such instruments have also used different pixels in their focal planes for different channels, multi-color pixels would once again naturally help address this challenge. In fact, SuZie-II has already demonstrated Background limited millimeter observations with a small focal-plane array of four multi-color pixels (*Benson et al.* [2003]). The highest channel was used to remove atmospheric fluctuations.

1.4 Outline

Chapters 2, 3, and the first half of 4 are background material that provide context for the original work described in later chapters. The second chapter summarizes the physics behind Cosmic Microwave Background Anisotropies and quantifies the foreground challenges with which future experiments will have to contend. The third Chapter contrasts TES-bolometers to competing technologies, summarizes the theory of their operation, and describes how the bolometers used in this thesis were fabricated and read-out. The fourth chapter describes the detectors to be used in the imminent Polarbear deployment. This design was the inspiration for the sinuous-based detectors. The chapter also discusses a raytracing script we wrote to account for the curved surface of our contacting lenses over the antennas in simulations.

The centerpiece of this thesis is the sinuous antenna, which is described at great length

in chapters 5 and 6. The sinuous is a dual-polarized antenna with a bandwidth of nearly two octaves. Chapter 5 describes the theory of it's operation and scale model measurements that demonstrate its valuable properties. Chapter 6 shows data from sinuous antennas coupled to TES bolometers through single band-defining filters.

Chapters 7 and 8 discuss microstrip circuits that we use to partition the antenna's bandwidth into narrow channels. Chapter 7 describes diplexer and triplexer circuits that would naturally avoid atmospheric lines in a terrestrial experiment. Measurements are presented demonstrating that the circuits work as designed when coupled to a sinuous antenna and bolometers. We also show measurements of a broad-band anti-reflection coating for the lenses above these devices. Chapter 8 describes a log-periodic channelizer design that can partition a continuous bandwidth into contiguous channels. We envision this design being used in satellite missions where our atmosphere is not a concern or in future spectroscopic experiments such SZ surveys and sub-millimeter observations of distant galaxy clusters. Both the channelizer and the antenna are log-periodic structures, which means they attain their large bandwidth from their self-similar design. We show measurements of the channelizer coupled to the sinuous and bolometers to demonstrate that it works roughly as expected.

This thesis concludes with chapter 9 that quantifies the advantages this design might hold over more traditional technology and discusses how it will be implemented into a focal plane for future experiments. Focal plane design is a common engineering challenge at all wavelengths, but most have monochromatic pixels above the sub-millimeter. However, both the radio-astronomy and sub-millimeter have experimented with multichroic arrays, and this chapter explains the considerations associated with this design. This chapter also discusses the primary unresolved issue with this technology: forming symmetric beams in pixels with more than a single filter. We mention a candidate balun design that should help balance the arms and produce the desired circular beams at all wavelengths.

Chapter 2

Cosmological Motivation

2.1 Introduction

This chapter summarizes the recent successes in CMB physics as well as the near-future polarization measurements that will be exciting but challenging. It is these prospects and challenges that ultimately motivated the detector development described in this thesis.

The standard model of cosmology and the theory of inflation are presented. The origin of the temperature and polarization anisotropies in the Cosmic Microwave Background are discussed in the context of these models as well as the cosmological parameters that have been or will be constrained by characterizing these anisotropies. Challenges associated with polarized foregrounds are also discussed.

2.2 Cosmological Expansion

There is strong observational evidence that the universe is expanding. Most notably, the distance between the Milky Way and neighboring galaxies is larger now than in the past, as evidenced by the spectral redshifting of distant galaxies relative to those nearby.

This expansion is well modeled by general relativity with the Friedmann-Walker-Robertson (FRW) metric:

$$ds^2 = -dt^2 + a(t)^2 \left[\frac{dr^2}{1 - Kr^2} + r^2(d\theta^2 + \sin^2\theta d\phi) \right] \tag{2.1}$$

where K is large scale curvature and $a(t)$ is the scale factor that records the history of the universe's dynamics. The scale factor vanished at the Big Bang and is currently unity (*Lyth* [1993]).

The time-time component of the Einstein Field Equation applied to the Equation 2.1 is commonly known as the Friedmann Equation:

$$\left(\frac{H(t)}{H_o} \right)^2 = \frac{\rho(t)}{\rho_o} - \frac{K}{a^2} \tag{2.2}$$

where the Hubble parameter $H(t) \equiv \dot{a}(t)/a(t)$ quantifies the expansion rate and is measured to currently be $H_o = 71km\ s^{-1}\ Mpc^{-1}$. $\rho_o \equiv 3H_o^2/8\pi G$ is the critical density needed to close the universe; if our universes density exceeds ρ_o, it will ultimately re-collapse. In this chapter, the overdots in all equations denote a time derivative.

The energy density $\rho(t)$ is a sum of contributions from matter, radiation, and a cosmological constant whose individual densities change with time through the scale-factor. Conservation of the Stress-Energy Tensor ($T^{\mu}_{\nu;\mu} = 0$) formally establishes these dependencies, but the results are physically intuitive. The energy density of matter is the rest mass of each particle times its number density. This energy drops as the volume increases and is proportional to a^{-3}. Cosmic expansion not only dilutes photons like it does massive particles, but it also decreases the energy of each photon by an additional factor of a as expansion stretches the wavelengths. As a result, radiation density falls as a^{-4}. A cosmological constant is assumed to have an energy density that does not scale with a (*Carroll* [2003]). With these relationships in a flat universe, Equation 2.2 becomes:

$$H(t)^2 = H_o^2 \left(\Omega_m a^{-3} + \Omega_r a^{-4} + \Omega_\Lambda \right)$$

where Ω_* is the energy in a particular species normalized to the critical energy density ρ_o. During much of the universe's history, the energy density was dominated by one of these species and the other terms in the Freidmann equations could be ignored. As a result, the behavior during these epochs was

$$a(t) \propto \begin{cases} t^{1/2} & \text{radiation dominated} \\ t^{2/3} & \text{matter dominated} \\ e^{H_o t} & \Lambda \text{ dominated} \end{cases}$$

The very early universe was dominated by radiation, but transitioned into a matter dominated universe at $a_{eq} = 4.15 * 10^{-5}/(\Omega_m h^2)$. In more recent times, the universe has transitioned once again into one dominated by a poorly understood Dark Energy whose energy density appears to be nearly constant and whose negative pressure is causing the universe's expansion to accelerate. The best fit models to date describe Dark Energy as a cosmological constant (*Carroll* [2003]).

The average temperature of the universe is tied to the most populous particle, the photon, and this temperature has dropped as a^{-1} in step with the scaling of the photon energies. The high temperatures in the very early universe kept baryonic matter ionized and in tight thermal equilibrium with the photons through Thompson scattering. This statistical equilibrium between ionized gas (e.g. electrons and photons), photons, and neutral hydrogen atoms can be approximated by the Saha Equation:

$$\frac{X_e^2}{1 - X_e} \approx \frac{1}{n_b} \left[\left(\frac{m_e T}{2\pi} \right)^{3/2} e^{-|m_e + m_p - m_H|/T} \right]$$

where the $n_b = \eta_b n_\gamma \sim 10^{-9} T^3$ is the baryon number density (*Rybicki and Lightman* [1979]). X_e is the ratio of free electron number density to proton number density and the high temperatures of the early universe held X_e close to unity (all matter ionized). While energetics favored hydrogen production at temperatures of a few eV, the large number of photons in the Wien tail of the thermal distribution (large η_b) kept the universe ionized

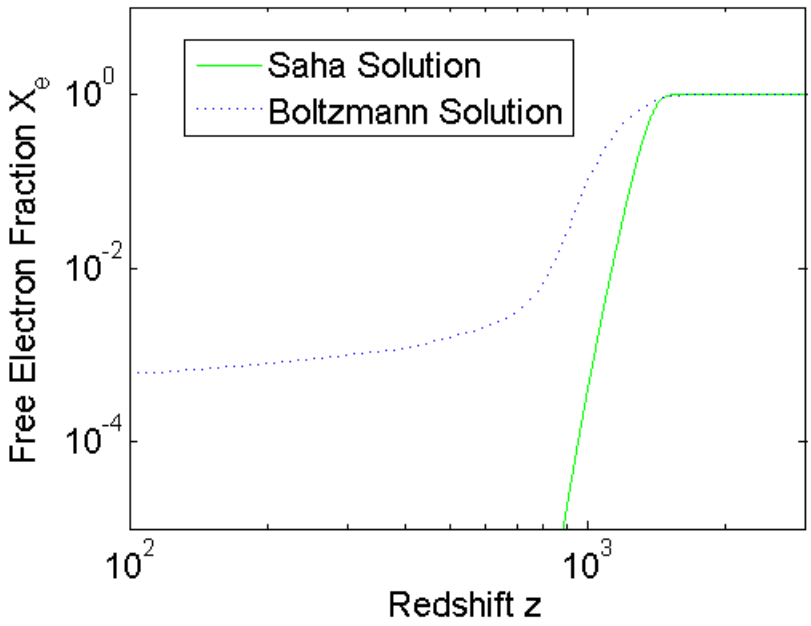

Figure 2.1. Free Electron fraction vs redshift for Equilibrium (Saha) and Non-equilibrium (Boltzmann) models. This figure is the result from an exercise from *Dodelson* [2003].

until $T \sim 0.25$eV, when X_e abruptly dropped and atomic hydrogen formed. This event is known as recombination and occurred at a redshift of $z = 1100$ (*Lyth* [1993]).

In reality, equilibrium between the photons and baryons was lost just before recombination in a phenomenon known as freeze-out where the Thompson scattering rate fell beneath the Hubble rate. Despite the lack of equilibrium, the Saha equation predicts a recombination redshift of $z \sim 1100$ in remarkable agreement with a more detailed numerical solution to the Boltzmann equation (See Figure 2.1) (*Dodelson* [2003]).

Subsequently, the photons freely streamed across the universe until they are seen in our telescopes today. Further expansion stretched their wavelength by a factor of 1100 into the millimeter range and this light source is known as the Cosmic Microwave Background (CMB). It is perhaps the most compelling evidence in favor of a hot Big Bang since once-competing "steady state" models of expansion had no natural way of explaining a near-uniform thermal radiation source at such a specific and high red-shift. Measurements by the Far InfraRed Absolute Spectrometer (FIRAS) instrument on the COsmic Background

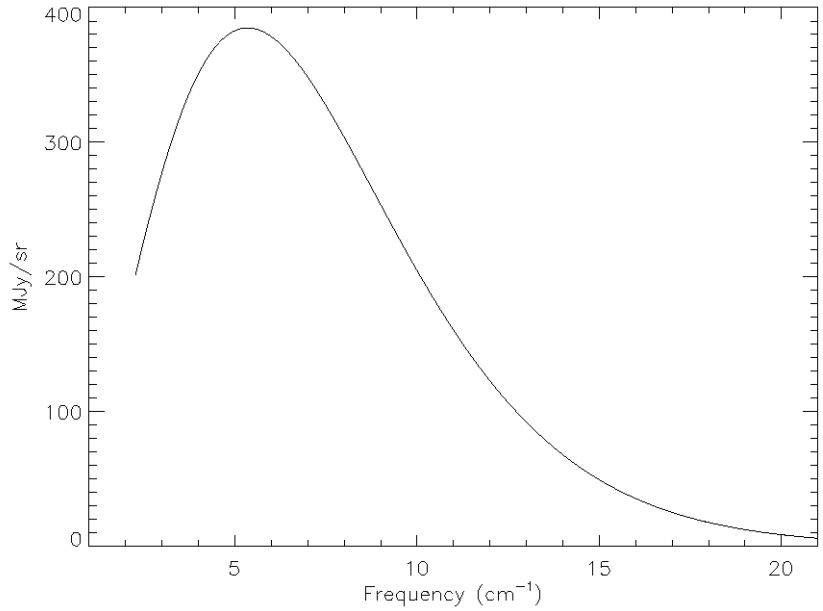

Figure 2.2. Frequency Spectrum measured by FIRAS. The data error-bars are famously smaller than the thickness of the theoretical co-plotted line. Figure from *Fixsen et al.* [1996]

Explorer (COBE) satellite have shown that it's frequency distribution is very closely modeled by a Plank Distribution (See Figure 2.2) that it is nearly isotropic, with temperature differences no larger than a few parts in 100,000 (*Fixsen et al.* [1996]).

2.3 Inflation

The Hot Big Bang scenario described in the previous section is well supported by measurements of the CMB and observations of Hubble's Law. In addition, predictions of the relative abundances of light elements (isotopes of Hydrogen and Helium) by Big Bang Nucleosynthesis agree well with the observed abundances in young galaxies (*Olive et al.* [2000]). Nonetheless, there are problems with the classic Hot Big Bang model.

Recent observations of the CMB anisotropies (see Section 2.5) suggest that the universe is nearly geometrically flat. Equivalently, the total energy density is very close to the critical

density, $\rho_c = 3m_{pl}^2 H_o^2/8\pi$, where m_{pl} is the Plank Mass. However, the Friedmann equation in a universe with curvature K can be rewritten as

$$\frac{|\rho(t) - \rho_c|}{\rho_c} = \frac{K}{(aH)^2} \propto t \tag{2.3}$$

where the proportionality applies to the early radiation dominated universe. For the current density to be $\rho_o \approx \rho_c$, the density at the plank scale temperatures would have to have been

$$\left| \frac{\rho(t_{plank})}{\rho_c} - 1 \right| \leq 10^{-59}$$

If this inequality was not met, the universe would have re-collapsed long before 13.7 Gyr, or it would have expanded so rapidly that it's average temperature would now be far lower than 2.7K. So the curvature of the very early universe must have been extremely close to flat. The hot big-bang model discussed above has no explanation for this required fine tuning (*Liddle* [1999]).

There are additional problems. The particle horizon is the maximum comoving distance that light could have traveled since the Big Bang:

$$\eta = \int_0^{\mathrm{t}} \frac{dt}{a(t')} = \int_0^1 \frac{da'}{a'^2 H(a')}$$

Objects separated by distances larger than the horizon have never been in causal contact. The horizon has increased as the universe has aged and was much smaller at reionization than it is today; regions that were casually connected at $z \sim 1100$ now only subtend an angle of 1.12^o on the sky. Points currently separated by larger angles than this should not have been in causal contact at recombination and should never have thermally equilibrated. Nonetheless, the CMB has been measured to be isotropic on large angular scales to a level of 1 part in 100,000. Physics beyond the classic Big Bang universe is needed to explain this remarkable isotropy.

Inflation is a hypothesis that solves these and other related problems by speculating

that the universe underwent an accelerated superluminal expansion very shortly after the Big Bang. The horizon size can be rewritten as a logarithmic integral over the the Hubble Radius $1/aH$:

$$\eta(a) = \int_0^a d[ln(a')] \frac{1}{a'H(a')} \tag{2.4}$$

The Hubble radius is the distance that particles can travel over one expansion time (doubling of a); it defines the maximum separation between particles that are in causal contact at a specific time. When the early universe inflates, a sudden increase in a causes the Hubble radius to rapidly shrink. This allows for regions larger than the current universe's Hubble Radius to have once been causally connected and in thermal equilibrium, explaining the apparent isotropy observed in the CMB.

Since many inflation models are driven by scalar fields operating at temperatures of at least 10^{15} GeV, the scale factor at the end of inflation would have been $a_{end} \approx T_o/10^{15}GeV \approx 10^{-28} \approx e^{64}$. So to ensure that all scales currently within the horizon today were also once within the horizon before they were pushed out by inflation, inflation must have expanded the universe by at least 64 e-foldings. Such an expansion explains the high level of isotropy in the CMB between points on the sky that would not have been causally connected in the classic Big Bang scenario (See Figure 2.3). This rapid expansion also solves the flatness problem with almost identical numerology, where the 10^{28} decrease in Hubble radius in Equation 2.3 causes the difference between ρ and ρ_c to drop to the required 10^{-60} level (*Dodelson* [2003]).

The time-time and space-space components of the Einstein equations may be combined to give:

$$\ddot{a} = -\frac{4\pi G}{3}(\rho + 3P)$$

where the ρ and P are the energy density and Pressure of the fields driving inflation. The comovng Hubble radius will shrink ($\frac{d}{dt}\frac{1}{Ha} < 0$) when $\ddot{a} > 0$, or when the universe's expansion accelerates. This would have happened during inflation if the pressure P was

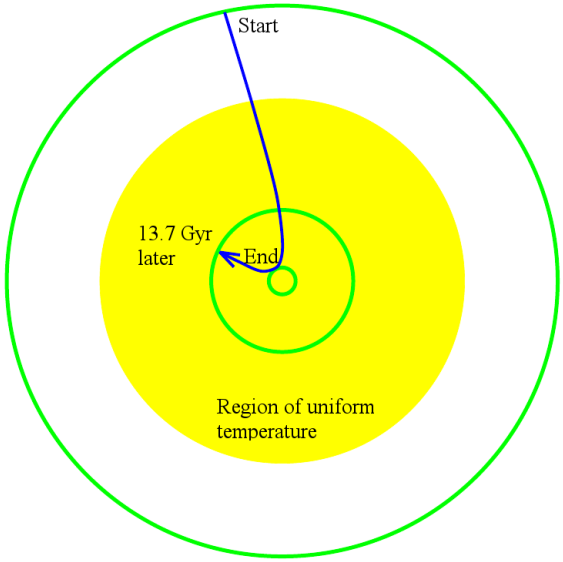

Figure 2.3. Cartoon showing how the Comoving Horizon (Hubble radius, Equation 2.4), pictorially shown by the green circles, shrinks between the Start and End of Inflation. Over the subsequent 13.7 Gyr, the our observable universe grows again, but not larger than the region of uniform temperature shown in yellow. This figure is adapted from a figure by Andrew Liddle (*Liddle* [1999]).

negative, specifically $P < -\rho/3$. Negative pressures arise when fields are trapped in a "false vacuum" with less Kinetic than Potential energy, allowing their difference, the pressure (T_i^i), to be negative.

While the detailed physics of inflation is not yet understood, many speculative models are driven by a scalar field potential $V(\phi)$ whose geometry is summarized by the slow roll parameters:

$$\begin{aligned} \epsilon &\equiv \frac{m_{Pl}^2}{2}\left(\frac{V'}{V}\right)^2 \\ \eta &\equiv m_{Pl}^2\frac{V''}{V} \end{aligned} \tag{2.5}$$

where $'$ denotes functional differentiation with respect to the field ϕ. Models frequently invoke the slow-roll approximation where $\epsilon << 1$ and $\eta << 1$, which ensures that inflation lasts long enough for the total scale expansion:

$$N \equiv \ln \frac{a_{end}}{a_{initial}} = \int_{t_i}^{t_e} H dt \cong -\frac{8\pi}{m_{pl}^2} \int_{\phi_i}^{\phi_e} \frac{V}{V'} d\phi$$

to exceed the required 64 e-foldings (*Liddle* [1999]).

2.4 Inflation as a Source of Structure

Inflation is not just a handy explanation for problems in the classic big bang model; it can also explain the origin of large scale structure in the universe. The gravitational ($g_{\mu\nu}$) and inflation ($\phi(x,t)$) fields have quantum mechanical fluctuations whose averages vanish, but whose variances do not. During inflation, the gravitational metric perturbations were amplified to cosmic scales outside the horizon where they are frozen in. The inflation field inflated too, but at the end we presume that it decayed into a hot bath of more familiar particles. These fields can be separated into homogeneous parts plus small fluctuations that are not spatially uniform:

$$\phi(x,t) = \phi_o(t) + \delta\phi(\mathbf{x},t)$$

$$g_{\mu\nu} = \begin{pmatrix} -1 & 0 & 0 & 0 \\ 0 & a^2 & 0 & 0 \\ 0 & 0 & a^2 & 0 \\ 0 & 0 & 0 & a^2 \end{pmatrix} + 2 \begin{pmatrix} \Psi(\mathbf{x},t) & 0 & 0 & 0 \\ 0 & a^2\Phi(\mathbf{x},t) & 0 & 0 \\ 0 & 0 & a^2\Phi(\mathbf{x},t) & 0 \\ 0 & 0 & 0 & a^2\Phi(\mathbf{x},t) \end{pmatrix}$$
$$+ a^2 \begin{pmatrix} 0 & 0 & 0 & 0 \\ 0 & h_+(\mathbf{x},t) & h_\times(\mathbf{x},t) & 0 \\ 0 & h_\times(\mathbf{x},t) & -h_+(\mathbf{x},t) & 0 \\ 0 & 0 & 0 & 0 \end{pmatrix}$$

where the first terms in these equations are the homogeneous parts (*Dodelson* [2003]). The metric tensor is given in rectangular coordinates for a flat universe with inhomogeneities

separated into the decoupled scalar and tensor terms. The tensor term is written only for modes traveling along the $\hat{z}$ axis. The space-space Einstein Equations to first order in $h_{+,\times}$ are:

$$\ddot{h_{+,\times}} + 2\frac{\dot{a}}{a}\dot{h_{+,\times}} + k^2 h_{+,\times} = 0 \tag{2.6}$$

This equation of motion models tensor modes as a harmonic oscillator (gravity waves) with a damping term created by the expansion of the universe (*Carroll* [2003]). When quantized, the expectation of the variance is $\left\langle \hat{h}^\dagger(k,\eta)\hat{h}(k,\eta) \right\rangle \equiv (2\pi)^3 P_h(k)\delta^3(k-k')$, where

$$P_h(k) = \frac{8\pi}{k^3}\frac{H^2}{m_{plank}^2}|_{aH=k} \propto k^{n_T-3}$$

The last proportionality defines the tensor spectral index n_T, which is nominally 0 for an ideal scale invariant (Harrison-Zeldovich) power spectrum $k^3 P_h(k)$ (*Liddle* [1999]).

Perturbations to the scalar and inflations fields inflate as well, producing a similar scalar spectrum $P_{\delta\Phi}$. However, the two fields couple as they are pushed out of the horizon, which complicated the mathematics considerably (*Dodelson* [2003]). The result of this analysis is that:

$$P_\Phi(k) = \frac{8\pi}{9k^3}\frac{H^2}{\epsilon m_{plank}^2}|_{aH=k} \propto \frac{1}{k^3}\left(\frac{k}{H_o}\right)^{n_S-1} \tag{2.7}$$

(*Liddle* [1999]). As above, the scalar spectral index n_S is nominally 1 for a scale invariant spectrum. COBE fixed the magnitude of the scalar spectrum on large scales at $\delta_H \sim 2\times10^{-5}$, which from Equation 2.7 fixes the energy scale of inflation to be similar to energy scales associated with GUT scales:

$$V^{1/4} \sim \epsilon^{1/4} 10^{16} GeV$$

While ϵ and η are the more fundamental parameters that characterize the inflationary

potential's shape, the figures n_S and n_T are more closely tied to observations and are often preferred in the observational literature. Logarithmic derivatives of the above spectra establish relationships between them:

$$n_S = 1 - 6\epsilon + 2\eta$$

$$n_T = -2\epsilon$$

Additionally, the tensor to scalar ratio defined in terms of CMB anisotropy C_ls can be shown to be

$$r \equiv \frac{C_l^T}{C_l^s} \cong 4\pi\epsilon$$

A successful measurement of r could constrain the energy scale of inflation and restrict the space of viable models for the inflationary potential (*Liddle* [1999]). Data from Large Scale Structure surveys and CMB maps have already constrained n_S and hence some inflationary potentials (see Figure 2.4). The space of viable models will no doubt decrease with improved measurements of the Microwave Background.

Finally, the two parameters ϵ and η suffice to summarize all slow roll inflation potentials, while the extra parameter in the set n_S, n_T, and r contais no new information. Eliminating n_S leads to a constancy relationship:

$$r = -2\pi n_T$$

This constancy relationship is generally true of *all* slow roll inflation potentials. Our field has yet to develop the means to measure a non-zero r, let alone n_T to test this relationship. However, it is unlikely that any mechanism other than slow roll inflation would relate the two spectra in this specific way. Detecting scalar and tensor perturbations with this relationship would constitute (for many scientists) a "smoking gun" confirmation of the inflationary paradigm.

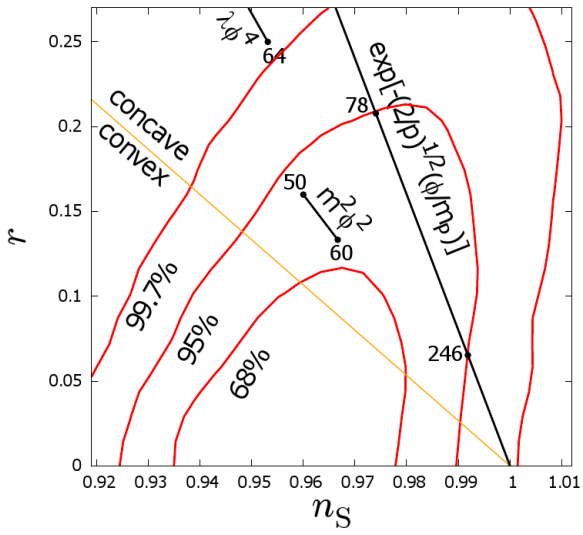

Figure 2.4. Large Scale structure data from Sloan Digital Sky Survey as well as CMB data from WMAP, ACBAR, QUAD, and BICEP constrain $r < 0.17$ and $n = 0.926 \pm 0.026$ a 95% confidence. Confidence contours are co-plotted with different inflation models, where the labeled points refer to the number of e-foldings. These data alread rule out a chaotic potential $\lambda\phi^4$ to high confidance. Figure from *Finelli et al.* [2010].

2.5 Temperature Anisotropies in the Microwave Background

The Microwave Background is not perfectly uniform in temperature; there are variations of 1 part in 100,000. These anisotropies are sourced by the metric perturbations discussed in the previous section and their time-evolution is modeled by the Boltzmann Equations. The Boltzmann Equations relate the statistical distribution of particles in different momentum states to the collision rates between these particles in a general way that does not require statistical equilibrium. A full discussion of this theory is beyond the scope of this thesis, and we just summarize results as needed in the remaining sections. We refer the interested reader to *Dodelson* [2003] and *Liddle and Lyth* [2000].

The Boltzmann Equations for the photons' anisotropic temperature $T(x, p, \eta) = T(\eta)[1 + \Theta(x, \hat{p})]$ are often decomposed into equations for different multipole moments:

$$\Theta_\ell \equiv \frac{1}{-i^\ell} \int_{-1}^{1} \frac{d\mu}{2} \mathcal{P}_\ell(\mu)\Theta(\mu)$$

where μ is the cosine of the angle between the wavenumber of the perturbation mode under consideration and direction of photon propagation and $\mathcal{P}_\ell$ is a Legendre Polynomial of order ℓ. For $\ell \geq 2$, the Boltzmann equations can be approximated as

$$\dot{\Theta}_\ell - \frac{k\ell}{2\ell+1}\Theta_{\ell-1} + \frac{k(\ell+1)}{2\ell+1}\Theta_{\ell+1} = \dot{\tau}\Theta_\ell \tag{2.8}$$

(*Hu and Dodelson* [2002]). Prior to recombination, the photons were tightly coupled to the electrons and nuclei. This era was characterized by photons having a mean free path much smaller than the Hubble radius ($\tau >> 1$), which suppresses the first and third terms of Equation 2.8, forcing $\Theta_\ell \sim \Theta_{\ell-1}/\tau$. As a result, only the first two moments were relevant before recombination. Combining the equations for the first two moments with a Boltzmann equation for the velocity of baryonic matter gives an equation for the photon monopole that is analogous to a driven and damped mechanical harmonic oscillator:

$$\left\{\frac{d^2}{d\eta^2} + \frac{\dot{R}}{1+R}\frac{d}{d\eta} + k^2 c_s^2\right\}[\Theta_o + \Phi] = \frac{k^2}{3}\left[\frac{1}{1+R}\Phi - \Psi\right] \tag{2.9}$$

where $R = 3\rho_b/4\rho_\gamma$ is the ratio of baryons to photons and $c_s = 1/\sqrt{3(1+R)}$ is the sound speed through the photon-baryon fluid (*Hu and Dodelson* [2002]). The combination of $\Theta_o + \Psi$ more closely relates to the observed temperatures than just Θ_o since the photons redshift as they climb out of the wells with a potential -Ψ.

Equation 2.9 says that modes of wavenumber k oscillate with a restoring force provided by the photon pressure (third term LHS) acting on the ionized baryonic matter while the gravitational wells assist compression (RHS). Inflation excites all modes with the same phase, so the most important are the harmonics reaching full compression or rarification at recombination; they are the modes that provide the CMB anisotropies with the greatest power. The age of the universe at recombination and the sound speed c_s determine the wavenumbers of these resonant modes. Cosmologies with higher baryon densities (larger R) will have lower sound speeds and hence lower wavenumber peaks in $\Theta_o + \Psi$.

The tight coupling approximation applies only to the largest scale modes. Over a Hubble time H^{-1}, the photons random walk a distance of

$$\lambda_D \sim 1/\sqrt{n_e \sigma_T H}$$

where σ_T is the scattering cross section and n_e the number density of electrons. Modes with wavelengths smaller than this are washed out, and so only the first few lowest wavenumber modes leave an observable imprint on the microwave background (*Dodelson* [2003]).

After recombination, the photons decouple from the baryonic matter and free-stream across the universe. Since $\tau \ll 1$ in a neutral universe, all terms of Equation 2.8 are relevant, and power leaks out of the first two multipoles and into the higher ℓ modes. Simply put, the modes with wavenumber k at recombination manifest themselves today as angular anisotropies with scale $\ell \sim k\eta_o$, where η_o is the Hubble radius of the last scattering surface. Cosmologists often resolve the observed photon energy into a basis of spherical harmonics:

$$\Theta(x, p, \eta) = \sum_{l=1}^{\infty} \sum_{m=-l}^{\ell} a_{\ell m}(x, \eta) Y_{\ell m}(p)$$

The coefficients' average should vanish $\langle a_{\ell m} \rangle = 0$, but the variance for a specific ℓ should not:

$$\langle a_{\ell m} a^*_{\ell' m'} \rangle = \delta_{\ell \ell'} \delta_{m m'} C_\ell$$

2.6 Parameters constrained by Temperature Anisotropies

Numerous experiments have measured the temperature anisotropies, and the results from WMAP and are shown in Figures 2.5 (*Larson et al.* [2010a]). The angular power spectrum has a series of pronounced harmonic peaks that are difficult to explain outside of an inflationary scenario. These measurements have had a profound influence on our understanding of the cosmos, allowing scientists to constrain multiple cosmological parameters

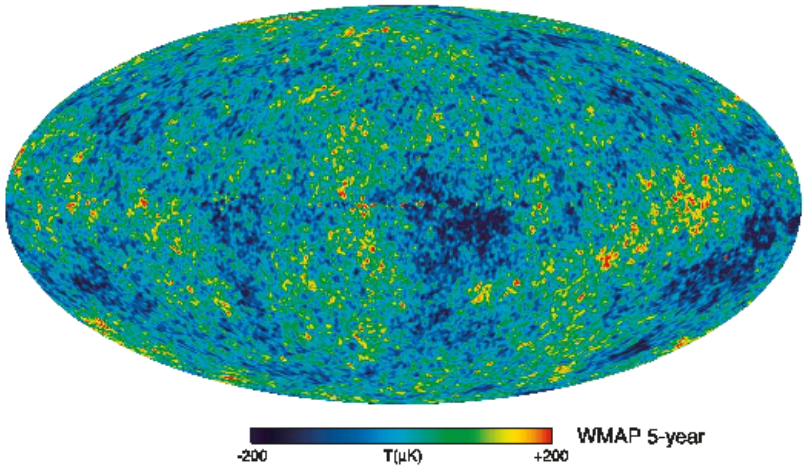

Figure 2.5. WMAP's full sky false color map of deviations in temperature from the 2.71K average. Figure from *Larson et al.* [2010a]

summarized in Table 2.1 (*Komatsu et al.* [2010]). While this is accomplished through likelihood estimators, many of the parameters have an intuitive connections to the features of the spectrum in Figure 2.6.

2.6.1 Curvature

The CMB has been used to demonstrate that the universe is geometrically flat on the largest observable scales. Were the universe not flat, rays that were initially parallel would converge or diverge and the original inhomogeneities discussed in the previous section would be projected onto respectively smaller or larger angular scales. The first anisotropy peak sits at $\ell \sim 200$, which is consistent with a flat Universe with $\Omega_K = 0$ and implies, from the Friedmann Equation, that the universe has a critical density ρ_c. The flatness of the universe is one of the key predictions of inflation confirmed by the CMB's angular power spectrum.

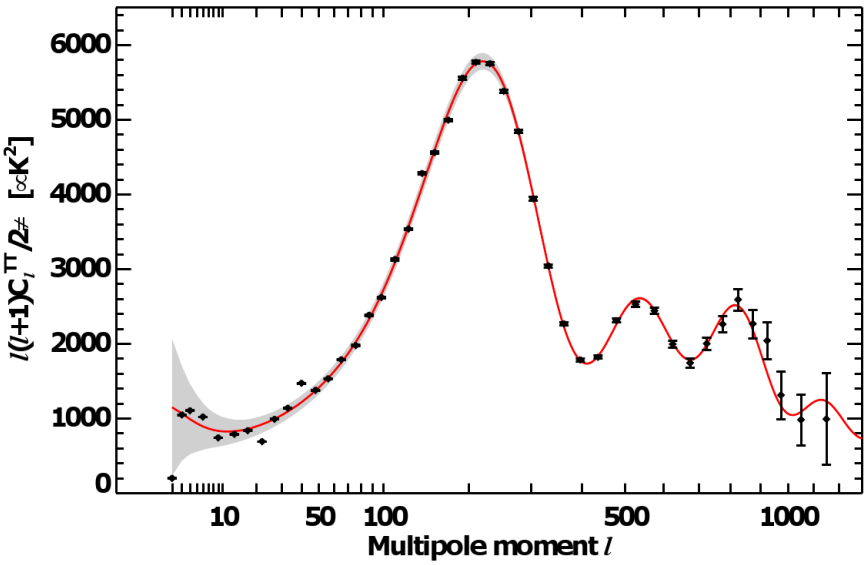

Figure 2.6. CMB Temperature Angular Power Spectrum of the full sky from seven years of WMAP data. This plots variance of spot temperature vs reciprocal of spot size Figure from *Larson et al.* [2010a].

2.6.2 Baryon Density

The right-hand side of Equation 2.9 is a driving term that introduces a particular solution in addition to the homogeneous terms, causing an offset to the zero point of oscillations. Since the observed temperature fluctuations are proportional to the variance of $\Theta_o + \Psi$, this offset will enhance the odd peaks while suppressing the even ones. This effect will be stronger for lower resonant wavenumbers, and hence larger values of R.

As a result, the ratio of the heights of the even and odd peaks can be used to constrain R. Since the photon density is tightly constrained by the CMB temperature, the baryon density was thus determined to be $\Omega_b = 0.0449 \pm 0.00288$. This figure is consistent with measured deuterium abundances in high redshift quasars when compared against the theory of Big Bang Nucleosynthesis, but it places an even tighter constraint than those measurements.

2.6.3 Matter Density

A cosmology with a low matter density will have an epoch of matter-radiation equality that is closer to recombination. Since the photons are neither able to cluster nor help gravitational wells grow, those gravitational modes that re-enter the horizon long before recombination decay away. The photons that compress into such a decaying gravitational well will see a lowered potential barrier when they rarify and can emerge much hotter. This effect results in enhanced power in the smaller acoustic peaks for lower matter density and has been used to constrain $\Omega_{CDM} = 0.222 \pm 0.026$.

2.6.4 Scalar Spectral Index

Equation 2.7 defines the scalar spectral index, where a scale-invariant power would correspond to $n_S = 1$. If $n_S < 1$, then the power in the gravitational wells, and hence the CMB anisotropies, will be smaller at small scales resulting in a tilt to the spectrum. Since the spectrum is often normalized around a point point of $\ell = 10$, this effect becomes very pronounced at the high-ℓ end of the spectrum focused on by ACBAR. By assuming that there is no running scalar-index (i.e, n_s is not a function of k), WMAP and ACBAR data constrain $n_S = 0.964 \pm 0.0114$ (*Komatsu et al.* [2010]).

Table 2.1. Parameters constrained from 7-year WMAP data set

Parameter	Fit	Description
$100\Omega_b h^2$	$2.258^{+0.057}_{-0.056}$	Baryon density
$\Omega_{CDM} h^2$	0.1109 ± 0.0056	Cold Dark Matter density
Ω_Λ	0.734 ± 0.029	Dark Energy density
Ω_k	$0.080^{+0.071}_{-0.093}$	Curvature density
n_S	0.964 ± 0.0114	Scalar Spectral Index
r	< 0.36 (95% CL)	Tensor Scalar Ratio
Σm_ν	$< 1.3eV$ (95% CL)	Neutrino mass sum
t_o	13.75 ± 0.13 Gyr	Current Age of the Universe
H_o	71.0 ± 2.5 km/s/Mpc	Current Hubble Parameter, $H = 100h$

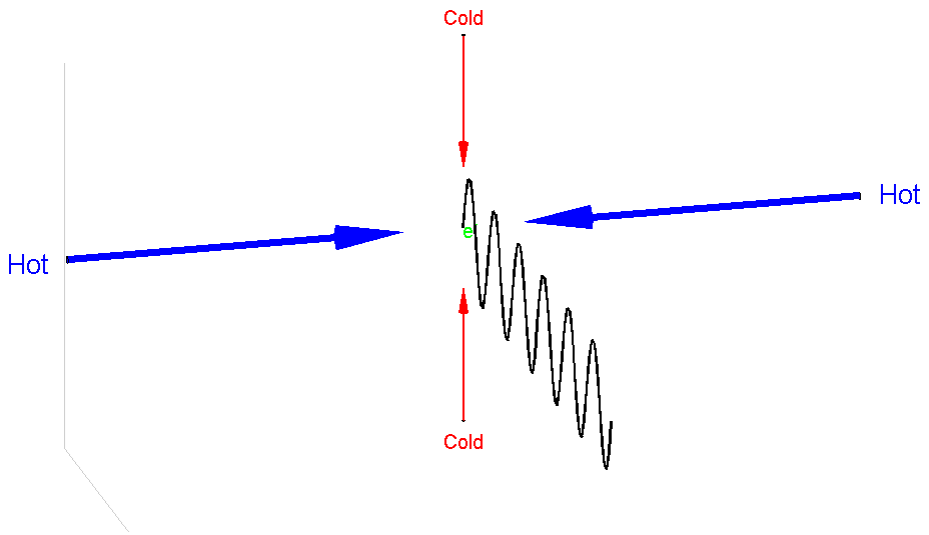

Figure 2.7. A Cartoon illustrating how Thomson scattering can convert a quadrupolar temperature distribution into polarized signal. In this case, the hot regions (blue) on the left and right drive the electron in vertical oscillations harder than the cooler region (red) above and below drive horizontal oscillations, resulting in scattered radiation that is partially polarized in the vertical, as depicted in black This figure is adapted from one in *Hu and White* [1997].

2.7 E mode Polarization Anisotropies

The Microwave Background is also polarized and mapping this is now the primary occupation in our field. This polarization arises because the CMB photons Thomson scatter off the primordial plasma. A photon traveling in the direction $\hat{n}^{inc}$ with polarization $\hat{\epsilon}(\hat{n}^{inc})$ will scatter off charged particles into the direction $\hat{n}$ and polarization $\hat{\epsilon}(\hat{n})$ with a cross section proportional to

$$\sum_{j=1}^{2} |\epsilon_i(n^{\hat{inc}})\epsilon_j(\hat{n})|^2 \tag{2.10}$$

(*Rybicki and Lightman* [1979]). Figure 2.7 shows a cartoons that is often cited to intuitively explain how polarization arises from Thomson scattering (*Hu and White* [1997]). If a scattering particle is illuminated uniformly, it will scatter unpolarized light. But if it is illuminated with hot sources along the $\hat{x}$ axis, but cool along the $\hat{y}$ axis, it will scatter light with a vertical partial polarization.

The polarization of light with wavevector in the $\hat{z}$ direction is characterized by the Stokes parameters (*Rybicki and Lightman* [1979]):

$$\begin{aligned} I &\equiv E_x^2 + E_y^2 \\ Q &\equiv E_x^2 - E_y^2 \\ U &\equiv E_{x+y}^2 - E_{x-y}^2 \\ V &\equiv E_{x+iy}^2 - E_{x-iy}^2 \end{aligned} \tag{2.11}$$

I is simply the intensity. Q is the difference in power polarized along $\hat{x}$ and $\hat{y}$ while U is that difference in power polarized on the pair of axis rotated 45^o from $\hat{x}$. These characterize the magnitude and orientation of linear polarization. V quantifies how circular the polarization is by differencing the two chiralities. Thompson Scattering should not produce circular polarizations, so V is expected to be zero.

Let the incident light upon a scattering particle have a temperature distribution $\Theta(k, \hat{k} \cdot \hat{n}^{inc})$, where k is the wavevector of a single acoustic mode. If we are positioned such that we only see light scattered in the $\hat{n} = \hat{z}$ direction, inserting Equation 2.10 into Equations 2.11:

$$\begin{pmatrix} Q \\ U \end{pmatrix} \propto \int d\Omega' \Theta(n') \sum_{j=1}^{2} \begin{pmatrix} \left|\hat{x} \cdot \hat{\epsilon_j}'\right|^2 - \left|\hat{y} \cdot \hat{\epsilon_j}'\right|^2 \\ \left|(\hat{x} + \hat{y}) \cdot \hat{\epsilon_j}'\right|^2 - \left|(\hat{x} - \hat{y}) \cdot \hat{\epsilon_j}'\right|^2 \end{pmatrix} \tag{2.12}$$

$$\propto \int d\Omega' \Theta(n') \begin{pmatrix} Y_{2,2}(\theta', \phi') + Y_{2,-2}(\theta', \phi') \\ Y_{2,2}(\theta', \phi') - Y_{2,-2}(\theta', \phi') \end{pmatrix} \tag{2.13}$$

which vanishes for all multipole moments of $\Theta(n')$ aside from $\ell = 2$ (*Kosowsky* [1996]). For a scalar mode traveling with a wavenumber in the $\hat{x}$ axis, the relevant moment is

$$\Theta(k, k \cdot \hat{n}^{inc}) \propto \Theta_2(k) \mathcal{P}_2(\hat{k} \cdot \hat{n}^{inc}) \tag{2.14}$$

So $Q(\hat{(}z), k) \propto \Theta_2(k)$ and $U(\hat{z}, k) = 0$ in that specific situation. More generally, the

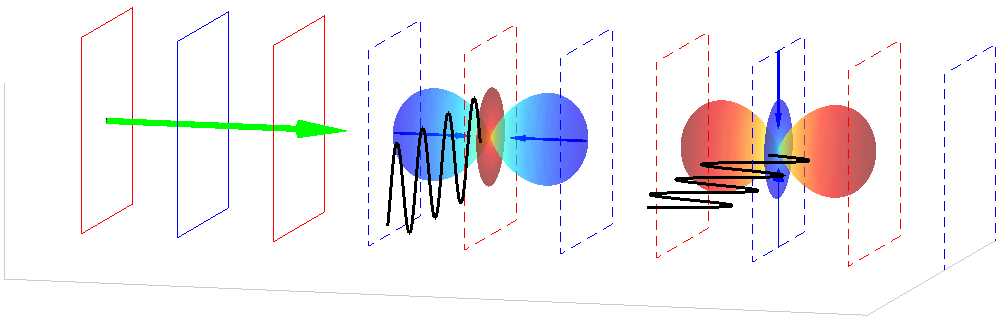

Figure 2.8. Cartoon illustrating E-mode polarization from a single fourier mode of scalar perturbation. Cool regions are red, hot are blue and the blue arrows represent the strongest incident optical power onto the charged particle. The scattered light is partially polarized, and the wave of the strongest polarization is depicted in black. Note that this must be either parallel or perpendicular to the wavevector (green) and hence the temperature gradient.

stokes parameters of photons scattering off a scalar mode traveling in the direction $\hat{k} = (\sin(\theta_k)\cos(\phi_k), \sin(\theta_k)\sin(\phi_k), \cos(\theta_k))$ are

$$\begin{pmatrix} Q \\ U \end{pmatrix} \propto (1 - (\hat{n}\cdot\hat{k}))^2 \Theta_2(k) \begin{pmatrix} \cos(2\phi_k) \\ \sin(2\phi_k) \end{pmatrix} \equiv \Theta_p(\hat{n}\cdot\hat{k}) \begin{pmatrix} \cos(2\phi_k) \\ \sin(2\phi_k) \end{pmatrix} \tag{2.15}$$

Just like the temperature anisotropies, the full distribution of polarized light $\Theta_P(k,\mu)$ is governed by a Boltzmann Equation. In the strong coupling limit, this reduces to the qradrupole distribution in Equation 2.14. After recombination, power from $\ell = 2$ leaks into the higher-ℓ anisotropies

$$\Theta_{P\ell}(k) \simeq -\frac{5k\Theta_1(k,\eta_*)\ell^2 j_\ell(k\eta_o)}{6\dot{\tau}(k\eta_o)^2} \tag{2.16}$$

(*Kosowsky* [1996]). The key feature of this distribution is that the orientation of the polarization is always parallel or perpendicular to the gradient in temperature, as illustrated in Figure 2.8. After a parity flip, the polarization is still be parallel or perpendicular to that gradient: the pattern is even under parity. Since there is no directional information to a scalar mode aside from it's own wavevector, the scattered light has no choice but to be polarized parallel or perpendicular to these directions, and this property is preserved even after the photons free-stream and move power into the higher ℓ modes in Equation 2.16.

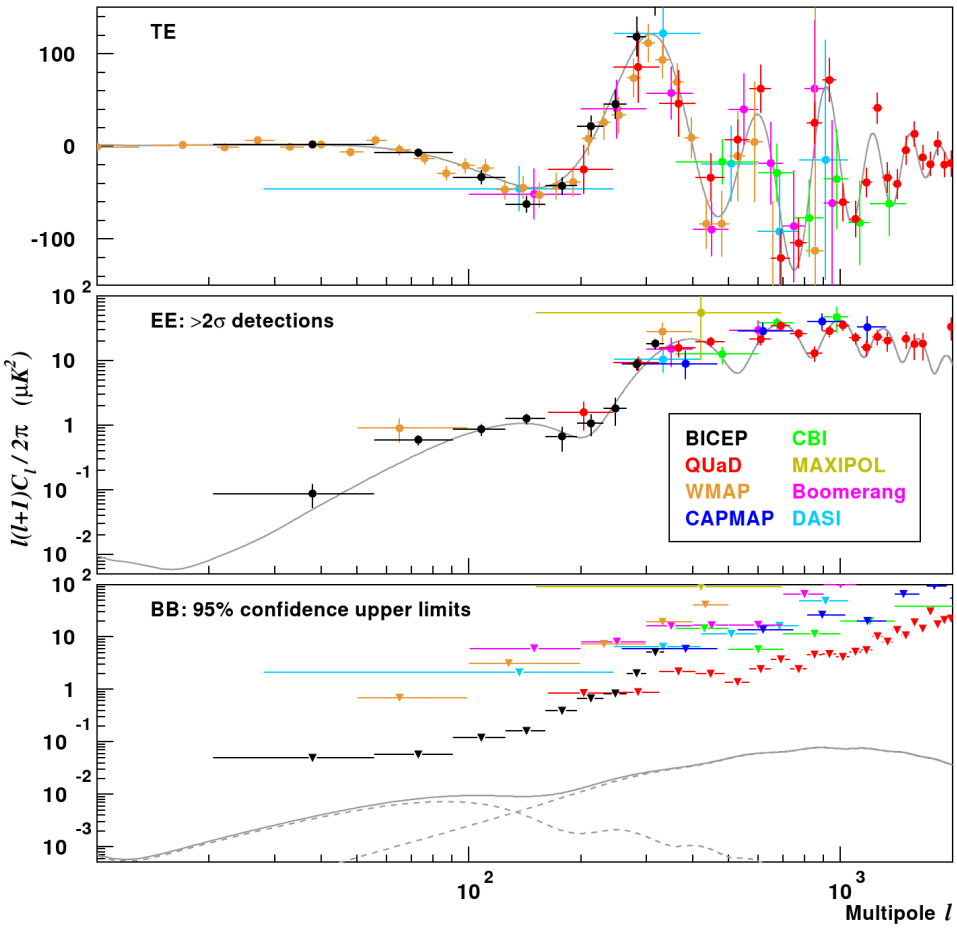

Figure 2.9. E-mode Angular Power Spectra from several experiments. Figure from *Chiang et al.* [2010].

The E-mode/B-mode decomposition reveals this underlying even-symmetry:

$$E(\ell) \equiv Q(\ell)\cos(2\phi_\ell) + U(\ell)\sin(2\phi_\ell)$$

$$B(\ell) \equiv -Q(\ell)\sin(2\phi_\ell) + U(\ell)\cos(2\phi_\ell)$$

where in this equation, ℓ is a vector projected on the sky making an angle ϕ_ℓ with respect to the $\hat{x}$-axis. For the even symmetry scalar mode generated patterns, $C_{BB}(\ell) = 0$ and $\lim_{\ell \gg 1} C_{EE}(\ell) = C_{P,\ell}$ (*Challinor and Peiris* [2009]). Recently, several experiments have measured these spectra as shown in Figure 2.9.

The EE spectra, particularly those measured by BICEP and QUAD, show similar fring-

ing as the temperature spectrum (Figure 2.6). However, the dipole moment at recombination primarily sourced the E-modes, in constrast the temperature anisotropies that were sourced by both monopole and dipole terms. As a result, the E-modes are a half-cycle out of phase from the temperature peaks, as revealed in the TE correlation spectrum. And because E-modes are only sourced by one moment, the peaks have a higher fractional power compared to the Temperature. Additionally, it's power is lower by an order of magnitude because the multipole moments at recombination drop by factors of $\dot{\tau}$ for each increase in ℓ. Finally, the B-mode power spectrum is consistent with zero, as predicted by the spectrum sourced by scalar perturbations.

2.8 B mode Polarization Anisotropies

Scalar modes are not the only polarization source in the CMB. Tensor perturbations also generate temperature quadrupole moments, but unlike the scalar perturbations, they have their own $(h_+, h_\times)$ polarization as well. This additional structure that is absent from the scalar modes allows the polarized photons to scatter into both even and odd parity patterns, as illustrated in the cartoons in Figure 2.10.

Photons were incident upon particles at last-scattering from all directions $\hat{n}^{inc} = (\sin(\theta)\cos(\phi), \sin(\theta)\sin(\phi), \cos(\theta))$. A tensor mode traveling in the $\hat{z}$ direction with polarization $h_\times$ has an angular dependence

$$\Theta^T \propto \sin^2(\theta)\sin(2\phi) = 2n_x^{inc}n_y^{inc}$$

For a gravity wave propagating in the general direction $(\sin(\theta_k)\cos(\phi_k)$ $, \sin(\theta_k)\sin(\phi_k), \cos(\theta_k))$, the general temperature distributions is just the result of rotating the $\hat{n}^{inc}$ by a matrix $\tilde{R}$ that would put $\hat{k}$ back along the $\hat{z}$ axis.

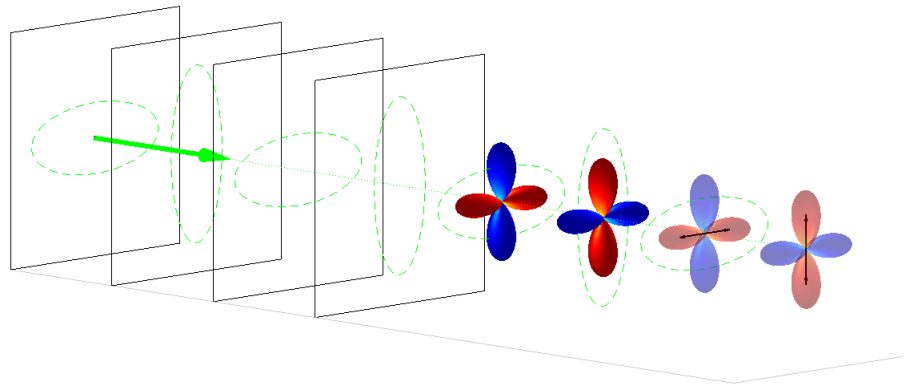

(a) E-modes from h_+ Gravity waves

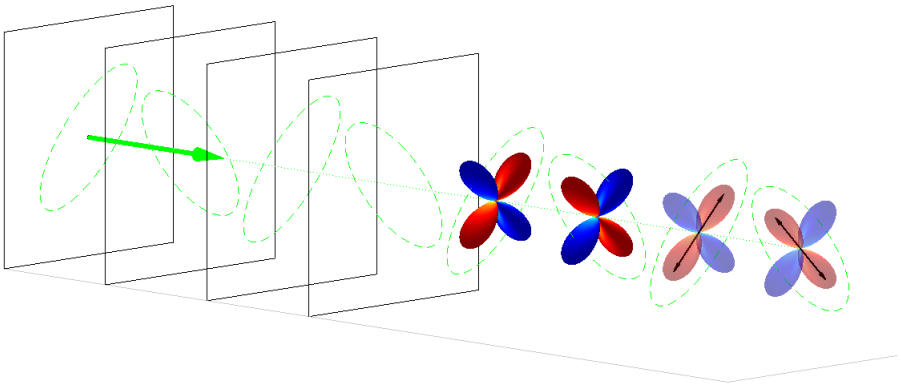

(b) B-modes from $h_\times$ Gravity Waves

Figure 2.10. Cartoons illustrating E-mode and B-mode polarization from a single fourier modes of tensor perturbations (gravity waves). Cool regions are red, hot are blue. The axis with the highest amplitude of electron oscillation is denoted with the double-headed black arrows. This will be the plane of oscillation, projected onto the sky. Note that in 2.10(b), the polarization is at a 45^o angle to the wavevector (in green) and hence temperature gradient. This Figure is adapted from one in *Kovac* [2004].

$$\begin{aligned}\Theta^T &\propto (\tilde{R}n^{inc})_x(\tilde{R}n^{inc})_y \\ &\propto \cos(\theta_k)\left[e^{-i2\phi_k}Y^*_{2,-2}(\theta,\phi) - e^{i2\phi_k}Y^*_{2,2}(\theta,\phi)\right] + \\ &\quad \sin(\theta_k)\left[e^{-i\phi_k}Y^*_{2,-1}(\theta,\phi) - e^{i\phi_k}Y^*_{2,1}(\theta,\phi)\right]\end{aligned}$$

(*Dodelson* [2003]). From Equation 2.13, the Q and U components pick out only the $m = 2$ Harmonics, yielding

$$\begin{pmatrix} Q \\ U \end{pmatrix} \propto \Theta_0^T(k)\cos(\theta_k) \begin{pmatrix} -\sin(2\phi_k) \\ \cos(2\phi_k) \end{pmatrix} \simeq \Theta_0^T(k)\hat{n}\cdot\hat{k} \begin{pmatrix} -\sin(2\phi_k) \\ \cos(2\phi_k) \end{pmatrix}$$

This results in a pure B-mode signal, one who's polarization is oriented 45^o from the intensity gradient. A similar analysis of h_+ polarized gravity waves would yield a pure E-mode contribution:

$$\begin{pmatrix} E \\ B \end{pmatrix} \propto \hat{n}\cdot\hat{k} \begin{pmatrix} h_+ \\ h_\times \end{pmatrix}$$

When a tensor perturbation re-enters the horizon, causal physics described by Equation 2.6 determine it's time evolution. The second term sourced by the Universe's expansion acts as a damping term and the waves rapidly decay away. As a result, there should be a strong peak in the B-mode anisotropy spectrum corresponding to the modes that were just re-entering the horizon at recombination and greatly suppressed power at other angular scales (see Figure 2.11). Additionally, the effects of Tensor perturbations on the Temperature power spectrum are degenerate with the Scalar perturbations. However, this B-mode signature cannot be produced by Scalar modes and can in principle be used to determine the tensor-to-scalar ratio r. As of the writing of this thesis, non-zero CMB B-modes have not been detected.

2.9 Gravitational Lensing

The CMB should be distorted by gravitational wells between us and the last scattering surface by lensing. Following an order of magnitude calculation from Lewis and Chanllinor (*Lewis and Challinor* [2006]), the impact on the temperature power spectrum will be minor. If only point sources of well depth 3×10^{-5} lens the CMB photons, then they will be deflected $\delta\alpha \sim 4\Psi \sim 1.2\times10^{-4}$. Since the matter power spectrum suggests that most of these wells have a comoving diameter of $\sim$ 150 Mpc, there should be around 100 such wells between us and the last scattering surface 14000 Mpc away. So the total random walk of the CMB

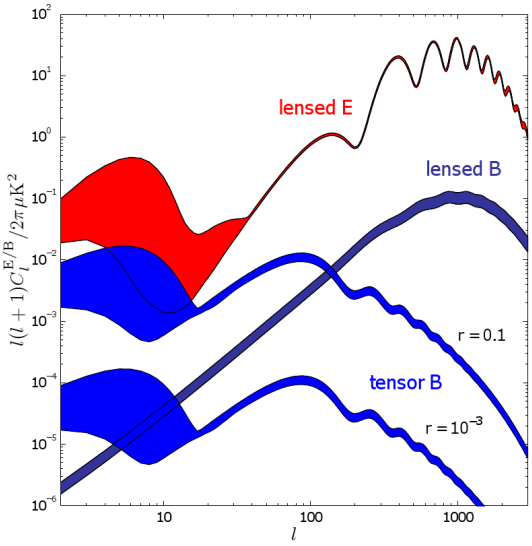

Figure 2.11. Simulated E-mode and B-mode angular power spectra. The lensing B-modes (see section 2.9) are separated from the primordial B-modes with $r = 0.1$ and $r = 10^{-3}$ possibilities. These were compiled with data available in 2006, displaying the 95% confidance intervals. Figure from *Lewis and Challinor* [2006].

photons will experience a total deflection of $\sqrt{10} \times 1.2 \times 10^{-4} \sim 1 \times 10^{-3}$ rad, or roughly 3 arcmin. This means that the lensing contribution only dominates on scales in excess of $\ell \sim 2000$. Lensing can have a subtle impact on the acoustic peaks because, for lensing sources half-way to last-scattering, the lensing will be correlated on scales 150/7000 rad $\sim 1.2^o$. This effect distorts the anisotropies at a $0.05^o/1.2^o \sim 2.5\%$ which will widen the accoustic peaks at the percent level.

However, lensing will have a more pronounced impact on the polarization. Lensing will distort the CMB photons' propagation direction by $d = \nabla\phi$, where the well-known lensing potential can be written as an integral over the gravitational potentials $\Psi(z)$:

$$\phi = 2\int_0^{z_{CMB}} \frac{dz}{H(z)} \frac{\chi(z) - \chi(z_{CMB})}{\chi(z)\chi(z_{CMB})} \Psi(z)$$

and where $\chi(z)$ is the comoving distance to a lensing well at redshift z. The stokes parameters will be modified by $X(\hat{n}') = X(\hat{n} + d)$, where X can be I, Q, or U. Even though lensing will not mix Q and U, it will shear E into B and vise versa (*Lewis and Challinor*

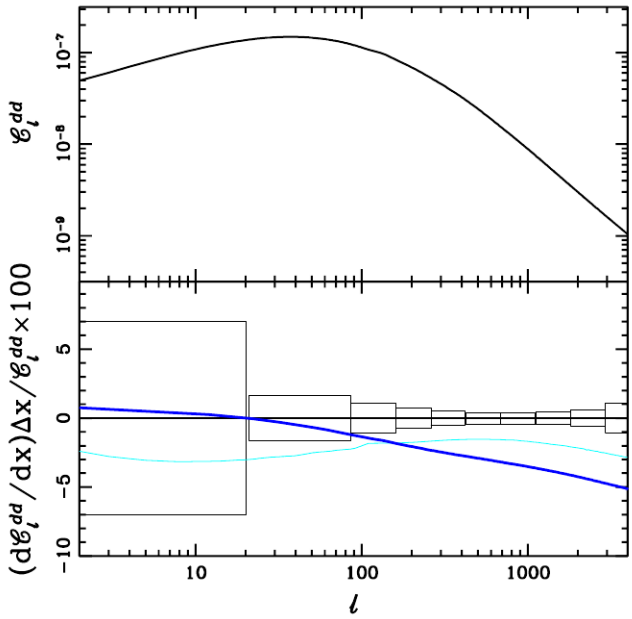

Figure 2.12. Simulated angular power spectrum for the lensing deflection angle $C_\ell^{dd} \equiv \ell(\ell+1)C_\ell^{phi}$. The top panel is simulated for $m_\nu = 0$ while the bottom shows deviations for $\Delta m_\nu = 0.1$ eV and $\Delta w = 0.2$. Figure from *Kaplinghat et al.* [2003]

[2006]). In particular, the much hotter E-modes will be partially reprocessed into B-modes with an angular power spectrum

$$C_\ell^B = \int \frac{d^2\ell'}{(2\pi)^2} \left[\ell' \dot{(}\ell - \ell')\right]^2 C^\phi_{|\ell-\ell'|} C^E_{|\ell'|} sin^2 2(\theta'_\ell - \theta_\ell) \tag{2.17}$$

where C^{phi} is the angular power spectrum of the lensing potential. This results in a lensing B-mode contribution shown in Figure 2.11 ((*Lewis and Challinor* [2006])).

While this may dominate over the primordial B-modes for many possible values of r, it will likely be scientifically interesting in it's own right. The lensing signal should be sensitive to parameters that impact structure formation late in our universes history, specifically the sum of the three generations of neutrino masses and the dark energy equation of state.

Figure 2.12 shows the simulated power spectrum for the lensing deflection angle as well as distortions from a change in total neutrino mass Δm_ν=0.1eV and the dark energy equation of state Δw=0.2. Massive neutrinos do not cluster on scales smaller than their Jean's length, which decreases as the universe cools. However, we do expect neutrinos to

cluster at scales larger than their jean's length at matter-radiation equality, which results in a slight decrement of power at high-ℓ.

Conversely, dark energy drives cosmic acceleration and suppresses structure at late times. As a result, it will suppress the deflection angle power spectrum more at low-ℓ. These two effects are sufficiently distinct that they may be simultaneously constrained by measurements of the lensing B-mode signature (*Kaplinghat et al.* [2003]).

The primordial B-modes will likely be dominated by lensing, but there are several proposals to mitigate this possibility should it arise. Maps that cover large portions of the sky from Plank and SPIDER may be sensitive to the B-mode reioniation peak at $\ell \sim 7$ where lensing is very weak. Additionally, the lensing statistics is non-gaussian, as seen from Equation 2.17 that convolves two gaussian distributions. There are several proposals that exploit this non-gausianity of the lensing distribution to statistically de-lens maps and possibly allow for detection of B-modes at the reionization peak even if r is very small.

2.10 Polarized Galactic Foregrounds

Efforts to detect B-mode polarization will likely be confounded by contamination from polarized galactic foregrounds. As of the writing of this thesis, few CMB experiments have had to remove these sources, but that may change in the near future as we seek to map the sky's millimeter polarization to even finer levels. Synchrotron emissions and thermal dust emissions are most likely the strongest foreground sources. Fortunately, they bear different spectral signatures than the CMB's 2.7K blackbody spectrum, so in principle, they can be characterized and removed from millimeter-wavelength maps if the sky is mapped at multiple frequency channels. For a foreground model with N components, an experiment will need at least $N + 1$ channels to remove the foregrounds from a CMB map. The spectral properties of synchrotron and thermal dust emissions are summarized in the next two subsections.

2.10.1 Synchrotron Emission

Synchrotron radiation is emitted by cosmic rays that are accelerated by the galactic magnetic field. The antenna temperature of these emissions is $T(\nu) \propto \nu^{\beta}$, where the exponent $\beta = -(p+3)/2$ is related to the power law for electron energies $N(E) \propto E^{-p}$. Synchrotron radiation can have a strong fractional partial polarization of

$$f = \frac{p+1}{p+7/3}$$

aligned with the magnetic field lines. For microwave frequencies with $\beta \approx -3$, this can be as high as 0.75, but line of sight averaging tends to reduce this significantly.

Mapping this foreground in the millimeter spectral range is still an active area of research, but the WMAP satellite has contributed significantly to our understanding of it. WMAP mapped the sky at five spectral bands spanning a microwave/millimeter range of 23GHz to 94GHz. For coarse 3.7^o pixels, the dominant polarization was consistent with a Synchrotron source with $\beta \approx -3$ (See figure 2.13). The precise synchrotron spectral index varied with position on the sky, dropping to -3.25 at 75^o off the galactic plane. This models will no doubt increase in complexity as higher resolution maps are made. Finally, the increased power in the 94GHz channel is consistent with thermal dust emissions with $\beta \approx 2$ discussed in the next subsection (*Kogut et al.* [2007]).

2.10.2 Thermal Dust Emission

Aspherical dust particles with strong magnetic moments can be aligned to magnetic fields in the interstellar medium, often with their longest axis perpendicular to the fields. As a result, they absorb and emit radiation with a partial polarization perpendicular to the field lines.

Dust emissions are frequently modeled as multiple thermal components with a frequency-dependent emissivity: $I(\nu) \sim \nu^{\beta} B_{\nu}(T)$. While these sources are expected to dominate over synchrotron emissions for frequencies above 100GHz, there is little data cur-

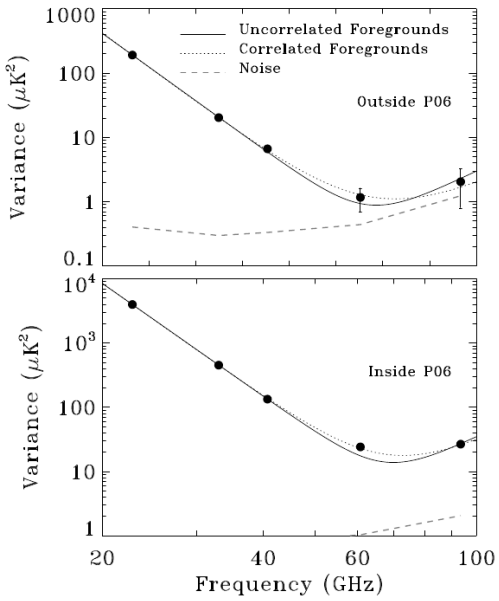

Figure 2.13. Polarized Foreground emissions from WMAP. They are consistent with a synchrotron emissions model with $\beta \approx -3$ except for the two highest frequency channels that are best described with a thermal dust emission model. Note that the foreground contributions decrease off the galactic plane. Graphi from *Kogut et al.* [2007]

rently available in the millimeter range. Data from the COBE satellite's Diffuse Infrared Background Experiment(DIRBE) mapped the sky with 6^o resolution at 100 μm and 240 μm (3000GHz and 1250GHz). These maps have been modeled with two components at Temperatures 9.5K and 16K, with β of 1.7 and 2.7 respectively (*Finkbeiner et al.* [1999]). However, the High Frequency Instrument (HFI) on the Plank satellite has six bands between 100GHz and 857GHz, the lowest four of which have polarization sensitivity. This instrument will like provide much more data on this in the near future.

2.11 Conclusions

Recent success in measuring the CMB's temperature and polarization anisotropies have driven the rapid progress in Cosmology over the past decade. There are potentially even greater rewards for those who can successfully separate the B-mode polarization from CMB

maps. However, these signals are extraordinarily weak and will likely be masked by polarized emissions from our own galaxy.

While existing technology has enabled great strides, it is unlikely to suffice for future CMB polarization measurements. As a field, we will need both increased optical throughput in our telescopes coupled with the ability to spectrally differentiate foregrounds from cosmic signals. Absent these motivations, the detector work described in this thesis is still an interesting exercise in electromagnetic design. However, with these cosmological challenges in mind, the novel design methodology may enable otherwise impossible advances in fundamental physics.

Chapter 3

Transition Edge Sensor Bolometers

3.1 Introduction

Transition Edge Sensor (TES) bolometers have enabled large detector arrays for several applications, including CMB measurements. Experiments such as SPT and ACT succeeded in their goals largely because of this technology and up-coming CMB polarimetry will depend on it as well. All millimeter devices fabricated and tested in this thesis used TES bolometers for the on-chip detectors.

The beginning of this chapter motivates TES bolometers by juxtaposing them with competing technologies, specifically HEMTS and NTD bolometers, in order to highlight the deficiencies that TESs avoid. We discuss the principle of electrothermal feedback and derive stability criteria and sensitivity equations. Finally, we describe how the bolometers in this thesis were fabricated as well as the electronics used to read them. Throughout the chapter, we show data from dark measurements of our bolometers demonstrating acceptable transition temperatures, saturation powers, and time constants. We describe the cryogenic dewar used for these measurements in detail in Chapter 6.

3.2 Quantum Mechanics of Detection

The paper "Thermal Noise and correlations in photon detection" (*Zmuidzinas* [2003b]) provides a useful framework that motivates many of our own design decisions, including those in chapters 7 and 8. We refer the reader to this paper for a more detailed description and only summarize the relevant results here.

Detectors can be regarded as a circuit where photons incident on the input port $i = 1$ are created by operator $a_1^\dagger(\nu)$ and those at the output ports $j \neq 1$ (connected to bolometers) are created by operators $b_j^\dagger(\nu)$ given by:

$$b_j^\dagger(\nu) = S_{1j} a_1^\dagger(\nu) + c_j^\dagger \tag{3.1}$$

where $c_j^\dagger$ create noise photons at the bolometer j and S_{ij} is the scattering matrix discussed in Chapter 4. In the time domain, a bolometer in a pixel with low internal noise ($c_j^\dagger \approx 0$) receives power created by $b_i^\dagger(t) = \int_o^\infty d\nu \sqrt{h\nu} \exp(i2\pi\nu t) b_i^\dagger$. If the incident photons are thermal with distribution $\left\langle a_o^\dagger(\nu) a_o(\nu') \right\rangle = n_0(\nu)\delta(\nu - \nu')$ where $n_o(\nu)$ is a plank function, then over a time τ, the bolometers will receive energy

$$\begin{aligned} \langle d_i \rangle &= \tau \int_o^\infty \left\langle b_i^\dagger(t) b_i(t) \right\rangle \\ &= \tau \int d\nu h\nu \left| S_{i1}(\nu) \right|^2 n_o(\nu) \end{aligned} \tag{3.2}$$

with variance

$$\begin{aligned} \sigma_{ij}^2 &= \langle d_i d_j \rangle - \langle d_i \rangle \langle d_j \rangle \\ &= \tau \int d\nu (h\nu)^2 \left| S_{i1}(\nu) \right|^2 n_o(\nu) \delta_{ij} - \tau \int d\nu (h\nu)^2 \left| S_{i1}(\nu) \right|^2 \left| S_{j1}(\nu) \right|^2 n_o^2(\nu) \\ &= \tau \int d\nu (h\nu)^2 \left| S_{i1}(\nu) \right|^2 n_o(\nu) \left(\left| S_{i1}(\nu) \right|^2 n_o(\nu) + 1 \right) \end{aligned} \tag{3.3}$$

Equations 3.2 and 3.3 apply to direct detectors, including bolometers. Alternatively, a receiver can include a high frequency amplifier (like a High Electron Mobility Transistor, or

HEMT), but this contributes additional "quantum noise" through the operator $c_j^\dagger$. Quantum noise arises when the detector Nyquist samples incoming radiation, but suffers a noise penalty in power from the Uncertainty Principle while sampling on such a short time scale. These photons adds to the energy and covariance in Equations 3.2 and 3.3, the details of which are discussed in *Zmuidzinas* [2003b].

3.3 Competing Technologies to TES Bolometers

3.3.1 Coherent Receivers

The microwave background poses a unique decision tree to experimental cosmologists because it's statistical occupation number $n_{CMB} = (\exp(h\nu/kT) - 1)^{-1}$ is approximately unity for the frequencies of interest in most experiments. By contrast, optical astronomers typically observe radiation in the Wein Tail of a Plank distribution where $h\nu \gg kT$ and so $n \ll 1$. Meanwhile, radio astronomers often observe in the Rayleigh-Jean's limit where $h\nu \ll kT$, corresponding to a large occupation $n \gg 1$. While these limits motivate the researchers in each field to build very different styles of detectors, cosmologists observing the CMB work in the occupation number cross-over regime where both sets of detection techniques can be appropriate.

The Noise Equivalent Power (NEP) is the incident power required to achieve a signal-to-noise ratio of unity over 0.5s of integration. For a background-limited detector whose greatest source of noise is that present in the incoming radiation itself,

$$NEP^2 = 2(h\nu)^2 \Delta\nu \frac{n(\nu)(1 + \eta n(\nu))}{\eta} \tag{3.4}$$

where η is the efficiency of absorption and $\Delta\nu$ is the bandwidth (*Zmuidzinas* [2003b]). We can construct this equation from the ratio of Equations 3.2 and 3.3 evaluated in the special case of a two-port circuit with $|S_{12}(\nu)|^2 = |S_{21}(\nu)|^2 = \eta < 1$. If that same detector is preceded by HEMT, then all scattering matrix elements vanish except $|S_{21}(\nu)|^2 = G(\nu) \gg 1$,

representing a large gain. In this limit, the NEP (referenced to pre-amplified input power) reduces to

$$NEP^2 = 2(h\nu)^2 \Delta\nu \left(\frac{(1 + \eta n(\nu))}{\eta} \right)^2 \tag{3.5}$$

The noise for such a receiver includes not only the background noise, but also a residual quantum noise present even when the detector is kept dark with no incident radiation (*Zmuidzinas* [2003b]). The ratio of noise for direct (Equation 3.4) to coherent (Equation 3.5) detection is

$$\frac{NEP^2_{quantum}}{NEP^2_{direct}} = \frac{\eta n(\nu) + 1}{\eta n(\nu)}$$

If $n(\nu) \gg 1$, then the NEPs are equal and there is no penalty for coherent detection. However, for a background primarily of 2.7K CMB photons (in a spacecraft for example), this ratio exceeds two and the detector becomes quantum noise limited above 100GHz for most reasonable efficiencies.

Numerous researchers have justified using coherent systems by focusing on the Rayleigh Jeans portion of the spectrum or by using terrestrial telescopes whose loading is dominated by the atmosphere with an effective temperature $\sim 20K$ (e.g. TOCO, DASI, and QUIET). For temperature maps where the foregrounds could safely be ignored, this was a successful strategy. However, as mentioned in Section 2.10, the polarized foreground minimum is likely between 80 and 150 GHz, and experiments that control for scattering off dust will need to receive even higher frequencies. At these frequencies, quantum noise is unacceptably high for space or balloon borne experiments. Making matters even worse, HEMTs often operate with noise levels a factor of several higher than the quantum noise limit.

3.3.2 NTD-Ge Bolometers

All thermal radiation detectors used in direct detection schemes utilize an absorbing element with a heat capacity C. The absorber sits in weak thermal contact with a heat

bath through a conductive link with conductance $G \equiv \partial P/\partial T$. If the power deposited on the detector increases from P to P', then the absorber will approach a new temperature $T' = T + P'/G$ with a thermal time constant

$$\tau_o = \frac{C}{G} \tag{3.6}$$

We can determine the incident power P by measuring the detector temperature T'. Bolometers are a special class of thermal detector that use a thermistor to monitor this temperature (*Richards* [1994]).

One of the most successful bolometers used for millimeter and submillimeter detection is the NTD-Ge bolometer. These bolometers have a semiconducting Germanium thermistor whose band properties have been modified by Neutron Transmutation Doping (NTD). Experiments such as ACBAR, MAXIMA, and BOOMERanG, suspended these thermistors on released spiderweb-shaped absorbing structures in the back of horn antennas. The spiderwebs maintain the weak thermal link between the thermistor and heat-bath. They efficiently absorb the microwaves, but have a low cross section to cosmic rays.

The internal noise of most bolometers is dominated by phonon noise in the thermally conducting legs that connect the suspended absorber-thermistor structure to a surrounding heat bath:

$$NEP_G^2 = 4kT_{bolo}^2 G = \frac{4kT_{bolo}^2 P_{incident}}{T_{bath-T_{bolo}}}$$

This noise is minimized by operating the bolometer at roughly twice the bath temperature (*Richards* [1994]). For a focal-plane cooled with a ^{3}He sorption fridge, the bath temperature is roughly $T_{bath} \approx 250mK$, so most bolometers in systems like these are ideally operated at $T_{bolo} \approx 500mK$

The statistical noise associated with the incident photons' bose distribution is

$$NEP_\gamma^2 = 2\int P_{incident} h\nu d\nu + \int P_{incident}^2 d\nu$$

where the thermal blackbody distribution is

$$P_{incident} = \frac{2h\nu}{e^{h\nu/kT} - 1} \tag{3.7}$$

(*Pathria* [1996]) Typical optical loading on a terrestrial telescope from the CMB, atmosphere, and optics is between 5 and 20 pW, corresponding to a NEP_γ $10^{-16} W/\sqrt{(Hz)}$ (*Halverson* [2004]). By contrast, the typical thermal carrier noise in the legs is $NEP_G = 2\sqrt{(kT_{bath}P_{incident})} \sim 10^{-17}$. NTD Bolometers achieved background limited measurements in ground-based telescopes and were the state-of-the art detectors of the last decade.

Despite these successes, the NTD bolometers do have some short-comings. A telescope's mapping speed quantifies how long a unit area of the sky must be observed to achieve a desired signal to noise ratio. Once a telescope's detectors have been made background limited, the only way to increase the mapping speed is to increase the number of electromagnetic modes that the focal-plane recevies. Up to the throughput limit $A\Omega$ set by the focal-plane's area A and the telescope's field of view Ω, more modes can be received by increasing the number of detectors in the array. Numerous experiments that will map the CMB polarization over the next decade will have nearly 1000 detectors. However, NTD bolometers cannot be lithographed into monolithic arrays. Assembling kilopixel NTD arrays would be tedious, prone to poor yield, and require bulky mounting hardware that would inefficiently use the focal plane real estate compared to a monolithic array.

Additionally, if each detector in a kilopixel array were individually biased with separate lines, the wires would thermally load the 4K stage to an unacceptably high level. As a result, several research groups have started to use SQUID-based multiplexing (MUX) to read multiple detectors through one line. In these systems, some (or all) of the SQUIDs function as ammeters in series with voltage biased bolometers. However, the high impedance of NTD bolometers makes it impractical to operate in a voltage biased mode. Instead, researchers current bias the NTD bolometers and read the voltage with a JFET, but the bandwidth of most JFETs is too low for use in a MUX circuit (*Lanting* [2006]).

Finally, many proposed polarization experiments will rotate a half-wave plate at a few

hertz frequency in the optics between the secondary mirror and focal plane to control several systematic effects in the telescope. This scheme is only tenable if the detectors are robust against microphonic excitation. Mechanical vibrations can vary the distance between each of the bias wires or their distance to the ground plane, giving rise to capacitive fluctuations that act as a current source. The high impedance of NTD bolometers again creates a problem by converting this current into a very large voltage signal that contaminates the data time-stream. This effect proved to be a major challenge for the MAXIPOL project that continuously rotated a half-wave plate in front of an array of NTD bolometers (*Johnson et al.* [2003]).

3.4 TES Bolometers and Electrothermal Feedback

The Transition Edge Sensor (TES) bolometer is a new type of detector that addresses many of the above deficiencies (*Guildemeister* [2000]). Over the past five years, physicists have successfully deployed CMB-telescopes with TES-bolometers including APEX-SZ, ACT, and SPT and they will utilize TESs in several more instruments in the coming years including Polarbear, EBEX, BICEP-II, SPIDER, and the Keck Array.

A TES is a thin film of metal that is voltage biased into it's normal-superconducting transition (*Irwin and Hilton* [2005]). At these temperatures, the typical TES resistance is roughly 1Ω, making it robust against the vibrational pickup that plagues the NTD-Ge bolometers. Thanks to the low resistance, we can also use SQUID amplifiers to measure the current through the TES bolometers. The SQUIDs' high bandwidth naturally facilitates MUX readout schemes, alleviating thermal loading through the bias lines. Finally, we fabricate these detectors by lithographing and etching thin films of sputtered metals. As a result, we can build the densely populated monolithic arrays needed to scale up to kilopixel focal planes (*Chervenak et al.* [1999] and *Lanting et al.* [2005]).

Not only is the resistance of a TES low, but it changes rapidly with temperature in the transition. The dimensionless parameter

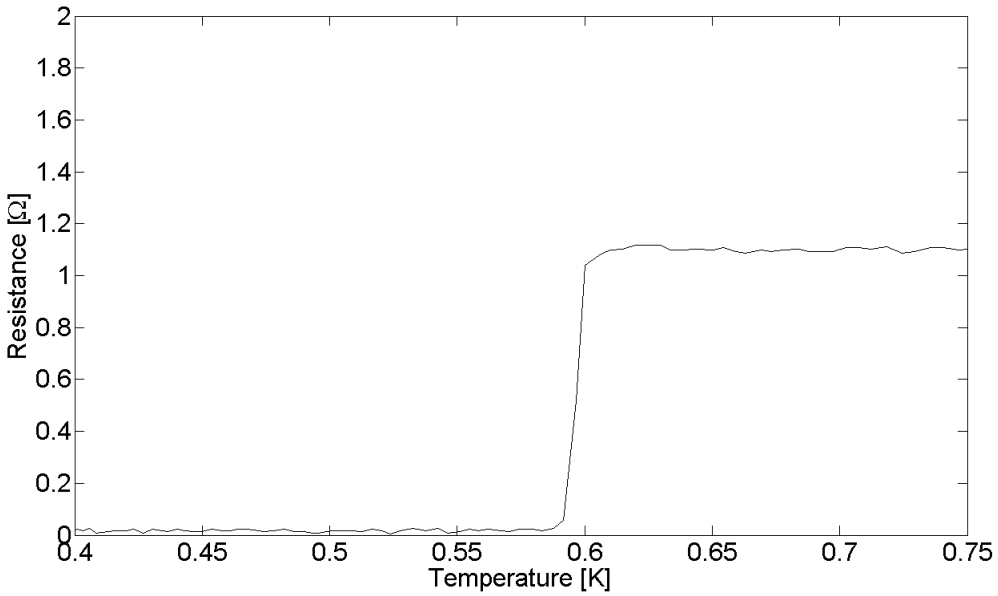

Figure 3.1. Resistance vs Temperature for a typical TES used in this thesis. This TES was unreleased, but was fabricated along-side fully functional bolometers. We monitored temperature with a Lakeshore GRT and measured the resistance with a four-point resistance bridge. For this film, $\alpha \approx 263$, $R_{normal} = 1.04\Omega$, and $T_c = 0.597K$

$$\alpha \equiv \frac{d(\log R)}{d(\log T)} = \frac{T}{R}\frac{dR}{dT}$$

characterizes the slope of this temperature dependence (*Richards* [1994]). While NTD-Ge bolometers have a negative α of order unity, TES bolometers have a positive α between 50 and 500.

Figure 3.1 shows the sharp change in resistance of a non-released TES vs temperature in the vicinity of the transition. In this measurement, we induced a gradual temperature drift in the entire mK-stage and monitored it with a Lakeshore Germanium Resistance Thermometer (GRT). We read both the GRT and TES resistances with a Bridge circuit to keep the power dissipated from the measurements far less than the power transmitted down the vespel legs of the mK-stage. Chapter 6 discusses the dewar design.

When biased into it's transition, small increases in optical loading P_{opt} induce small increases in the temperature of the TES. But thanks to the large positive α, these small

temperature changes create sizable increases in resistance. As a result, the joule heating from the bias circuit

$$P_{bias} = \frac{V^2}{R(T)}$$

drops. Conversely, decreases in the optical loading power induce increases in the joule heating power. This electrothermal feedback ensures a constant total loading power $P_{opt} + P_{bias}$ as the optical P_{opt} changes.

Energy conservation for thermal power flowing through the bolometer requires that

$$\begin{aligned} P_{opt} + P_{bias} - P_G &= \frac{dE}{dt} \\ P_{opt} + \frac{V^2}{R(T)} - GT &= \frac{dE}{dT}\frac{dT}{dt} \\ &= iC\omega T \end{aligned} \tag{3.8}$$

where the last line refers to a specific fourier mode of frequency ω. A change in P_{opt} will induce a change not only in the bolometer temperature T, but also the resistance R(T):

$$\begin{aligned} \frac{dT}{dP_{opt}} &= \left[i\omega C + \frac{V^2}{R^2}\frac{R}{T}\alpha + G \right]^{-1} \\ &= \frac{1}{G(1+\mathcal{L})(1+i\omega\tau)} \end{aligned}$$

where the definition of loop gain is analogous to that in electronic feedback systems:

$$\mathcal{L} \equiv -\frac{\partial P_{bias}}{\partial(P_{opt} + P_{bias})} = \frac{\alpha P_{bias}}{GT} \tag{3.9}$$

and the bolometer's time constant has decreased to

$$\tau = \frac{\tau_o}{\mathcal{L} + 1} \tag{3.10}$$

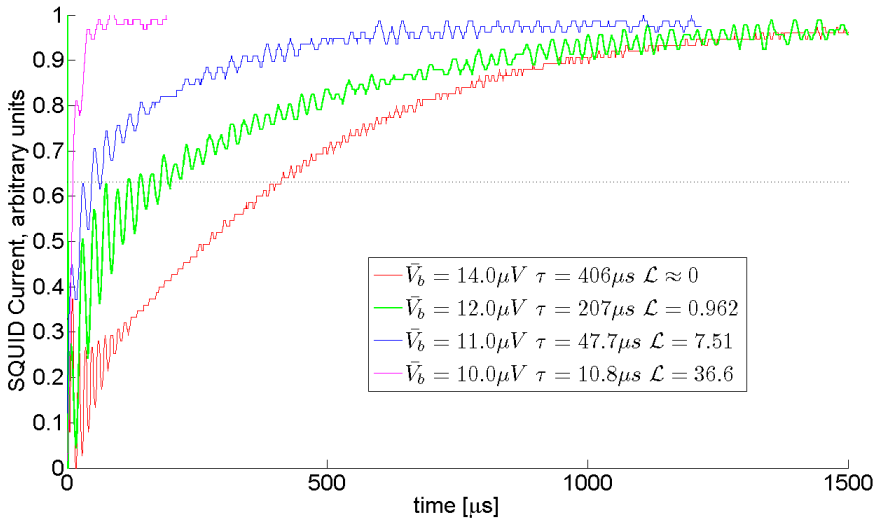

Figure 3.2. Arbitrarily normalized SQUID current vs time for a typical TES-bolometer. We biased the bolometers with the DC offset of an analog function generator carrying a small amplitude (2 μV) square-wave. As the bias passes through the transition point at 12 μV, the thermal time constant (Equation 3.10) drops dramatically. The red curve is well above the transition, the green is at the turn-around, and the purple is just above instability. The black dashed line guides the eye to the $1/e$ points.

Figure 3.2 shows measurements of the time constant at different bias voltages for a typical TES bolometer used in this thesis. When biased at it's IV-curve turn-around, the loop gain is 1 and the measured time constant is simply half of the thermal time constant given in Equation 3.6. These data suggest that the thermal time constant for our bolometers is $\tau_o \sim 400\mu s$, but that that deep in the transition we can speed it up with loop gains of $\mathcal{L} \sim 40$.

The SQUID reads the current through the voltage-biased TES, and the change in resistance alters this current:

$$\frac{\partial I}{\partial T} = \frac{\partial}{\partial T}\left(\frac{V}{R(T)}\right) = -\frac{\mathcal{L}G}{V}$$

So the sensitivity for the detector is

$$s \equiv \frac{dI}{dP_{opt}}$$
$$= \frac{\partial I}{\partial T}\frac{\partial T}{\partial P_{opt}} = -\frac{1}{V}\frac{\mathcal{L}}{\mathcal{L}+1}\frac{1}{1+i\omega\tau}$$

If we observe optical signals changing slowly ($\omega \ll 1/\tau$) with a detector operating deep in its transition ($\mathcal{L} \gg 1$), the changes in P_{bias} will exactly compensate the changes in P_{opt}. In this strong-electrothermal feedback limit, the sensitivity is simply

$$s \simeq -\frac{1}{V} \tag{3.11}$$

and the detector response is linear over a wide range of optical loading, independent of the bolometer's physical properties (*Guildemeister* [2000]).

TES-bolometers have a distinctive IV-curve that is linear in it's resistive regime, but "turns around" when the voltage bias is sufficiently low that the bolometer enters it's transition (See figure 3.3). In the transition, the resistance drops rapidly enough that further decreases in bias voltage actually cause increases in current. Deep in the transition, this power is held constant, resulting in a PV-curve that is flat in the transition (See figure 3.4). For a dark measurement such as that in Figure, $P_{opt} = 0$ and the power dissipated in the transition must equal P_G carried away through the legs. P_G is often called the saturation power P_{sat} because if the total power dissipated in an optically active bolometer exceeds P_{sat}, it will climb out of it's transition and be driven normal. The range of linearity of a TES is thus limited to $P_{tot} = P_{bias} + P_{opt} < P_{sat}$.

3.5 Fabrication

We fabricate our bolometers on 10-cm diameter 0.5mm thick silicon wafers and a picture of one is shown in Figure 3.5. The suspended TES sits on a 10000Å thick film of Low Stress silicon Nitride (LSN). While a 1 μm film of stoichiometric Silicon Nitride (Si_3N_4) can have an internal stress of a few GPa, the silicon rich LSN typically has an internal stress of only

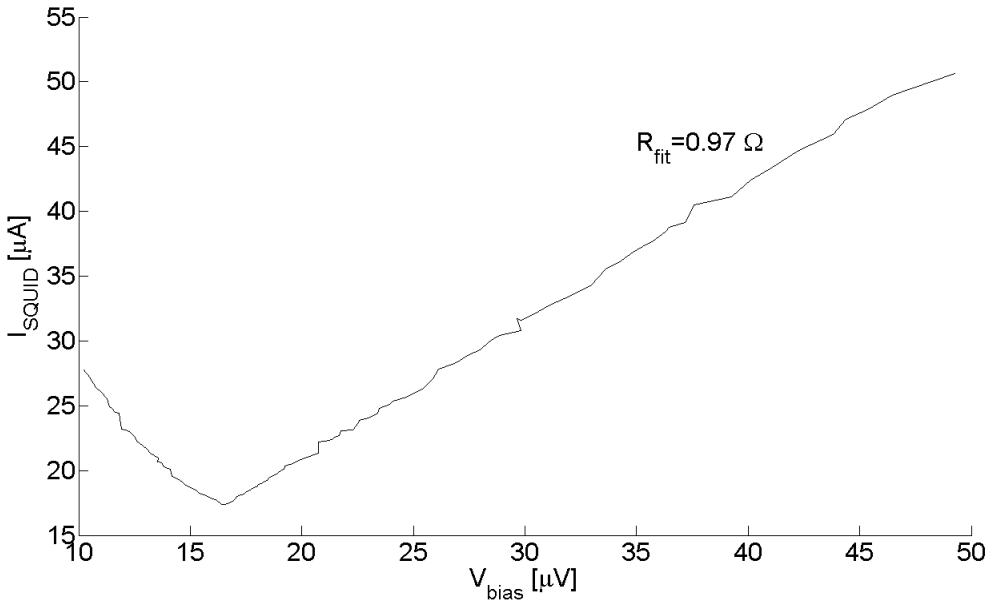

Figure 3.3. Plot of SQUID current vs bias Voltage for a 220GHz Dark Bolometer. The resistive portion of the curve is 0.97 Ω. This Bolometer was designed to receive 30% bandwidth at 220GHz.

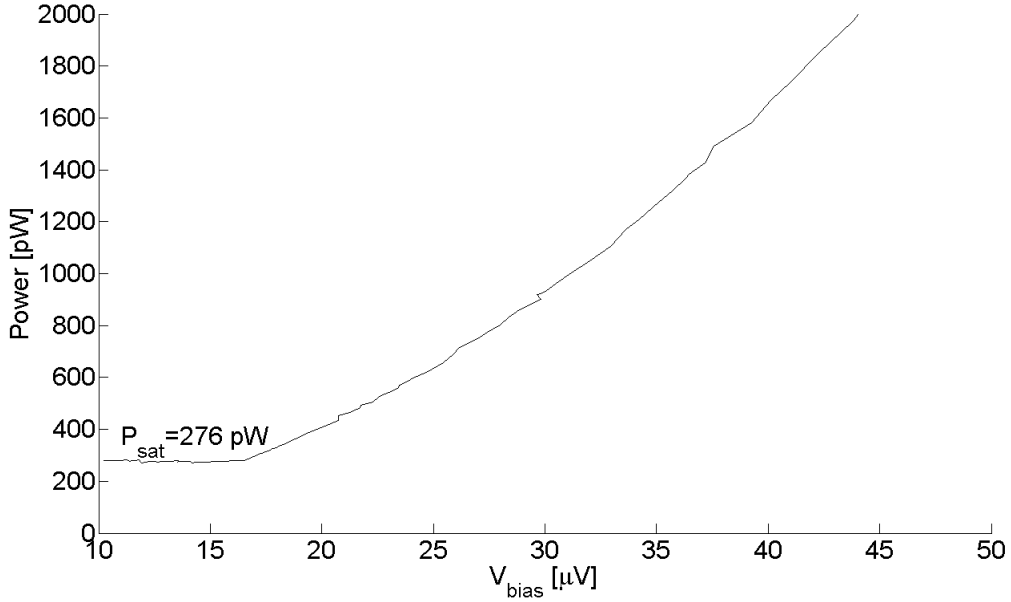

Figure 3.4. Plot of Power dissipated in the bolometer from Figure 3.3 vs bias Voltage for a 220GHz Dark Bolometer. The saturation power in the strong electrothermal feedback regime is 276pW for this bolometer, so we had to use an optical attenuator to avoid saturation when looking at room-temperature.

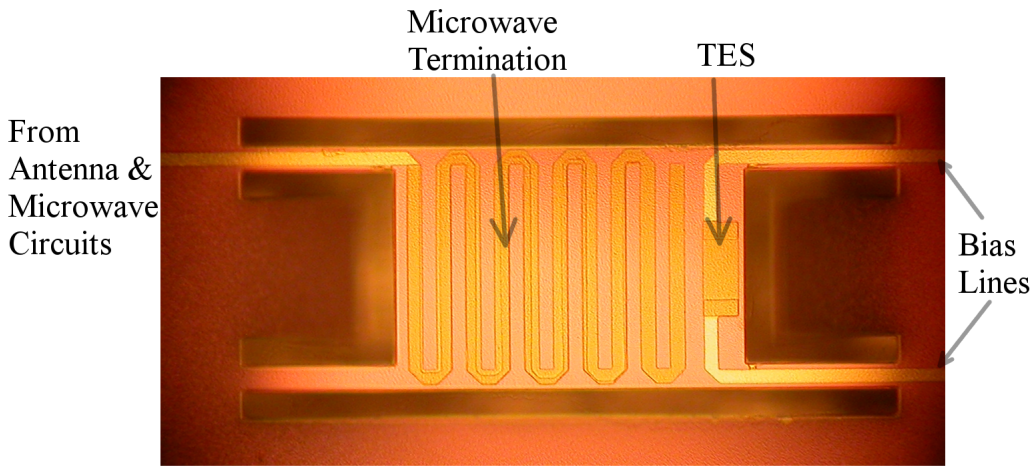

Figure 3.5. Released TES bolometer. The out-of-focus regions are silicon several microns below the released bolometer.

100 MPa (*Chang* [2010c]). A bolometer with higher stress would not survive the release procedure described below.

The TES is comprised of an aluminum-titanium bilayer with sputtered 400 Å Aluminum (Al) covering 800 Å Titanium (Ti) (*Chang* [2010a]). Aluminum's superconducting transition temperature of $T_c = 1.2K$ is too high to minimize phonon noise to a 250 mK heat bath. The titanium, whose $T_c = 0.39K$ decreases the bilayer's effective transition temperature to $\approx 500mK$ by the proximity effect. Cooper pairs from the Al leak into the otherwise normal Ti and quasiparticles from the Ti leak into the aluminum, resulting in a lower transition temperature. The proximity effect is strongest when the bilayer thickness matches the cooper pair coherence length (*Werthamer* [1963]). We chose the total film thickness of 1200 Å to ensure efficiently proximitizing and chose the Ti:Al thickness ratio of 2:1 to give the desired $T_c \approx 500mK$. Measurements suggest this was a little higher, closer to $T_c \sim 600mK$ (see Figure 3.1).

We fabricated both the microstrip circuits that couple optical power to the bolometer and the bolometer bias lines from the same 6000 Å thick film of Niobium (Nb), whose transition temperature is nominally $T_c = 8.2K$ (*Van Duzer* [1998]). The power in the

microstrip circuits terminates on resistive loads and lossy transmission lines that are in tight thermal contact with the TES and were etched from the same Al-Ti bilayer as the TES. We defer the discussion of the microwave designs on sky-side of the resistive until later chapters.

We etched holes through the LSN around the bolometers with an SF_6 plasma and used a Xenon-diflouride (XeF_2) gas to attack and remove the Silicon from under the bolometer, leaving a suspended structure (*Chang* [1998]). Our goal was to realize the suspension legs that carry a sufficiently high power to prevent the detectors from saturating when the cryostat looked at a 300K thermal load. The power flowing through each leg is

$$P(x) = Ak(T)\frac{dT}{dx}$$

In addition to the LSN, the legs have films of 3000Å Nb, 5000Å SiO_2, and 6000Å Nb. Since the Nb is superconducting, the only conduction should be through phonons whose heat conductivity $k(T) = k_o T^3$ ((*Van Duzer* [1998])), so the power flowing down N legs of length L and cross sectional area A integrates to:

$$P_G = N\frac{Ak_o}{4L}(T_{TES}^4 - T_{bath}^4) \tag{3.12}$$

We attempted to use Equation 3.12 to tailor our bolometer legs from previously measured saturation powers of Polarbear detectors. Ideally, we would have built our bolometers to have $P_G = P_{tot} > 2P_{opt,max}$ for the maximum possible loading to ensure they would not saturate. In the Rayleigh-Jean's limit, a single polarization of incident Power in Equation 3.7 is summed across a square band of width $\Delta\nu$ provides a loading

$$P_{opt} = \eta k T \Delta\nu \tag{3.13}$$

where η is the total receiver's efficiency. With 30% fractional bandwidths and *perfect efficiency*, the optical loading powers from a 300K source range from 111pW to 277pW for our detectors.

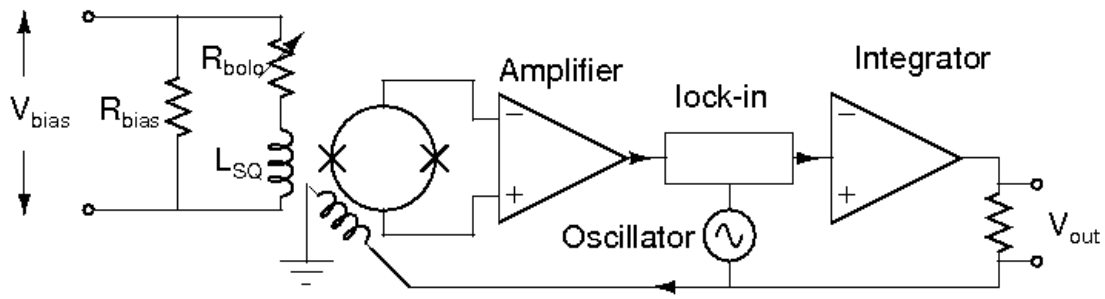

Figure 3.6. SQUID readout electronics. The electronic to the left of the SQUID were made in Berkeley for our test-system. The warm electronics to the right of the SQUID use a lock-in amplifier and a feed-back loop to reduce noise and linearize the SQUID. The details of the warm circuitry are not shared by the manufacturer, Quantum Design Corp.

Unfortunately, many of our detectors' measured saturation powers were less than twice this maximum loading. Table 3.1 summarizes the Chapter 8 bolometers' thermal properties. For reference, the right column is twice the maximum anticipated optical loading without any attenuation. To remedy this problem, we had to use an optical attenuator to shade our detectors for those measurements. Our Bolometers are significantly larger than the Polarbear bolometers, so we suspect that we experienced low saturation power because to achieve full release , we etched our devices with XeF_2 100-150% longer. This longer etching likely thinned the legs and depressed the saturation powers. The bolometers in chapter 6 were of comparable size to the Polarbear detectors and did not saturate; their saturtion powers all exceeded twice their maximum loading.

Table 3.1. Measured Thermal Characteristics of Ch 8 Bolometers

f_o [GHz]	τ_o [μs]	P_{sat} [pW]	$2P_{opt,max}$ [pW]
86	406	155	224
104	336	190	258
126	296	208	312
151	256	231	376
183	246	253	454
222	222	277	550

3.6 Bolometer stability and readout electronics

The bolometers in this thesis are in series with an input coil with inductance L that magnetically couples to Superconducting QUantum Interference Devices (SQUIDs). Our DC-SQUDIS were purchased from the Quantum Design Corporation, which operate in an AC flux-locked-loop mode (see Figure 3.6)

We biased the bolometers with a 6V battery box and varied the applied voltage with potentiometers. That voltage was further divided between a warm $2k\Omega$ reference resistor and a 4K bias resistor R_{bias} in parallel with both the bolometer (R_{bolo}) and the SQUID input coil (see Figure 3.6 for the 4K portion of this electronics). We chose the value of $R_{bias} = 0.02\Omega$ to ensure that the bias circuit applies $V_{bias} = 1 - 60\mu V$ across the bolometer for 0.1-6V voltage drops measured across the warm $2k\Omega$ resistor. This applied bias voltage

$$V_{bias} = L\frac{dI}{dT} + IR(T)$$

is coupled to the thermal equations 3.8 through the temperature dependence in the resistance (*Irwin and Hilton* [2005]). Expanding the variables I, P, V, and T to first order about their DC values, the resistance is:

$$R = R_o(1 + \alpha\frac{\partial T}{To})$$

and the thermal equations become:

$$\begin{aligned} P_G &= P_{Go} + G\partial T \\ P_{bias} &= P_{Jo} + 2I_oR_o\partial I + \frac{1-\mathcal{L}}{\tau_o}\partial T \end{aligned} \tag{3.14}$$

Without the DC therms, Equations 3.14 are:

$$\frac{d}{dt}\begin{pmatrix} \partial I \\ \partial T \end{pmatrix} = \begin{pmatrix} \frac{1}{\tau_{el}} & \frac{\mathcal{L}G}{I_oL} \\ -\frac{2I_oR_o}{C} & \frac{1}{\tau'} \end{pmatrix} \begin{pmatrix} \partial I \\ \partial T \end{pmatrix} + \begin{pmatrix} \frac{\partial V}{L} \\ \frac{\partial P}{C} \end{pmatrix} \tag{3.15}$$

where $\tau_{el} = L/R$ is the electrical circuit's time constant and $\tau' = \tau_o/(\mathcal{L}-1)$. The homogeneous solutions of Equation 3.15 have the form $\partial T_{hom} \propto A_+ V_+ e^{-t/\tau_+} + A_- V_- e^{-t/\tau_-}$, where the eigenvalues are

$$\frac{1}{\tau_\pm} = \frac{1}{2}\left[\frac{1}{\tau_{el}} + \frac{1}{\tau'} \pm \sqrt{\frac{1}{\tau_{el}} - \frac{1}{\tau'} - 8\frac{R_o\mathcal{L}}{L\tau_o}}\right]$$

The solutions are stable and will relax back to the DC values provided that the real part of the eigenvalues are positive. If it is critically damped ($\tau_+ = \tau_-$), then the solutions will still be stable provided that the circuit inductance L is between the critical values:

$$L_\pm = \left(1 + 3\mathcal{L} \pm \sqrt{2\mathcal{L}(1+\mathcal{L})}\right)\frac{R_o\tau}{(\mathcal{L}-1)^2}$$

In the strong electro-thermal feedback limit, $\mathcal{L} \gg 1$ and this reduces to the condition that the inductance L must be between

$$L_\pm/R_o = \left(3 \pm 2\sqrt{2}\right)\frac{\tau}{\mathcal{L}}$$

which is the well known condition that the electrical time constant must exceed the thermal one (sped by feedback) by at least 5.8 to ensure stability (*Irwin and Hilton* [2005]). Our Quantum Design SQUIDS have an input inductance of $2\mu H$, which means the electrical time constant with a 0.02Ω resistance is $100\mu s$. While this is indeed less than the bolometer's typical thermal time constant of $\sim 400\mu s$ (no feedback), it is insufficient in the transition where we have achieved loop gains of nearly 40, and hence thermal time constants drop to $\sim 10\mu s$.

For multiplexed arrays, our group combats a similar stability problem by adding 1-2 μm thick films of gold onto the bolometer islands to add heat capacity and drastically increase the thermal time constants (*Mehl et al.* [2008]). However, the devices in this thesis are only prototype devices read with non-multiplexed DC SQUIDS and stimulated with very 100K bright signals. Since the gold-deposition complicates the fabrication process,

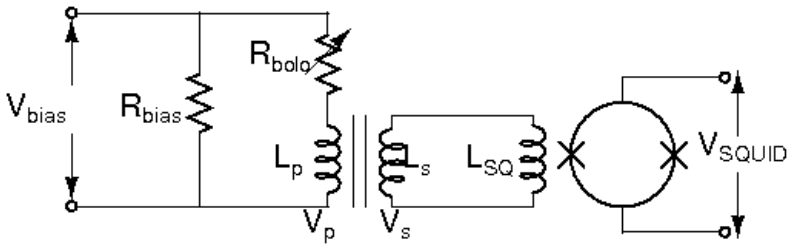

Figure 3.7. Circuit diagram the cold section of our electronics. The output V_{SQUID} is processed further by the electronics in the warm control circuit shown in Figure 3.6. We have inserted a hand-wound transformer, where the coil in DC contact with the bolometer has inductance L_P and the coil in DC contact with the SQUID pickup inductor has inductance L_S.

we alternatively modified the bias circuit to decrease τ_{el} by installing a superconducting transformer (see Figure 3.7) between the bolometer and the SQUID input coil (L_{SQ}).

If the primary and secondary coils have N_p and N_s windings, with corresponding self-inductances L_p and L_s, then the voltage on the secondary is

$$V_s = \frac{N_s}{N_p} V_p = \sqrt{\frac{L_s}{L_p}} V_p.$$

The current fed through the SQUID input coil is

$$\begin{aligned} I_{SQ} &= \frac{V_s}{i\omega(L_s + L_{SQ})} \\ &= \frac{\sqrt{L_s/L_p}}{i\omega(L_s + L_{SQ})} V_p \\ &= \frac{\sqrt{L_s/L_p}}{i\omega(L_s + L_{SQ})} (i\omega L_p I_{bolo}) \end{aligned}$$

So

$$\frac{I_{SQ}}{I_{bolo}} = \frac{\sqrt{L_p L_s}}{L_s + L_{SQ}} \tag{3.16}$$

(*Guildemeister* [2000]).

We hand-wound transformers with Nb wire around a 1.5mm diameter teflon tube with

a N_p : N_s=15:10 ratio of windings, resulting in a drop in current of 1/4 (in Equation 3.16) from the bolometers to SQUIDs, and a corresponding jump of 4 in voltage. As a result, the bolometers see an impedance and hence inductance that was 16 times lower than it would with just the bare SQUID, providing an electrical time constant that was much less than the thermal one. Operated with these transformers, the bolometers were stable. We determined the coupling efficiency of our transformer-coupled SQUIDs by measuring the IV curves' slopes for metal-mesh resistors in lieu of bolometers. These resistors had a previously measured 4K resistance of $R \sim 0.5\Omega$, so the efficiency is simply the ratio of the IV curve slope to the expected $2\mho$ that would have arisen if $I_{SQ} = I_{bolo}$.

The factor of 4 penalty in signal means that this solution is only acceptable for prototype devices that will never be used in the field where high sensitivity is required. However, for the prototyping described in this thesis where the detectors were stimulated with bright sources (100K), this loss is acceptable provided that it is understood.

3.7 Conclusions

This chapter discussed the theory of TES bolometers and explained the advantages they offer over competing technology. We described the fabrication, readout electronics, and dark tests of bolometers. These bolometers were integrated into the microwave circuits as high-sensitivity power meters described in later chapters.

Since this thesis seeks to explore broadband optical coupling schemes, TES bolometers are not a unique choice for this prototyping work. In principle, the microwave electronics described in later chapters could be coupled to a wide range of detectors including MKIDS, SIS-junctions, or even old fashioned NTG-bolometers. Some of the prototyping described in chapter 5 was even done warm at 1-10GHz with diodes and network analyzers. Additionally, the multichroic pixels will demand readout capable of supporting 3-10 times more channels per pixel that existing focal planes use, which makes MKIDS a compelling detector option in the future.

However, the microwave structures have been designed with CMB-polarimetry in mind

and TES-bolometers are currently the technology of choice in these measurements for the reasons outline above. As a result, it is necessary to integrate our antennas and filter networks with TES-bolometers in order to prove their viability to the other researchers in the field. This is demonstrated in chapters 6,7 and 8.

Chapter 4

Contacting lenses for Antenna-coupled bolometers

4.1 Introduction

The transition from NTD-Ge bolometers to TES bolometers was arguably the key innovation in bolometric receivers over the last decade. The greatest advancement of this decade will likely be remembered as integrating lithographed transmission lines between the antennas and bolometers. Several up-coming CMB experiments, including Berkeley's Polarbear, will use this technology. This chapter begins by contrasting the emerging antenna-coupled devices with more traditional schemes for coupling radiation onto the bolometers. We describe simulations of Polarbear's crossed doubled-slot antenna performed with both Agilent's ADS-momentum and Ansoft's HFSS. These simulations are important for subsequent chapters since the sinuous-antenna design draws it's inspiration from the crossed-double slot antenna. The meat of this chapter is a description of a raytracing script that accounts for the contacting lens in our simulations. This algorithm is well known and has been used by several researchers in the field, but the literature lacks a detailed explanation that this chapter tries to remedy.

All references to measured results in this chapter come from Mike Myers and Kam

Arnold. As previously noted in the acknowledgments, I owe a special thanks to Jen Edwards who pointed out that we must include image currents in the diffraction integral.

4.2 Antenna coupling vs traditional coupling schemes

4.2.1 Horn-Coupled Bolometers

Traditionally, bolometers have coupled to incident radiation with a horn (*Chattopadhyay et al.* [2003]). Often, low-pass "metal mesh" filters on the sky-side of the horns define the upper band edge while waveguide in the back of the horns defines the lower edge. A thermally dissipating structure, such as a spiderweb or PSB (Polarization Sensitive Bolometer), sits a quarter-wavelength above a backshort that maximizes coupling to the detector. A thermistor, such as a TES or NTD-Ge crystal, sits on this released structure to measure the power. Collectively, the thermistor and released structure form the bolometer. Modern CMB experiments that have used this design include QUAD, BICEP-1, APEX-SZ, and SPT.

4.2.2 NIST's Horn-couped Bolometers

NIST has developed a platelette horn-coupled bolometer that replaces the absorbing spiderweb with an orthomode-transducer in the back of the horn (*Yoon et al.* [2009]). The orthomode transducer separates the power into two linear polarizations and couples it onto two separate superconducting microstrip transmission lines. However, before reaching the bolometers, the millimeter waves pass through in-line microstrip band-defining filters which obviate some of the bulky optical filtering that would otherwise be needed in the telescope. This simplifies the required filter stack and helps eliminate ghosting effects often associated with unwanted reflections off the optical filters. Compared to other designs (see sections 4.2.3 and 4.3) that integrate transmission lines between the antenna and bolometers, NIST's is the most traditional because of their choice of a horn antenna.

4.2.3 Caltech/JPL's Array-coupled bolometers

Caltech/JPL has produced an alternative design that replaces the horn with a 12x12 array of slot antennas fed by microstrip lines (*Chattopadhyay et al.* [2007]). Slot antennas are preferred to classic wire dipole antennas because the continuous ground plane can provide RF shielding and also allow for easy integration with microstrip transmission lines. The detectors' beam forming is done entirely in the lithographed antenna array, so the bulky horns with high heat capacity are no longer needed. Aside from this significant difference, the design is otherwise similar to NIST's: the pixels are dual-polarized and integrate band-defining filters between the antennas and detectors.

4.3 Crossed Double-Slot Antenna

At Berkeley, we have developed a design similar to Caltech/JPL's, but with only a 2 element array per polarization in a Crossed-Double-slot Antenna shown in Figure 4.1 (*Myers et al.* [2005]). The first season of Polarbear will deploy a telescope with bolometers coupled to these antennas centered at 150 GHz (*Lee et al.* [2008]). These detectors have 667 μm long slots carved into a 3000Å thick layer of Niobium. Like the competing designs described above, these detectors are also dual polarized with in-line band defining filters. However, to achieve comparable gain to the NIST and Caltech/JPL designs, we have to use a contacting lens that is discussed at length in section 4.4.

4.3.1 Impedance

We simulated the antenna's impedance and beam characteristics in Agilent's Advanced Design Suite (ADS) Momentum. The antenna was drawn as magnetically conducting slots carved into a perfectly conducting ground plane. This plane was at the interface between an infinite half-space of silicon with $\epsilon_r = 11.8$ (on which we fabricate the real detectors) and vacuum. ADS Momentum is a frequency-domain simulator that partitions 2-D planar geometries into tessellating cells called a mesh. It then solves for electric currents in metal

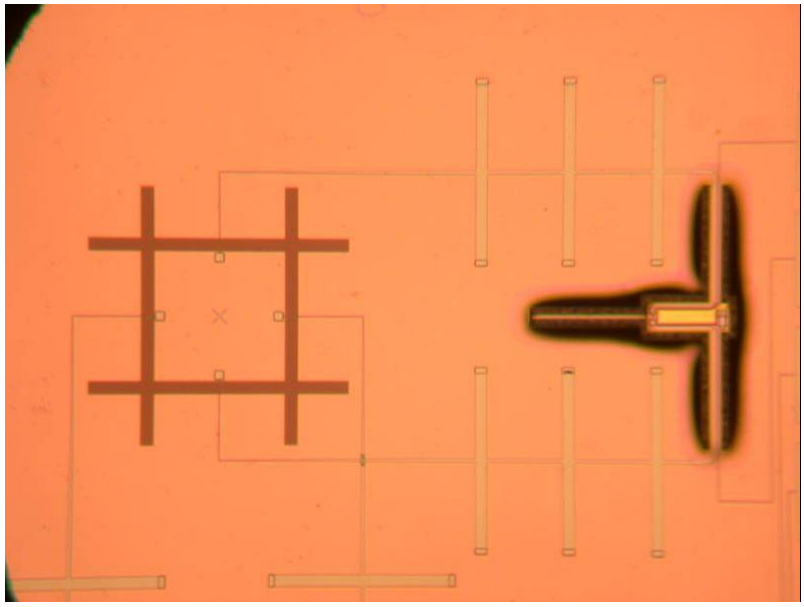

Figure 4.1. Photograph of a Polarbear pixel. The antenna is the "tic-tac-toe" shaped slots in the ground plane at left that couple power to a microstrip transmission line. Similar Bolometers to this one are discussed at length in Chapter 3 and the filter is discussed in Chapter 6

and fictitious magnetic currents in slots by imposing the requirement that electric fields must be normal to a perfect electric conductor and magnetic fields must be normal to magnetic conductors (slots) (*Agilent* [2006]).

One of the primary functions of Momentum and similar simulation packages is to calculate the scattering parameters

$$S_{ij} = \frac{V_i^-}{V_j^+}$$

S_{ij} quantifies what outgoing voltage V_i^- is produced at a port i if a voltage V_j^+ is applied to port j (*Pozar* [2004]). By convention, this definition presumes that each port is normalized to 50 Ω if not otherwise specified. In our simulation, the ports connect to short pieces of microstrip transmission lines that cross the slots and short to the ground-plane on the interior square of the antenna. This is similar to how we couple transmission lines to the slots in our real devices.

The impedance matrix Z_{ij} quantifies what voltage results on a port i when a current flows through port j. The impedance matrix is related to the scattering parameters by:

$$Z_{ij} = (1 + S_{ij})(1 - S_{ij})^{-1}$$

where 1 is an identity matrix (*Pozar* [2004]). This definition assumes that all other ports are open, but in practice, we attach the other ports to transmission lines of matched impedance. The actual input impedance looking into any one port is the ratio of the sum of voltages at that port to the current there. For the crossed-double slot antenna, the input impedance seen looking into port one is:

$$\begin{aligned} Z_{in} &= Z_{11} + \frac{I_2}{I_1} Z_{12} + \frac{I_3}{I_1} Z_{13} + \frac{I_4}{I_1} Z_{14} \\ &= Z_{11} - Z_{13} \end{aligned}$$

where the last three terms represent leakage of power from the other three ports to the first. In practice, little power couples between the two polarizations ($|S_{12}| < -20dB$) and the second and fourth terms can be ignored. The two parallel slots must be driven in phase to construct the proper beam, which means that $I_3 = -I_1$. The simulated input impedance is plotted in Figure 4.2.

This antenna is resonant and has a real impedance near the band center (see Figure 4.2). We operate at the second resonance where the input resistance is a manageable 26 Ω and the total impedance is changing much more slowly than at the first resonance at 71 GHz. The stable impedance provides a 39% fractional bandwidth when matched to an ideal 26 Ω transmission line, in close agreement with other studies on this antenna (*Chattopadhyay and Zmuidzinas* [1998]). The impedances of millimeter wave devices are notoriously difficult to measure, and we have made no attempts to explicitly do so. However, the measured optical throughput of the entire test cryostat with these devices is $\sim$ 50% over a 30% bandwidth when matched to transmission lines designed for 30Ω impedance. From this success, we suspect that the antenna's actual impedance is close to simulation.

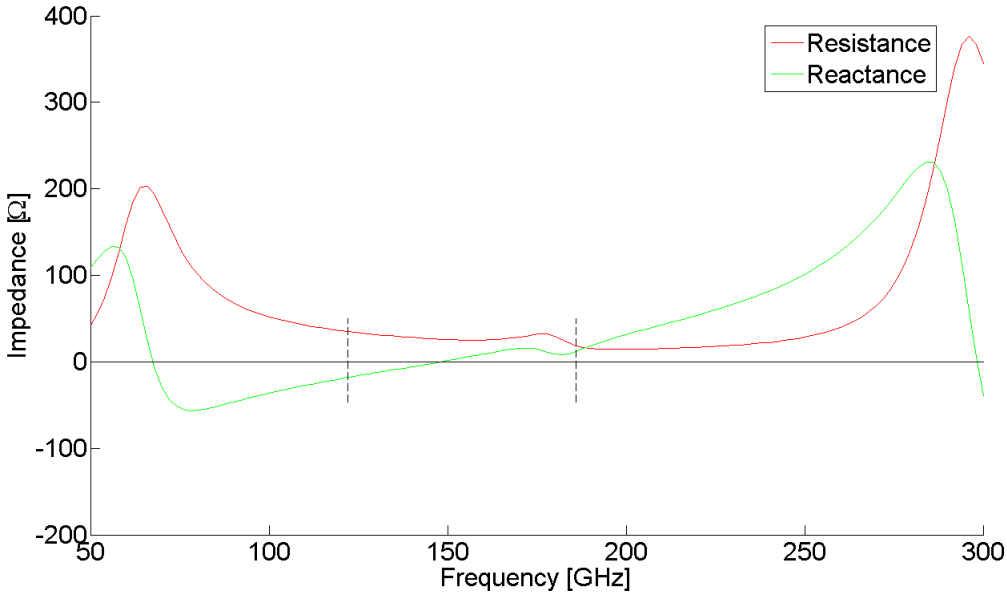

Figure 4.2. ADS simulation of input impedance vs Frequency for the Crossed double-slot antenna. The vertical dashed lines show where the reflection between the antenna and a 26 Ω transmission line rises above -10dB.

4.3.2 Beam Characteristics

Viewed in a time-reversed broadcasting sense, the current in each cell of the surface mesh radiates and the far-field beam pattern is simply the interference pattern from all cells. Thanks to the time-reversal symmetry of Maxwell's equations, the angular sensitivity of the antenna while receiving is identical to this broadcasting beam-pattern.

Figure 4.3 shows the results of this beam simulation. Note that the cross-polarized power as defined in Ludwig's Third Definition (*Ludwig* [1973]), vanishes on axis and only climbs to 1% outside the 10dB edge of the beam. We discuss the beam properites in more detail in Section 4.6 after the contacting lens has been acounted for.

4.3.3 Backlobe Power

If operated in free space, planar antennas have a bi-directional beam pattern with identical power radiated into both directions. However, it is energetically favorable for the antenna on a substrate to radiate predominantly into the substrate side. Depending on

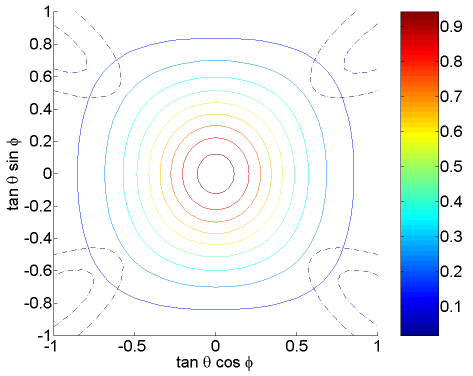

Figure 4.3. ADS simulation of the Crossed Double Slot antenna *without* a lens. The Solid contours are co-polarized power, the dashed are cross-polarized, and the power is on a linear scale normalized to the peak power on boresight.

the antenna geometry, this varies between $\epsilon^{1/2}$ and $\epsilon^{3/2}$, where ϵ is the substrate's relative permittivity.

Part of this effect arises simply because the antenna is driving power into two media in parallel with impedances proportional to $\epsilon_r^{-1/2}$, so the ratio of power into the silicon versus vacuum is $\sqrt{\epsilon}_r$:1. As a result, the Caltech/JPL antenna radiates only 75-80% of it's beam into the forward direction and the lost sensitivity must be recovered with a $\lambda/4$ back-short.

However, the crossed double-slot antennas and sinuous antennas described in later chapters have an even larger power-ratio thanks to the localized currents in the antenna's plane. The electric fields across the slots in the antenna's plane $E(r)$ will have a Fourier Transform $\tilde{E}(k_{xy})$, where k_{xy} resides in the antenna plane. The antenna will radiate waves with wavevectors

$$k_z^2 = \epsilon_r \omega^2/c^2 - k_{xy}^2 \tag{4.1}$$

For these waves to propagate, $k_{xy} < \sqrt{\epsilon_r}\omega/c$; otherwise, the wave exponentially decays with distance (*Goodman* [1968]). The power radiated is

$$P \propto \int dk_{xy}^2 |E(k_{xy})|^2$$

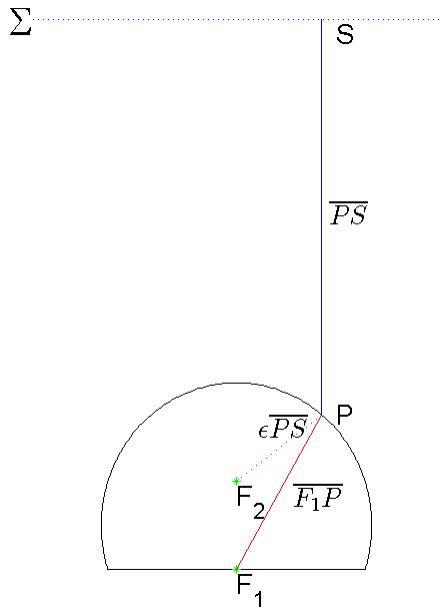

Figure 4.4. Rays leaving the antenna at F_1 strike the lens surface at P and travel to points on the directrix plane Σ. If the eccentricity $\epsilon = 1/n$, then the refracted rays will be parallel to the optic axis.

where from Equation 4.1, the area of integration is proportional to ϵ. For a large slot array antenna, the fields are distributed over a wide physical area, so the Fourier transform $E(k_{xy})$ is highly localized and vanishes over most of the integral. However, antennas with wide beams radiating *uniformly* into a half space do not vanish. As a result, the integral adds an extra factor of ϵ to the power ratio, $\epsilon_r^{3/2} : 1$ and only 3% power is in the back-lobe.

In practice, ADS momentum simulations of the double-slot antenna show a beam with a 53^o -3dB full-width, 71^o at -10dB, and 9% power in the backlobe. This is slightly more than the ideal case, but sufficiently low that we have not worried about installing a back-short.

4.4 Lens Coupling

The Polarbear optics have an f/1.9 and hence need detectors with 30^o wide beams at -10dB. The crossed double-slot antenna will not match these optics on it's own. To meet this requirement, we modify our detector beams with a contacting extended hemispherical lens.

An ellipsoidal piece of silicon with the antenna located at one of the foci is an ideal lens for this application (See Figure 4.4). A broadcasting antenna will most efficiently use it's cross-sectional area if the lens transforms the outgoing spherical wavefronts from the antenna within the lens into planar-waves outside the lens. It will accomplish this task if the optical path-length from the antenna at the focus F_1 to any point on the directrix plane Σ is a constant through every point P on the ellipse. Ellipses have the property that the distance $\overline{F_2P}$ from the upper focus F_2 to any point P on the curve is equal to the ellipse eccentricity ϵ time the distance $\overline{PS}$ from that point P to the directrix Σ (*Apsotle* [1967]). But the sum of the distances from any point on the ellipse to the two foci is a constant, so

$$\begin{aligned} \text{const} &= \overline{F_1P} + \overline{F_2P} \\ &= \overline{F_1P} + \epsilon\overline{PS} \end{aligned} \tag{4.2}$$

If we choose the eccentricity to be the reciprocal of the index of refraction n ($\epsilon = 1/n$), then Equation 4.2 becomes

$$\text{const} = n\overline{F_1P} + \overline{PS}$$

which shows that the total optical path length from antenna to a plane beyond the tip of the lens is indeed a constant.

In practice, it is difficult and costly to machine a true ellipsoid, so instead we make lenses from extended silicon hemispheres where the antenna is offset from the hemisphere's center by a silicon extension of thickness L_{ext}. The choice $L_{ext}/R = 0.39$ provides an optimal fit to the ellipse with eccentricity ϵ=1/n=0.29 for silicon (n=3.43) (*Filipovic et al.* [1993]). This geometry is commonly known as a synthesized ellipse and is shown in Figure 4.5.

If a ray strikes a point on the hemisphere at an angle θ from boresight as measured at the spherical center, then it would have departed from the antenna at an angle

$$\theta' = \arctan\left(\frac{R\sin\theta}{L_{ext} + R\cos\theta}\right) \tag{4.3}$$

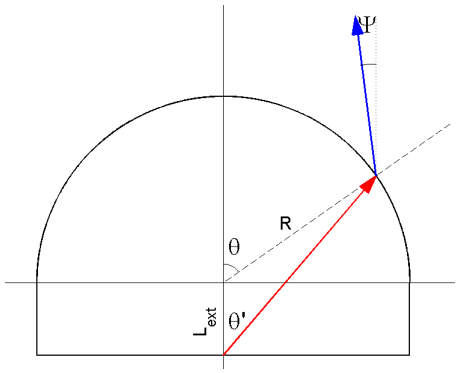

Figure 4.5. The extended hemispherical lens has a radius R and extension L_{ext}. A ray leaving the antenna at θ' from boresight strikes the lens surface at location θ from boresight measured from the lens center. It is refracted into a ray that propagates at an angle Ψ relative to the optic axis.

The refracted ray will propagate away at an angle

$$\Psi = \theta - \arcsin\left(\frac{ng\sin\theta}{\sqrt{1+2g\cos\theta+g^2}}\right) \tag{4.4}$$

where $g \equiv R/L_{ext}$. Figure 4.6 shows a plot of refracted vs initially radiated angles for different values of L_{ext}/R. For an ideal ellipsoid, this would be a flat line $\Psi = 0$. The choice of $L_{ext}/R = 0.39$ minimizes deviations of Ψ from zero for all angles out to 47^o where total internal reflection starts.

4.5 Raytracing Script

The effects of the lens over the simple crossed double-slot antenna can be simulated with a full 3-D simulator such as Ansoft's frequency-domain High Frequency Structural Simulator (HFSS). HFSS partitions the 3-D space surrounding an antenna into a mesh of cells and directly solves for the electric and magnetic fields in each cell by minimizing the the action associated with those fields. It uses an adaptive-mesh algorithm that iteratively refines the mesh in regions where the field is changing rapidly with each adaptation until the fields satisfy a user-provided convergence criterion.

HFSS simulations of the Polarbear antenna with the lens required roughly 5GB RAM

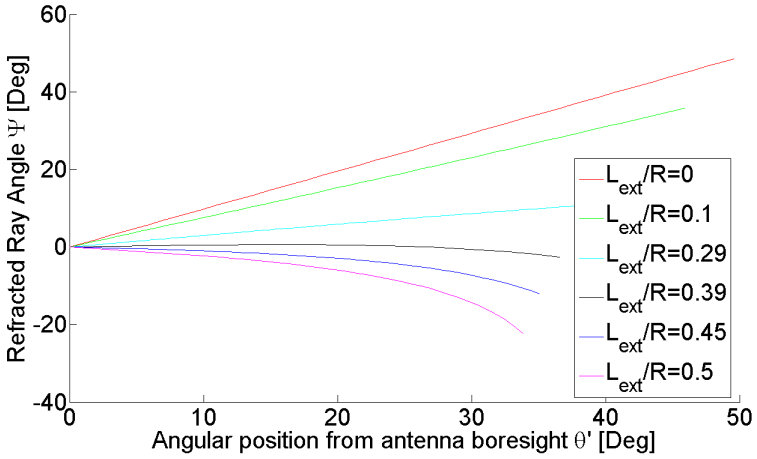

Figure 4.6. Refraction angle Ψ (Equation 4.4) is plotted against angle of radiation measured at the antenna θ' (Equation 4.3) for different lens geometries. Note that an ellipsoidal lens would have $\Psi = 0$ for all θ', so the synthesized ellipse $L_{ext}/R = 0.39$ is a good fit to this ideal

.

to converge. However, the more complicated antennas described in subsequent chapters required a denser mesh in the space surrounding the antenna than the cross-double slot needs. Because of this, the simulations need more RAM than our computer had (32GB). Since these memory requirements cannot be practically met, we instead simulated the log-periodic antennas in ADS where the memory requirements for a 2-D mesh were much lighter. We then accounted for the presence of the lens with a home-made raytracing script (*Filipovic et al.* [1993]) printed in Appendix 1. The following subsections describe the physics behind this algorithm.

Our software assumes that the lens is in the antenna's far field and invokes standard optics principles at that interface. The script exploits time-reversal and calculates beam-patterns as if the antenna were radiating back to the sky. In the far field (Fraunhofer) range, the wavevectors from different radiative elements on the antenna are assumed to be parallel, with phase errors associated with non-parallel rays not exceeding $\pi/8$. This typically begins at a distance of

$$r_{ff} = \frac{2D^2}{\lambda}$$
$$= \frac{2\lambda}{\Omega}$$

where in the D^2 is the effective area of the antenna and the antenna theorem for a single-moded antenna has been invoked in the second line (*Collin* [1985]). Waves at 150GHz in silicon have $\lambda = 0.58$mm, so the far field for Polarbear's crossed double-slot antenna begins at $r_{ff} = 1.99$mm. Since the equator of the 6.35mm diameter lens hemisphere is 3.4mm away from the antenna (for a synthesized ellipse), the lens surface is safely within the far-field and our algorithm is justified. The measurements and simulations of the log-periodic antennas in subsequent chapters used a lens with a 14mm diameter, so the algorithm was also justified for them as well, even at frequencies as low as 70GHz.

4.5.1 Refraction at the lens surface

Our code partitions the lens surface into a tessellating mesh of surface patches and interpolates the ADS-simulated fields at the patches' angular locations (θ', ϕ) measured at the antenna . If the lens's hemispherical surface has unit normal vectors $\hat{\mathbf{n}}$ and the outgoing rays strike with incident unit wavevectors $\hat{\mathbf{k}}$, then the refracted field's unit wavevectors (outside the lens) $\hat{\mathbf{k}}^{\mathbf{t}}$ are simply a rotation of the incident within the Plane Of Incidence (POI) by an angle of

$$\Psi = \arcsin(n_{lens} \sin(\hat{\mathbf{k}} \cdot \hat{\mathbf{n}})) - \hat{\mathbf{k}} \cdot \hat{\mathbf{n}}$$

towards boresight. The vectors $\hat{\rho_\perp} \equiv \hat{\mathbf{n}} \times \hat{\mathbf{k}}$ and $\hat{\rho_\parallel} \equiv \hat{\rho_\perp} \times \hat{\mathbf{k}}$ are respectively perpendicular to and within the POI and form a local basis with the vector $\hat{\mathbf{k}}$. The refracted wavevector in this basis is:

$$\hat{\mathbf{k}}^{\mathbf{t}} = \cos(\Psi)\hat{\mathbf{k}} + \sin(\Psi)\hat{\rho_\parallel}$$

The incident fields can also be written in this basis, where the field components normal to the plane of incidence $(\mathbf{E}\cdot\hat{\rho_\perp})\hat{\rho_\perp}$ and $(\mathbf{H}\cdot\hat{\rho_\perp})\hat{\rho_\perp}$ are eigenvectors of refraction, only modified in magnitude by their respective transmission coefficients $\tau_\perp$ and $\tau_\parallel$. The transmitted field components within the POI are

$$\begin{aligned}
{\mathbf{E}_\parallel}^t &= \eta {\mathbf{H}_\perp}^t \times \hat{\mathbf{k}}^t \\
&= \tau_\parallel E_\parallel^o(\cos(\Psi)\hat{\rho_\parallel} - \sin(\Psi)\hat{\mathbf{k}}) \\
{\mathbf{H}_\parallel}^t &= \frac{1}{\eta}\hat{\mathbf{k}}^t \times {\mathbf{E}_\perp}^t \\
&= -\tau_\perp H_\parallel^o(\cos(\Psi)\hat{\rho_\parallel} - \sin(\Psi)\hat{\mathbf{k}})
\end{aligned}$$

where η is the impedance of free space. These components rotate by Ψ around the $\hat{\rho_\perp}$ axis, much like $\hat{\mathbf{k}}$.

For a lens without a coating, the transmission coefficients are given by the Fresnel Equations that require the tangential components of the electric and magnetic fields to be continuous across the interface:

$$\begin{aligned}
\tau_\perp &= \frac{2\cos\theta_i \sin\theta_t}{\sin(\theta_i + \theta_t)} \\
\tau_\parallel &= \frac{2\cos\theta_i \sin\theta_t}{\cos(\theta_i - \theta_t)\sin(\theta_i + \theta_t)}
\end{aligned}$$

4.5.2 Anti-reflection Coating

For a lens with an anti-reflection coating, the tangential field components must be continuous at *both* the inner and outer interfaces of that film. Assuming that the film is roughly planar, these requirements result in a set of equations relating the fields just inside the lens $[E_o H_o]$ to those just outside $[E_t H_t]$ through the transfer matrix $\mathcal{M}$:

$$\begin{pmatrix} E_o \\ H_o \end{pmatrix} = \begin{pmatrix} \cos(k_o h) & i\sin(k_o h)/\Upsilon_{\text{ar}} \\ i\Upsilon_{\text{ar}}\sin(k_o h) & \cos(k_o h) \end{pmatrix} \begin{pmatrix} E_t \\ H_t \end{pmatrix} \equiv \mathcal{M} \begin{pmatrix} E_t \\ H_t \end{pmatrix} \tag{4.5}$$

where $h = nd\cos(\theta_{\rm ar})$ is related to the film with thickness d and angle of incidence $\theta_{\rm ar}$ and the admittance $\Upsilon_{\rm ar}$ depends on the polarization of the mode under consideration

$$\Upsilon_{\rm ar} = \frac{n_{\rm ar}}{\eta} \begin{cases} \cos(\theta_{\rm ar}) \text{ for TE modes} \\ \sec(\theta_{\rm ar}) \text{ for TM modes} \end{cases}$$

An elementary description of the lens would sum the fields associated with multiple rays reflecting through the coating. However, this approach would be an onerous when considering the multilayer films discussed in Section 7.5. The transfer-matrix formulation is more powerful because multiple coatings can be modeled by simply multiplying transfer matrices to produce one effective matrix (*Born and Wolf* [1999]). The electric field transmission coefficient is

$$\tau = \frac{2\Upsilon_o}{\Upsilon_o \mathcal{M}_{11} + \Upsilon_o \Upsilon_{\rm lens} \mathcal{M}_{12} + \mathcal{M}_{21} + \Upsilon_{\rm lens} \mathcal{M}_{22}} \tag{4.6}$$

where the admittance for the free space and lens materials are defined in a similar way as above, but independent of polarization:

$$\Upsilon_{\rm lens,0} = \frac{n_{\rm lens,o}}{\eta} \cos(\theta'^{,t})$$

The wavevector and fields within the plane of incidence will still rotate by the angle given above despite the extra film layer(s), so that part of the algorithm from uncoated lenses carries over for lenses with a coating.

4.5.3 Deviations from an ideal anti-reflection coating

Our software assumes that the coatings are planar and of uniform thickness across the hemisphere. However, the coatings are not planar, which can give rise to field alignment errors. Additionally, the coatings should be tapered in thickness because a uniform thickness creates phase errors in the film off boresight that can degrade it's properties. In the following two subsections, I argue that these are not practical concerns for our application.

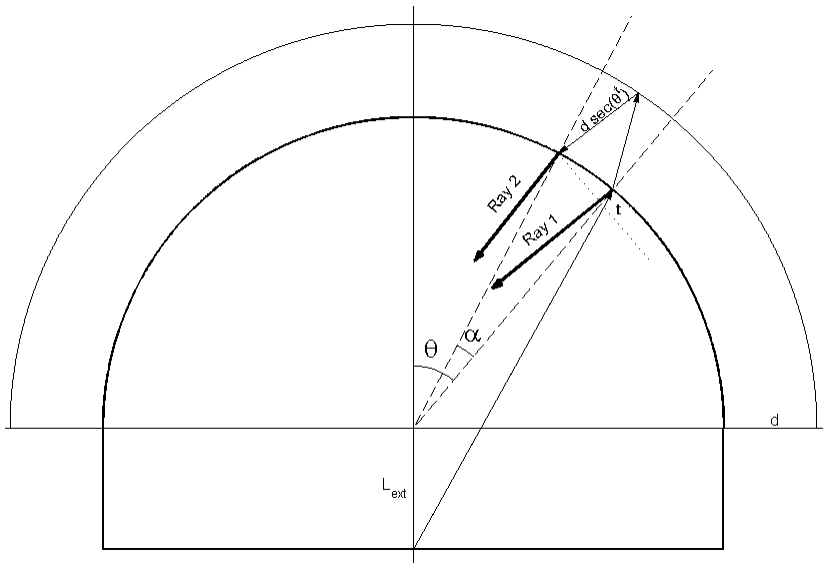

Figure 4.7. Cross sectional Cartoon of the lens with a single layer coating with an exaggerated thickness. The two reflected rays Ray 1 and Ray 2 must destructively interfere for the coating to work. However, the rays are not parallel; one is rotated with respect to the other by α. On boresight, Ray 2 will have a 90^o phase shift relative to Ray 1 from it's extra travel of $2d$ through the film. But off boresight, Ray 2 travels an extra $2d(\sec\theta^t - 1)$ while Ray 1 travels an extra $t = 4d\tan\theta^t \sin\theta^t$

Field Alignment Errors

For radiation normally incident on a flat AR-film, a $\lambda/4$ thickness will ensure that the multiple rays reflected from the interface will be 180^o out of phase and destructively interfere. Additionally, a film index that is the geometric mean of the inner and outer media's will ensure the ray's powers are matched in order to maximize this interference. But this cancellation happens because the reflected fields from the beams are parallel. While this is guaranteed for a flat coating where the two surfaces are parallel planes, it is not always the case when the two surfaces are concentric spheres. The reflected beams will still make the same angle with respect to the local normal vectors at the inner surface. However, those radial normal vectors themselves are not parallel, so the second beam will be rotated from the first by an angle of

$$\alpha \approx 2\arcsin\frac{d}{R}\frac{n_{lens}}{n_{ar}}\frac{\sin\theta}{\sqrt{1+2R/L_{ext}\cos\theta+(R/L_{ext})^2}}$$

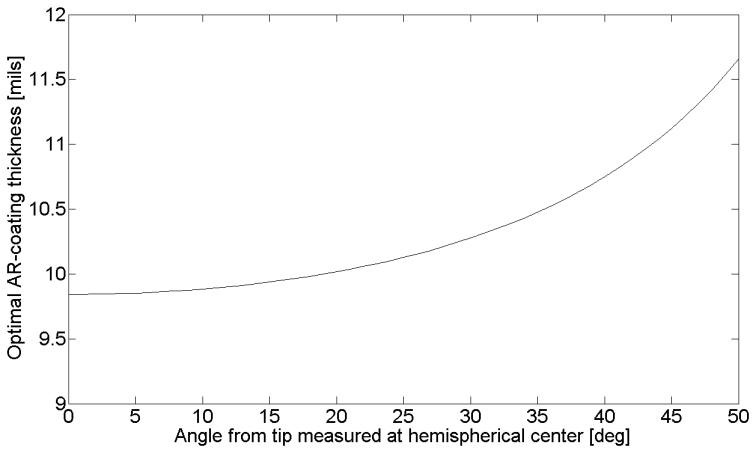

Figure 4.8. Ideal AR-coating thickness vs angle on the hemisphere. This would compensate for phase errors between the reflected beams off boresight. It is unlikely that we could actually make this compensation since the film thickness varies by less than 2 mils while a highly skilled machinist will often achieves 1 mil tolerances.

.

where d is the film thickness, R the inner radius, and θ the angle at the surface relative to the hemispherical center. For the polarbear detectors, this angle is no greater than 6.6^o, which means that the power of the mis-aligned field components in the plane of incidence is 0.004% of the total field power at the beam's -10dB contour. This error is negligable.

Phase Errors

We have only fabricated AR-coating films of uniform thickness. On boresight, the $\lambda/4$ thick film generates a $\pi/2$ phase delay between the first and second beams in Figure 4.7. Off axis, the second ray is delayed by $2n_{ar}d\sec\theta^t$ because it must travel further. However, the first ray *also* experiences an additional delay of $4n_{lens}d\tan\theta^t\sin\theta^t$. Surprisingly, the first ray's phase-delay is longer than the second ray's and to compensate, the film must be made thicker at large angles from boresight.

For a stycast coating with $n = 2$, this coating must be 9.84 mils thick. However, the film thickness is only 11.3 mils at the angles where Total-internal reflection starts (see Figure 4.8), which is likely within the machine tolerances of any AR coating that we attempt to mold.

4.5.4 Diffraction through the lens

The antenna beam also diffracts through the lens. A vectorial diffraction theory is needed in this case to properly account for the polarization properties of the antenna-lens system. The vector Kirchhoff integral relation follows from a simple application of Green's Second Identity:

$$\mathbf{E(x)} = \oint_{S'} [i\omega(\mathbf{n}\,'\times\,\mathbf{B}_t)G + (\mathbf{n}\,'\times\,\mathbf{E}_t)\times\nabla' G + (\mathbf{n}\,'\cdot\,\mathbf{E}_t)\nabla' G]da' \tag{4.7}$$

This equation quantifies Huygen's wavelet principle; it describes how a set of fields $\mathbf{E}_t$ and $\mathbf{B}_t$ with known values on the closed surface S' (which has a normal vector $\mathbf{n}'$) interfere to created a diffracted field $\mathbf{E(x)}$ (*Jackson* [1998]). All of the information relevant to the far field is contained in the fields on the surface, regardless of what currents are interior to that surface. The subscript t is a reminder that fields are those transmitted through the lens surface as determined by the refraction equations of the previous subsection.

At an observation point $\mathbf{x}$ far from the lens surface, the Greens function is

$$G(\mathbf{x},\mathbf{x}') = \frac{e^{ikr}}{4\pi r}e^{-i\mathbf{k}\cdot\mathbf{x}'}$$

and it's gradient is $\nabla' G = -i\mathbf{k}\ G$. Inserting this into Equation 4.7 and replacing the magnetic induction $\mathbf{B}$ with the magnetic field $\mu\mathbf{H}$ yields

$$\mathbf{E(x)} = \frac{ike^{ikr}}{4\pi r}\oint_{S'} e^{-i\mathbf{k}\cdot\mathbf{x}'}[\eta(\mathbf{n}\,'\times\,\mathbf{H}_t) - \hat{r}\times(\mathbf{n}\,'\times\,\mathbf{E}_t) - \hat{r}(\mathbf{n}\,'\cdot\,\mathbf{E}_t)]da' \tag{4.8}$$

where η is impedance of free space and the wavevector $\mathbf{k}$ was assumed to be propagating radially outward.

Engineers often substitute fictitious electric and magnetic surface currents and charges over the surface S' into this equation:

$$\mathbf{J}_E = \mathbf{n}\,' \times \mathbf{H}_t \tag{4.9}$$

$$\mathbf{J}_M = -\mathbf{n}\,' \times \mathbf{E}_t \tag{4.10}$$

$$\rho_E = \epsilon_o \mathbf{n}\,' \cdot \mathbf{E}_t \tag{4.11}$$

(*Collin* [1985]). In addition to beautifying otherwise ugly equations, these aid intuition by acting as tangible sources that re-radiate into a scattered wave. The spherical components of the far-field diffracted wave in Equation 4.8 are:

$$E_r = \frac{ike^{ikr}}{4\pi r} \oint_{S'} e^{-i\mathbf{k}\cdot\mathbf{x}'} [\eta \hat{r} \cdot \mathbf{J}_E - \rho_E/\epsilon_o] da' \tag{4.12}$$

$$E_\theta = \frac{ike^{ikr}}{4\pi r} \oint_{S'} e^{-i\mathbf{k}\cdot\mathbf{x}'} [\eta \hat{\theta} \cdot \mathbf{J}_E + \hat{\phi} \cdot \mathbf{J}_M] da' \tag{4.13}$$

$$E_\phi = \frac{ike^{ikr}}{4\pi r} \oint_{S'} e^{-i\mathbf{k}\cdot\mathbf{x}'} [\eta \hat{\phi} \cdot \mathbf{J}_E - \hat{\theta} \cdot \mathbf{J}_M] da' \tag{4.14}$$

The first term is identical to the second in the brackets of 4.12, so E_r vanishes as expected for a transverse traveling wave. The remaining components (Equations 4.13 and 4.14) can be written in terms of electric and magnetic vector potentials ($\mathbf{N}$ and $\mathbf{L}$):

$$E_\theta \propto \eta \mathbf{N} \cdot \hat{\theta} + \mathbf{L} \cdot \hat{\phi}$$

$$E_\phi \propto \eta \mathbf{N} \cdot \hat{\phi} - \mathbf{L} \cdot \hat{\theta}$$

where

$$\mathbf{N} \equiv \oint_{S'} e^{-i\mathbf{k}\cdot\mathbf{x}'} \mathrm{J}_E da'$$

$$\mathbf{L} \equiv \oint_{S'} e^{-i\mathbf{k}\cdot\mathbf{x}'} \mathrm{J}_M da'$$

The integral must be performed over a closed surface, and our code closes this surface by including an image hemisphere below the ground plane with image currents on that

imaginary-surface. To ensure that all electric fields at the perfectly conducting ground plane remain normal to that surface, the electric-current image components perpendicular to ground must be the in the same direction as the original, while the components parallel to ground must be in the opposite direction (see Figure 4.9(a)). The opposite is true for the magnetic-current images to ensure that magnetic-fields are tangential to the ground-plane (see Figure 4.9(b)). The code does not integrate over the cylindrical extension surface since it starts 69^o from boresight in a synthesized ellipse, and the bare antenna power is well below 1% of that at boresight in that region.

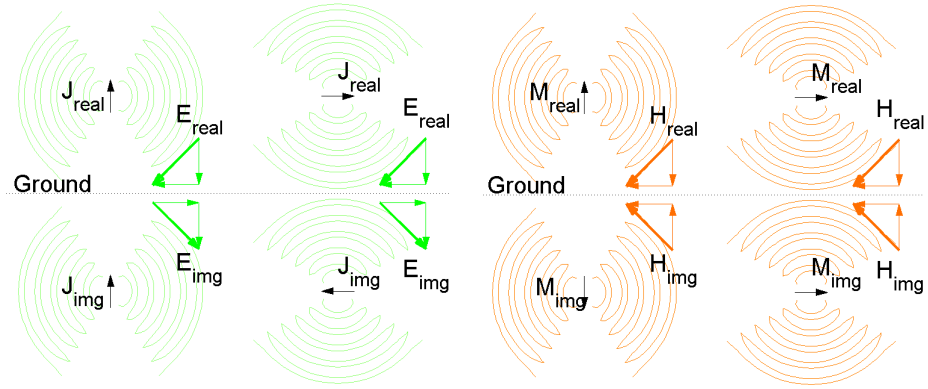

(a) Electric Image Currents (b) Magnetic Image Currents

Figure 4.9. Boundary conditions for image current construction. Real and image currents are black vectors, green curves and arrows are electric fields **E**, and orange curves and arrows are magnetic fields **H**. The field contours are for far-field dipole radiation; any antenna's far-field is the superposition of these fields. The components of the fields at a point on the ground plane are broken into components parallel and perpendicular to ground to make clear how the choice of image current guarantees that the tangential electric fields and normal magnetic fields vanish there.

4.6 Comparison to HFSS simulations

To vet our algorithm, we compared the results of computations against HFSS's full 3-D simulations, the geometry of which can be seen in Figure 4.10. The slot antenna is located near the origin on the x-y plane and has a geometry identical to the one described in the ADS simulations. We excited the slot parallel to the x-axis with a lumped voltage across the slot on a line along the y-axis. The lens models the ones to be used in the Polarbear

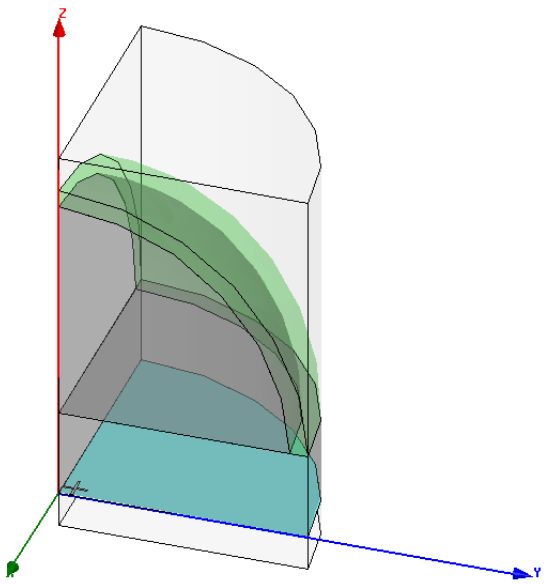

Figure 4.10. Layout for HFSS simulation. The yz-plane (facing the viewer) is a "Perfect-H" symmetry plane, while the xz-plane facing left is a "Perfect-E". All other external surfaces are perfect radiation absorbers.

experiment. It is silicon with a relative permittivity of 11.8, a diameter of 6.35mm (1/4 inch), and an elliptical extension of 1.24mm. The AR-coating (shown in green) is a 0.25mm film of stycast-2850, with a relative permittivity of 4. It is a quarter-wavelength thick at 150GHz.

To reduce the memory requirements of the simulation, we only simulated 1/4 of the antenna in HFSS and exploited the four-fold symmetry of the antenna by use of symmetry planes. The x-z plane is a "perfect-E" symmetry plane that force the electric fields there to be normal. This symmetry plane also ensures that there will be an image-source with opposite polarity across the image slot parallel to the x-axis. Similarly, the y-z plane is a "perfect-H" symmetry plane that forces Electric fields there to be tangential to that plane. The fields would have these properties in a simulation of the entire lens, but with this geometry, only 8Gb of RAM were required and our computer completed a simulation of a single frequency in under 20 minutes.

The beams from the two simulations are shown separately in the side-by-side contour plots in Figure 4.12. The beams are also co-plotted as cuts in Figure 4.11. The E-plane is

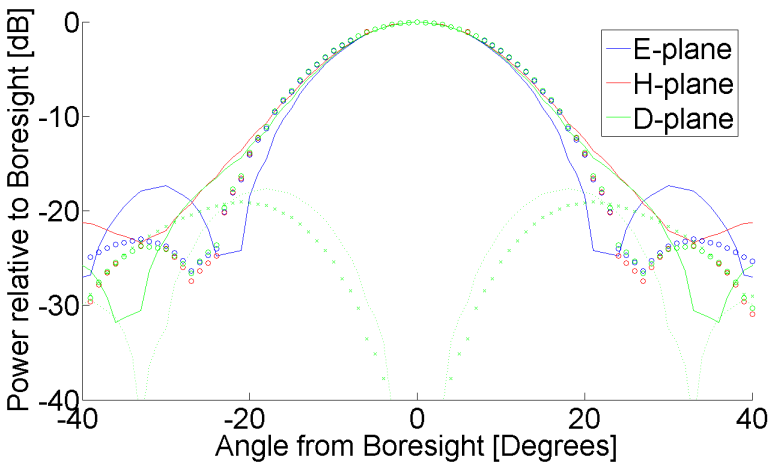

Figure 4.11. Cuts of HFSS and ADS-lensed simulations. Solid and Dashed lines are co and cross polarized power from HFSS. Points marked 'o' and 'x' are co and cross polarized power from ADS and raytracing.

the axis parallel to the polarization, H-plane is perpendicular, and the D-plane is at a 45^o between them. The two simulations produce beams with comparable features at high powers (above -10dB), but diverge at lower powers. In particular, the ADS-raytracing calculates significantly lower side-lobe and cross-pol levels than HFSS.

Table 4.1 summarizes the beam properties from the two simulations. In addition to the parameters already discussed, it also cites ellipticity, gain, and beam waist. The ellipticity is defined as

$$e = \frac{a-b}{a+b} \tag{4.15}$$

where a and b are the angular widths of the semi-major and semi-minor axis at a contour of a specific power. Gain is the ratio of antenna power on boresight to that from isotropic radiator; it quantifies how focused the beam is. The beam waist is the radius of the $1/e^2$ power contours where the beam is most narrow. We infer it from the $1/e^2$ half-angle angle in the far field:

$$w_o = \frac{\lambda}{\pi\theta_{FF}} \tag{4.16}$$

The beam waists are roughly 70-80% of the lens radius, as our UCSD collaborators have previously measured for a synthesized ellipse. For comparison, a uniformally illuminated aperature of 6.35mm diameter would have it's first Airy-ring diffraction minimum at an angular diameter of 45^o.

Table 4.1. Antenna Beam Properties

Parameter	ADS-Raytrace	HFSS
E-plane -3dB Width [Deg]	19.7^o	18.0^o
H-plane -3dB Width [Deg]	19.9^o	18.6^o
E-plane -10dB Width [Deg]	34.5^o	31.5^o
H-plane -10dB Width [Deg]	34.7^o	34.9^o
E-plane Beam Waist [mm]	2.24	2.47
H-plane Beam Waist [mm]	2.22	2.25
Peak Side-lobe Levels [dB] (E-plane)	-22.0	-17.3
Peak cross-pol [dB] (D-plane)	-19.1	-17.6
Gain [dB]	13.7	15.4
Ellipticity	0.5%	1.6%

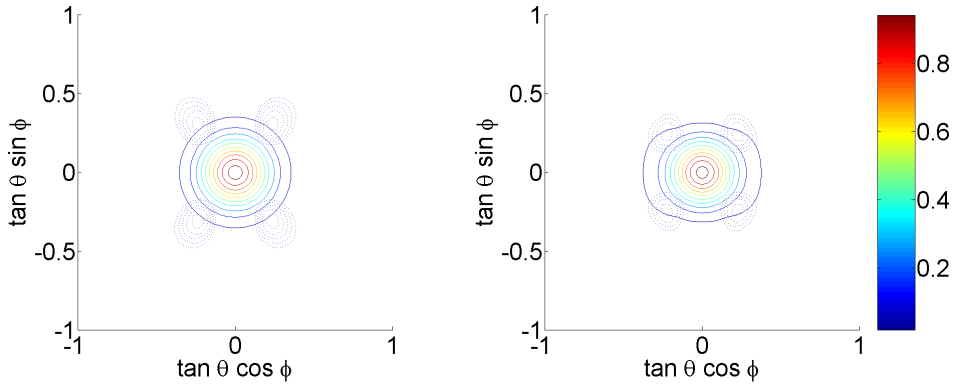

(a) ADS-Raytracing Script Beam

(b) HFSS Beam

Figure 4.12. Contour plots of ADS simulation modified with the raytracing script (left) and from HFSS simulations (right). Solid lines are co-polarized power, dashed are cross-polarized, and the power is on a linear scale. They agree in many of their course features, but not in the fine details (See table). Notice that these are half as wide as the un-lensed beam in Figure 4.3.

4.7 Conclusions

We described the double-slot antenna in detail since it motivates the antenna development in subsequent chapters and because it is an established yet simple design that we used to test our raytracing script. We have also motivated the use of contacting lenses to boost the gain of a detector's antenna so we can match it to a telescope's optics. Our raytracing algorithm seems to produce lens-coupled antenna beams that agree with the industry-standard HFSS at the 10% level, but differs in the finer details. We consider these differences in later chapters when we compare results from this model against our measurements.

Chapter 5

The Sinuous Antenna

KISS: Keep It Simple, Stupid!

– *Ancient Engineering Proverb*

5.1 Introduction

Arrays with broadband pixels will increase the optical throughput of a camera. In this chapter we describe a novel modification of the sinuous antenna, which has five valuable properties. The antenna:

1. is **broadband** over *at least* 1.5 octaves
2. is **planar** and thus scalable to large arrays
3. is **dual-polarized**, with low cross-polarization
4. has **high gain**, to match telescope optics
5. has a **stable impedance** with frequency.

We start this chapter with a discussion of log-periodic antennas, but identify polarization wobble as a common flaw. The sinuous antenna is a special type of planar log-periodic that has an acceptable level of wobble. In free space, the sinuous antenna is self-complimentary and we discuss how this influences the input impedance of our lens-coupled antenna. Finally,

we show measurements of 1-12GHz scale-models to demonstrate the antenna's promising beam characteristics. The sinuous antenna had not been previously studied on a contacting lens, so these measurements were an important step to confirm antenna properties before fabricating the millimeter-wavelength devices in the following chapters.

5.2 Log-Periodic Antennas

Maxwell's Equations lack an intrinsic scale, so if one rescales the physical dimensions of a system, the solutions will be unchanged aside from a reciprocal rescaling of the frequencies. An infinite spiral antenna with arms following $r = e^{a\theta}$ also lacks any specific dimensional scales. So rescaling this antenna will reproduce the exact same antenna up to a rotation. Since both Maxwell's equations and the antenna are scale invariant, the beam and impedance properties are the same for all frequencies (*Rumsey* [1966]). In reality, the antenna must terminate at some finite inner and outer radii which determine the upper and lower frequency band-edges. But aside from this restriction, the continuous bandwidth of these antennas can be arbitrarily large. Unfortunately, these antennas couple to circularly polarized waves and it is not possible to make them dual polarized. Since we require dual polarized antennas that receive a linear polarization, spiral antennas are not an appropriate choice for our application.

Log-periodic antennas are closely related to the frequency independent spirals, but they are invariant *only* when rescaled by a factor of σ (*Rumsey* [1966]). An example of this is shown in Figure 5.1(a), where σ =10%. Properties such as impedance and beam shape of these antennas will repeat everytime the frequency f_n is rescaled to f_{n+1} by a multiplicative factor of σ, or equivalently whenever $\log(f_n)$ is changed by an additive factor of $\log(\sigma)$:

$$f_{n+1} = \sigma f_n$$

$$\log(f_{n+1}) = \log(f_n) + \log(\sigma)$$

If σ is sufficiently small, then these properties will undergo only minor variations within each log-period. As above, the inner and outer termination scales fix the the upper and

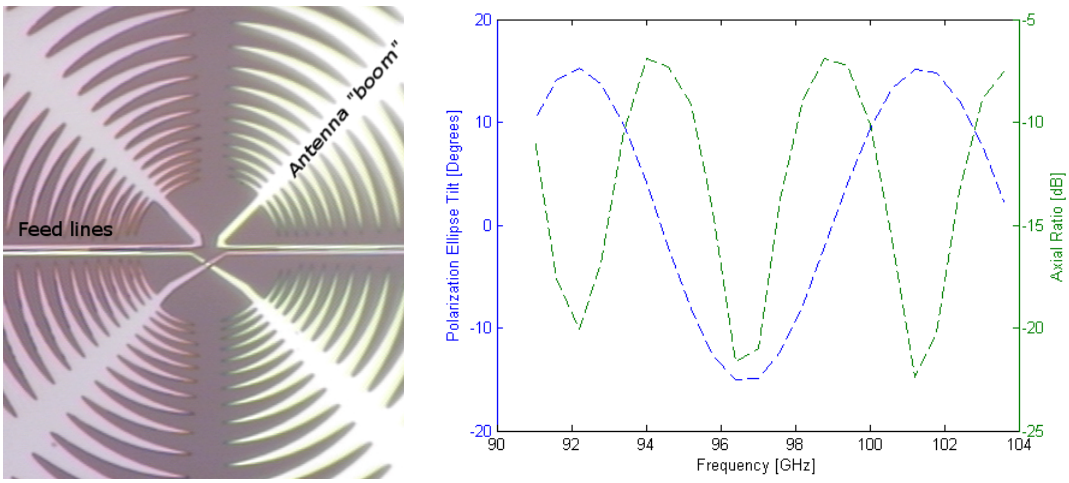

(a) Early Log-Periodic Antenna

(b) Simulated Polarization Tilt and AR

Figure 5.1. Photograph showing the interior of an early Log-Periodic Antenna. The photo is roughly 100 μm on a side, but the entire antenna has a $\sim$ 3mm diameter. The plot at right shows simulated polarization tilt (blue, left axis) and Axial Ratio (dashed green, right axis) against frequency for for the antenna without the horizontal feeds. Even without the feeds, the polarization performance is poor.

lower band edge frequencies. Fortunately, these antennas couple to linear polarizations and it is possible to fold-two antennas together to make a dual-polarized pixel.

Figure 5.1(a) was fabricated in the Fall of 2006 in an early attempt to coupled a broad-band antenna with a contacting lens to TES bolometers. It is a dual-polarized version of the original planar log-periodic antenna pioneered by DuHammel and Isbel in the 1950s (*DuHamel and Isbell* [1957] and *Engargiola et al.* [2005]) . When we rotated a polarizing grid between the detector and a chopped thermal load, the received power only dropped to $\sim$ 70% of peak (*O'Brient et al.* [2008a]); if the antenna efficiently discriminated between linear polarizations, this figure should have been no more than a few percent. ADS simulations revealed that the feed lines coupled the orthogonal sets of arms to produce an elliptically polarized beam with large axial ratio (defined in figure 5.2). But even if the feeds are moved onto the backs of the antenna booms to supress this coupling, polarization problems persist.

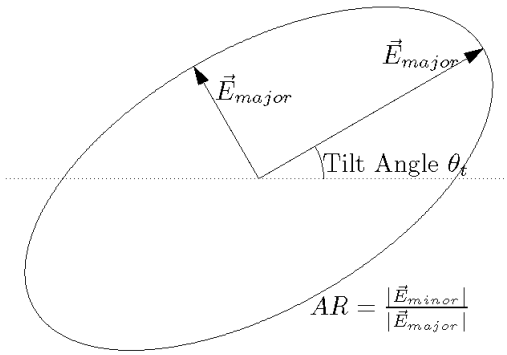

Figure 5.2. Axial ratio and Polarization tilt defined. The tilt measures the angle of the semi-major axis to a reference line while the Axial Ratio AR is the ratio of field strength on the semi-minor and semi-major axes. AR=0 for linearly polarized fields while AR=1 for circularly polarized fields.

5.3 Polarization Wobble

The polarization ellipse is the curve traced by the electric fields of a free-traveling electromagnetic wave; it's associated tilt and axial ratio are defined in Figure 5.2. A planar log-periodic antenna's polarization tilt is not fixed for all frequencies; it "wobbles" as frequency changes, repeating every log-period (*Kormanyos et al.* [1993] and *Gitin et al.* [1994]). Figure 5.1(b) shows the ADS simulated polarization tilt on boresight vs frequency for our planar log-periodic *without* the feedlines. This effect arises because the radiating fins protruding from the antenna boom alternate sides and are not parallel. Non-planar dual-polarized antennas have been built for the Allen Telescope Array that avoid this effect by bending the four arms into a pyramidal endfire antenna (*Engargiola* [2003]). However, this design is not planar and not amenable to thin film production; it would be challenging to scale them to kilopixel arrays.

Since our bolometers integrate the signal over a relatively wide band-width of 30%, it is imposible to perfectly align the antenna to a polarized test source for every frequency in the band. This rapid and large-amplitude wobble leaks as much as 13% of the crossed-polarization's power into a specific channel. Since we plan to difference two orthogonal polarization channels within a pixel, this will subtract away, but only at the expense of optical efficiency.

Figure 5.1(b) also plots the axial ratio AR. For a planar log-periodic antenna in free space, this number is very low and the beam is linearly polarized. But on a half-space of silicon, simulations suggest that the AR can climb to -8dB between tilt extrema where the beam becomes elliptically polarized. This is a second mechanism that leaks another 15% of the crossed-polarization and further degrades the efficiency. Our collaborators at UCSD have seen these effects in prior studies as well (*Kormanyos et al.* [1993]).

5.4 The Sinuous Antenna

The sinuous antenna (pictured in 5.3(a)) is a specific type of log-periodic that has an extensive heritage in the defense industry (*Bond* [2010]) ever since it's invention in the late 1980s. The edges of the switch-backing arms follow the defining equation (*DuHamel* [1987]):

$$\phi = \alpha \sin \frac{\pi \ln(r/R_o)}{\ln \tau} \pm \delta \qquad \text{for } R_o < r < R_o \tau^N \tag{5.1}$$

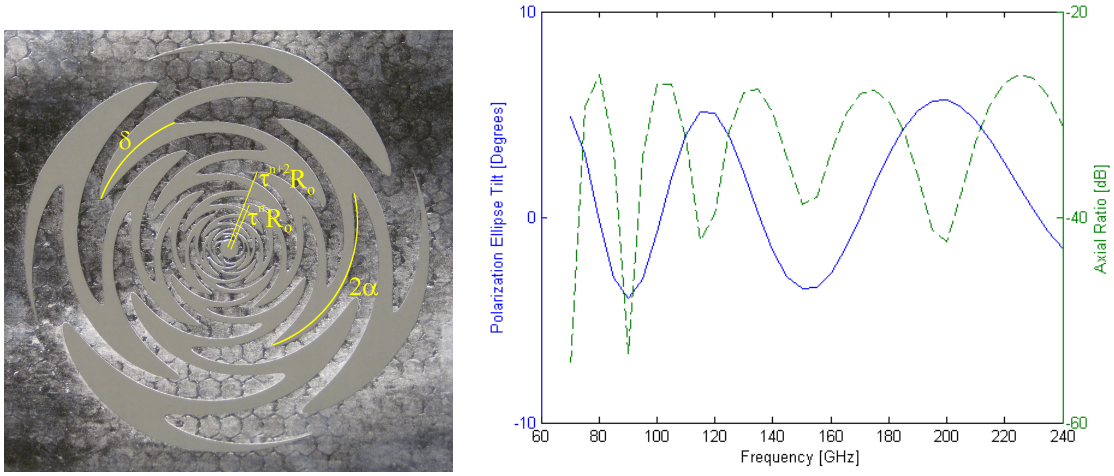

(a) A Sinuous Antenna

(b) Simulated Polarization Tilt and AR

Figure 5.3. Photograph showing a 1-3GHz scale model Sinuous; the hex pattern on the metal is an artifact of the deposition process. The plot at right shows simulated polarization tilt (blue, left axis) and Axial Ratio (dashed green, right axis) against frequency, much improved over the other log-periodic antenna.

Each of the four arms snake through an angle of $\pm\alpha$ every rescaling of τ^2. The angle δ determines the angular width of each arm and is used to control the antenna impedance

(see Section 5.6). Typical values of α are between 30^o and 70^o , while typical values of τ are between 1.2 and 1.5. This antenna is inherently dual-polarized. If we excite a pair of opposite arms with equal power and 180^o phase difference, they will couple to one of the two linear polarizations (*Saini and Bradley* [1996]).

The antenna is very similar to the log-periodic antenna of the previous section, but the boom in the center of each arm was sacrificed to merge the teeth into a continuous winding structure. ADS simulations suggest that power radiates predominantly from the sections between the switch-backs, and those sections are more closely aligned than the teeth of the classic log-periodic in Figure 5.1(a). As a result, the wobble amplitude is much lower and the axial ratio is greatly suppressed as well, as seen in Figure 5.3(b) (*O'Brient et al.* [2008b]). The antenna in this simulation has $\tau = 1.3$. Simulations also suggest that antennas with even smaller values of τ have even lower amplitudes of wobble, but they are difficult to fabricate. We only measured antennas in this thesis with $\tau = 1.3$.

The sinuous emits and radiates long wavelengths from the exterior regions and short wavelengths from the interior regions, preferentially along the $\lambda/2$ sections between the switch-backs. For an antenna driven to couple to linear polarizations, the opposite arms act as a two element array separated by $\lambda/2$, analogous to the crossed double-slot antenna. The outer-most radius $R_{out} = R_o\tau^N$ of the antenna fixes the low frequency cutoff:

$$\lambda_L/4 = R_{out}(\alpha + \delta) \tag{5.2}$$

The antenna requires a buffer region separating the feedlines from the high frequency radiating cells to maintain useful beam patterns and impedance (*DuHamel* [1987]). Most engineers conservatively pick $R_{in} = R_o$ such that

$$\lambda_H/8 = R_{in}(\alpha + \delta) \tag{5.3}$$

The useful polarization properties of the sinuous are not surprising since it is the simplest broadband generalization of the crossed-double slot antenna from Chapter-4. Topologically, the crossed double-slot is similar to a ring-slot antenna (*Raman and Rebeiz* [1996]), and our

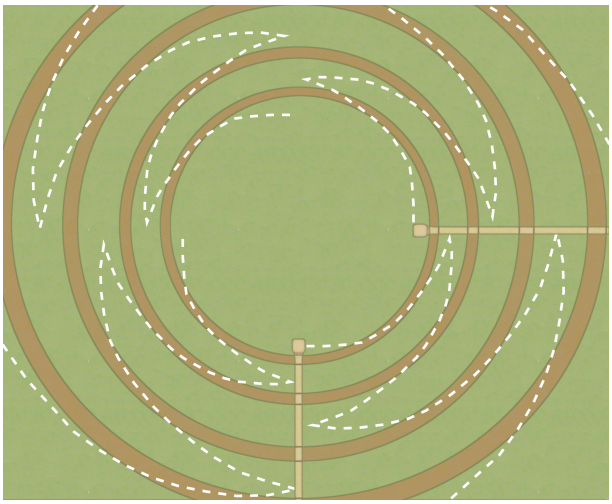

Figure 5.4. Nested Rings: The crossed double-slot antenna is similar to a single ring slot antenna. Nested rings (rust colored) with microstrips crossing into the interior do not work as a broadband antenna because the high-frequencies couple to the high-order modes of the outer rings instead of the fundamental modes of the interior. However, if we deform each quadrant of the rings into the curves shown in white dashed lines, then we open a continuous path of ground plane (green) for the microstrips to drive the antenna in the center.

collaborators at UCSD have already explored a set of two and three concentric ring-slots as a broadband alternative (*Behdad and Sarabandi* [2004]). They found that the planar transmission lines couple the high frequencies to the outer rings before they can reach the interior, leading to poor efficiency and low quality patterns at the upper band-edge (*Edwards* [2008]).

However, we can partition the rings into four quadrants and construct switch-backed curves in each to open-up a continuous stretch of ground from the exterior to interior. The result is an antenna that mimics the original rings, but is also nearly identical to the sinuous. This heritage is clear in Figure 5.4. DuHammel, the antenna's inventor, found that curves with constant width, such as those sketched in dashed white in the figure, produce unacceptable reflections at the highly inductive switchbacks and that the widened turn-arounds from Equation 5.1 capacitively load each arm to cancel out that inductance. Widening the switchbacks also interlocks the arms, which aligns the radiating $\lambda/2$ sections and suppresses wobble (*DuHamel* [1987]).

5.5 Driving a planar sinuous antenna

All log-periodic antennas must couple to their driving transmission lines at the high frequency end (*Rumsey* [1966]). If fed at the low end, the high frequency modes will never reach the regions where they should radiate; instead, they will excite high-order modes in the larger low frequency elements and form a non-Gaussian beam with low efficiency. This is identical to the problem UCSD experienced with the nested slot-rings. For planar log-periodic antennas, the high-frequency area is in the center, which is challenging to access if fed with planar transmission lines.

Historically, the sinuous was fed with coaxial cables normal to the antenna's plane (*Saini and Bradley* [1996]). However, this method is not amenable to the thin-film fabrication that we need to construct large arrays of millimeter-wavelength devices. Alternatively, some researchers have placed detectors (Diodes or Hot Electron Bolometers) in the center (*O'Brient et al.* [2008b] and *Liu et al.* [2009]). While this approach is acceptable for the scale model tests described in Section 5.7, it would preclude channelizing with microstrip circuits.

A third option is to run microstrip transmission-lines between interior and exterior down the backs of the antenna arms, using the arms as finite ground planes. This has already been used for spiral-antennas (*Nurnberger and Volakis* [1996] and *Dyson* [1959]), and we have found that it works for the sinuous as well. Examples of this feed are visible in Figure 5.6. Simulations suggest that power will negligibly leak from the microstrip to the adjacent slots provided that the line does not come within a dielectric thickness of the edge. For the devices described in the following chapters, this required clearance is 0.5 μm.

5.6 The Sinuous Antenna's Input Impedance

In free-space, a planar antenna's compliment is the same antenna but with metal and slots exchanged. Because electric fields orient themselves across the slots and tangent to the plane of the antenna, a slot will have normal magnetic fields and act as a perfect magnetic

conductor to fictitious magnetic currents. These currents are defined exactly like those on the surface of the lens in the previous chapter. If an antenna produces fields $(\mathbf{E}, \mathbf{H})$ (both near and far), it's compliment will have exchanged magnetic and electric currents that radiate dual fields:

$$\begin{aligned} \mathbf{E}' &= -\eta_o \mathbf{H} \\ \mathbf{H}' &= \mathbf{E}/\eta_o \end{aligned} \tag{5.4}$$

where η_o is the impedance of free space. Meanwhile the total currents and voltages between each feeding port are proportional to line integrals of the fields there:

$$\begin{aligned} V &= -\int \mathbf{E} \cdot \mathbf{dx} = -a\,|\mathbf{E}| \\ I &= \frac{1}{\mu_o} \oint \mathbf{H} \cdot \mathbf{dx} = \frac{2b}{\mu_o}\,|\mathbf{H}| \end{aligned} \tag{5.5}$$

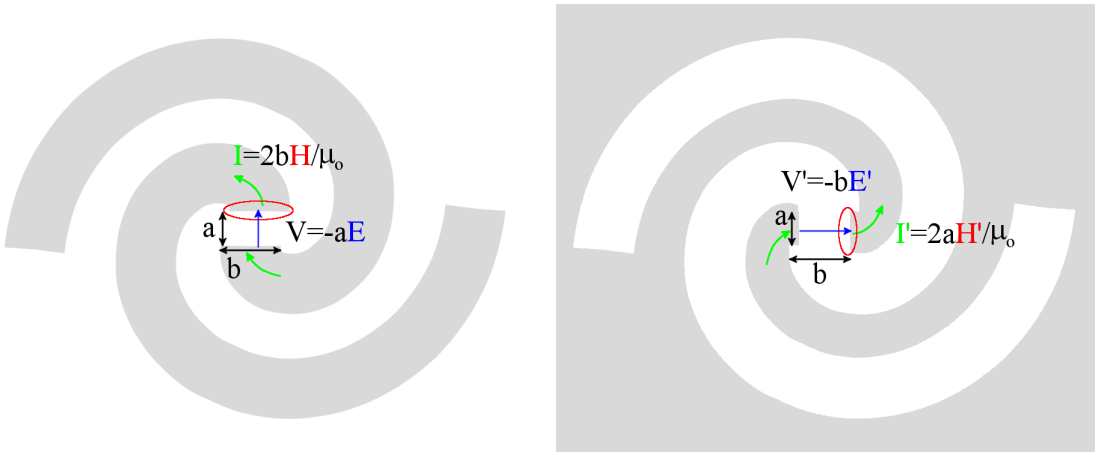

(a) A one-port antenna

(b) Antenna Compliment

Figure 5.5. Figure 5.5(a) is a two port spiral antenna, where gray is metal, white is slot. Electric and Magnetic fields are shown in blue and Red. Figure 5.5(b) is the compliment. Since the antenna is nearly self-complimentary, if it continued indefinitely, the impedances $Z = E/H$ and $Z' = E'/H'$ would be nearly equal, constant, and real

where a is the distance between the terminals and b the width of each (See Figure 5.5). Similar equations relate (V',I') to (E',H') on the complimentary antenna, but with a and b exchanged. Finally impedance matrices Z_{ij} and Z'_{ij} relate the voltages to the currents

at the ports of each antenna. Eliminating all variables but the impedances from Equations 5.4 and 5.5 relates Z'_{ij} to Z_{ij}. For the simple case of a two conductor antenna with just one port, this relationship is known as Babinet's principle (*Booker* [1946]):

$$ZZ' = (\eta_o/2)^2 \tag{5.6}$$

An antenna is *self*-complimentary when the antenna and compliment are identical. In this case, $Z{=}Z'{=}\eta_o/2{=}189\Omega$. The impedance of such antennas is real and independent of frequency (*Rumsey* [1966] and *Mushiake* [1996]). Examples of these can include two-armed bow-tie, spiral, and log-periodic antennas. The sinuous antenna is self-complimentary provided that the angular width of each arm is $\delta = 22.5^o$. However, it is a four-port structure, so we cannot calculate it's impedance without a more general form of 5.6 that relates 4×4 impedance matrices. Deshampes formula does this for the special case of N-armed rotationally N-point-symmetric antennas, and it's simplest form is in the basis where the impedance matrix is diagonalized:

$$Z_m Z'_m \sin^2\left(\frac{m\pi}{N}\right) = \left(\frac{\eta_o}{4}\right)^2 \tag{5.7}$$

where $m{=}[1, 2, ..., N]$ is one of N eignemodes, denoted M_n (*Deschamps* [1959]). In this basis, the impedance relates the voltages present on all the arms when current is applied to all the arms in one of the modes. In particular, the current applied to each arm $n = [1, 2, ..., N]$ for these modes is

$$I_{m,n} = e^{i2\pi\frac{mn}{N}} \tag{5.8}$$

where by convention, the the arms' labels n reflect their circumferential ordinality. For an antenna with $N{=}4$ arms, the M_0 and M_2 modes induce 0^o and 180^o phase shifts between each neighboring arm, driving even-symmetry modes on the antenna. The beam patterns from these cancel on boresight and are not useful to us. The other modes M_1 and $M_3{=}M_{-1}$ drive $\pm 90^o$ phase shifts between the arms. Their beams do not vanish on

boresight, launching left and right handed circularly polarized radiation. For a given mode, all arms have the same impedance relative to a virtual ground at center, and the $m = \pm 1$ modes are degenerate. When the antenna is self-complimentary ($Z_m = Z'_m$), the arms for both modes will have $Z_{\pm 1} = \eta_o/(2\sqrt{2})$ relative to ground. Figure 5.6 displays the effective circuit over photographs of our fabricated millimeter-wavelength devices, where each arm sees the same impedance $Z_{\pm 1}$. These impedances are real and independent of frequency, so free space sinuous antennas can efficiently couple to TEM transmission lines whose impedances are also independent of frequency.

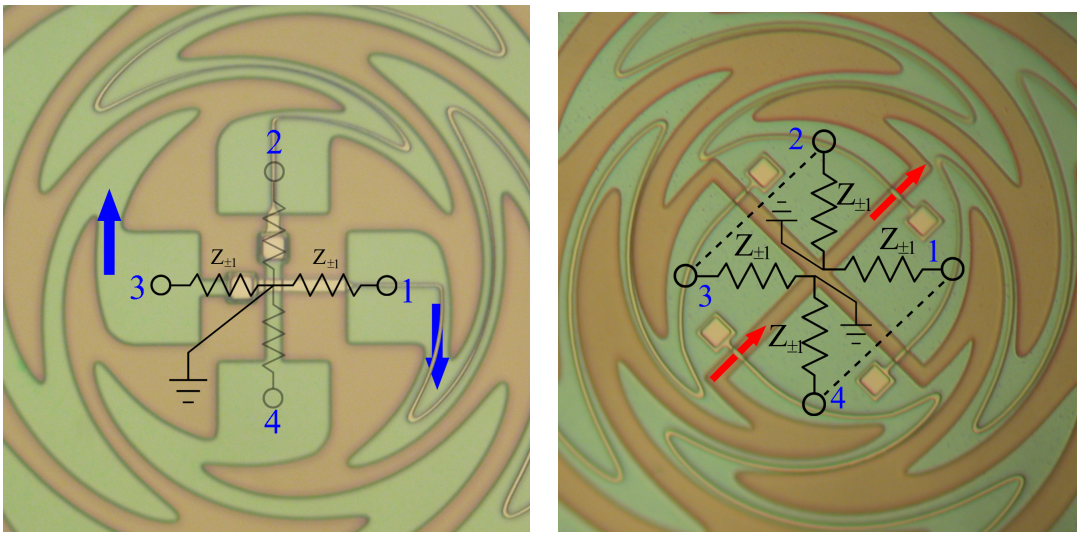

(a) H-V Excitation

(b) $D_{\pm 45^o}$ Excitation

Figure 5.6. Photographs overlaid with effective circuits for the H-V and $D_{\pm 45^o}$ excitations. Green is ground plane, pink is microstrip, and rust-color is the slot carved between the antenna arms. There is a virtual ground in the center of each antenna and the blue and red arrows represent the excited electric and magnetic currents that travel outward to a $\lambda/2$ section where they radiate. When driven in the H excitation as shown in Figure (a), the resistors to 2 and 4 carry no current, so we grayed them out. When driven in the D_{+45^o} excitation as shown in Figure (b), port 2 is at the same potential as 3 and 1 is at the same as 4, as shown in the dashed lines. As a result, magnetic currents do not flow down the slots between these. Is it genuius, or the warped creation of a siphalitic mind?

Any linear combination of modes $M_{\pm 1}$ is also an eigenstate with that same impedance. In particular, excitations with just 180^o phase shifts between opposite arms (e.g. 1 and 3) and no power on the others (e.g 2 and 4) are an alternative sub-basis with the same eigenvalues $Z_{\pm}1$. These current patterns are the best choice for our applications since

they correspond to the linear polarizations we want to receive. The two linearly-polarized excitations V and H are:

$$(H, V) = M_{+1} \pm M_{-1} \tag{5.9}$$

where the minus sign refers to the V excitation. Note also that V has a 90^o phase shift from H in this definition.

These models for a free-space antenna break down when applied to our antennas that are fabricated on high-dielectric substrates. To convert our antenna into it's compliment, we must additionally exchange high permittivity materials with high permeability materials. Our sinuous antenna's compliment has to be on an extended hemisphere of high-μ material, so the antenna is not truly self-complimentary. In practice, it's input resistance will vary some with frequency and have a modest reactance. Despite this shortcoming of the model, we can invoke the popular approximation that the half-space is equivalent to a homogeneous space with an average permittivity:

$$\eta = \frac{\eta_o}{\sqrt{(\epsilon_o + \epsilon_{Si})/2}} \tag{5.10}$$

We have explored two methods to couple the integrated microstrip transmission lines to this antenna. The first (Figure 5.6(a)) places a gap-voltage between opposite arms (e.g.,1 and 3) by shoring the upper conductor of one of the two microstrips to the opposite arm's ground-plane. Since the effective circuit has two resistors of $Z_{\pm 1}$ in series between opposite arms, the total impedance, using Equations 5.7 and 5.10, is

$$Z_{in} = \frac{\eta_o}{\sqrt{1 + \epsilon_{lens}}} = 105\Omega \tag{5.11}$$

where the evaluation is for a silicon lens with $\epsilon = 11.8$. The two microstrips snake out on the back of the antenna arms and connect to the channelizer circuits in Chapters 7 and 8. Figure 5.7(a) shows ADS simulations of the input impedance $Z_{in} = Z_{11} - Z_{13}$ that agree with this model, but with the added reactance caused by the antenna nor being perfectly

self-complimentary. If the transmission lines have an impedance of 105 Ω, then the only 5% power is reflected at the interface on average. In practice, this is difficult to fabricate (See discussion in Chapter 6), but a 65 Ω line that is easier to fabricate results in a refleciton of only 8%.

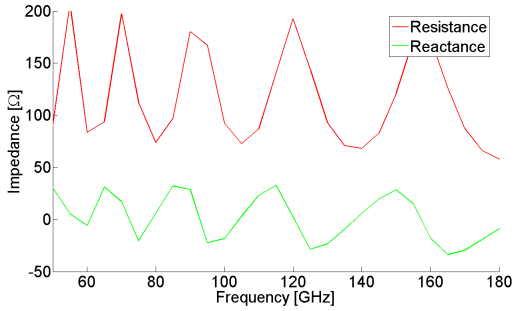

(a) Simulated Input Impedance on Silicon

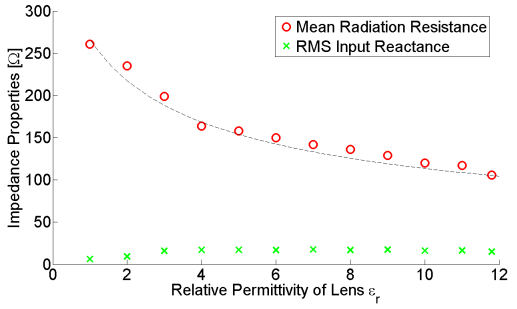

(b) Impedance characteristics in different lenses

Figure 5.7. Figure 5.7(a) shows ADS simulations of input impedance of a sinuous on silicon with the H-V feed. Results are similar for the $D_{\pm 45^o}$ excitation. Figure 5.7(b) shows how impedance properties change with the lens material. The right-most point is for silicon, the left is an antenna in free space. The dashed line is from Equation 5.11

Figure 5.7(b) shows the average input resistance $\bar{R}_{in}$ and RMS Reactance X_{in} as a function of lens permittivity. When $e_r = 1$ on both sides, the reactance nearly vanishes, but the impedance is a much higher 256 Ω.

Our second feeding scheme operates in a rotated basis that excites both of the linear and horizontal polarization modes simultaneously:

$$D_{\pm 45^o} = H \mp iV = (1 \pm i)M_{+1} + (1 \mp i)M_{-1} \tag{5.12}$$

where the notation $D_{\pm 45^o}$ reminds us that this polarization is on a diagonal between V and H. In this scheme, microstrips on the back of each arm short to adjacent arms through two resistors of $Z_{\pm 1}$, providing the same impedance as above. This is not surprising since the basis in Equation 5.12 is simply the dual of the feed in basis 5.9, and the antenna is presumed to be self-complimentary in this calculation. Opposite pairs of microstrips driven with a 180^o phase difference excite the two linear-polarizations in a manner that is very similar to the Polarbear detector antenna-feeds. The microstrips excite magnetic currents that travel outward in the slots between arms. Unfortunately, this feeding scheme also requires either a broadband balun or differentially feeding a lumped resistive load next to the TES to establish the required 180^o phase. The later option would greatly complicate the wiring by requiring several microstrip cross-overs and bias lines that cross the microstrips.

Finally, our collaborators at UCSD have devised a third feed. It is similar to the (H, V) feed, except that each polarization is excited by a pair of microstrips on opposite arms that meet in the middle without any vias to the ground plane. If the opposite arms have a 180^o phase shift, there will still be a virtual-ground in the center, but each arm will only see a termination of $Z_{\pm 1} = 53\Omega$, which is easier to match with Berkeley Microlab microstrips. Unfortunately, this still requires the same complicated wiring as the $D_{\pm 45}$ feed.

The team at UCSD is currently endeavoring to measure the impedance of these antennas in scaled models similar to those described in Section 5.7. However, the parasitic reactance associated with coupling the antennas to coaxial transmission lines have complicated their measurements and as of the writing if this thesis, they have not produced a conclusive result.

5.7 Sinuous Beam Patterns

As already described in Section 5.5, the antenna radiates and receives power on the $\lambda/2$ segments between switch-backs. So for a specific wavelength, a free space antenna's effective area should be proportional to λ^2. For a single-moded antenna, the throughput $A\Omega$ is also λ^2, so the antenna beam's solid angle of radiation Ω should vary little with frequency,

repeating every log-period. However, the contacting lens over the antenna establishes a specific scale (namely, the radius R) and breaks this self-similar nature of the antenna. As the wavelength drops, the beam will be narrow and if the lens is a synthesized ellipse, the beamwidth will drop as λ/R.

We felt it necessary to test the beam-patterns and cross-pol rejection of these designs in easy to fabricate cm-wavelength antennas before fabricating the millimeter devices. We worked closely with the UCSD team on these measurements and performed them in their anechoic chamber (*O'Brient et al.* [2008b]).

The Saturn Electronics Corporation made our antenna on a 0.635mm (0.025") thick substrate of Roger's 3010 with a relative permittivity of 10. The inner and outer radii of 0.24mm and 11.7mm provide upper and lower band edges of 12GHz and 5GHz. We fed the antenna by mounting low-barrier chip diodes (Metallic's MSS 30, 148-B10) across opposite arms in the center. In this way, the antenna is fed in the balanced version of the (H,V) excitations. We current biased the diodes with 240mA current provided by coaxial cables clad in Capcom EMI absorbing material. Finally, we rotated the antenna on a foam rotation stage in an anechoic chamber while horizontally facing a fixed standard gain horn (Dorado GH1-12N) 182cm (6'). The horn broadcasted a 1mW 1kHz and we measured the received power with a Stanford SR-830 lock-in amplifier.

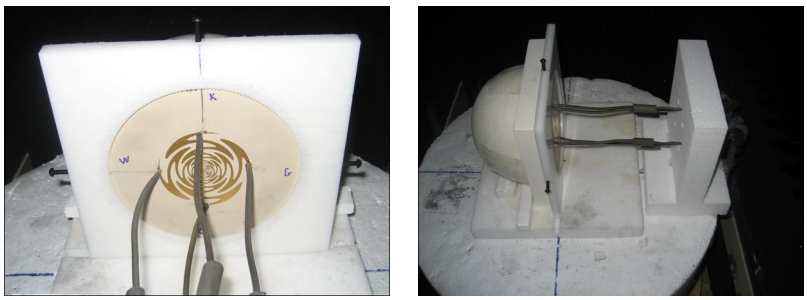

(a) Antenna Scale-Model

(b) Side-view of Eccostock extended hemispherical lens

Figure 5.8. Photographs of the 5-12GHz scale model antennas.

Figure 5.8 shows the antenna and lens on the rotating foam-platform in the UCSD anechoic chamber. The lens was made of Emmerson-Cuming's Eccostock HiK 12 material

whose index closely matches that of silicon. The hemisphere is 15.2 cm (6") in diameter and the extension is 3.8cm (1.5"), forming a lens that is beyond the elliptical point. A synthesized ellipse would have an extension 3.0cm (1.17") thick.

For our integration times of 5s, we observed a signal to noise ratio of roughly $S/N \sim 65$ that was constant for all sinuous antenna angles. This constant fractional noise is expected when the illuminating power is sufficiently strong that the noise is limited by the incident radiation and hence proportional to the incident power. The simulations predict a central-lobe beam-pattern that is roughly Gaussian, so $\log(P)$ should be linear with respect to θ^2. Taking the logarithms also removes the heteroscedasticity associated with the background limited noise, providing a standard deviation in log-space of $\delta P_i/_i P$ which is roughly constant.

Figure 5.9 shows the measured beam-patterns in the E and H planes co-plotted with ADS beam-simulations that were modified with the ray-tracing script developed in chapter 4. The cross-polarization is also low, at the 1-2% level, although our simulations routinely underestimate the cross-pol power.

The final figure of this group (Figure 5.9(e)) shows several co-plotted H-cuts at different frequencies to demonstrate that the beams narrow with increasing frequency as advertised. We fit gaussian profiles to the patterns above the 10dB power level and found a strong fit with reduced χ^2 between 0.6 and 1.4. Figure 5.10 plots the fit gaussian beam waists vs frequency for both E and H plane, and the solid lines are simulation predictions. Clearly, the simulations and data follow similar trends and have similar values, but the tight error bars on the data preclude a statistically significant agreement.

There are other more subtle disagreements between simulations and measurements. Most notably, the measured beams show subtle asymmetries. Since our direct involvement, the team at UCSD has demonstrated that the asymmetries are caused by inhomogeneities in the eccostock itself and that they vanish when the eccostock lens is replaces with a silicon one. The simulations predict stronger side-lobes than the measured beams, but our collaboration has found that these are strongly suppressed both in simulations and

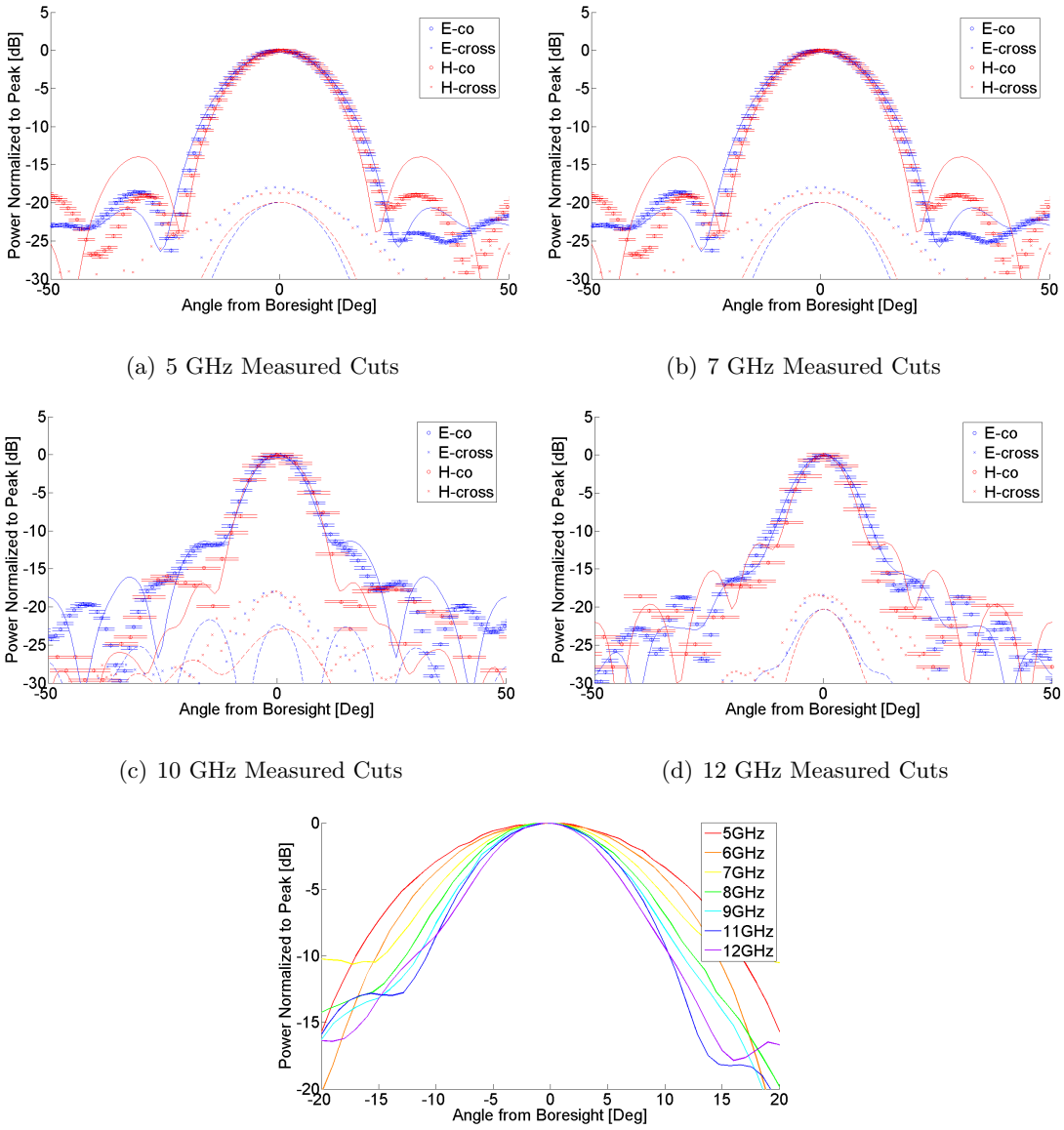

(a) 5 GHz Measured Cuts

(b) 7 GHz Measured Cuts

(c) 10 GHz Measured Cuts

(d) 12 GHz Measured Cuts

(e) Several channels of H cuts

Figure 5.9. Measured beam-patterns on scale mode devices. Blue is E-plane and red is H-plane. The circular markers are co-polarized while the x-markers are cross-polarized. The solid and dashed curves are simulations for co- and cross-polarization. The last picture shows several H-plane cuts co-plotted.

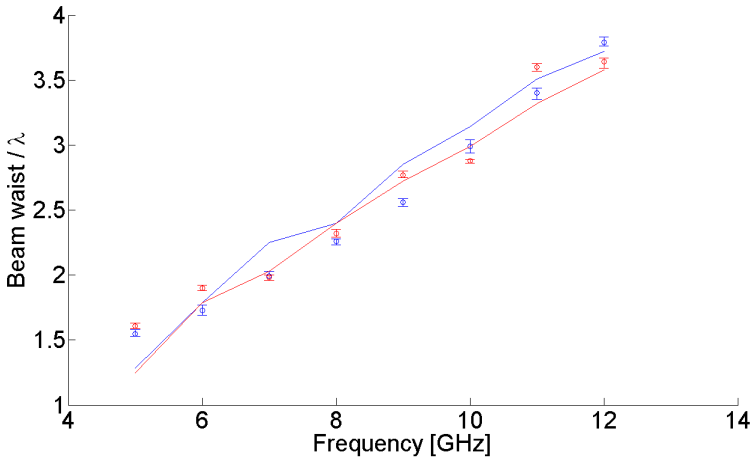

Figure 5.10. Gaussian Beam-waist vs Frequency. Solid lines are simulation

measurements by adding an anti-reflection (AR) coating to the lens. The UCSD team used quarter wavelength rexolite coatings on their silicon lens to suppress the sidelobes and also to suppress the cross-polarized power to under the -20dB level.

The silicon lens that UCSD is currently using is a synthesized ellipse of silicon with 5.08cm (2") diameter and they are testing it with a smaller antenna. Additionally, they mounted the feed-horn on it's own rotational stage to control the polarization tilt angle of the incident wave and to demonstrate the wobble shown in Figure 5.11. This amplitude is appears to be consistent with our simulations, although the UCSD team has not yet done a full statistical comparison. The tilt does not perfectly repeat after a log-period, as seen in both measurements and simulation *Edwards* [2008]. We do not yet understand the origin of this effect, but it is sufficiently subtle that we do not anticipate it compromising the polarization properties in our prototype detectors.

5.8 Conclusions

This chapter introduced the sinuous antenna as a log-periodic with desirable polarization properties on a contacting dielectric lens. We also derived the approximate input impedance for a self-complimentary antenna (δ=22.5^o). Finally we tested the design in 5-12GHz "scale-

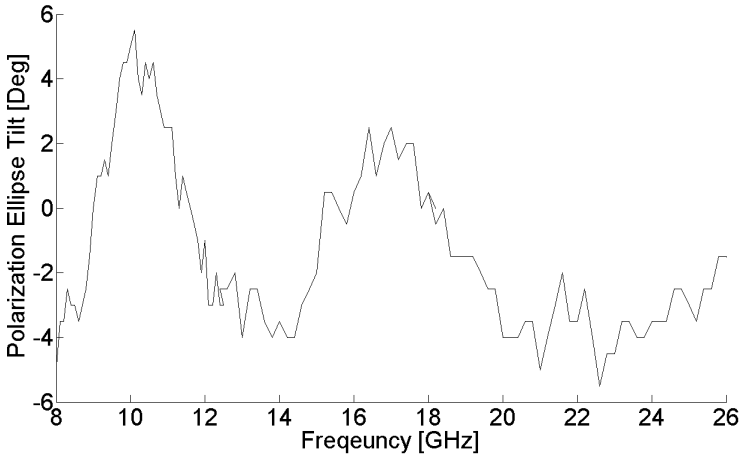

Figure 5.11. Polarization tilt τ vs frequency. The tilt oscillates $\pm 4^o$ every log-periodic scaling of frequency 1.3^2. Thanks to Jen Edwards for providing this figure (*Edwards* [2008]).

model" devices to verify that the design had beam patterns consistent with our simulations. The initial results show some deviations, but were none-the-less encouraging. Since then, the UCSD team has suppressed many of the high side-lobe and cross-pol levels in their measurements by changing lens materials and adding an AR-coating, providing data that agrees much more closely with the models. Meanwhile, the Berkeley side of the collaboration proceeded to fabrication and testing of the millimeter devices described in chapters 6-8.

Chapter 6

Sinuous Antenna Coupled TES bolometers

6.1 Introduction

Results from Chapter 5 suggest that the sinuous antenna is a promising candidate for coupling to TES-bolometers in CMB detectors. In this chapter, we describe the design, fabrication and testing of prototype pixels that are the simplest possible integration of the sinuous with the proven detector technology from Polarbear. Measurements of these devices demonstrate successful coupling of the sinuous to bolometers with high optical throughput and desirable beam characteristics.

The chapter begins with a discussion of the microwave electronics used to couple the sinuous antenna to our bolometers. We also describe our optical test cryostat used for all measurements in this thesis as well as an interferometer used to verify the filters' spectra. Finally, we show the results of several optical measurements and compare them against simulations.

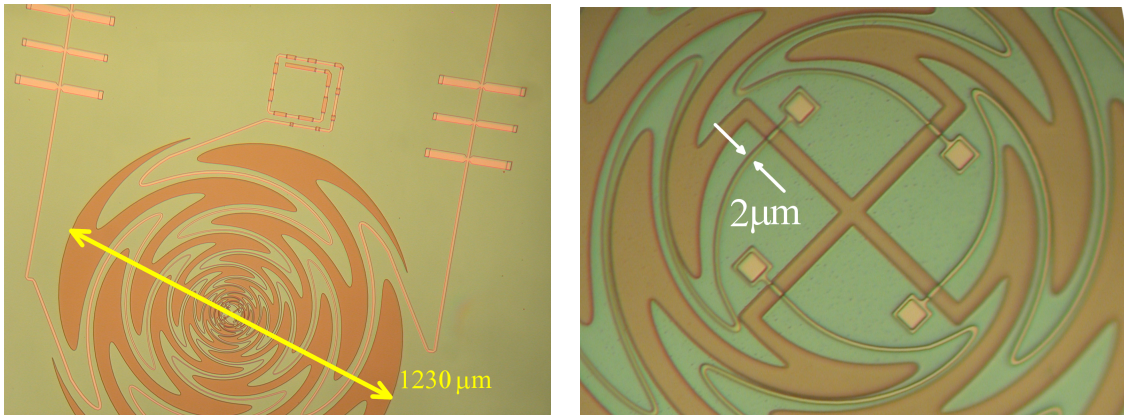

(a) Prototype Pixel (b) Zoom of Antenna Center

Figure 6.1. (a) Photograph of a prototype sinuous antenna; one polarization is terminated, the other passes through identical bandpass filters before the bolometer (not pictured). (b) Zoom of the antenna interior. The 1 μm microstrip alignment error in this picture was not present on the tested devices.

6.2 Microwave design considerations for the Prototype Chips

Figure 6.1 is a photograph of a prototype pixel. To optically characterize the antenna beams in different spectral regions, we fabricated five different devices with identical antennas but different bolometers and filters tuned to receive 30% passbands centered at 86GHz, 110GHz, 150GHz, 180GHz, and 230GHz . After the antenna, the power:

1. couples to microstrip transmission lines integrated onto antenna arms
2. passes through band defining microstrip filters
3. thermally deposits power at the bolometer on a lumped resistive load (not shown)

In the following subsections, we describe each of these stages.

6.2.1 Microstrip transmission lines

Microstrip transmission lines have a conducting metallic strip of width W separated from a ground plane by an insulating dielectric material of thickness h. Currents that travel in the upper conductor are mirrored by return currents in the ground plane. The currents generate electric fields between the two conductors and magnetic fields that circulate the

upper conductor (See figure 6.2). Microstrip transmission lines are popular for lithographed circuits because they are simple to fabricate in thin films.

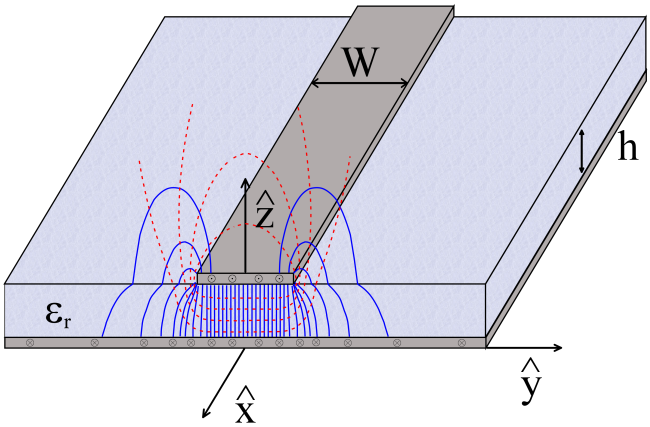

(a) Microstrip fields

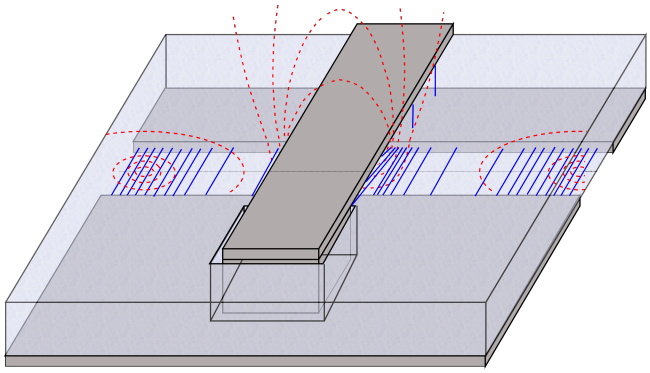

(b) Slot-transition fields

Figure 6.2. Drawing of Microstrip (a). Nb is gray, SiO_2 is light blue. Electric fields are in solid blue, while magnetic fields are dashed red. They kink at the free-space/dielectric interface. At a slot (b), the E-fields "fold" across the slot leaving the magnetic fields normal. Power propagates down the slot away from the microstrip.

We couple slot antennas (such as our sinuous) to microstrips by carving slots into the ground plane, crossing the upper conductor over the slots, and finally shorting to ground on the opposite side. This feed geometry forces the electric fields from the transmission lines onto the antenna's plane, oriented across the slots. The magnetic fields are normal to the slots, so the electric currents a the slot edge are equivalent to magnetic currents that propagate down the slot's interior (*Gupta et al.* [1996]). cross the slots. The magnetic fields

are normal to the slots, so the electric currents a the slot edge are equivalent to magnetic currents that propagate down the slot's interior (*Gupta et al.* [1996]).

Fabrication

In order of deposition, the microstrips are composed of:

1. 3000 Å sputtered Niobium (Nb) ground-plane. (nominally, $\lambda \sim 1000$Å)
2. 5000 Å PECVD SiO_2 dielectric layer ($\epsilon_r = 3.9$)
3. 6000 Å sputtered Nb upper-conductor.

PECVD stands for Plasma Enhanced Chemical Vapor Deposition and is a process that forms the oxide entirely from reacting gases N_2O and SiH_4 (*Chang* [2010b]). The Nb sputtering process also uses an Argon plasma to knock Nb atoms from a target and deposit them on our wafers. We deposited these layers between the LSN and Al-Ti layers described in the bolometer fabrication section of Chapter 3. To ensure a superconducting connection between Nb layers at via shorts, as well as between Nb and Al-Ti at the bolometers terminations, we sputter etch with an Ar plasma to remove native Nb-oxide prior to those metallic depositions.

We chose the SiO_2 thickness of 5000Å to provide relatively high impedance lines, but not so thick that it would cause mechanical issues through internal stress or electrical issues associated with step coverage through the vias between upper and lower Nb films. We chose the Nb ground thickness of 3000 Å to exceed the superconducting magnetic field penetration depth of 1000 Å (*Kerr* [1999]) and the upper Nb thickness of 6000 Å to ensure step coverage in the vias.

We defined all of our features with standard optical photolithography and etched the films with a CF_4 plasma (*Hamilton* [2010]). We mixed the CF_4 with trace amounts of O_2 to wear away the photoresist during etching, providing more gradual side-walls that further helps step-coverage. In principle, the lithography can provide sub-micron resolution (*Meng* [2010]), but the O_2 over-etches the features, rendering it impractical to make features finner

than 1 μm in the 6000 Å thick Nb. We can improve the etching resolution with thinner films of Nb in the upper-layer, but not without compromising step coverage in the vias. Our group is currently exploring new fabrication techniques to address this constraint, but all devices described in this thesis were limited in resolution to 1 μm. Other research groups have achieved sub-micron widths of Niobium lines with comparable thickness by using liftoff lithography and this may be a possible solution for our process in the future.

Fringing fields

Despite being relatively easy to make, microstrip is not true TEM transmission line because of the kink in the fringing fields between fee-space and dielectric (see Figure 6.2). At that interface, the Magnetic fields **H** are continuous because μ_r=1. The change Δ in normal field H_z across the interface is related to the tangential electric fields (E_x, E_y) there through Faraday's law:

$$\begin{aligned} 0 &= \Delta\left[\mathbf{H}_z\right] \\ &= \Delta\left[(\nabla \times \mathbf{E})_z\right] \\ &= \Delta\left[\frac{\partial E_x}{\partial y}\right] - \Delta\left[\frac{\partial E_y}{\partial x}\right] \end{aligned}$$

Because ϵ_r changes as the fields cross this surface, E_y is also discontinuous there. To keep **H** continuous, the fringing longitudinal component E_x cannot vanish. A similar argument shows that **H** also has longitudinal components. Since these components are small compared to the fields between the conductors, microstrips are "quasi-TEM" transmission lines and are only slightly dispersive (*Gupta et al.* [1996]). But we must account for these fringed fields when calculating microstrip impedance.

Kinetic Inductance

Superconducting effects enter into this calculation. The circuit model for an ideal *lossless* transmission line has series inductance L and shunt capacitance C per unit length, providing

an impedance $Z = \sqrt{L/C}$ and wave speed $v = 1/\sqrt{LC}$. A *lossy* normal transmission line has shunt resistance per length corresponding to dielectric losses and series resistance per length from Ohmic losses in the metal (See figure 6.3(a), *Pozar* [2004]). However, superconductors are *not* just ideal, lossless metals; the ohmic series resistance R_Ω present from normal metals becomes an extra source of inductance L_K (See figure 6.3(b)).

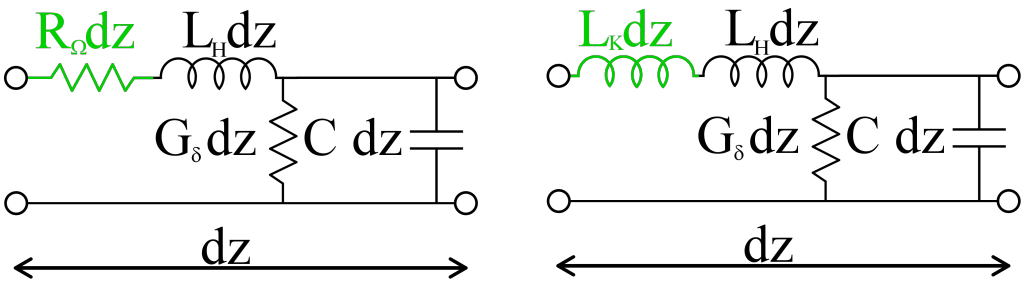

(a) Normal Transmission line (b) Superconducting Transmission line

Figure 6.3. Circuit Models for transmission line section of length dz. When cooled below the conductor's superconducting transition, the ohmic series resistance becomes inductive.

In the Drude-model of conduction, electrons in a metal experience forces from applied fields E and well as a frictional forces cause by collisions every time-constant τ (*Kittel* [2004]).

$$m\frac{d\langle v\rangle}{dt} = -eE - m\frac{\langle v\rangle}{\tau}$$

The conductivity is proportional to the velocity with which the electrons travel through the metal. For a superconductor with no collisions, $\tau \to \infty$, so currents with frequency ω will have a conductivity:

$$\sigma = -j\frac{ne^2}{m\omega} \tag{6.1}$$

where n is the number-density of current-carrying particles (*Van Duzer* [1998]). In contrast to the real σ for a normal metal, this causes the current to lag behind the voltage

just like an inductor. For a conductor of cross sectional area A, the inductance per unit length of this metal is

$$L_K = m/(ne^2A)$$

and the associated energy per volume is

$$\frac{L_K I^2/2}{A} = n\frac{1}{2}m\langle v\rangle^2$$

This phenomenon is termed kinetic inductance because it's created by the large kinetic energy that current carrying particles acquire in superconductors. It is suppressed in normal metals by the low scattering times τ (*Van Duzer* [1998]).

Electromagnetic waves are screened from the interior of superconductors beyond a penetration depth $\lambda = \sqrt{m/\mu_o ne^2}$. So the kinetic inductance is only relevant in the volume on the outer surface with cross-sectional area $A = W\lambda$, providing an inductance per unit length of:

$$L_K = \mu_o\lambda/W \tag{6.2}$$

(*Kerr* [1999]). Ignoring fringing fields, the magnetic inductance is $L_H/ = \mu_o h/W$. For our transmission lines with oxide films 5× thicker than λ, L_K is about 20% of L_H. So this effect makes a substantial contribution of $\sim$ 10% to the impedance and wavespeed. It is convenient to express the inductance in units per square of material, so L_K=$\mu_o\lambda\approx 0.13pH/\square$.

The shunt conductance to ground G_Ω in Figure 6.3 represents losses in the SiO_2 dielectric medium. We have previously measured the loss tangent of our SiO_2 to be $\tan(\delta)$=0.005, which corresponds to 4% loss per millimeter at a frequency of 150GHz.

Yassin and Witherton developed a detailed model for superconducting microstrips with fringed fields (*Yassin and Withington* [1996]). However, it is cumbersome to integrate this model with full-wave EM simulators like Sonnet EM. Sonnet uses a very similar algorithm to ADS-momentum, modeling the non-perfect conducting metallic surfaces with a surface

impedance to allow for small tangential electric fields. Sonnet is the best choice for broadband superconducting applications because it allows the user to choose to input a surface inductance (*Kerr* [1999]). We have found good agreement of microstrip impedances and wave speeds between the analytic model and ADS with a surface inductance.

Dolph-Chebyshev Transformer

The average impedance of the sinuous antenna is Z_{ant}=105Ω, but we normalized our microstrip circuits to an impedance of Z_{line}=10Ω which corresponds to 10 μm wide lines. Such an abrupt change in impedance would reflect away over 80% of the power. Instead, we gradually change the impedance with a tapered line width. We taper our impedance with the a Dolf-Chebyshev transformer:

$$Z(x) = Z_{ant} \exp\left\{\frac{1}{2}\ln\left(\frac{Z_{low}}{Z_{high}}\right)\left[\sin\left(\pi\left(\frac{x}{L}-\frac{1}{2}\right)\right)+1\right]\right\} \tag{6.3}$$

along the backs of the antenna arms over a length L=4.5mm (*McGinnis and Beyer* [1988]). In practice, we cannot fabricate lines with impedance any higher than ∼60Ω without a major change to our fabrication process (*Meng* [2010]), but this mismatch only reflects 8% of the power. We leave fabrication of 100 Ω lines to future efforts. As described below, this mismatch creates a standing wave that we use to constrain the antenna impedance.

6.2.2 Quarter-wavelength shorted stub filters

Terrestrial observations require bands that are wide enough to received high integrated power, but also edges that are steep enough to reject atmospheric lines. Steeper edges can provide higher throughput, but they require more resonant poles which have enhanced loss over non-resonant microstrip features. A good compromise is a 3-pole filter. For more detail on this optimization, we refer the reader to Kam Arnold's thesis (*Arnold* [2008]).

Figure 6.4 shows a generic 3-pol filter. The values of the inductors and capacitors can

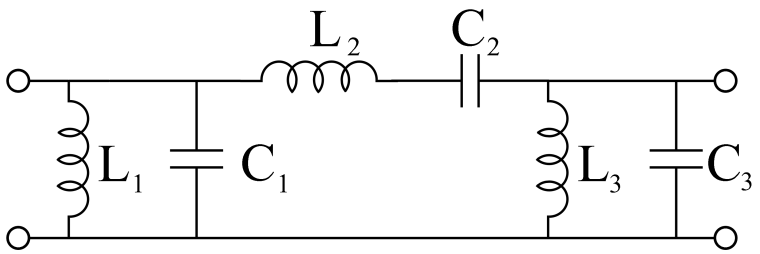

Figure 6.4. Generic 3-pole bandpass filter. At resonance, the series resonator conduct and parallel resonators to ground open.

be chosen to tailor the filter's bandwidth and ripple (*Matthaei et al.* [1980]). The parallel LC resonators on the left and right have an impedance of

$$\begin{aligned} Z_{parallel} &= \left(j\omega L + \frac{1}{j\omega C} \right)^{-1} \\ &\approx -\frac{j}{2\omega_o C} \frac{\omega_o}{\delta\omega} \end{aligned} \tag{6.4}$$

where the last line is an expansion for small differences in frequency $\delta\omega$ from the resonant frequency ω_o. Likewise, the series LC filter in the center has impedance:

$$\begin{aligned} Z_{series} &= j\omega L + \frac{1}{j\omega C} \\ &\approx j2\omega_o L \frac{\delta\omega}{\omega_o} \end{aligned} \tag{6.5}$$

It is challenging to realize these lumped electrical components in millimeters wave circuits because their properties will depend on fine micron-scale dimensional details. Alternatively, we can make equivalent circuits with distributed resonators on transmission lines (*Myers et al.* [2005]). Waves on a transmission line with impedance Z_o will partially reflect off a termination Z_L and interfere with the incoming waves to form a standing wave. At a distance ℓ from the load on a *lossless* line, the ratio of voltage to current in the standing waves creates a transformed impedance of

$$Z_{in} = Z_o \frac{Z_L + jZ_o \tan(2\pi\ell/\lambda)}{Z_o + jZ_L \tan(2\pi\ell/\lambda)} \tag{6.6}$$

(*Pozar* [2004]). If the line is $\ell = \lambda_o/4$ long with impedance Z_1 and the loading impedance is a short to ground ($Z_L = 0$), the input impedance expanded around the resonant frequency ω_o is:

$$\begin{aligned} Z_{in} &= jZ_1 \tan\left(\frac{\pi}{2}\frac{\omega_o + \delta\omega}{\omega_o}\right) \\ &= jZ_1 \cot\left(\frac{\pi}{2}\frac{\delta\omega}{\omega_o}\right) \\ &\approx -jZ_1\frac{2}{\pi}\frac{\omega_o}{\delta\omega} \end{aligned} \tag{6.7}$$

This is exactly the same form as the impedance of the parallel LC resonator. If we choose the impedance Z_1 to match the pre-factor in Equation 6.4, a shorted $\lambda/4$ transmission line will behave identically to the LC filter for frequencies near ω_o.

When we view a general load impedance Z_L through a $\lambda/4$ long line of impedance Z_{inv}, Equation 6.6 reduces to

$$Z_{in} = \frac{Z_{inv}^2}{Z_L} \tag{6.8}$$

The $\lambda/4$ line with impedance Z_{inv} is an inverter that inverts the load impedance (*Pozar* [2004]). If the load is the shorted $\lambda/4$ resonator described above (but with another impedance Z_2), then it's impedance will look like:

$$Z_{in} = j\frac{\pi}{2}\frac{Z_{inv}^2}{Z_2}\frac{\delta\omega}{\omega_o} \tag{6.9}$$

which has the same form as the series resonator. As before, this will behave identically to a series resonator with the proper choice of Z_{inv} and Z_2 .

We can replace the three-pole filter in Figure 6.4 with the filter shown in 6.5 (*Matthaei et al.* [1980]). It has three pairs of $\lambda/4$ shorted stubs separated by two $\lambda/4$ inverters. Once we have chosen a pass-band center frequency ω_o, we can control the input impedance, band ripple and width with the impedances of (1) the outer stubs, (2) the inner stub, and (3) the inverter. In practice, it is easiest to do this numerically with an optimizer algorithm and

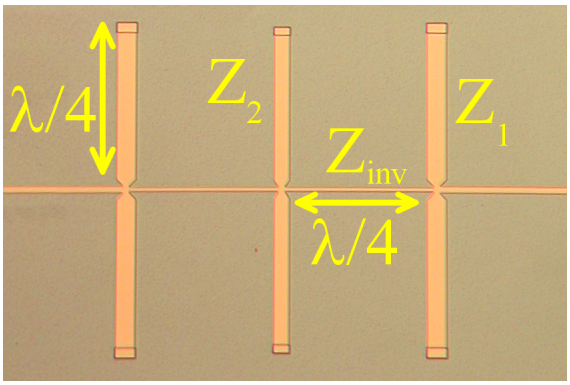

Figure 6.5. Stub filter with shorts through the square vias at the ends.

we chose the impedances, widths and lengths shown in the Chart 6.5. We build pairs of parallel stubs instead of single stubs to avoid microstrips so wide that they might be driven in non-fundamental modes.

The transmission-line filter only approximates the ideal filter at frequencies near resonance. At resonance, the $\lambda/4$ stubs transform the shorts to opens, and current passes by as if the stubs were not there. Off resonance, the impedance is complex and poorly matched to the input ports, so it reflects power back. However, at an odd-integer multiple of the resonant frequency ω_o, there will be satellite bands where the stubs also transform the short to open. Additionally, at very low frequencies, the filter will look like a short to ground.

6.2.3 Differentially feeding a load-resistor

Finally, the microstrips terminate on 400 Å Ti sitting in close thermal contact with the TES (6.6). The incident radiation exceeds the band gap in Ti and this material is very lossy. However, for the antenna to operate in the D_{45^o} mode, the opposite transmission lines need a 180^o relative phase shift. We accomplish this by driving the 4-square piece of Titanium differentially, providing 20 Ω with a virtual ground at the center, properly terminating each 10Ω side.

The incident wave on the left of the load with voltage V_L partially reflects with with a voltage $(R - Z_o)/(R + Z_o)V_L$. The wave incident on the right will partially transmit a wave

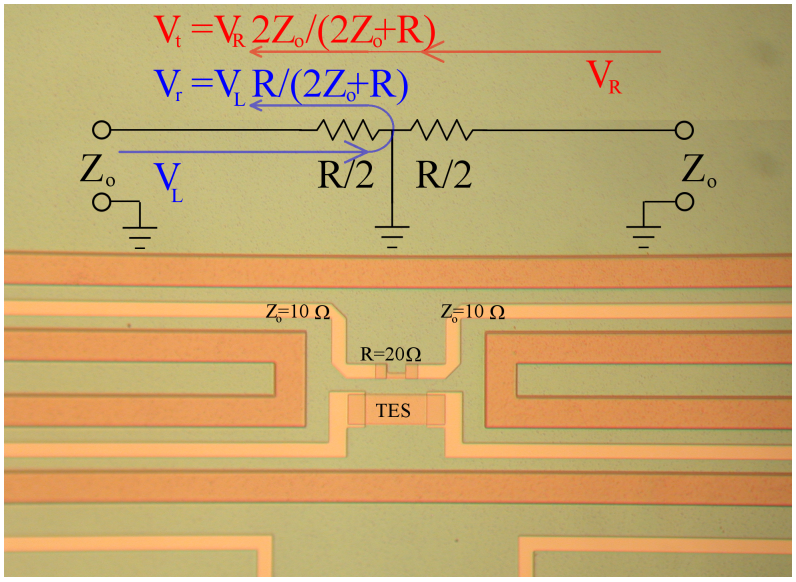

Figure 6.6. Picture of an un-released bolometer shows the Resistive load next to the TES. There is an equivalent circuit above and as well as voltage wave amplitudes. Blue is for waves originating on the left, red from the right.

with $(2Z_o)/(R+Z_o)V_R$ that interferes with the reflected wave. If the antenna only receives an odd antenna mode with V_L=$-V_R \equiv V_o$, then the voltage of the non-terminated wave

$$V = V_o \frac{R - 2Z_o}{R + 2Z_o} \tag{6.10}$$

which vanishes when R=$2Z_o$=20Ω. This design is fairly forgiving of errors in R; if R is 25% too low or high, it only reflects away 2% of the power. On the other hand, the antenna's unwanted even mode will have V_L=V_R, and this feed will reject 100 % of that power, regardless of the value of R.

To drive both polarizations, two of the transmission lines must cross in a microstrip cross-over (*Myers et al.* [2005]). This requires extra deposition and lithography steps that complicate the fabrication for what is intended as a simple test prototype. Instead, we only coupled one polarization to the bolometers, and terminated the other in lossy Al-Ti transmission line.

6.3 Optical Test Cryostat

We preformed all device measurements in an IR-labs dewar (serial number 576) retrofitted for optical measurements with a window and optical filter stack. Figure 6.7 shows a solid-works image of the dewar in cross-section as well as a photograph of the interior with radiation-shields removed.

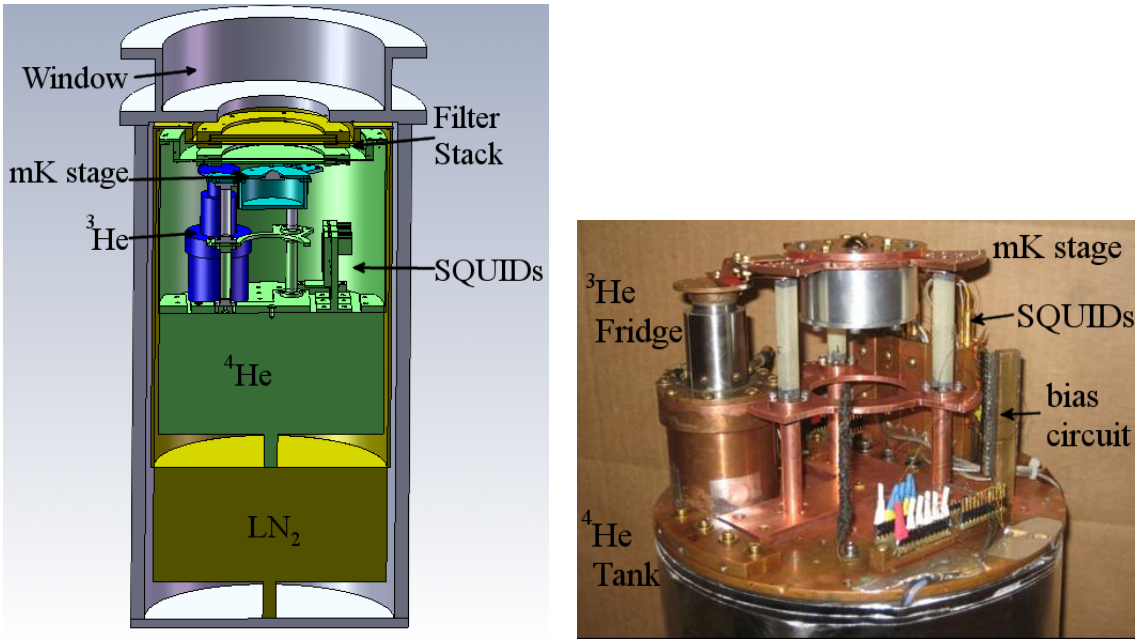

(a) Cross-sectional Dewar Drawing

(b) Photograph of Dewar interior

Figure 6.7. Stub filter with shorts through the square vias at the ends.

6.3.1 Dewar Cryogenics

The dewar buffers the millikelvin (mK) stage from room temperature (300K) with a Liquid Nitrogen (LN2) stage at 77K and a Liquid Helium (LHe) stage. While the helium boils at 4.2K at atmospheric pressures, we drop it's temperature to 1.3K by pumping. Each of these tanks enclose the inner stages with a radiation shield that we covered with 10-layers of Multi-Layer-Insulation (MLI) to insulate against radiative loading.

The mK-stage is cooled with a home-made closed-cycle ^{3}He sorption fridge. We drove helium from activated charcoal with heating resistor, allowing the helium to fall onto a 1.3K

condensation plate and collect on the fridge-head. Once we stop heating the charcoal, an annealed-tin heat switch thermally shorts it back to 1.3K, and the charcoal's large surface area pumps on the pool of ^{3}He, cooling it to temperatures as low as 0.26K (*Weisend* [1998]).

We isolated the mK-stage from the LHe stage on three 6.89mm (1.75") long Vespel legs with diameter 1.57mm(0.4") and wall thickness 0.020mm (0.005"). With a thermal conductivity of $k(T) = 1.8 \times 10^{-5} T^{1.2}$ W/m·K (*Woodcraft and Gray* [2009]), we estimate that the legs conduct roughly 6 nW, while the fridge is known to provide a cooling power of $\sim$10 nW. The cycle time for our ^{3}He fridge in these conditions varied between 6-12 hours.

6.3.2 Optical Filter Stack

We installed a 10.16cm (4") diameter 5.08cm (2") thick zote-foam window (*Takahashi* [2008]) on the bottom of the 300K shell. This foam has closed cells filled with N_2 gas, providing only modest scattering of millimeter radiation but sustaining vacuums of less than 1×10^-8 torr. It is crucial that the window hold such a low vacuum. We initially pump the dewar space with a turbo-pump, but after we transfer LHe, we remove the turbo and rely on cryo-pumping to keep the pressure low since the turbo vibrations provide unacceptable noise in our system.

We placed 0.762cm (0.3") of porous (expanded) Teflon at the LHe radiation shield window. Teflon absorbs Infra-red (IR) radiation, but it's index of refraction of 1.4 can reflect away some incident power. The company Porex creates porous Teflon by sintering Teflon particles in a way that leaves air voids, dropping the materials index of refraction. Measurements of the similar material Zitex suggest it's index is 1.2 (*Benford et al.* [2003]).

We also use a metal-mesh filter at 77K to reflect away radiation above 18 cm^{-1} wavenumber (540GHz). We installed additional low-pass metal mesh filters at the 4K radiation shield window that cut-off above 14 cm^{-1} (420GHz)and 12 cm^{-1} (360GHz). Peter Ade's group (University of Cardiff) provided these filters. There was ample room between the mK stage and the 4K window to optionally install an extra filter at 6 cm^{-1} (180GHz) to suppress the 90GHz filter's first satellite band as well as an optical attenuator to prevent saturation

from room-temperature thermal loads. Our attenuator was 0.635cm (0.25") of Emmerson-Cuming's MF110 pre-cast stycast material. It was not used with the devices of this chapter, but was used with those in the chapters 7 and 8.

6.4 Spectral Response

Our circuits operate in a 70-300 GHz spectral range where narrow-band coherent sources, such as those in network analyzers, are prohibitively expensive. Instead, we use a broadband thermal source and a Fourier Transform Spectrometer. The interferometer's source is a HPK 125W high-pressure mercury lamp from Msscientific (previously manufactured by Philips) that sits at the focus of a collimating parabolic mirror. Our interferometer is shown in Figure 6.8. A nominally 0.039mm (0.010") thick sheet of mylar splits the beam between two arms, one with a fixed mirror (top) and a second one with a movable mirror (right). The beams re-combine in the mylar and are redirected into the dewar with light-pipe.

The end of the light-pipe acts as a isotropic point source and we re-converge the beam onto our devices with a warm (300K) TPX-lens. The TPX lens focal-ratio was roughly f/2.5, while the detector's ratio varies from f/5.7 at the upper band edge to f/2.2 at the lower edge. As a result, the radiation from the interferometer over-illuminates the antenna's fundamental mode at all but the lowest frequency channel and the antenna receives only $A\Omega = \lambda^2$ throughput over most of the band. This simplifies the analysis because a lens that under-illuminates the antenna would produce measured spectra that are a convolution of the filter and throughput spectra.

If the bulb were a monochromatic source that emitted only a wavenumber $\bar{\nu}$ with intensity I_o, then when the mirrors have a path-length difference $\Delta = 2(d_1 - d_2)$, the device under test will receive an intensity

$$I(\Delta) = I_o/2\left[1 + \cos\left(2\pi\bar{\nu}\Delta\right)\right] \tag{6.11}$$

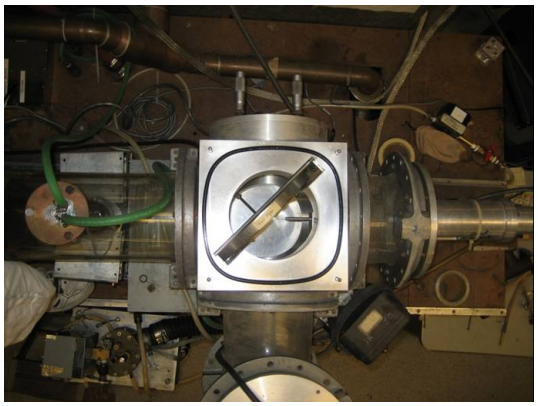

(a) Fourier Transform Spectrometer (FTS)

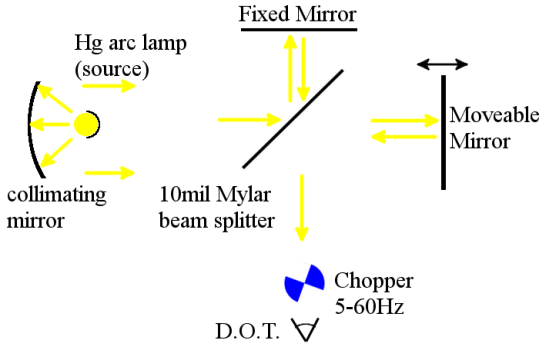

(b) FTS Schematic

Figure 6.8. (a) Photograph of FTS Spectrometer used in these measurements, viewed from above. The dewar with the Device Under Test (DUT) is not visible. (b) Schematic of FTS optics.

However, the bulb actually emits a broad spectrum and the bolometer will see a wide fractional bandwidth with a spectrum $I(\bar{\nu})$ that is defined by both the Device Under Test (DUT) *and* the interferometer's optics. Integrating Equation 6.11 over $\bar{\nu}$ with intensity $I_o = I(\bar{\nu})d\bar{\nu}$ yields the total power the bolometer receives at each mirror position Δ:

$$J(\Delta) = I_o/2 + \int_{\bar{\nu}=0}^{\infty} \frac{I(\bar{\nu})}{2} \cos\left(2\pi\bar{\nu}\Delta\right) d\bar{\nu} \tag{6.12}$$

In principle, we can recover the system's spectral response $I(\bar{\nu})$ from the Fourier Transform of the interferogram $J(\Delta)$. In practice, we only sample the interferogram at finite steps

over a finite total length and perform a discrete fast-fourier-transform on the data. The step spacing between mirror positions determines the maximum resolvable frequency, so we must sample the interferogram at sufficiently fine steps to Nyquist sample the spectrum up to the lowest optical-filter cutoff at 12 cm^{-1} (360GHz). The throw of the movable mirror arm is 42mm, which limits the spectral resolution of $I(\bar{nu})$ to 0.06 cm^{-1} (1.8GHz) (*Bell* [1972]).

The measured spectra are the product of those from the interferometer, dewar, and DUT. However, we are primarily interested in the response of only the detector, so we normalized the spectrometer against a different bolometer within a different dewar with a known and constant spectral response. Dividing the DUTs' spectra by the normalization spectrum removes the "null" in the beam-splitter at 330GHz and other spectral properties of the spectrometer optics.

Finally, we normalized the spectra's total optical throughput by measuring the power received from a chopped 77-300K thermal source (with δT=223K) that fills the antenna beam. The single-moded antenna can receive at most

$$\Delta P = k\Delta T \int I(\bar{\nu}) d\nu \tag{6.13}$$

while the a bolometer operated in strong electrothermal feedback will receive

$$\Delta P = V_b \Delta I_{SQ} \tag{6.14}$$

as discussed in chapter 3. The ratio of the two powers ΔP is the total camera fractional throughput (including optical filters).

Figure 6.9 shows the normalized spectral response of four devices centered at different frequencies. We fabricated an additional one that would have received power centered at 150GHz as well as a device with no filters, but design errors compromised those devices. The bold percentages show the band-averaged optical throughput through our test dewar to the bolometers. The inefficiencies are closely mirrored by simulations that account for

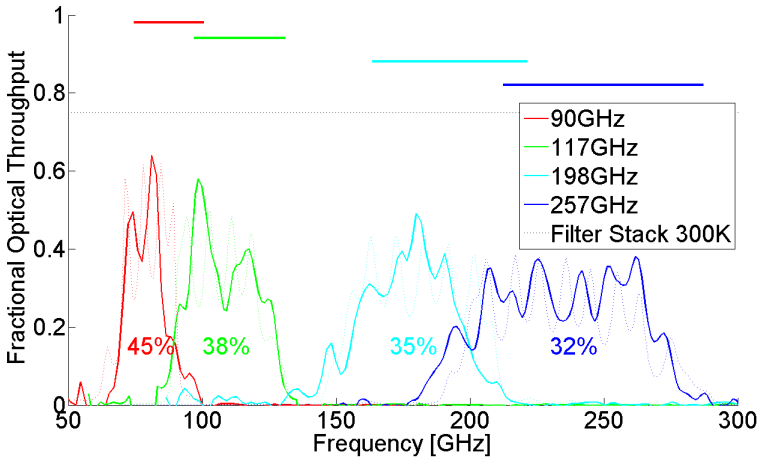

Figure 6.9. Solid curves show measured spectra, the colored dashed lines show simulations of the filter with microstrip lines between antenna and bolometer load. The dashed line is the average transmission of the filter stack at 300K. The solid lines at the top depict the designed -3dB bandwidths.

loss in the optical filter stack, reflections at the antenna-microstrip, and microstrip-load interface, reflections at the contacting lens surface, and dielectric loss in the microstrip.

The downward slope of throughput as frequency increases is due to the lossy transmission lines having a longer electrical length at those frequencies and suggests a loss-tangent of $\tan(\delta) = 0.008 \pm 0.002$, which is consistent with our group's previous measurements of loss-tangent in our SiO_2 of $\tan(\delta) = 0.005 \pm 0.001$. We summarize the other sources of loss in Table 6.1 and note that the expected fractional throughput is similar to the measured values. However, the throughput through the filter stack is poorly understood because we have only performed the measurements warm in the middle of a gap in light-pipe.

Table 6.1. Losses in the single filter sinuous devices

Component	Power Transmitted
Optical Filters	≈70%
curved AR-coating	86%
Antenna Front-lobe	91%
Antenna-microstrip interface	88%
Dielectric Loss	70-90%
Total	35-45%

The solid bars at the top of the spectrum depict the filters' designed bands (-3dB).

The spectral band centers are all 9% lower in frequency than designed, which is likely caused by wavespeeds $(LC)^{-1/2}$in the lines being 10% lower than expected, or LC being 23% higher. We control the SiO_2 dielectric thickness to a high level of precision (around 5%). In Section 8.6, we compare pass-bands of this type with a different design to conclude that the oxide permittivity is likely $\epsilon_r = 0.46$ and that the Niobium's surface inductance is $L_s = 0.18$ pH/sq. Our group is currently developing techniques to test our lithographed circuit components at 4K, but at slightly lower frequencies of 40GHz and we hope to resolve this issue in the near future.

We designed our filters to have a -3dB fractional band-width of 30%. With the exception of the 90GHz channel, all the bands have a best fit width that is within an error-bar of design. The 90GHz channel fits to a narrow 22% fractional width because the upper-third of the band's transmission is supressed. We do not understand what causes this, but it is present in the 90GHz channels in later chapters. Again, we hope our scale-model measurements may shed light on this.

We also observe significant fringing within the bands, which we attribute to a fabry-perot cavity between impedance mismatches somewhere within our optics or microwave circuits. If the impedance mismatches produce voltage reflection coefficients $R_1(\nu)$ and R_2 and transmission coefficients $T_1(\nu)$ and T_2 at each of the two interfaces and there is a phase delay $\Delta\phi(\nu)$ for each pass, then the total transmission from all partial waves is:

$$|T|^2 = TT^* = \frac{|T_1(\nu)T_2|^2}{1 - 2\,|R_1(\nu)R_2|\cos(2\Delta\phi(\nu)) + |R_1(\nu)R_2|^2} \tag{6.15}$$

(*Born and Wolf* [1999]). We can identify the source of fringing by comparing the fringe-spacing in spectra with the phase-differences ($\Delta\phi(\nu)$) between different possible mismatches and we can then constrain the product of reflection coefficients $R_1(\nu)R_2$ (and hence impedances) through the fringe depths. As discussed in Chapter 5, the antenna impedance should be on average 105Ω with reactance that is at most $\pm 20\Omega$ (which is why $R_1(\nu)$ and $T_1(\nu)$ bear a frequency dependence on Equation 6.15). Further we measured the bolometer loads with a resistance bridge to be 26 Ω (13 Ω between the microstrip line and virtual

ground). The phase shift a wave experiences between two mismatches reflects the changing wave speed on the impedance transformer in the antenna feed as well as the greatly reduced wave speed in the filter and produces an average fringe-spacing of 8.2GHz, which closely matches the fringe spacing in our spectra of 8.7 ± 0.4 GHz (averaged over the all bands). The dashed lines in Figure 6.9 include not only the filters, but also the simulated antenna impedance, measured load resistance, lines in between, and loss in the optical filter stack. The ratio of fringed trough to peak averaged across all bands is 0.63 ± 0.12, while the simulations suggest an average value of 0.57. This agreement suggests that our measurements are consistent with an antenna impedance simulated and modeled in chapter 5. However, Figure 6.9 reveals only a rough similarity between simulation and experiment through a few statistical parameters; the simulations clearly show differences from the measurements suggesting systematic effects that our simple model does not reflect.

Lastly, it is possible that the bolometer itself is inefficient in transferring the thermal power from the load to TES. However, our group has previously characterized similar bolometers' transfer functions by driving the RF-termination with a DC power supply (instead of an antenna). We found that the power received in the TES matches that deposited from the DC supply (*Myers* [2008]).

6.5 Beam Patterns

The spatial distribution of power reived by the bolometers is just as important as the frequency distribution when characterizing our device. However, our bolometers will average over all frequencies transmitted through the in-band filter, so it is most useful to measure the beam-patterns with a broadband source. Figure 6.10 shows the setup for these measurements. Our source is a 300-77K chopped thermal load with an aperture size of 1.27cm (0.5") that sits in a plane (5" to 11.5") below the plane with the contacting lens' tip. We moved the source within a plane on the pair of linear translation stages seen in Figure 6.10.

The un-polarized beam maps are shown in Figure 6.11: Figure (a) shows 2-D simulations, (b) 2-D measurements, and (c) simulations (dashed lines) and measurements in three

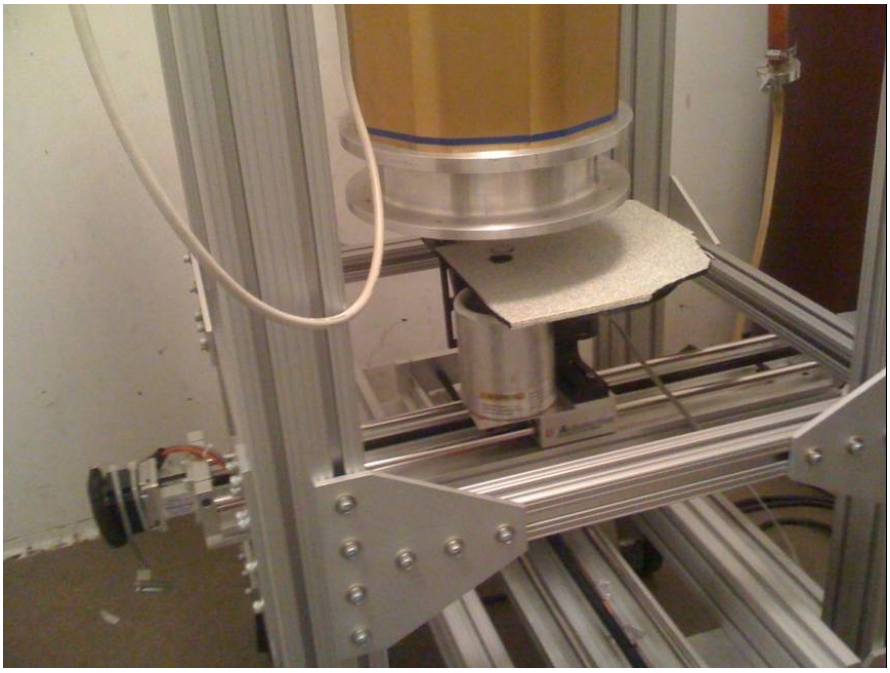

Figure 6.10. Chopped thermal load used for pattern measurements. We extended the 300K surface defining the aperture with more eccosorb than shown to completely block the chopping wheel everywhere except the aperture.

cuts through the beam. As the source moves off axis by an angle of θ, the area subtended by the source decreases by $\cos(\theta)$, so we have corrected the powers in these maps by that factor. Additionally, the simulated beams in (a) are an average of patterns weighted by the measured spectral response seen in Figure 6.9, all normalized to their peak power on boresight.

Figure 6.11.c shows that the measurements seem to agree more closely with simulation in the higher two frequency channels than at the low ones, but none agree well enough to have a low reduced χ^2. The simulations account for the presence of the lens with a single-layer anti-reflection coating, but they do not account for the rays (10% of power) that partially reflect between the antenna and lens surface. Nor do they account for reflections off the low-pass metal-mesh filters that are notorious for complicating beam patterns in cameras. These systematics may explain some of the observed discrepancies.

The best fit beam widths are shown in Table 6.2. As the center band frequency increases from 83GHz to 230GHz (a factor of 2.8), the beam only narrows by 2.5. This discrepancy

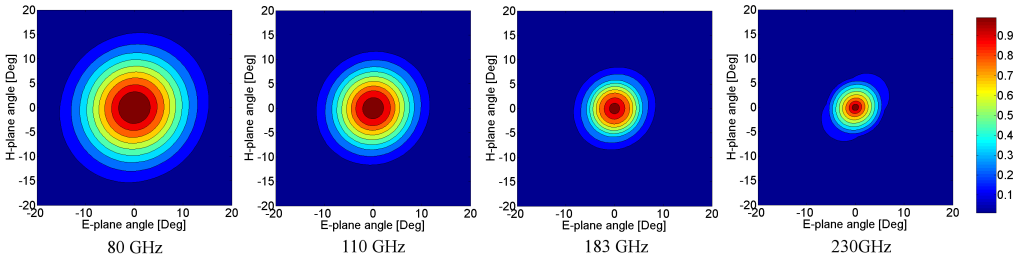

(a) 2-D Beam Simulations

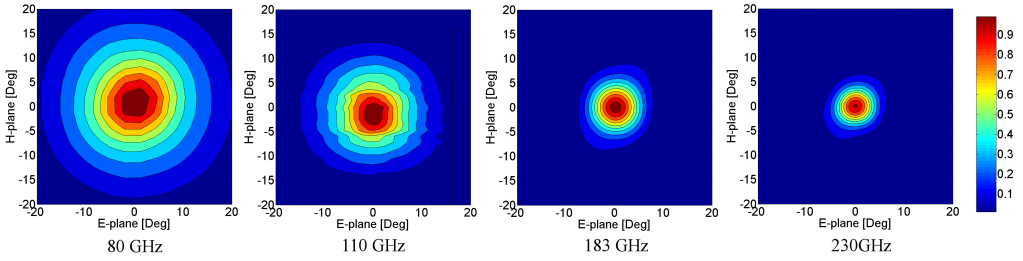

(b) 2-D Beam Measurements

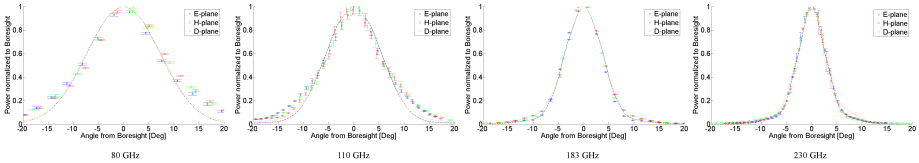

(c) Beam Cut Simulations and Measurements

Figure 6.11. Simulations and Measurements of Sinuous Beams

arises because the lens is not a true synthesized ellipse, but is rather between the elliptical and hyperhemispherical geometries, which suppresses the decrease in beam size.

6.6 Cross-polarization Rejection

As stressed in Chapter 5, this antenna must efficiently reject cross-polarized power if it is to be useful for polarimetry. If an antenna is well aligned to a polarized source, it should reject all cross-polarized power on boresight over a narrow band. The polarization tilt wobble ensures that the band-averaging bolometers will see a small amount of the wrong polarization.

Table 6.2. Beam Geometry

Channel	ellipticity	E-plane FWHM	H-plane FWHM	Boresight Cross-Pol Rejection
80 GHz	$1.1\% \pm 0.2\%$	$15.1^o \pm 0.7^o$	$15.6^0 \pm 0.7^o$	
110 GHz B	$2.8\% \pm 0.2\%$	$10.9^o \pm 0.4^o$	$11.8^o \pm 0.4^o$	
183 GHz B	$0.4\% \pm 0.1\%$	$8.1^o \pm 0.3^o$	$8.2^o \pm 0.3^o$	
230 GHz B	$2.0\% \pm 0.2\%$	$5.9^o \pm 0.3^o$	$6.2^o \pm 0.3^o$	

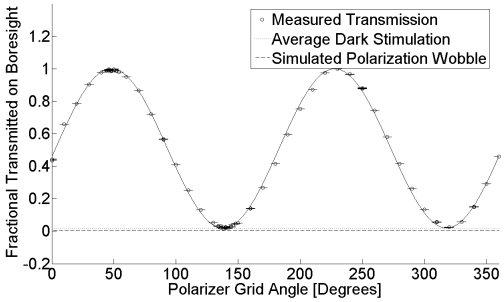

Figure 6.12. Power transmitted from a chopped thermal load on boresight to antenna through a polarizing grid. This antenna's circuit filtered the 110GHz band; other devices with different filters had similar polarization response.

We characterized this leakage by placing the chopped thermal load from Figure 6.10 on boresight and rotating a polarizing grid between the load and dewar window. Figure 6.12 shows the result of this measurement and best fit line for one of the channels and has the expected sinusoidal form. Table 6.2 summarizes the fraction of cross-polarized power leaked from all the channels, and it is roughly 2% on average. The grid itself is known to leak between 1-2% (*Myers* [2008]), which explains most of the systematic offset between the grid and the expected leakage from wobble.

6.7 Conclusions

In this chapter, we have demonstrated that TES bolometers can be coupled to the sinuous antenna in a way that is very similar to the Polarbear feeding scheme. This design provides high optical coupling efficiency with desirable beam characteristics. However, the differential feeding scheme requires complicated wiring or broadband hybrids if it couples

to bolometers through the channelizer circuits in Chapters 7 and 8. Since these alternatives are difficult to implement, we did not use the slot-coupling in the later designs.

Chapter 7

Diplexer and Triplexer Circuits

7.1 Introduction

In chapters 5 and 6, we presented data that suggest the sinuous antenna can couple to TES bolometers and provide a large boost in bandwidth over narrow-band antennas like the crossed double-slot. However, to control for foregrounds, we need to divide this bandwidth into narrow channels with microstrip circuits, which is the subject of this and the next chapter.

This chapter begins with a discussion of photometry vs spectroscopy to address why we chose simple channelizing circuits over an autocorrelator design that more directly mimics the FTS described in the last chapter. The simplest possible schemes are diplexer and triplexer circuits that extract two and three non-adjacent bands for observation in a terrestrial experiment. We discuss the design methodology of these circuits and show data from dual polarized antenna-coupled bolometers with desirable beam and spectral characteristics.

We have also fabricated a broadband Anti-reflection coating that uses three layers of monotonically increasing index. We discuss the design methodology behind this and show encouraging prototype test results.

7.2 Filter Manifolds vs Autocorrelation

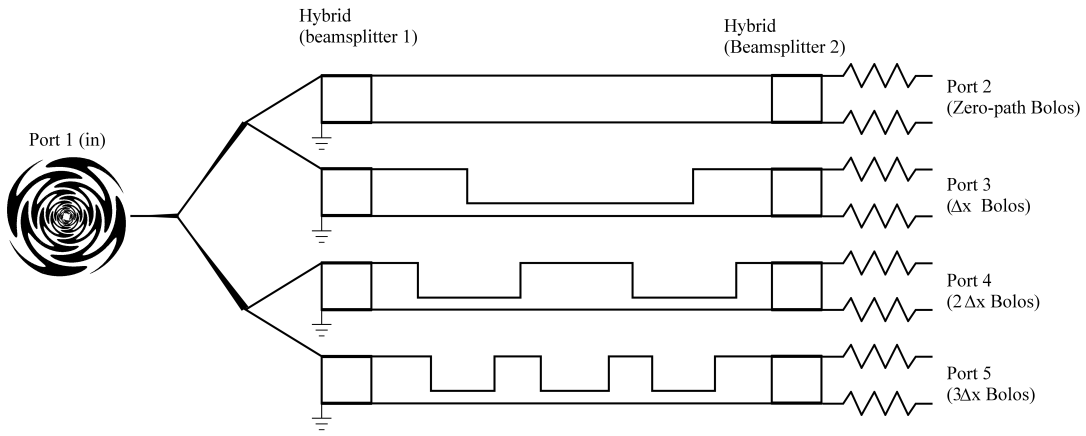

Figure 7.1. Schematic design of an autocorrelator in an antenna-coupled bolometer. In practice, we need several more bifurcations to Nyquist sample up to the lowest optical filter's cutoff.

This chapter and the next focus on microstrip filter manifold that sort the antenna's bandwidth into narrow frequency channels. However, in the previous chapter, we reported on successful spectral measurements of millimeter wavelength devices using a Fourier Transform Spectrometer. This motivates a natural question: Can we implement a similar autocorrelation spectrometer on our chips in microstrip circuits in lieu of filter manifolds?

For example, a cascade of microstrip-tees as shown in Figure 7.1 could split the broadband output of each polarization of the sinuous into full-bandwidth lines with equal power. A set of quadrature hybrids playing the role of a beam splitter could then divide each line into two arms, one with a phase delay relative to the other. Finally, a second set of hybrids could re-combine the signals and terminate all the power of bolometers. In principle, this design could provide arbitrary resolution, limited only by the length of the longest arm. Additionally, we could low-pass filter the signal between the antenna and bifurcation so we would only need to bifurcate enough to Nyquist sample up to that cut-off. The primary challenges behind implementing this scheme are building a hybrid with two octaves bandwidth and keeping the loss in the lines between the hybrids low.

Even if these challenges are met, Zmuidzinas argued in a series of papers ((*Zmuidzinas*

[2003a]) and *Zmuidzinas* [2003b]) that this design is only tenable when the incident radiation has high occupation number ($n(\nu) \gg 1$). We summarize those arguments here since they are an important part of our design decisions that eliminate on-chip autocorrelation as a possibility for CMB polarimetry detector designs.

The discrete Fourier transform of an interferogram does not perfectly re-construct the frequency spectrum. Instead, it results in a histogram where the spectrum is resolved into a basis of displaced top-hat functions:

$$n(\nu) = \sum_{c=1}^{N_{chan}} n_c \sqcap_c (\nu) \tag{7.1}$$

where

$$\sqcap_c(\nu) = \begin{cases} 1 : \nu_c \leq \nu \leq \nu_{c+1} \\ 0 : \text{else} \end{cases}$$

and n_c is the number of photons in a channel c between ν_c and ν_{c+1}. The length of the longest path determines the resolution $\Delta\nu = \nu_{c+1} - \nu_c$ while the number of bifurcations determines the highest resolvable frequency $\nu_{N_{chan}}$. Expanding the incident spectrum in this basis, the energy received by the i^{th} bolometer (Equation 3.2) during time τ is

$$\begin{aligned} E_i^{(B)} &\equiv \tau \langle d_i \rangle \\ &= \sum_c \{(h\nu_c)\tau n_c \Delta\nu\} \left[\frac{1}{\Delta\nu} \int_{\nu_c}^{\nu_{c+1}} d\nu \left| S_{i1}(\nu) \right|^2 \right] \equiv \sum_c E_c^{(f)} p_{ic} \end{aligned} \tag{7.2}$$

where the term in curled brackets is the energy $E_c^{(f)}$ in one frequency channel and the term in square brackets is the probability p_{ic} that photons from frequency channel c are received by bolometer i.

Meanwhile, the energy covariance in the detectors (Equation 3.3) expanded in $\sqcap_c(\nu)$ is

$$
\begin{aligned}
C_{ij}^{(B)}(\nu) &\equiv \tau^2 \sigma_{ij}^2 \\
&= h\nu E_i^{(B)} \delta_{ij} + \sum_c (h\nu_c) n_c \left\{ (h\nu_c) \tau n_c \Delta\nu \right\} p_{ic} p_{jc} \left[\frac{1}{p_{ic} p_{jc} \Delta\nu} \int_{\nu_c}^{\nu_{c+1}} d\nu \left| S_{i1}(\nu) \right|^2 \left| S_{j1}(\nu) \right|^2 \right] \\
&\equiv h\nu E_i^{(B)} \delta_{ij} + \sum_c h\nu_c n_c E_c^{(f)} p_{ic} p_{jc} \rho_{ijc}
\end{aligned}
\tag{7.3}
$$

. The figure ρ_{ijc} (in square brackets of second line) expresses the probability that photons in channel c stimulate correlated responses in bolometers i and j. In the limit of high occupation number in the incident beam ($n_c \gg 1$), the second term of the covariance is dominant. For an auto-correlation spectrometer, $\rho_{ijc} \approx 1$, so the covariance between bolometers is

$$
C_{ij}^{(B)} = \sum_{c,c'} p_{ic} \left(\frac{(E_c^{(f)})^2}{\Delta\nu_c \tau} \delta_{cc'} \right) p_{c'j} \tag{7.4}
$$

In an autocorrelation spectrometer, the vector of energies received by the bolometers $E_i^{(B)}$ needs to be transformed into a vector of energies in each spectral channel through a Fourier transform, which in this case is the inverse probability matrix: $E_c^{(f)} = \sum_i p_{ic}^{-1} E_i^{(B)}$ (*Bell* [1972]). The covariance of energy fluctuations in the bolometers transforms into a *diagonal* spectral covariance:

$$
\begin{aligned}
C_{cc'}^{(f)} &\equiv \sum_{i,j} p_{ij}^{-1} C_{ij}^{(B)} p_{jc'}^{-1} \\
&= \frac{(E^{(f)})^2}{\Delta\nu_i \tau} \delta_{cc'}
\end{aligned}
\tag{7.5}
$$

So the fluctuations $E^{(f)}/\sqrt{\Delta\nu\tau}$ are uncorrelated and independent of p_{ic}. Since the choice of p_{ic} is arbitrary, autocorrelation can provide sensitivities comparable to filter manifolds. Recall that a filter manifold has diagonal p_{ic} and the data does not need to be Fourier transformed.

However, in the low occupation number limit ($n_c \ll 1$), the first term of C_{ij}^B dominates. While this matrix is diagonal, the Fourier transformed frequency correlations are not, which

can add considerably to the noise in each frequency channel. We can avoid this problem if p_{ic} is diagonal, in which case the frequency spectrum's covariance is also diagonal and independent of p_{ic}:

$$C_{cc'}^{(f)} = E_c^{(f)} \delta_{cc'} \tag{7.6}$$

and each channel has Poisson statistics. But as noted above, the probabilities p_{ic} are only diagonal when we use a filter bank to sort the frequency channels into separate bolometers.

In the low occupation limit ($n_c \ll 1$), the signal-to-noise ratio of a measurement relative to a filter bank degrades as $\sqrt{N_{chan}}$, so it is very costly to use autocorrelation. To be specific, if the incident power is composed of 2.7K CMB photons and little additional loading (as in a satellite mission), the plank distribution exceeds $n_c = 1$ above 40GHz. A spectrometer that achieves 2GHz resolution up to 300GHz has a sensitivity 12 times lower than a filter bank. Even from the ground where atmospheric loading produces an effective temperature of 30K, n_c only exceeds unity above 300GHz and the sensitivity is degraded by a factor of several. As a result of these considerations, filter banks are decidedly superior to autocorrelation for multi-chroic CMB detectors except for applications where high resolution spectroscopy is required. Current and future experiments all favor high mapping speeds over spectral resolution.

7.3 Terrestrial Measurements

The atmosphere absorbs and emits in the millimeter range as well, and this is a concern for any terrestrial experiment. However, the atmosphere does not absorb continuously; it is active only at specific spectral lines. Figure 7.1 shows the atmospheric transmission as simulated by the Caltech Submillimeter Observatory (CSO) for precipitable water vapor content at sites on White Mountain (Eastern California), the Atacama Desert (Chile), and the South Pole. The peaks at 60 and 120 GHz are from O_2 and are present with the same intensity at all locations. The line at 183GHz and the loading in the 200-300 GHz range

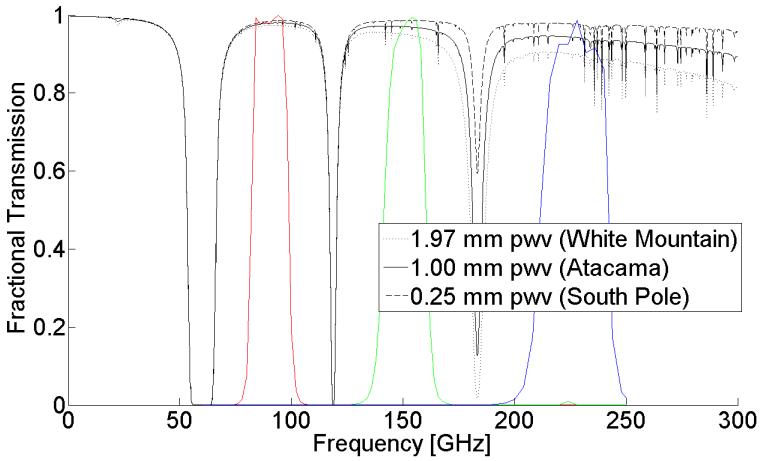

Figure 7.2. Atmospheric Transmission for typical Precipitable Water Vapors (PWV). We have co-plotted a simulation of our Triplexer circuit to illustrate where observing bands can be placed between lines. Atmospheric Data from (*Lis* [2010]).

are from H_2O and their strength depends on how dry the observing location is (*Pardo et al.* [2001]). These features are also not uniform across the sky (*Bussmann et al.* [2005]).

It is crucial that our detectors receive limited power from these lines, since they have an effective temperature of 30K. Not only will they overpower the extraterrestrial signals of interest, but their high power can also saturate our detectors and drive them normal. Several experiments have deployed with bands spaced in between these lines at 90GHz, 150GHz, and 220GHz. For example, SPT has a focal plane with these bands so they can look for Sunyaev-Zeldovich spectral distortions to identify high-redshift galaxy clusters. However, this experiment, like most others, only receives one of those three channels in each detector (*Carlstrom et al.* [2009]).

A notable exception to this design methodology is SuZie-II, which had four Winston-cone horns in it's focal-plane that each fed three detectors behind the horns centered at three different bands. While the optical throughput was not uniform across all four channels, each pixel did simultaneously receive 150, 200, 350 GHz. The highest channel received significant loading from atmospheric water vapor and the researchers used this to monitor and control for atmospheric fluctuations (*Benson et al.* [2003]). The multi-chroic detectors described in this chapter could allow for similar control.

7.4 Diplexer Circuits

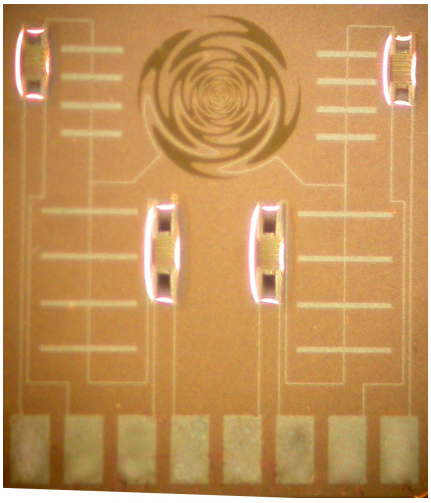

(a) 90GHz-150GHz Diplexers

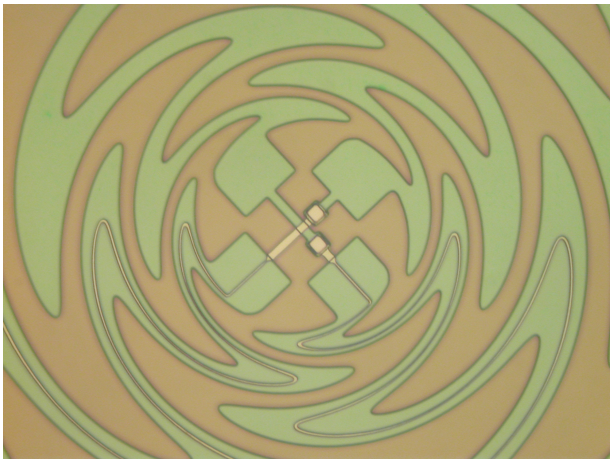

(b) Feed in Antenna Center

Figure 7.3. Dual Polarized Sinuous Antennas coupled to TES-Bolometers through Diplexers (a). The Antenna is 1.2mm in diameter and the interior feed (b) drives the H-V Excitation

The simplest filter-bank design branches two filters with non-contiguous pass-bands from a common node (See Figure 7.3). Each filter has an impedance that matches that of the input and output transmission lines' (10Ω) at resonance, but is reactive off resonance. While this is necessary to reject out-of-band power, it also complicates the multi-channel circuit's design. Looking from the antenna side into microstrip-T, the out-of-band filter will present a complex impedance in parallel to the in-band filter's 10Ω that can reflect away much of the incident power.

As discussed in the Chapter 6, a transmission line transforms the impedance of a load to an input impedance that is a function of the length and impedance of the transforming line (see Equation 6.9). We chose the length and impedance of each line between the node and filter such that at the filter's band-center, the input impedance from the other filter is infinite (open). Figure 7.4 illustrates this. The impedance of a filter changes rapidly at the band edge, so the bands in this circuit cannot be adjacent. Fortunately, the atmospheric lines require non-contiguous bands, so this design methodology is still appropriate for focal planes

in terrestrial experiments. In Chapter 8, we discuss a design that allows for contiguous bands that would be desirable for a balloon-born or satellite mission.

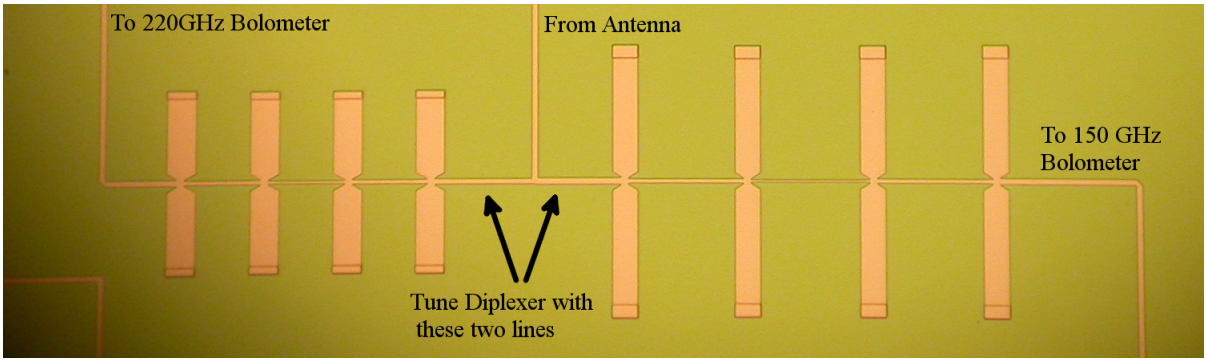

Figure 7.4. 150-220GHz Diplexer

7.4.1 Prototype pixel design

Figure 7.3(b) shows the interior of the sinuous antenna and reveals that it is fed in the $(H - V)$ modes. This feed only uses one microstrip per polarization and significantly simplifies the wiring between the antenna and filter-bands. Additionally, the required 180^o phase is established by the microstrip antenna feed and we no longer need a differentially fed load in the bolometer interior. The thermalizing load near the TES is a coiled stretch of transmission line that gradually transitions from superconducting Nb to lossy Al-Ti. This is visible in Figure 3.5 Finally, *both* polarizations are wired to bolometers through filter banks in these devices.

Spectral measurements from Chapter 6 suggest that the wave speed in our transmission lines is lower than expected, so we compensated by shortening the length of all the stubs and inverters in our filters by 10% (based on recent measurements from another project *Arnold* [2008]). Finally, we used 4-pole filters instead of 3-pole because we require the steep roll-off to supresss interactions between the channels in frequency-space.

7.4.2 Diplexer Spectroscopy

We subjected these devices to the same battery of optical tests described in chapter 6 with the same optical test cryostat. However, these detectors (and the ones from Chapter 8) saturate while exposed to 300K radiation through the filter stack described in chapter 6. To avoid saturating the detectors, we shaded them with 0.635cm (0.25") of MF110 stycast. In all figures of optical throughput, we divided away the additional loss associated with the sytcast attenuator since this loss is ultimately necessitated by the bolometer's non-ideal thermal characteristics and is not a property of the microwave circuits we are actually trying to test. We characterized the loss from the stycast by repeating a set of measurements with twice the stycast 1.27cm (0.5"). The loss associated with 0.25" stycast is just the ratio of the two measurements and we summarize these loss parameters in Table 7.1.

Table 7.1. Optical Power Transmission through MF110

f_{center}	Fractional Transmission
90	55%
150	29%
220	11%

We also used 14mm diameter sintered-alumina lenses instead of Silicon because they are cheaper and more mechanically durable. The relative permittivity is 10.5 and the loss tangent of Alumina at 300K is $\tan(\delta) \sim 1 - 10 \times 10^{-4}$, so it is an acceptable substitute for the more brittle silicon. As in chapter 6, we coated each lens with a single layer of ultem-1000. For the 90-150GHz diplexer, we used a 0.35mm (0.014") thick film (nominally centered at 120GHz), while for the 150-220GHz diplexer, we used an 0.23mm (0.009") thick film (nominally centered at 180GHz). The alumina extension was 2.43mm thick, so the optical path length through this material *plus* that through the 0.5mm silicon substrate produces the correct phase delay to form a synthesized ellipse.

Figure 7.5 shows the spectral response of the detectors in both polarizations of both the diplexers. The pass-bands are only 3% low, and have 15% fractional bandwidths that match their designs. We made the bands conservatively narrow to avoid atmospheric lines; with better control over pass-band center, we should be able to safely expand the filter

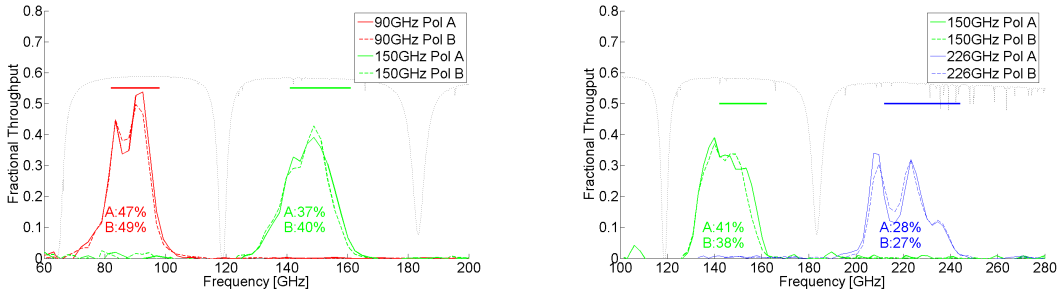

(a) 90GHz-150GHz Diplexer Spectra

(b) 150GHz-220GHz Diplexer Spectra

Figure 7.5. Measured Spectra for the Diplexer circuits. The vertical axis is total receiver throughput. The black dashed line shows the atmosphere in arbitrary units and the horizontal lines show the designed -3dB bandwidth. We list the band-averaged throughputs for each channel as well.

bandwidths in future designs. Some of the bands exhibit fringing that is remeniscient of the fringing in the single filter prototypes (chapter 6), but there is no obvious mismatch at the bolometer's distributed load. We have not been able to trace the fringes to specific lengths due to the complexity of this circuit.

The optical throughputs are slightly lower than comparably located bands in the devices from chapter 6. One possible explanation is that our microstrip feed depicted in Figure 7.3(b) is not driving the antenna in a purely odd mode, but rather in a superposition of the even and odd mode. Since the even mode has a quadrupolar pattern that vanishes on boresight, a partial excitation of this mode might slightly degrade the throughput. Alternatively, the alumina lens material may be more lossy than expected. Owing to instability of our spectrometer's lamp, we have not yet managed to measure the loss in our lens material.

7.5 Triplexers with broad-band anti-reflection coated lens

The Diplexer circuit design can easily generalize to three bands in a circuit called a Triplexer shown in Figure 7.6. This circuit has three bands centered at 90, 150, and 226GHz. Because each line between the branching node and filter has two free parameters - the length and impedance - they can transform their filters' impedance into an open in the center of

the two other filters' pass-bands. The simulated scattering parameters of this circuit are shown in Figure 7.2.

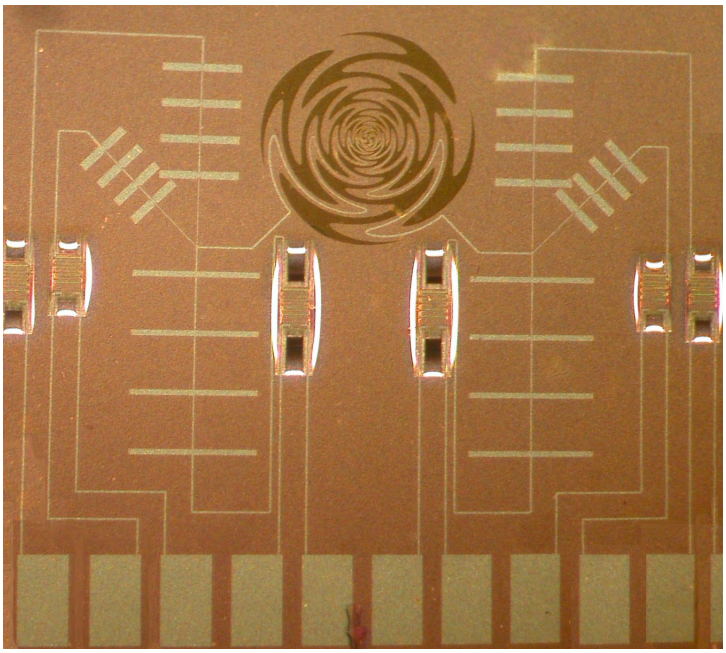

Figure 7.6. Sinuous Antenna coupled to TES bolometers through two Triplexers.

The single anti-reflection coating does not have a sufficient bandwidth to cover all three channels, so we implemented a multilayer coating instead. The coating has two layers of TMM from the Roger's corporation and one of porous Teflon. TMM is a circuit board material whose index can be adjusted by loading with a proprietary high-dielectric dopant. Roger's Corp sells TMM as preset boards with relative permittivities of 3, 4, 6, and 10. While Roger's Corp's intended application of these boards is for microwave frequency circuits, we have measured the loss-tangents and relative permittivities in the millimeter spectral range with a Fourier Transform Spectrometer and concluded that they still have the same designed permittivities and have acceptably low loss tangents of $\tan(\delta) \sim 10^{-3}$.

Roger's Corp forms their circuit boards by thermosetting the material in a mold. We have specially obtained *un*-thermoset TMM from Rogers so we can mold it onto the hemispherical contacting lenses. We machined a series of presses shown in Figure 7.7 that apply films summarized in Table 7.2. The surfaces of the press must be anodized to keep the

coatings clean of aluminum-oxide residue. We set each film in the press in a N_2 oven at 300 ^{o}C for 1 hour and encourage adhesion between layers with a thin layer of Stycast 1266 that we apply after baking. The outer-most layer is porous Teflon (porex) that we thermoset at a much lower temperature of 90 ^{o}C. The design thicknesses and permittivities are summarized in Table 7.2

Table 7.2. 3-layer Antireflection Coating Designed Parameters

Material	nominal ϵ_r	thickness [inches]
Alumina	10.5	NA
TMM6	6	0.007
TMM3	3	0.010
Porous Teflon	1.4	0.015
Vacuum	1	NA

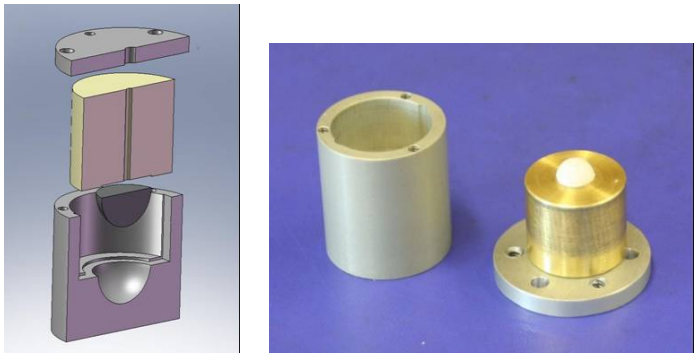

(a) Mechanical Drawing of AR-coating press

(b) Photograph of Press with lens

Figure 7.7. 3-layer Anti-reflection coating press

Table 7.3. Throughput with and without the 3-layer coating

Channel	Throughput, no coating	Throughput with coating	Fractional increase
90 GHz A	34%	44%	29%
90 GHz B	35%	44%	27%
150 GHz A	26%	33%	28%
220 GHz A	22%	26%	19%
220 GHz B	21%	24%	17%

We characterized the detectors' spectra as with the diplexer circuits and show those results in Figure 7.8. Because of a design flaw, one of the two 150GHz channels was open

between the filter and bolometer and provided no useful data. As table 7.3 indicates, the coating enhanced the throughput by nearly 30%.

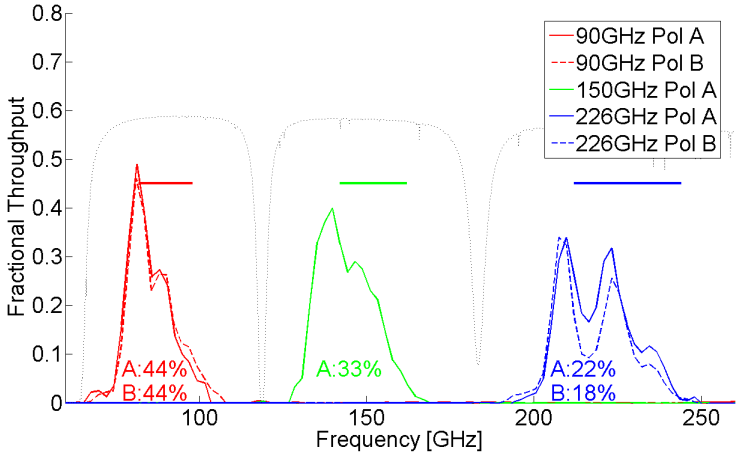

Figure 7.8. Triplexer Spectra. Vertical axis is total receiver throughput. The dashed line is 1mm pwv atmosphere, arbitrary units. Band Averaged throughputs are listed under spectra. 150B yielded no useful data because of a design flaw.

7.6 Beams of single-ended feed Sinuous

The simplified feeding scheme shown in Figure 7.3(b) is significantly different from that used in Chapter 6 (Figure 8.11(b)). As noted above, this may be responsible for the slightly decreased efficiencies in the diplexer and triplexer devices compared to the devices from chapter 6, but further measurements are needed to confirm this. However, the feed seems to impact the beam ellipticity in a more significant way. We measured the beam shapes with the chopped thermal load, similar to the measurements in Chapter 6. The same bands in the diplexer and triplexer circuits had very similar beams, so we only show the triplexer beams in Figure 7.9 for brevity.

We note that the beams in the 220GHz channels are elliptical (see Table 7.4). Simulations of just the antenna (without the lens) show that the feed slightly steers the beam off boresight by roughly 2^o compared to the balanced feed in Chapter 6. Diffraction of this steered beam through the lens then generates a ellipticity comparable to and in the same

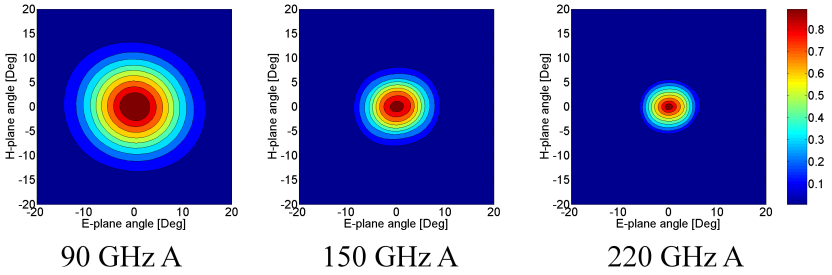

(a) 2-D Beam Simulations, Pol A

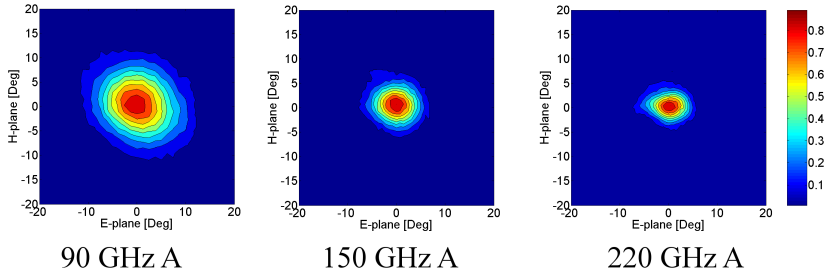

(b) 2-D Beam Measurements, Pol A

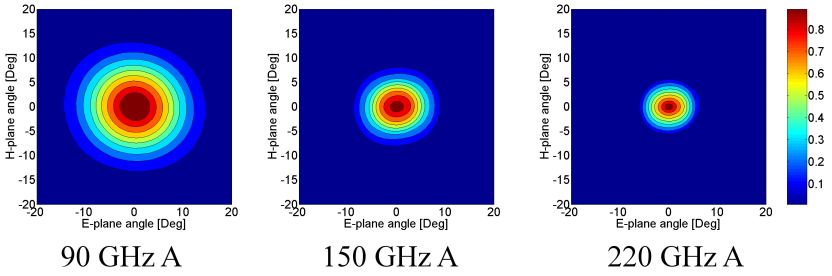

(c) 2-D Beam Simulations, Pol B

(d) 2-D Beam Measurements, Pol B

Figure 7.9. Simulations and Measurements of Triplexer device beams.

direction as the measurements. Several experiments deploying over the next years will help demonstrate what levels of beam ellipticity are tolerable. Theoretical studies suggest that a telescope with beams exceeding 4% ellipticity will not be able to detect primordial B-modes with $r < 0.1$ without some optics to control or supress this systematic.

Table 7.4. Beam Geometry

Channel	ellipticity	E-plane FWHM	H-plane FWHM	Boresight Cross-Pol Rejection
90 GHz A	5.4% ± 0.3%	$11.1^o \pm 0.5^o$	$10.8^0 \pm 0.5^o$	2.7% ± 1.7%
90 GHz B	4.6% ± 0.3%	$11.3^o \pm 0.5^o$	$10.7^0 \pm 0.5^o$	2.3% ± 0.7%
150 GHz A	1.1% ± 0.1%	$7.0^o \pm 0.2^o$	$6.2^0 \pm 0.2^o$	3.4% ± 2.7%
220 GHz A	9.6% ± 0.5%	$6.0^o \pm 0.5^o$	$4.9^0 \pm 0.5^o$	4.9% ± 3.4%
220 GHz B	7.7% ± 1.8%	$5.6^o \pm 0.8^o$	$4.4^0 \pm 0.8^o$	5.1% ± 4.6%

We can mitigate this effect by rotating a cryogenic broad-band half-waveplate or by using a sufficiently large primary such that these features are a smaller scale on the sky than any relevant CMB temperature anisotropies. Researchers have developed half-waveplates with more than an octave bandwidth and upcoming experiments may demonstrate that we need waveplates even with perfectly circular beams *Pisano et al.* [2006]. However, we would like to avoid these strategies for high-altitude measurements where weight and moving cryogenic components can greatly increase an experiment's cost.

Differentially feeding lumped rf-loads at the bolometers avoids this problem in the narrow-band devices, but it is not practical to extend this scheme to multi-channel pixels. Multi-channels pixels with differentially fed loads would require much longer lengths of transmission line that would greatly increase dielectric losses. Additionally, those circuits would need uniform films and etch properties across a surface area of several square millimeters to avoid the phasing errors that those circuits would be trying to avoid in the first place. The Polarbear detectors described in chapter 4 manage to avoid this by maintaining a small footprint, but the multichroic pixels would have a footprint similar to the lens. The Caltech/JPL phased antenna arrays show beam asymmetries that the team traces to non-uniform films, and those have a similar foot-print to our multichroic pixels. We describe a possible feeding circuit in the concluding chapter (chapter 9) that may solve this problem.

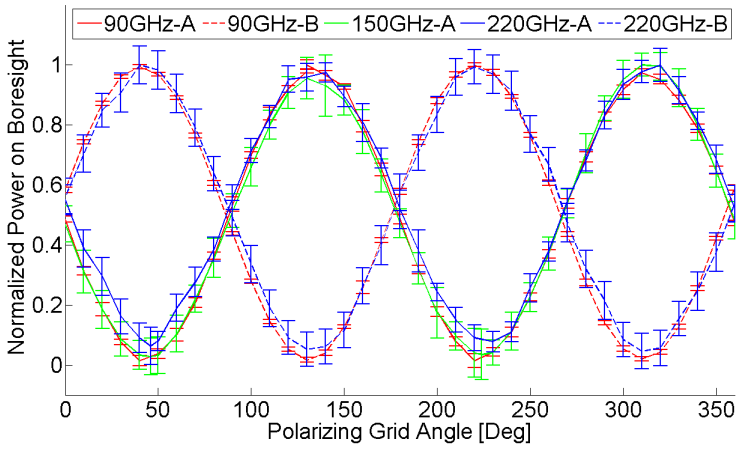

Figure 7.10. Optical response to the chopped load on boresight through a polarizing grid. Again, 150B yielded no useful data because of a design flaw.

The antenna rejects cross-polarized power to 1.5% in the 90 and 150GHz (Figure 7.10), which is similar to the rejection in the devices of Chapter 6. The 220GHz channel leaks nearly 3% and this elevated leakage seems to come from the slight beam steering in the highest channel. As before, the leakage is far worse without the anti-reflection coating, leaking between 5 and 10%.

Finally, beam measurements suggest that the coating layers must be concentric with tight tolerances of roughly 1-mil centering. After damaging the press, we molded coatings onto a lens that had 2-3mil errors in alignment and we generated beams with high-asymmetry and strong coma-lobes. 1-mil tolerancing is possible, but must be strictly observed.

7.7 Conclusions

In this chapter we have demonstrated that we can couple a dual polarized sinuous antenna to diplexer and triplexer circuits that partition the bandwidth into narrow channels between atmospheric emission lines. The anti-reflection coating technology is also promising.

The specific designs show here cannot be easily extended to more than three channels because the lowest frequency filter's satellite band interacts with the higher frequency channels. However, other researchers have built four-channels filter banks by using quasi-lumped filters that do not have a satellite band. But even with this modification, the filter manifolds cannot support contiguous bands because the reactance of each filter would change too rapidly in the pass-band of their neighbor, making it impossible to tune away the impedance with a simple transmission line.

We solve this problem of non-contiguous bands in the next chapter with a log-periodic channelizer that intentionally exploits the off-resonance reactance of each filter instead of trying to tune it away. With this change, we can build filters with an arbitrary number of channels and contiguous bands.

Chapter 8

A Log-periodic Channelizer inspired by the Mammilian Cochlea

8.1 Introduction

Chapter 7 discussed the design and fabrication of diplexer and triplexer circuits with non-adjacent bands that can be used in terrestrial measurements. This chapter discusses a log-periodic channelizer inspired by the workings of the human ear. It has an arbitrary number of adjacent channels with an arbitrary total bandwidth. However, the filters' band centers are spaced log-periodically in frequency, making it difficult to position them between atmospheric lines. Instead, this channelizer is best suited for high-altitude applications.

We begin by discussing how the cochlea is similar to a transmission line and how it motivates a powerful channelizer design methodology. These first sections summarize prior efforts by our collaborators at UCSD to build circuits with lumped components. We then discus how the same components can be realized with printed features in our millimeter wavelength circuits. Finally, we show measurements of a sinuous antenna coupled to TES

bolometers (shown in Figure 8.1) through a cochlear channelizer and compare those results against simulations.

Figure 8.1. The cochlea removes monotonically lower frequencies as an acoustic pulse travels deeper into the ear. The mechanical resonant frequency of each section is related to it's neighbors by a geometric scaling factor. It is a biological example of a log-periodic structure. Cartoon taken from *Doe* [2010].

8.2 A cochlear channelizer

Channelizer circuits are similar to the filter manifolds discussed in the previous chapter, but have an arbitrary number of contiguous channels. Their synthesis has long been a major challenge to radio engineers. Most design methodologies use many components that must be constrained by extensive CAD (*Rauscher* [1994]) or they isolate filters with numerous hybrids that each have a very large foot-print (*Matthaei et al.* [1980]). However, in recent years, a community of radio-engineers have started using the physiology of the human ear as an inspiration for channelizers that are compact and require minimal CAD optimization (*Sarpeshkar et al.* [2007], *Galbraith* [2008], and *Watts* [1993]). Many of these approaches utilize active feedback, but our collaborators at UCSD have developed a methodology that

is entirely passive with just reactive components, making the designs realizable at cryogenic temperatures.

In most mammals, the cochlea converts acoustic energy into mechanical motion before triggering electrical signals within nerves. In the simplest models, the cochlea couples acoustic waves onto a basilar membrane whose local mechanical resonant frequency decreases *geometrically* with distance as the waves propagate (see the cartoon in Figure 8.2). When the sections resonate, they absorb and dissipate a narrow frequency range of acoustic waves, exciting signals within local nerve cells. The ear is channelizer that removes the highest frequencies first and lower frequencies later with each section's frequency related to it's neighbors by a geometric scaling factor. Because of this structure, the ear is log-periodic in an analogous way to the antennas discussed in chapter 5. The human ear covers nearly three octaves and can differentiate tones that fractionally differ in frequency by only 0.5%, corresponding to over 1000 contiguous channels! (*Galbraith et al.* [2008])

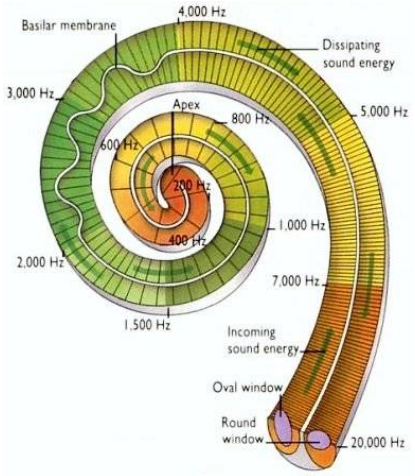

Figure 8.2. The entire log-periodic pixel. Each polarization of the sinuous couples to TES bolometers (at bottom)through separate cochlear channelizers. The antenna is roughly 1.2mm in diameter. Figure from *Doe* [2010]

The wave equation for pressure in the ear has a dispersion relation that is a nontrivial function of several physiological parameters. However, electrical engineers realized that this equation is equivalent to the voltage wave equation in the relatively simple circuit shown in Figure 8.3. This model essentially says that the ear is similar to a transmission

line, except with resistively-loaded single-pole LC-resonators shunting to ground instead of the pure capacitance found in a standard line. The filters' have identical Q, but their resonant frequencies monotonically decrease from left to right, each related to it's neighbors' resonance through a geometric scaling factor.

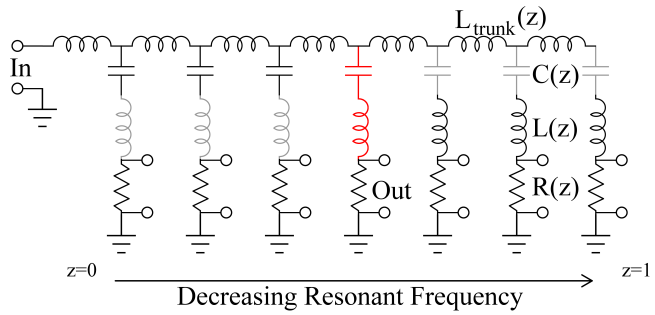

Figure 8.3. Single-pole channelizer

If a monochromatic wave enters the circuit in Figure 8.3 at the left with a frequency that resonates at a filter in the middle of the manifold (shown in red), the filters it passes prior to dissipation will have a higher resonant frequency and provide non-zero reactance that isolates the wave from ground. Their impedance will look approximately capacitive, and the manifold closely resembles a transmission line. We have drawn the capacitors at left in Figure 8.3 in gray to illustrate this effect. Most of that wave will dissipate in the red filter; the power that leaks through will see lower frequency filters that look like shunt inductors and will reflect the leaked wave back towards the correct filter. In contrast to most filter manifolds (including the diplexers and triplexers), this design does not seek to isolate filters; rather, it intentionally exploits each filters' non-resonant impedance.

Constructing the wave equation for an ideal transmission line is standard fare for most introductory electronics textbooks (e.g. *Pozar* [2004]) and we do not explicitly reproduce that here. To summarize, the wave equation results from the following procedure:

1. Calculate the voltage and current drops across each section from the Kirchoff circuit-junction rules.

2. Convert these to differential equations in the limit where the length of each section $\Delta z \to 0$.
3. Combine the two equations into one second order equation, typically for voltage.

This same procedure applies to the Circuit in Figure 8.3, except that we must generalize $1/j\omega C$ in the equation for current to $1/\left(1/j\omega C(z) + j\omega L(z) + R(z)\right)$. These components are a function of the distance z from the input port, but they change slowly so the changes in series inductance $L_{\text{trunk}}(z)$ can be neglected when differentiating the voltage equation. The result of this analysis is a Voltage wave equation

$$\frac{d^2V(z)}{dz^2} + \frac{L_{\text{trunk}}(z)C(z)}{1 + j\omega R(z)C(z) - \omega^2 L(z)C(z)}\omega^2 V(z) = 0 \tag{8.1}$$

where z is defined between $z = 0$ at the input and $z = 1$ at the far right. This equation is identical in form to the pressure wave in the human ear, which means that the ear's structure can inform the decisions we make in choosing the components in each section. The ear's channels have constant fractional bandwidth (or $1/Q$), and physiological comparisons suggest that the dispersive terms must bear the following relationships:

$$L(z)C(z) = A_1 e^{\alpha z} \tag{8.2}$$

$$R(z)C(z) = A_2 e^{\alpha z/2} \tag{8.3}$$

$$L_{\text{trunk}}(z)C(z) = A_3 e^{\alpha z} \tag{8.4}$$

(*Galbraith et al.* [2008]). This realization reduces a circuit with potentially dozens of free parameters to four! In terms of these parameters, the passband center of each filter is simply

$$\omega_c = 2\pi f_c = \frac{1}{\sqrt{L_2(z)C(z)}} = \frac{e^{\alpha z/2}}{\sqrt{A_1}} \tag{8.5}$$

and the Q of each filter is:

$$Q = X/R = \sqrt{A_1}/A_2 \tag{8.6}$$

The end filters with pass-bands f_N and f_1 correspond to $z = 0$ and $z = 1$. The choices of Q,f_1, and f_N constrain three of these parameters:

$$A_1 = 1/(2\pi f_N)^2 \tag{8.7}$$

$$A_2 = \sqrt{A_1}/Q \tag{8.8}$$

$$\alpha = 2\log(f_N/f_1) \tag{8.9}$$

We can find the last parameter A_3 from a WKB solution of Equation 8.1 where we assume that the voltage wave's phase at each band center is an arbitrary constant, as suggested from physiological studies of the cochlea (*Galbraith et al.* [2008]). However, it is more practical to simply optimize this single free remaining parameter in CAD software.

8.3 Three-pole channelizer circuits

Most CMB cameras utilize filters that role off faster than single pole. Fortunately, the single-pole filters in Figure 8.3 can be replaced with higher-order ones provided that the filters have the correct limiting impedance. In particular, each filer's reactance still must be capacitive below it's pass-band and inductive above. While this is automatically satisfied by a single-pole filter, it is not always so for multi-pole filters. For example, the filter described in chapter 6 has off-resonance reactance that is opposite this, being *capacitive above* resonance and *inductive below*. Moreover, at frequencies far below resonance, the stubs in the filters short to ground. If implemented in a channelizer, the low frequency shorts would reflect nearly all incident power back towards the antenna. The shorted-stub filters are not appropriate for this application.

The Rebeiz group realized that filters like those in Figure 8.4(a) do have the required

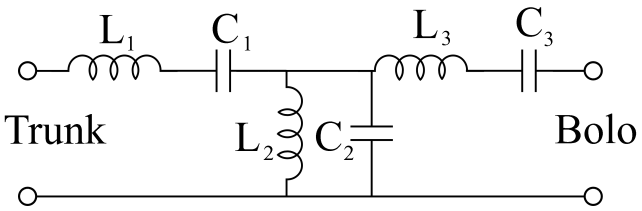

(a) Basic Filter

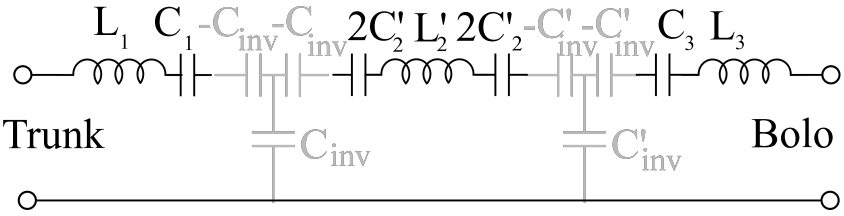

(b) Filter with Capacitive-T Inverters

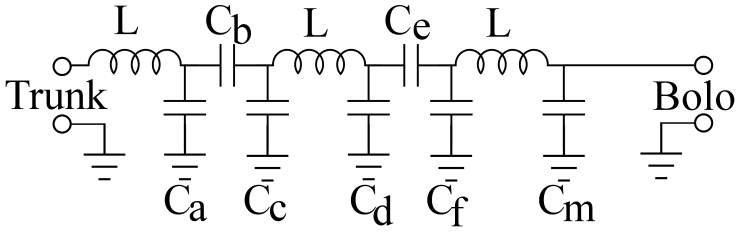

(c) Tubular Filter

Figure 8.4. (a) An ideal 3-pole filter for the channelizer, (b) the same filter with the inner resonator inverted with a T-network, and (c) a tubular filter where pi-networks replace the T-networks.

limiting reactance (*Galbraith and Rebeiz* [2008]). This filter differs from those in Chapter 6 because each resonator has been inverted. Unfortunately, the lumped shunt inductance to ground is challenging to fabricate. To mitigate this difficulty, the Rebeiz group inverted the inner parallel resonator into a series one and surround it with a pair of capacitive T-networks with negative series capacitance (See Figure 8.4(b)). These networks are functionally similar to the $\lambda/4$ inverters in the filter described in Chapter 6, transforming a load impedance Z_L into X^2/Z_L, where $X \equiv 1/\omega C_{inv}$ is the magnitude of the capacitors' reactance. In practice, the negative capacitors are simply absorbed into the resonators' smaller series caps. Other groups developing submillimeter channelizers have also used this filter (*Kumar* [2007]).

The required T-networks have large series and small shunt capacitors, which are difficult to fabricate in thin films in a way that ensures proper step-coverage over lower layers. However, converting these to pi-networks drastically decreases the series capacitors relative to the shunt capacitors, resulting in components that are easier to fabricate. This filter is known as a tubular filter (*Swanson* [1989]). We followed the lead of the Rebeiz group and chose the three series inductors to be identical within each filter and also included a matching shunt capacitor at the end to allow the filter's normalized input impedance to differ from the 10 Ω transmission line that terminates at the bolometers(*Pozar* [2004]).

The components in the these filter models are constrained entirely by (1) the pass-band center, (2) the filter bandwidth, and (3) the circuit impedance normalization. In practice, the filters' pass-bands are wider in the channelizer circuit than in isolation, so we cannot simply calculate this width from the relative band locations. Instead, we must numerically vary all three of these parameters as well as a normalization to the trunkline inductors $L_{\text{trunk}}(z) = L_o \exp(\alpha z/2)$ and an input shunt capacitor C_{in} in order to minimize the reflection coefficient S_11 back to the antenna. We show the results of this optimization as well as the other components from Figure 8.4(c) in Tables 8.1 8.2.

Table 8.1. Resonator Component Target Values

Component	Admittance or Impedance
L_{end}	$23.8m\mho$
L_{center}	$23.8m\mho$
Π_1, Y_{11}	$24.6m\mho$
Π_1, Y_{12}	$6.3m\mho$
Π_1, Y_{22}	$49.3m\mho$
Π_2, Y_{11}	$21.9m\mho$
Π_2, Y_{12}	$6.1m\mho$
Π_2, Y_{22}	$45.7m\mho$
C_{match}	11.6Ω

Table 8.2. Trunkline Component Target Values

Component	Inductance or Capacitance	Admittance
L_{222}	1.88 pH	381 $m\mho$
L_{184}	2.11 pH	410 $m\mho$
L_{152}	2.37 pH	442 $m\mho$
L_{126}	2.65 pH	477 $m\mho$
L_{104}	2.97 pH	515 $m\mho$
L_{86}	3.33 pH	556 $m\mho$
L_{71}	3.73 pH	601 $m\mho$
C_{in}	69 fF	

8.4 Millimeter-Wavelength channelizers

The Rebeiz group designed their circuits to work at microwave frequencies where it is possible to solder lumped components onto boards. Specifically, they soldered off-the-shelf series inductors and series capacitors into their circuits. This is neither possible nor practical for large arrays of millimeter-wavelength devices; *all* components must be printed in thin films. Figure 8.5 shows one of our printed tubular filters with a circuit diagram above. The capacitive pi-networks are MIM parallel-plate components, the resonator inductors are short high-impedance co-planar waveguide, and the trunk-line inductors are short microstrip lines. In this section, we discuss how we designed and fabricated all of these components using short sections of transmission line.

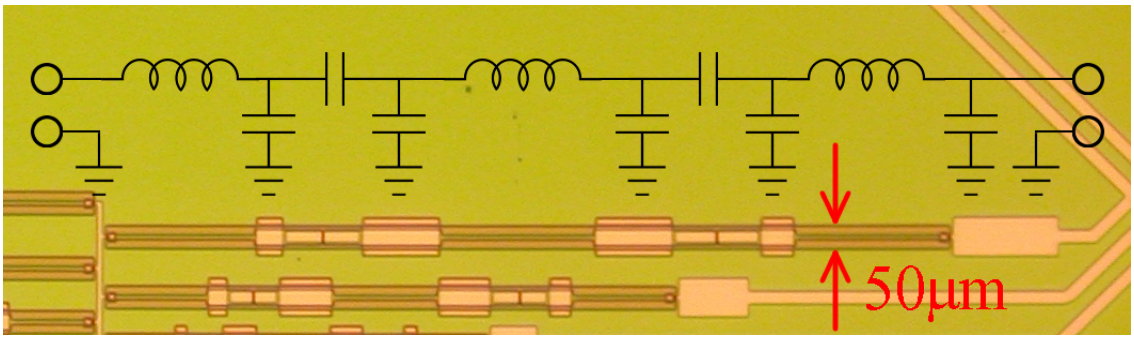

Figure 8.5. Photograph of a tubular filter in the channelizer with effective circuit drawn above. For scale, we labeled the total width of the CPW.

8.4.1 Short Transmission Lines

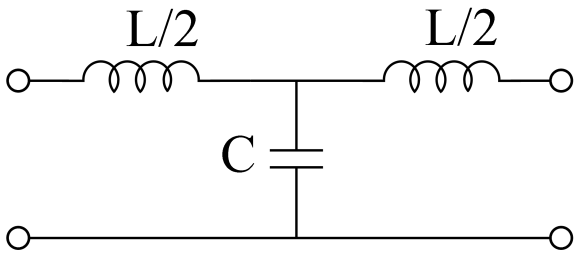

Figure 8.6. A T-network for a short transmission line

A short stretch of transmission line (shorter than $\lambda/8$) is equivalent to a tee-network with series inductance and shunt capacitance (See figure 8.6). The impedance matrix for this network is

$$Z_T = \begin{pmatrix} j\omega L/2 + 1/j\omega C & 1/j\omega C \\ 1/j\omega C & j\omega L/2 + 1/j\omega C \end{pmatrix} \tag{8.10}$$

The impedance matrix for the original transmission line with impedance Z and length ℓ is

$$Z_{tline} = -jZ \begin{pmatrix} \cot(2\pi\ell/\lambda)\ \csc(2\pi\ell/\lambda) \\ \csc(2\pi\ell/\lambda)\ \cot(2\pi\ell/\lambda) \end{pmatrix} \tag{8.11}$$

Equating components between 8.10 and 8.11

$$L = \frac{2Z}{\omega}\left(\csc(2\pi\ell/\lambda) - \cot(2\pi\ell/\lambda)\right) \tag{8.12}$$

$$= \frac{2Z}{\omega}\tan(\pi\ell/\lambda) \tag{8.13}$$

$$\simeq Z\ell/v \tag{8.14}$$

where the last line only holds when $\ell \ll \lambda$ and where v is the phase velocity. Similarly,

$$C \simeq Z^{-1}\ell/v \tag{8.15}$$

A short but high impedance line will look like a series inductor while a low impedance line will look like a shunt capacitor (*Pozar* [2004]). These results are intuitive for microstrip: a wide low-impedance line looks like a parallel plate capacitor and will store energy in the electric fields between the conductors. Conversely, a narrow high-impedance line allows more energy to be stored in the magnetic fields circulating the upper conductor, boosting the line's inductance. The magnitude of both increase with the length of the section, but diverge from this simple model when ℓ becomes a significant fraction of a wavelength.

8.4.2 Trunk-line Inductors

In the operating band of the channelizer, the trunk-line inductors have reactances between 1.66 and 2.63 Ω, which is much smaller than the bolometer terminations' normalizing impedance of 10 Ω. We realized these inductors with 7 μm wide, 15 Ω microstrip lines that have lengths between 17 μm and 39 μm long.

8.4.3 Resonator Inductors

The resonator inductors are significantly larger than those in the trunk-line; at the band centers, the reactances are 41 Ω. Even the thinnest and highest impedance microstrips that we can fabricate would be a significant fraction of a wavelength and would diverge from the model in Equation 8.14.

Coplanar waveguide (CPW) is an alternative transmission line that can have significantly higher impedance than microstrip. This higher impedance is achieved by splitting the ground plane into a wide slot and moving the upper-conductor down into the center of that slot, making it "coplanar." Since the ground can be moved significantly farther away from the center-conductor than in microstrip, the shunt-capacitance per unit length can be

much lower and the impedance higher. At the same time, removing the ground-plane in the vicinity of the line provides more space for the magnetic fields to build up, enhancing the inductance. Electrical currents in the center conductor are mirrored by half-magnitude return currents in the ground on each side of the slot. Equivalently, the slots conduct magnetic currents on each side of the center conductor with equal magnitude but opposite direction. This design has already been used by other researchers in the field; Caltech/JPL has used CPW for quasi-lumped inductance in several of their on-chip filter designs, including all of their antenna-coupled TES bolometers (*Goldin et al.* [2002] and *Chattopadhyay et al.* [2007])

Our CPW has a center conductor 10 μm wide, separated from the ground by 20 μm on each side, so they can be repeatably fabricated. They have 0.5 μm SiO_2 above, and 1 μm LSN plus $\sim$8 mm Si below. This geometry simulates in Sonnet to have an impedance of 82 Ω, so the inductors that ranged between 30 and 94 pH had lengths between 44 μm and 141 μm, all less than $\lambda/8$. Like the microstrip, all simulations assumed a penetration depth into the Nb of 1000 *AA* (*Kerr* [1999]).

The inductors in the outside resonators of each filter must transition to microstrip so they can interface with the trunkline and bolometers. We implemented this with a standard microstrip-to-CPW transition where the opposing slots magnetically short. The microstrip's upper conductor crosses this slot and shorts to the center conductors through a superconducting via(*Simons* [2001]). The transition creates parasitic capacitance that we compensated for by shortening the end inductors.

8.4.4 Capacitive Pi-networks

The lumped series capacitors are actually a pair of identical capacitors in series. We formed them across 2 μm gaps in the CPW's center-conductor that were covered by an additional plate above the 0.5 μm SiO_2. This design made each of the two capacitors larger than a single one and hence more robust against over-etching. The series design also makes the total capacitance more robust against alignment errors. A shift of one Nb layer relative

to the other parallel to the propagation direction will reduce one of the capacitors while simultaneously increasing the other, compensating for the shift. We also made the lower conductor wider than the upper one to make the capacitor more tolerant against alignment errors transverse to the propagation direction.

Discontinuities in CPW can excite an unwanted even mode that has no current on the center conductor and oppositely oriented current on the two ground-planes. This current pattern is similar to those around a slot dipole antenna and *can radiate* ((*Simons* [2001])). Engineers often suppress this with a bridge that shorts the two grounds, forcing them to be equipotential. We surrounded the series capacitors with bridges, but made them and the center-conductor below wider to simultaneously provide the two shunt capacitors in the pi-network. To tune the pi-networks (e.g. for the first network in Figure 8.4(c)), we varied the lengths of both shunt and series capacitors in a Sonnet optimization such that:

$$|Y_{12}| \rightarrow \omega C_b$$
$$|Y_{11} - Y_{12}| \rightarrow \omega C_a$$
$$|Y_{22} - Y_{12}| \rightarrow \omega C_c$$

Optimizing with these goals compensates for parasitic capacitance in each of the three individual capacitors by modifying the other two.

8.4.5 Matching shunt capacitors

We matched the filters' normalized impedance (7 Ω) to the 10 Ω output transmission lines with a large shut capacitor realized with a wide section of microstrip as per Equation 8.15 (*Pozar* [2004]). This component is far-larger than our 1μm resolution limit and is robust against all over-etch and alignment concerns. We loaded the input port from the antenna with a similar microstrip shunt capacitor.

Figure 8.7 shows an ADS simulation of the entire microwave circuit. Original optimization of the ideal lumped components resulted in $S_{11} < -15dB$ across the band, but

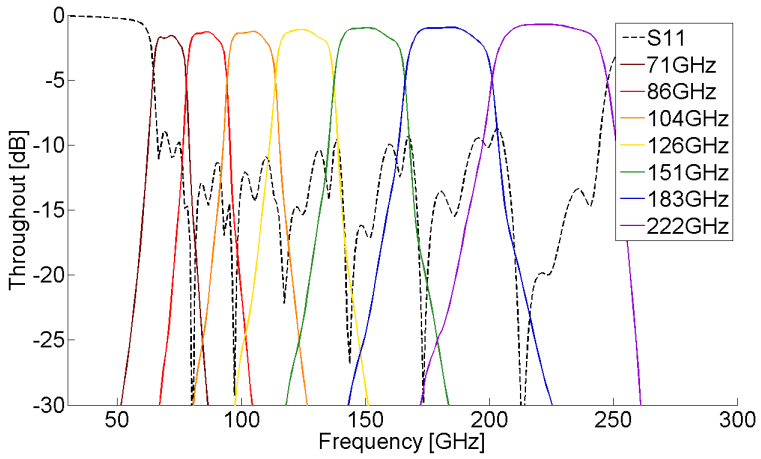

Figure 8.7. Channelizer scattering parameters simulated in ADS

the physical components have degraded this slightly by causing S_{11} to rise to nearly -10dB between bands. The lowest channel also suffers from greater reflection.

8.5 Measurements of a sinuous antenna coupled to TES bolometers through a cochlea circuit

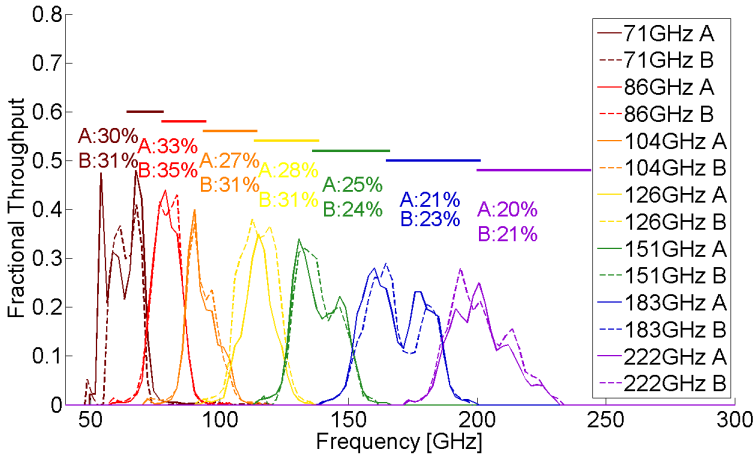

Figure 8.8. Cochlear Spectra measured with an FTS. Solid and dashed lines are the two polarization while the solid line above denotes the -3dB bandwidth. The band-averaged fractional throughputs are printed above the spectra.

Figure 8.1 shows the entire microwave structure. Each polarization from the antenna couples to the bolometers through a channelizer. We performed the same set of tests on this device as those in in chapters 6 and 7. As in chapter 7, we installed a 0.125 inch thick attenuator and Table 8.4 shows the measured attenuation for our system.

Figure 8.8 shows the normalized spectra, with the designed -3dB bandwidths depicted above. These pass-bands are 10% lower than expected, which we attribute to the oxide permittivity being a $\epsilon_r = 4.4$ instead of 3.8. In contrast to the diplexers and triplexers, we made no attempt to correct for spectral shifts since we had little prior experience with these filters.

While the inductance in the filters comes predominantly from magnetic fields, the inductance in the trunkline is from a mixture of magnetic and kinetic conductance. In simulation, the unexpected change in the oxide permittivity detunes the trunkline inductors, increasing the reflections off the channelizer input to and average of 8.4% accross all bands. For comparison, a correctly tuned channelizer should only reflect 2-3%. In Table 8.3, we show the loss from each optical component in the system and demonstrate that the total expected throughput is comparable to the measured values. After adding an AR coating to the lens and retuning the channelizer, we expect the receiver throughputs to increase to 30%-40%.

Table 8.3. Losses in the Channelizer Throughput

Component	Power Transmitted
Optical Filters	≈70%
Lens-vacuum interface	72%
Antenna Front-lobe	91%
Antenna-microstrip interface	88%
Dielectric Loss	70-90%
1-S_{11} channelizer	91%
Total	22-30%

Figure 8.9 shows the measured beam patterns compared to simulation. These measurements were imperfect because the 3-layer coated lens de-laminated before this test and damage to the press precluded replacing it. As of the writing of this thesis, a lens has not been repaired with a working multi-layer coating and all tests of the cochlear channelizer used a bare lens. As a result of the missing coating the cross-polarized leakage was much

Table 8.4. Optical Power Transmission through MF110 with the Log-periodic Channelized device

f_{center}	Fractional Transmission
80	63%
97	49%
117	36%
140	31%
170	24%
207	16%

higher and the throughput was lower than expected. However, we expect that these will improve with a properly coated lens. Nonetheless, there are significant asymmetries in the beams that suggest the antenna is not radiating in the intended modes as it did in the single channel differentially-fed devices of chapter 6. We suspect this occurred because the currents on the antenna were not properly balanced. While the lens can smooth power asymmetries in the beam, it can still generate non-circular beams when excited with a phase that is not circularly symmetric about boresight. In fact, we can use the script from chapter 4 to produce beams with qualitatively similar features as those measured in 8.9. We will likely correct these issues by feeding the antenna with a balun.

8.6 A simultaneous measurement of oxide permittivity and surface inductance

The filters in chapters 6 and 7 resonate at frequencies where the shorted stubs and inverters are $\lambda/4$. This resonance is set by the physical length of the lines and the wavespeed in those lines, which is a function of the oxide permittivity (through the capacitance per length) and the Niobium surface impedance (through the inductance per length; $v = 1/(c\sqrt{CL})$). The inductance is a mixture of magnetic and kinetic and as we argued in chapter 6, the kinetic makes a significant contribution because the line impedance is so low.

By contrast, the filters in this chapter resonate at frequencies set by the inductance and capacitance of *short* stretches of transmission line. Once again, the oxide permittivity influences the resonance through the capacitors. However, the inductance from the 82Ω

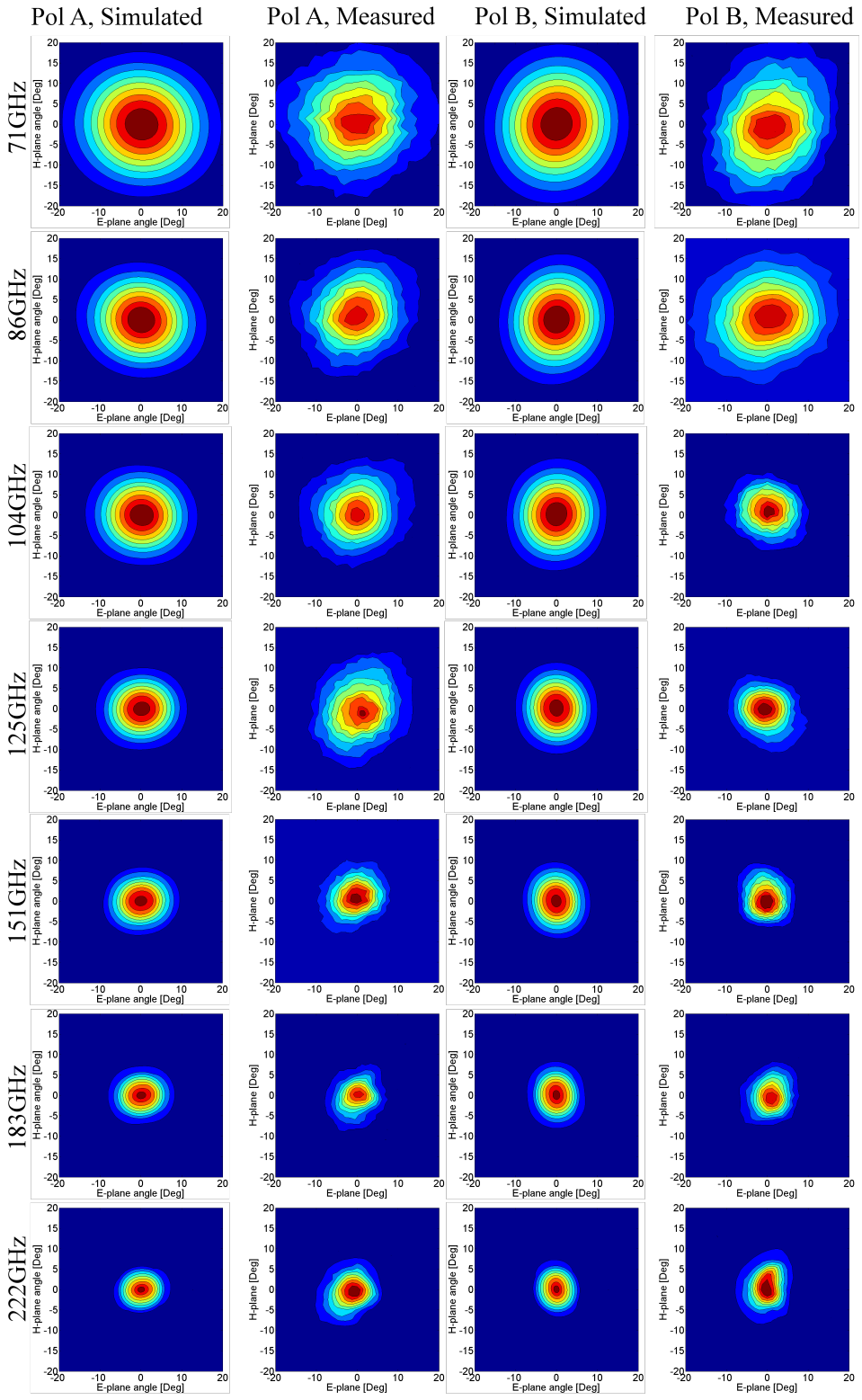

Figure 8.9. Simulations and measurements of sinuous beams through the channelizer.

CPW is almost entirely magnetic; kinetic inductance is subdominant. Because these two filters' resonances are presumably set by different combinations of ϵ_r and L_s, in principle, we can use data from the two filters to simultaneously constrain both material properties; we can break the degeneracy between material properties present in single filter measurements.

We simulated the filters' throughput S_{21} in Sonnet while sweeping ϵ_r from 3.0 to 7.0 and L_s from 0.06 to 0.26 pH/sq. For each parameter combination, we computed an *unnormalized* χ^2 between measured and simulated data. We emphasize that we only simulated the individual filters and not the entire channelizer or Diplexer structures for computational ease. In practice, the entire circuit narrow the pass-bands and full simulations that reflect this effect would provide tighter constraints on (ϵ_r,L_s). Because these relevant systematic effects that are not reflected by the simulations, we have not bothered to normalize the χ^2 values and so the absolute magnitude does not indicate confidence; only the best fit values can be inferred.

Figure 8.10(a) shows the chi^2 for different models (ϵ_r,L_s) in the distributed filter from chapters 6 and 7. The contours slope across the plot because the transmission-line wavespeeds depend on a combination of the two material properties. Figure 8.10(b) shows the same plot for the quasi-lumped filters from the log-periodic channelizer and it's contours clearly depends on a different combination of the parameters. The band-positions is only a weak function of L_s because of the CPW's strong magnetic inductance. Finally, Figure 8.10(c) shows the sum of the two plots, indicating that $\epsilon_r = 4.4$ and $L_s = 0.18$ pH/sq. Figure 8.11 shows the co-plotted fits on the two filter data sets.

It is surprising that the surface inductance appears to be so high. Were it a lower but more expected value of 0.1 pH/sq, the two χ^2 curves from the different measurements would intercept at a larger angle and provide a tighter constraint on the material properties. This large inductance suggests a penetration depth that is comparable to the film thicknesses. A more complete model (*Kerr* [1999]) for the surface impedance than Equation 6.2 is

$$Z_s = j\omega\mu\lambda \frac{(\eta + j\omega\mu\lambda)e^{t/\lambda} + (\eta - j\omega\mu\lambda)e^{-t/\lambda}}{(\eta + j\omega\mu\lambda)e^{t/\lambda} - (\eta - j\omega\mu\lambda)e^{-t/\lambda}} \tag{8.16}$$

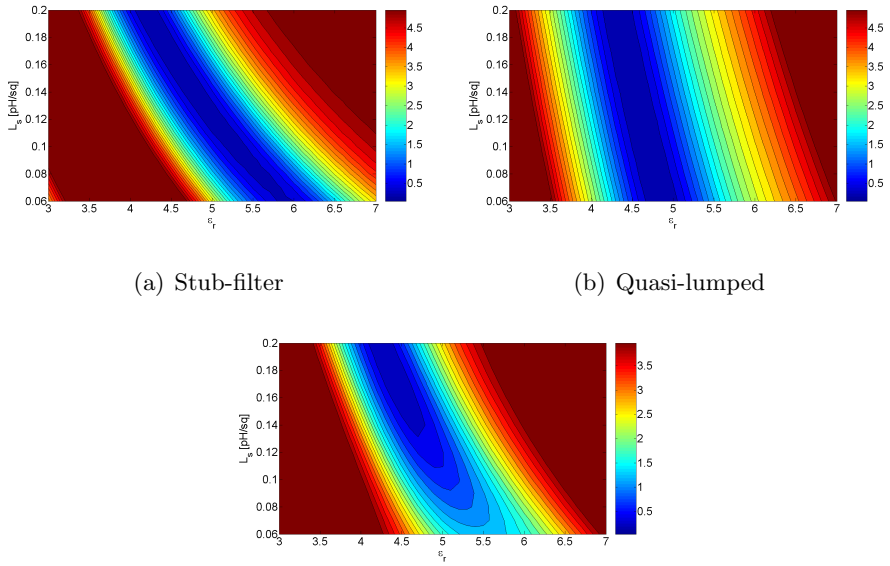

(a) Stub-filter

(b) Quasi-lumped

(c) Both

Figure 8.10. Un-normalized χ^2 between measured bands at 150GHz and simulations with different values of oxide ϵ_r and Niobium L_s. The data show a preference for $\epsilon_r = 4.4$ and $L_s = 0.18$ pH/sq

where η is the impedance of free space and t is the Niobium film thickness. Inverting Equation 8.16 shows that our Niobium films have a penetration depth close to 0.24 μm, which is nearly as large as the ground plane thickness of 0.3 μm. Such a high penetration depth compromises the superconductor and could be responsible for some of the excess loss we have seen in our devices at higher frequencies.

The most significant source of systematic error in this analysis is our poor understanding of the oxide film thickness. While it is nominally 0.5 μm thick, we originally deposit 0.57 μm oxide expecting the Ar sputter etch that we use to remove Nb-oxide in the vias to also remove 0.07 μm. However, the oxide etch rate of this step is poorly characterized and could explain the deviations from traditional measurements that we see in our inferred material properties. For example, a reasonable 9% over-etch of the oxide film with the sputter etch would bias our permittivity result from 4.0 to 4.4. More work needs to be done to characterize this step.

This unexpected shift in material properties changes the microstrip-based trunkline

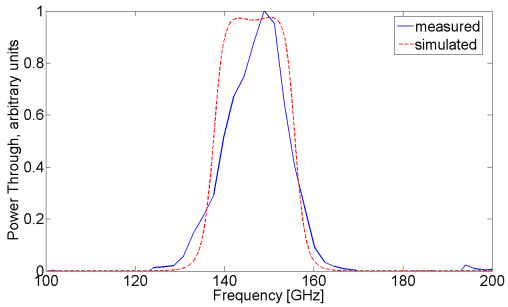

(a) Best fit Stubs

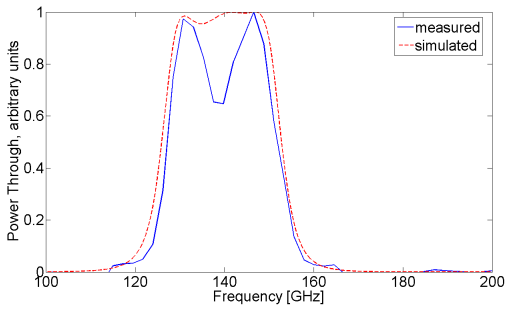

(b) Best fit Quasi-lumped

Figure 8.11. Best fit models co-plotted worth the two types of filter. Recall that we adjusted the stub filter in the diplexers and triplexers (this one's from the 90-150 Diplexer) to retune the center band while we made no such adjustments to the channelizer filters.

inductors in a different way than the CPW-based resonator inductors. As a result the entire circuit is de-tuned and simulating the channelizer with the new values suggests a reflection of $S_{11} \approx 16\%$. This helps explain the total throughput in our measurements and also suggests that we can re-claim this by re-tuning the channelizer with the new material properties. The throughput losses are summarized in Table 8.5

8.7 Conclusions

In this chapter, we summarized the design cochela-inspired methodology for channelizers that our UCSD collaborators have developed and also discussed how this can be realized in monolithic printed circuits needed for millimeter and sub-millimeter applications. The measurements are encouraging, showing high optical throughput in the expected frequency channels and beam patterns that are consistent with diplexer and triplexer devices. How-

Table 8.5. Losses in the Channelizer Throughput measurements

Source	Power Transmitted
Optical Filters	≈70%
Alumina-vacuum Lens surface	72%
Antenna Front-lone	91%
Antenna-Microstrip interface	88%
Transmission line loss ($\tan(\delta) = 0.008$)	70-90%
$1 - S_{11}$ of Channelizer	84%
Total	22-34%

ever, the measurements should be repeated with a properly coated lens to demonstrate higher throughput and lower cross-pol contamination.

As mentioned in chapter 7, we can likely improve the beam shape with a different feeding scheme, and we discuss this in the concluding chapter.

There is one obvious modification that would improve the microwave design. Because the CPW 10 μm slot width is much larger than the 0.5 μm SiO_2 film thickness, it is not important that the center conductor be coplanar; it could just as well be in the layer above the oxide. In this case, the shunt-capacitor bridges would cross under the center conductor, as would the second plate for the series capacitor, residing in the ground plane. The merits of this design are that (1) the capacitors are completely robust against transverse alignment errors between the two Nb layers (although the inductor is not) and (2) no vias are required in the channelizer (although they are still needed at the antenna feed point). As of the writing of this thesis, we have not implemented this re-design.

Chapter 9

Conclusions and Future Work

9.1 Introduction

This concluding chapter discusses the next steps that need to be taken in this on-going project. Correcting the beam asymmetries is of paramount importance. We suggest two possible solutions to address this challenge.

We have also delayed a discussion of potential advantages this technology may offer over competing detectors until this final chapter so we can use results from previous chapters. We take up this topic in this final chapter as well.

9.2 Status of work

We argued in chapters 1 and 2 that there is compelling science in CMB B-mode searches and that the faint B-mode signal masked by galactic foregrounds requires high optical throughput through multiple colors. Historically, required increases in sensitivities have been driven by advancements in detector technology, and we hope to continue this trend with log-periodic pixel designs.

Log-periodic antennas and circuits achieve high bandwidth through their self-similar design, and we have demonstrated that the sinuous antenna has desirable properties. It

has high optical throughput in both linear polarization channels with circular beams and high cross-pol rejection. It can couple to TES bolometers through planar microstrip circuits, so it can be scaled to large arrays. When driven with a properly balanced feed, the beam properties show rough agreement with beams simulated in ADS and corrected with a raytracing script.

Additionally, we have demonstrated that we can partition this bandwidth into narrow frequency channels in planar microstrip circuits, also with high throughput. The diplexers and triplexers (chapter 7), allow band placement between atmospheric lines and is best suited to a terrestrial experiment. The log-periodic circuit (chapter 8) has several adjacent channels and may be advantageous for a satellite mission.

We have also made an initial demonstration of a multi-layer anti-reflection coating for the contacting lenses. These coatings were realized with the commercially available material TMM. They increased the optical throughput as much as 30% and retained beams that were similar to those through quarter-wavelength coatings.

The last outstanding issue with these pixels is the beam asymmetry in the channelized pixels. These problems were likely created by the feed design and we are pursuing schemes to correct this.

9.3 Correcting the beam asymmetries with a balun

9.3.1 A Dyson balun

The differentially fed resistive loads on the bolometers of chapter 6 reject 100% of the even mode and only terminate the odd mode. Provided that the transmission lines and filters between the antenna and termination are identical, the pixel is guarenteed to have a centered beam that is symmetric around the axis between the two opposite arms. The beams of chapters 7 and 8 clearly lack this desird symmetry and we hypothsize that this occurred because the antenna was not fed with a properly balanced feed; the currents on opposite arms were not forced to be identical.

One possible solution is to add another cell to the antenna's interior and to keep the ground plane as narrow as the microstrip's upper conductor width at the feed point. These changes would help ensure that both conductors of the transmission line appear identical to the antenna at the feed and thus that the antenna arms are fed identically. The ground plane then gradually widens as the feed lines wind outward. This feed is very similar to the Dyson balun was originally implemented with coax-cable soldered to the back of two armed log-spiral antennas (*Dyson* [1959]). *Nurnberger and Volakis* [1996] have since used this scheme to feed a two-armed arithmetic-spiral antenna with microstrip in a manner similar to our attempted feed.

There is room for an additional cell in the interior of the antenna; in fact the antennas in chapter 6 had this additional cell. The simulations of the antenna with these two feed corrections are encouraging (see Figure 6.11). However, the simulations of the antennas in chapters 7 and 8 looked far better than the measured results, so there may be systematic effects not reflected in these simulations.

9.3.2 CPW to reject an even-mode

A more aggressive solutions feeds the antenna differentially (two lines per polarization) as in chapter 6, but using a lithographed circuit that itself ensures rejection of the even mode before channelizing. An ideal circuit would be a broadband directional coupler. These circuits can combine incident waves from two input ports into sum and difference modes and can be made with multiple sections to achieve a decade band-width . Engineers prefer these circuits for this application because they can resistively terminate the sum port (even mode) instead of reflecting it away, leaving absolutely no question as to where power in this unwanted mode goes.

Unfortunately, we have not succeeded in designing these circuits in either microstrip or CPW. The currents in the two microstrip upper conductors of a directional coupler can be expressed as a combination of even and odd modes, where the even mode has equal currents in the two coupled conductors, while the odd mode has equal but opposite currents (These

modes are distinct from the antenna's even and odd modes). To mix the two input signals with even weight, the capacitive coupling between the lines must be much larger than the shunt capacitance to ground and the even and odd-mode wavespeeds between the coupled line must be well matched. However, these lines are quasi-TEM, as discussed in Chapter 6, so the two wavespeeds are not well matched. This greatly degrades the coupler's balance and phase stability. The thin dielectric film also precludes strong capacitive coupling between microstrip lines.

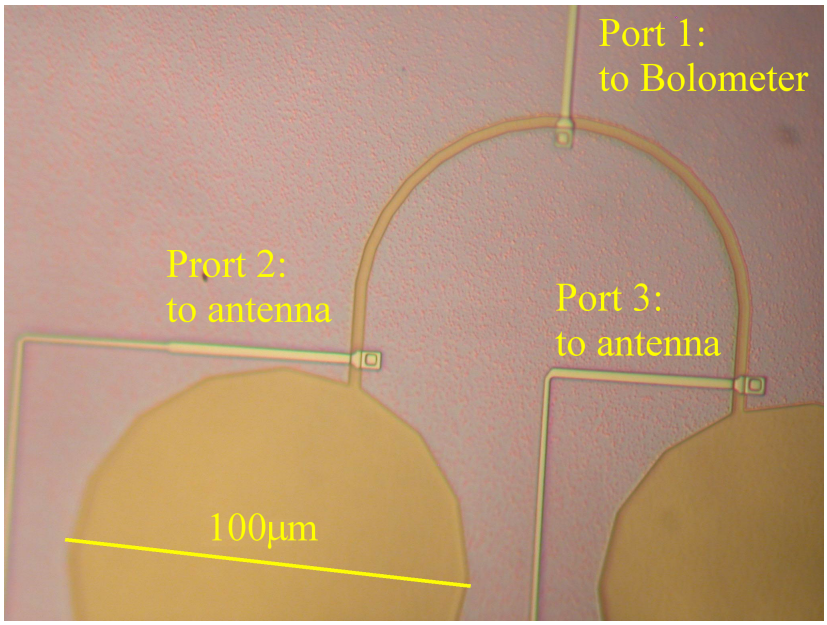

Figure 9.1. Un-tested Slot-line balun that divides power from port 1 evenly between ports 2 and 3 with a 180^o phase shift.

We have alternatively designed a circuit that couples signal on microstrip from each arm onto a slot-line with electrically-open ends. We then couple the summed power onto a third microstrip in the center. Figure 9.1 shows a fabricated slot balun that we never tested because of a fabrication error. If the input lines cross the slot from opposite sides, then the desired odd-mode will constructively interfere at the center microstrip while the even mode will destructively interfere at that point. Slotlines have been used as inverters in microwave applications and this design is similar in spirit. The undesired even-mode reflects back to the antenna, making it electromagnetically similar to the Polarbear feed discussed in chapters 4 and 6.

Slot-lines can radiate; in fact, the Polarbear crossed double slot-antenna is a set of slot-lines that efficiently radiate. By curving the slot-line into a horse-shoe, the line is similar to a short stretch of low-impedance CPW. As a result, some components of the far fields destructively interfere to reduce the radiated power. With this geometry, the input impedance is 38 Ω and the radiated power is 3% (See figure 9.2). Currently, the line length is $\lambda/8$ long at 220GHz, which is why it begins to radiate and decreasing this length should further supress this, but the shorter lines also have higher impedances at the ports. We would like to reduce the radiation below 1% with useable impedances and further work is needed to realize this.

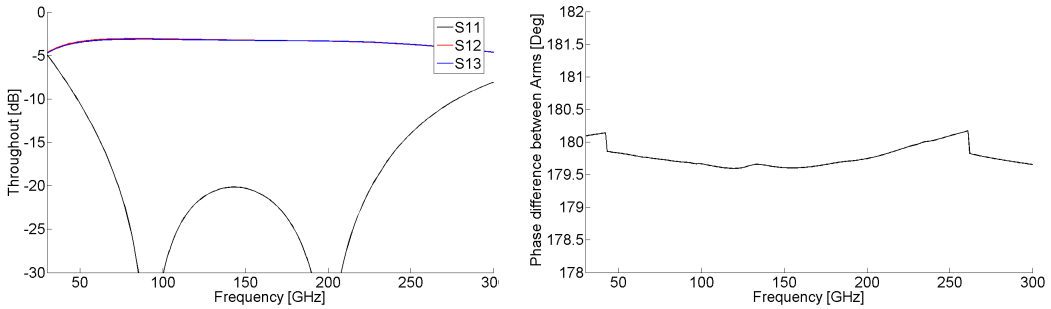

(a) Scattering parameters' magnitude

(b) Phase difference

Figure 9.2. Simulated Scattering parameters of the proposed balun circuit with each port terminated with 38 Ω. $|S_{12}|$ and $|S_{12}|$ are well matched, but the downward slope shows a slight radiation of about 3% at 225GHz. This needs to be reduced to less than 1% before the balun will be acceptable.

Finally, feeding the antenna with two arms instead of one resolves the challenge of matching the microstrip impedance to the high impedance of the antenna. If the lines feed the antenna in the H-V excitation, then there will be a virtual ground at the center and each arm will only need to match to 52 Ω instead of the much higher 104 Ω of the feeds discussed in chapters 6-7 (See Figure 9.3). This feeding scheme was only recently realized by our UCSD collaborators and if it is necessary to feed each polarization with two lines, this is clearly the most promising way to optimize the impedance match.

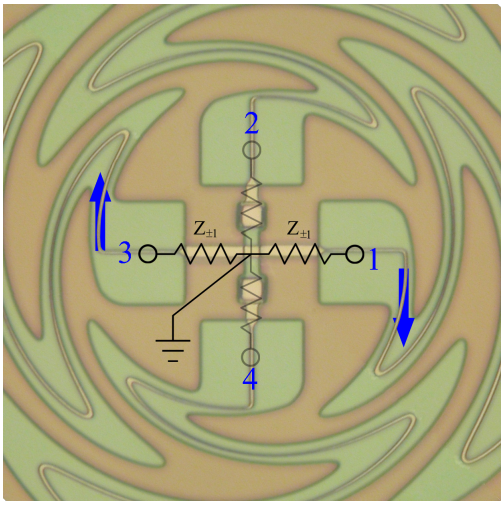

Figure 9.3. A balanced H-V feed where each arm will only see 52 Ω relative to the virtual ground at center. One polarization is grayed out and the antenna current is shown in the blue arrows. **This is photo-shopped for purposes of explanation - we have not fabricated it yet.**

9.3.3 Differentially-fed terminations

In principle, we could channelize the signal from each arm first and then differentially feed the termination as in chapter 6. This solution is undesirable because it would involve excessive microstrip crossovers as well as microstrip-bias line crossovers. Additionally, it requires that the channelizer circuits on each arm be identical; any differences will steer the beam from center or cause one arm's band to shift relative to the other. This is especially worrisome because the footprint of the multi-channel devices is much larger than the single channel Polarbear devices and the films must be uniform on this large area. With any of these defects, the antenna would couple to the even mode. We have seen some evidence of this problem in some of the Polarbear pixels as well. Additionally, the detectors from Caltech/JPL that couple through large antenna arrays have experienced beam steer which they attribute to non-uniform film properties.

9.4 Comparison of Log-periodic detectors to competing technology

After the success of the devices described in chapter 6, we are optimistic that we can suppress the beam asymmetries in the sinuous antenna. Once that final challenge is met, this device will be competitive with other currently deployed or deploying technologies. In this section, we describe how we envision constructing a focal plane with these pixels and then compare how it would compete against existing technologies.

9.4.1 Relative Mapping speeds

The signal-to-noise ratio of a measurement is

$$snr = \frac{P_s\sqrt{2\tau}}{NEP} \tag{9.1}$$

where τ is integration time, P_s the signal power, and if the measurement is background noise limited, then $NEP \propto \sqrt{P_s}$ (*Griffin et al.* [2002]). The mapping speed quantifies how quickly a target signal to noise at a given point on the sky can be achieved and goes as $Speed \propto Nsnr^2$ (*Griffin et al.* [2002]), where N is the number of pixels in a focal plane. All of the polarized CMB anisotropies that we intend to map will be much larger than the beam. In this limit,

$$speed \propto \frac{N\eta_S^2}{\eta_S B_{ext} + (1 - \eta_S B_{int})} \tag{9.2}$$

$$\propto N\eta_S \tag{9.3}$$

where B_{int} and B_{ext} are the internal and external brightness and η_S is the spillover efficiency- the fraction of the pixels' power that couples to the telescope's primary diffraction limiting optic *Halverson* [2004]. In many applications, this efficiency is set with a cold aperture stop so the spillover can be terminated on a surface of known and controlled

temperature. The last line applies to a camera where the stop is chilled to millikelvin temperatures ($B_{int} \ll B_{ext}$).

In all of these calculations, we compare the mapping speeds in specific channels between two instrument designs. Clearly, optimizing a deploying experiment would involve weighting each of the spectral channels to reflect their astrophysical importance. However, the preferred weights will likely shift as Plank and the next generation of experiments learn more about the galactic foregrounds. Instead, we only seek to quantify the potential gains that this technology offers over traditional focal-planes in a "toy-calculation" where we weight the value of every channel evenly.

9.4.2 Proposed Focal-plane design

Chapter 4 discusses how an antenna radiating a wavelength λ under a contacting synthesized ellipse with radius R has a beamwidth that scales as λ/R. Data from chapters 7 and 8 corroborate this model. Since the beam size changes with channel, the pixels can only have an optimal $2f\lambda$ spacing at one frequency. Several experimenters mapping extended sources choose to space the pixels at $2f\lambda$ because it results in high spillover efficiency and high pixel density.

We envision designing a focal plane with $2f\lambda$ spacing at the highest channel for a camera with a cold stop that terminates this beam at the -10dB contour. For the triplexer or log-periodic channelizers discussed in previous chapters, this occurs at roughly 225GHz, or 1.3mm in free space. The longer-wavelength beams will be wider and will spill onto the stops at higher powers contours. However, the pixels receiving in these longer wavelength channels will be denser than a monochromatic array with $2f\lambda$ spacing, which roughly compensates for the power lost to the stop. But if there are N channels in the telescope, then focal planes with multichroic pixels will provide an additional factor of N in mapping speed over a system with monochromatic pixels. This simple fact yields a dramatic boost in mapping speeds, and we quantify this in Figures 9.4 and 9.5. In these charts, we compare our proposed design against a multi-channel telescope where the focal plane is partitioned into

large sections with monochromatic pixels spaced at $2f\lambda$ (e.g. EBEX). Alternatively, the telescope could have multiple cameras with monochromatic 2fλ focal planes where each camera is dedicated to one of several frequencies (e.g. SPIDER). These architectures are commonly used in most contemporary telescopes.

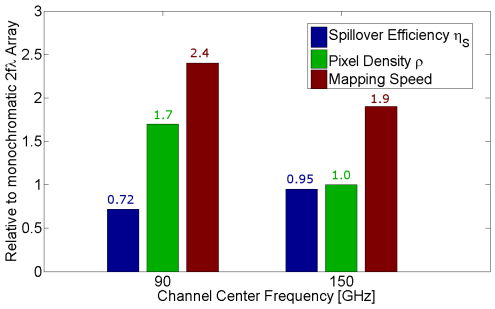

(a) 90-150 Diplexed Pixels

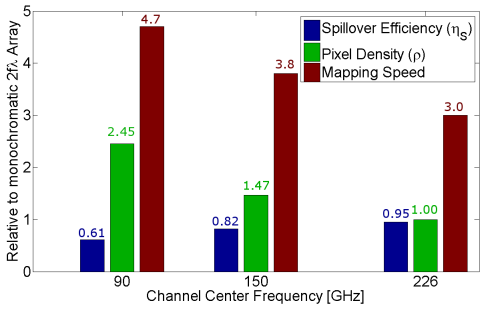

(b) 90-150-220 Triplexed Pixels

Figure 9.4. Array parameters relative to a 2fλ monochromatic array. Each channels' speed gets a boost of a factor of 2 (figure a) or 3 (figure b) because there are respectively 2 or 3 channels per pixel.

Several terrestrial CMB-polarization experiments have deployed recently or will deploy over the next year with antenna-coupled TES bolometers. These include BICEP-2, Keck Array (formerly SPUD), Polarbear, and SPT-pol. All of these experiments plan to receive multiple frequency channels at combinations of 90, 150 and 220GHz band-centers. But with the exception of Polarbear, they will use monochromatic pixels. If these experiments were upgraded to 2-3 channel pixels, these experiments could achieve mapping speed gains roughly equal to those in Figure 9.4.

This increase in throughput clearly comes at the cost of more required read-out channels.

Several groups are developing microwave frequency (1-10GHz) SQUID multiplexing that may dramatically increase the number-count of TES focal planes. Alternatively, MKIDs naturally down-convert to microwave frequencies when multiplexing and may be a viable replacement to TES bolometers in the future.

Recent advancements in MKID technology have shown that the white noise dominated by two-state transitions varies strongly with the electric fields strength, and they have suppressed that noise by building resonators with inter-digitated capacitors instead of lumped MIM capacitors. While this changed allows for background limited measurements, the footprint of the detector is sufficiently large that it drastically reduces the useful focal-plane real-estate in antenna array-coupled pixels. The detector architecture described in this thesis would naturally allow the bulky MKID resonator hide under he contacting lenses, dramatically boosting the packing density while still maintaining the wide bandwidth.

9.4.3 Application in a Satellite Mission

Satellites experiments do not have to avoid atmospheric lines and can receive contiguously placed channels. Current CMB satellites include WMAP and Plank, but their focal planes use technology that is not as scalable as lithographed TES arrays and do not make for a useful comparison. Alternatively, balloon-bourn experiments are often a demonstration of technology for future space missions, and two such modern experiments are EBEX and SPIDER. They will both have between 1000 and 2000 pixels spanning 1.5 octaves, although SPIDER will be dual polarized. These experiments still position band-centers between atmospheric lines to reduce external loading, but if orbital versions are made, they can place bands arbitrarily. Table 9.5 shows how a SPIDER or EBEX-like satellite experiment would benefit from a multi-chroic upgrade.

Figure 9.5 shows that mult-chroic pixels can significantly boost the throughput for a focal plane of fixed size. Alternatively, the multi-chroic pixels could reduce the physical size of a camera for a fixed target speed. Since both Plank and WMAP have utilized multiple channels over a two octave bandwidth, log-periodic pixels would be a viable architecture

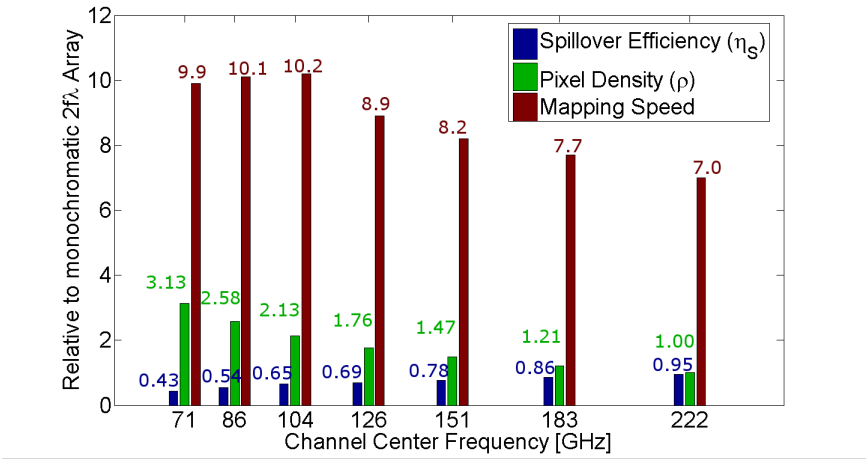

Figure 9.5. Array parameters relative to a 2fλ monochromatic array. Each channels' speed gets a boost of a factor of 7 because there are 7 channels per pixel.

that would decrease the size by a similar factor of 7-10. Since the cost of satellite missions often scales with weight of the payload, this can dramatically the cost of satellite missions. Low cost alternatives like this may be necessary to secure funding for future B-mode search satellites.

9.5 Future Work

We plan to upgrade the single-channel pixels for the Polarbear focal plane to multi-channel pixels at some point in the future. The first stage of upgrade will replace the crossed-double slot with the sinuous but with only one channel behind it. This will provide an opportunity to study the sinuous beams through the entire telescope without the added complications of extra channels. The next fabrication will have antennas with a properly implemented balun, but if that does not provide adequate beams, an additional fabrication could produce an array of dual-polarized versions of the Chapter 6 pixels, differentially feeding the lumped terminations at the bolometers. This geometry will require a microstrip cross-over, but this has already been successfully demonstrated with the current Polarbear focal plane.

Polarbear-2 will upgrade the current single color camera to one with a focal plane of

90-150 diplexers. This is the simplest possible upgrade with nearly acceptable beams as currently implemented. Such an upgrade will increase the throughput by a factor of roughly 2 while allowing for the control of one foreground. To utilize such a pixel, the rest of the optics, such as the HDPE lenses and waveplate, must be made comparatively broad-band, and our collaborators at KEK are pursuing many of these challenges.

Bibliography

Ade, P., et al., First Season QUaD CMB Temperature and Polarization Power Spectra, *apj*, *674*, 22–28, doi:10.1086/524922, 2008.

Agilent, *Advanced Design Suite Momentum v6u2, User Manual*, Agilinet, 2006.

Apsotle, T., *Calculus, Vol. 1: One-Variable Calculus with an Introduction to Linear Algebra*, Wiley, 1967.

Arnold, K., personal communication, 2008.

Behdad, N., and K. Sarabandi, Wideband double-element ring slot antenna, *Electronics Letters*, *40*(7), 408 – 409, doi:10.1049/el:20040292, 2004.

Bell, R., *Introductory Fourier Transform Spectroscopy*, Academic Pr, 1972.

Benford, D. J., M. C. Gaidis, and J. W. Kooi, Optical properties of Zitex in the infrared to submillimeter, *ao*, *42*, 5118–5122, doi:10.1364/AO.42.005118, 2003.

Benson, B. A., et al., Peculiar Velocity Limits from Measurements of the Spectrum of the Sunyaev-Zeldovich Effect in Six Clusters of Galaxies, *apj*, *592*, 674–691, doi:10.1086/375864, 2003.

Bond, J., I could tell you, but then I'd have to kill you, 2010.

Booker, H., Slot aerials and their relation to complementary wire aerials (Babinet's principle), *Electrical Engineers - Part IIIA: Radiolocation, Journal of the Institution of*, *93*(4), 620 –626, doi:10.1049/ji-3a-1.1946.0150, 1946.

Born, M., and E. Wolf, *Principles of Optics: Electromagnetic Theory of Propagation, Interference and Diffraction of Light*, Cambridge University Press, 1999.

Bussmann, R. S., W. L. Holzapfel, and C. L. Kuo, Millimeter Wavelength Brightness Fluctuations of the Atmosphere above the South Pole, *apj*, *622*, 1343–1355, doi:10.1086/427935, 2005.

Carlstrom, J. E., et al., The 10 Meter South Pole Telescope, *ArXiv e-prints*, 2009.

Carroll, S., *Spacetime and Geometry: An Introduction to General Relativity*, Benjamin Cummings, 2003.

Challinor, A., and H. Peiris, Lecture notes on the physics of cosmic microwave background anisotropies, in *American Institute of Physics Conference Series*, *American Institute of Physics Conference Series*, vol. 1132, edited by M. Novello & S. Perez, pp. 86–140, doi:10.1063/1.3151849, 2009.

Chang, J., Xenon Difluoride Etching System (XETCH), *Manual Nanoolab Manual section 7.13*, UC Berkeley, Berkeley, Ca, USA, 1998.

Chang, J., CPA Sputtering System, *Manual Nanoolab Manual section 6.04*, UC Berkeley, Berkeley, Ca, USA, 2010a.

Chang, J., Oxford Plasmalab 80plus PECVD System, *Manual Nanoolab Manual section 6.29*, UC Berkeley, Berkeley, Ca, USA, 2010b.

Chang, J., Tystar17 Non-MOS Low Stress Nitride and High Temp. Oxide LPCVD Furnace, *Manual Nanoolab Manual section 5.17*, UC Berkeley, Berkeley, Ca, USA, 2010c.

Chattopadhyay, G., and J. Zmuidzinas, A dual-polarized slot antenna for millimeter waves, *Antennas and Propagation, IEEE Transactions on*, *46*(5), 736 –737, doi:10.1109/8.668920, 1998.

Chattopadhyay, G., J. Glenn, J. Bock, B. Rownd, M. Caldwell, and M. Griffin, Feed horn coupled bolometer arrays for SPIRE - design, simulations, and measurements, *Microwave Theory and Techniques, IEEE Transactions on*, *51*(10), 2139 – 2146, doi:10.1109/TMTT.2003.817428, 2003.

Chattopadhyay, G., C.-L. Kuo, P. Day, J. Bock, J. Zmuidzinas, and A. Lange, Planar antenna arrays for CMB polarization detection, in *Infrared and Millimeter Waves, 2007 and the 2007 15th International Conference on Terahertz Electronics. IRMMW-THz. Joint 32nd International Conference on*, pp. 184 –185, 2007.

Chervenak, J. A., K. D. Irwin, E. N. Grossman, J. M. Martinis, C. D. Reintsema, and M. E. Huber, Superconducting multiplexer for arrays of transition edge sensors, *Applied Physics Letters*, *74*(26), 4043–4045, doi:10.1063/1.123255, 1999.

Chiang, H. C., et al., Measurement of Cosmic Microwave Background Polarization Power Spectra from Two Years of BICEP Data, *apj*, *711*, 1123–1140, doi:10.1088/0004-637X/711/2/1123, 2010.

Collin, R., *Antennas and Radiowave Propagation*, Mcgraw-Hill, 1985.

de Bernardis, P., et al., Detection of anisotropy in the Cosmic Microwave Background at horizon and sub-horizon scales with the BOOMERanG experiment, *ArXiv Astrophysics e-prints*, 2000.

Deschamps, G., Impedance properties of complementary multiterminal planar structures, *Antennas and Propagation, IRE Transactions on*, *7*(5), 371 –378, doi:10.1109/TAP.1959.1144717, 1959.

Dodelson, S., *Modern cosmology*, Academic Press, 2003.

Doe, J., `http://universe-review.ca/`, 2010.

DuHamel, R., Dual polarized sinuous antennas, United States Patent 4658262, 1987.

DuHamel, R., and D. Isbell, Broadband logarithmically periodic antenna structures, in *IRE International Convention Record*, vol. 5, pp. 119 – 128, 1957.

Dyson, J., The equiangular spiral antenna, *Antennas and Propagation, IRE Transactions on*, *7*(2), 181 –187, doi:10.1109/TAP.1959.1144653, 1959.

Edwards, J., personal communication, 2008.

Engargiola, G., Tapered microstrip balun for integrating a low noise amplifier with a nonplanar log periodic antenna, *Review of Scientific Instruments*, *74*, 5197–5200, doi:10.1063/1.1622975, 2003.

Engargiola, G., W. Holzapfel, A. Lee, M. Myers, R. O'Brient, P. Richards, H. Tran, and H. Spieler, Planar channelized log-periodic antenna, in *Microwave, Antenna, Propagation and EMC Technologies for Wireless Communications, 2005. MAPE 2005. IEEE International Symposium on*, vol. 1, pp. 306 – 309 Vol. 1, doi:10.1109/MAPE.2005.1617910, 2005.

Filipovic, D., S. Gearhart, and G. Rebeiz, Double-slot antennas on extended hemispherical and elliptical silicon dielectric lenses, *Microwave Theory and Techniques, IEEE Transactions on*, *41*(10), 1738 –1749, doi:10.1109/22.247919, 1993.

Finelli, F., J. Hamann, S. M. Leach, and J. Lesgourgues, Single-field inflation constraints from CMB and SDSS data, *Journal of Cosmology and Astro-Particle Physics*, *4*, 11–+, doi:10.1088/1475-7516/2010/04/011, 2010.

Finkbeiner, D. P., M. Davis, and D. J. Schlegel, Extrapolation of Galactic Dust Emission at 100 Microns to Cosmic Microwave Background Radiation Frequencies Using FIRAS, *apj*, *524*, 867–886, doi:10.1086/307852, 1999.

Fixsen, D. J., E. S. Cheng, J. M. Gales, J. C. Mather, R. A. Shafer, and E. L. Wright, The Cosmic Microwave Background Spectrum from the Full COBE FIRAS Data Set, *apj*, *473*, 576–+, doi:10.1086/178173, 1996.

Galbraith, C., Cochlear-inspired channelizing filters for Wideband Radio Systems, Ph.D. thesis, The University Michigan Ann Arbor, 2008.

Galbraith, C., and G. Rebeiz, Higher Order Cochlea-Like Channelizing Filters, *Microwave Theory and Techniques, IEEE Transactions on*, *56*(7), 1675 –1683, doi:10.1109/TMTT.2008.925574, 2008.

Galbraith, C., R. White, L. Cheng, K. Grosh, and G. Rebeiz, Cochlea-Based RF Channelizing Filters, *Circuits and Systems I: Regular Papers, IEEE Transactions on*, *55*(4), 969 –979, doi:10.1109/TCSI.2008.916537, 2008.

Gitin, M., F. Wise, G. Arjavalingam, Y. Pastol, and R. Compton, Broad-band characterization of millimeter-wave log-periodic antennas by photoconductive sampling, *Antennas and Propagation, IEEE Transactions on*, *42*(3), 335 –339, doi:10.1109/8.280719, 1994.

Goldin, A., J. J. Bock, C. Hunt, A. E. Lange, H. Leduc, A. Vayonakis, and J. Zmuidzinas, SAMBA: Superconducting antenna-coupled, multi-frequency, bolometric array, *Low Temperature Detectors*, *605*, 251–254, doi:10.1063/1.1457640, 2002.

Goodman, J., *Introduction to Fourier Optics*, McGraw-Hill Science, 1968.

Griffin, M. J., J. J. Bock, and W. K. Gear, Relative Performance of Filled and Feedhorn-Coupled Focal-Plane Architectures, *Appl. Opt.*, *41*(31), 6543–6554, 2002.

Guildemeister, J., Voltage-Biased Superconducting Bolometers for infrared and mm-waves, Ph.D. thesis, University of California Berkeley, 2000.

Gupta, K., G. Garg, B. Bahl, and P. Bhartia, *Microstrip Lines and Slotlines 2nd Ed.*, Artech House Publishers, 1996.

Halverson, N., NEP and Mapping speed for 92 GHz and 150 GHz, *Internal Technical Memo EPEX-SZ-041211a*, UC Berkeley, Berkeley, Ca, USA, 2004.

Halverson, N. W., et al., Degree Angular Scale Interferometer First Results: A Measurement of the Cosmic Microwave Background Angular Power Spectrum, *apj*, *568*, 38–45, doi: 10.1086/338879, 2002.

Hamilton, B., Plasma-Therm Parallel Plate Etcher, *Manual Nanoolab Manual section 7.09*, UC Berkeley, Berkeley, Ca, USA, 2010.

Hanany, S., et al., MAXIMA-1: A Measurement of the Cosmic Microwave Background Anisotropy on Angular Scales of 10'-5deg, *apjl*, *545*, L5–L9, doi:10.1086/317322, 2000.

Hu, W., and S. Dodelson, Cosmic Microwave Background Anisotropies, *araa*, *40*, 171–216, doi:10.1146/annurev.astro.40.060401.093926, 2002.

Hu, W., and M. White, A CMB polarization primer, *New Astronomy*, *2*, 323–344, doi: 10.1016/S1384-1076(97)00022-5, 1997.

Irwin, K., and G. Hilton, Transition-Edge Sensors, in *Cryogenic Particle Detection*, pp. 63–149, Springer-Verlag, Heidlberg, 2005.

Jackson, J. D., *Classical Electrodynamics Third Edition*, Wiley, 1998.

Johnson, B. R., et al., MAXIPOL: a balloon-borne experiment for measuring the polarization anisotropy of the cosmic microwave background radiation, *New Astronomy Reviews*, *47*(11-12), 1067 – 1075, doi:DOI:10.1016/j.newar.2003.09.034, 2003.

Kaplinghat, M., L. Knox, and Y. Song, Determining Neutrino Mass from the Cosmic Microwave Background Alone, *Physical Review Letters*, *91*(24), 241,301–+, doi: 10.1103/PhysRevLett.91.241301, 2003.

Kerr, A., Surface Impedance of Superconductors and Normal Conductors in EM Simulators, *Internal Technical Memo Alma Memo No. 245*, National Radio Astronomy Observatory, Green Bank, W. Va, USA, 1999.

Kittel, C., *Introduction to Solid State Physics, 8th Ed*, wiley, 2004.

Kogut, A., et al., PAPPA: Primordial anisotropy polarization pathfinder array, *New Astronomy Review*, *50*, 1009–1014, doi:10.1016/j.newar.2006.09.024, 2006.

Kogut, A., et al., Three-Year Wilkinson Microwave Anisotropy Probe (WMAP) Observations: Foreground Polarization, *apj*, *665*, 355–362, doi:10.1086/519754, 2007.

Komatsu, E., et al., Seven-Year Wilkinson Microwave Anisotropy Probe (WMAP) Observations: Cosmological Interpretation, *ArXiv e-prints*, 2010.

Kormanyos, B., P. Ostdiek, W. Bishop, T. Crowe, and G. Rebeiz, A planar wideband 80-200 GHz subharmonic receiver, *Microwave Theory and Techniques, IEEE Transactions on*, *41*(10), 1730 –1737, doi:10.1109/22.247918, 1993.

Kosowsky, A., Cosmic microwave background polarization., *Annals of Physics*, *246*, 49–85, doi:10.1006/aphy.1996.0020, 1996.

Kovac, J. M., Detection of polarization in the cosmic microwave background using DASI, Ph.D. thesis, THE UNIVERSITY OF CHICAGO, 2004.

Kovac, J. M., E. M. Leitch, C. Pryke, J. E. Carlstrom, N. W. Halverson, and W. L. Holzapfel, Detection of polarization in the cosmic microwave background using DASI, *nat*, *420*, 72–787, doi:10.1038/nature01269, 2002.

Kumar, S., Submillimeter wave camera using a novel photon detector technology, Ph.D. thesis, California Institute of Technology, 2007.

Lanting, T., Multiplexed Readout of Superconducting Bolometers for Cosmological Observation, Ph.D. thesis, University of California Berkeley, 2006.

Lanting, T. M., et al., Frequency-domain multiplexed readout of transition-edge sensor arrays with a superconducting quantum interference device, *Applied Physics Letters*, *86*(11), 112511, doi:10.1063/1.1884746, 2005.

Larson, D., et al., Seven-Year Wilkinson Microwave Anisotropy Probe (WMAP) Observations: Power Spectra and WMAP-Derived Parameters, *ArXiv e-prints*, 2010a.

Larson, D., et al., Seven-Year Wilkinson Microwave Anisotropy Probe (WMAP) Observations: Power Spectra and WMAP-Derived Parameters, *ArXiv e-prints*, 2010b.

Lee, A. T., et al., POLARBEAR: Ultra-high Energy Physics with Measurements of CMB Polarization, in *American Institute of Physics Conference Series*, *American Institute of Physics Conference Series*, vol. 1040, edited by H. Kodama & K. Ioka, pp. 66–77, doi:10.1063/1.2981555, 2008.

Lewis, A., and A. Challinor, Weak gravitational lensing of the CMB, *physrep*, *429*, 1–65, doi:10.1016/j.physrep.2006.03.002, 2006.

Liddle, A. R., An Introduction to Cosmological Inflation, in *High Energy Physics and Cosmology, 1998 Summer School*, edited by R. L. Walsworth & D. F. Phillips, pp. 260–+, 1999.

Liddle, A. R., and D. H. Lyth, *Cosmological Inflation and Large-Scale Structure*, Cambridge University Press, 2000.

Lis, D., CSO Atmospheric Transmission Interactive Plotter, `http://www.submm.caltech.edu/cso/weather/atplot.shtml`, 2010.

Liu, L., H. Xu, R. R. Percy, D. L. Herald, A. W. Lichtenberger, J. L. Hesler, and R. M. Weikle, Development of Integrated Terahertz Broadband Detectors Utilizing Superconducting Hot-Electron Bolometers, *IEEE Transactions on Applied Superconductivity*, *19*, 282–286, doi:10.1109/TASC.2009.2018268, 2009.

Ludwig, A., The definition of cross polarization, *Antennas and Propagation, IEEE Transactions on*, *21*(1), 116 – 119, 1973.

Lyth, D. H., Introduction to Cosmology, *ArXiv Astrophysics e-prints*, 1993.

Matthaei, G., E. Jones, and L. Young, *Microwave Filters, Impedance-Matching Networks, and Coupling Structures*, Artech House Publishers, 1980.

McGinnis, D., and J. Beyer, A broad-band microwave superconducting thin-film transformer, *Microwave Theory and Techniques, IEEE Transactions on*, *36*(11), 1521 –1525, doi:10.1109/22.8916, 1988.

Mehl, J., et al., TES Bolometer Array for the APEX-SZ Camera, *Journal of Low Temperature Physics*, *151*, 697–702, doi:10.1007/s10909-008-9738-1, 2008.

Meng, X., GCA 6200 Wafer Stepper, *Manual Nanoolab Manual section 4.13*, UC Berkeley, Berkeley, Ca, USA, 2010.

Miller, A. D., et al., A Measurement of the Angular Power Spectrum of the Cosmic Microwave Background from L = 100 to 400, *apjl*, *524*, L1–L4, doi:10.1086/312293, 1999.

Mushiake, Y., *Self-Complementary Antennas: Principle of Self-Complementarity for Constant Impedance*, New York Academic Press, 1996.

Myers, M., personal communication, 2008.

Myers, M. J., et al., An antenna-coupled bolometer with an integrated microstrip bandpass filter, *Applied Physics Letters*, *86*(11), 114103, doi:10.1063/1.1879115, 2005.

Nurnberger, M., and J. Volakis, A new planar feed for slot spiral antennas, *Antennas and Propagation, IEEE Transactions on*, *44*(1), 130 –131, doi:10.1109/8.477538, 1996.

O'Brient, R., et al., A Multi-Band Dual-Polarized Antenna-Coupled TES Bolometer, *Journal of Low Temperature Physics*, *151*, 459–463, doi:10.1007/s10909-007-9698-x, 2008a.

O'Brient, R., et al., Sinuous antennas for cosmic microwave background polarimetry, in *Society of Photo-Optical Instrumentation Engineers (SPIE) Conference Series*, *Society of Photo-Optical Instrumentation Engineers (SPIE) Conference Series*, vol. 7020, doi: 10.1117/12.788526, 2008b.

Olive, K. A., G. Steigman, and T. P. Walker, Primordial nucleosynthesis: theory and observations, *physrep*, *333*, 389–407, doi:10.1016/S0370-1573(00)00031-4, 2000.

Pardo, J., J. Cernicharo, and E. Serabyn, Atmospheric transmission at microwaves (ATM): an improved model for millimeter/submillimeter applications, *Antennas and Propagation, IEEE Transactions on*, *49*(12), 1683 –1694, doi:10.1109/8.982447, 2001.

Partridge, R., *3K: The Cosmic Microwave Background Radiation*, Cambridge University Press, Palo Alto, 1995.

Pathria, R., *Statistical Mechanics, 2nd Edition*, Butterworth-Heinemann, 1996.

Pearson, T. J., et al., The Anisotropy of the Microwave Background to l = 3500: Mosaic Observations with the Cosmic Background Imager, *apj*, *591*, 556–574, doi:10.1086/375508, 2003.

Pisano, G., G. Savini, P. A. R. Ade, V. Haynes, and W. K. Gear, Achromatic half-wave plate for submillimeter instruments in cosmic microwave background astronomy: experimental characterization, *ao*, *45*, 6982–6989, doi:10.1364/AO.45.006982, 2006.

Pozar, D., *Microwave Engineering*, Wiley, 2004.

Raman, S., and G. Rebeiz, Single- and dual-polarized millimeter-wave slot-ring antennas, *Antennas and Propagation, IEEE Transactions on*, *44*(11), 1438 –1444, doi:10.1109/8.542067, 1996.

Rauscher, C., Efficient design methodology for microwave frequency multiplexers using infinite-array prototype circuits, *Microwave Theory and Techniques, IEEE Transactions on*, *42*(7), 1337 –1346, doi:10.1109/22.299727, 1994.

Reichardt, C. L., et al., High-Resolution CMB Power Spectrum from the Complete ACBAR Data Set, *apj*, *694*, 1200–1219, doi:10.1088/0004-637X/694/2/1200, 2009.

Richards, P. L., Bolometers for infrared and millimeter waves, *Journal of Applied Physics*, *76*(1), 1–24, doi:10.1063/1.357128, 1994.

Rumsey, V., *Frequency Independent Antennas*, New York Academic Press, 1966.

Rybicki, G. B., and A. P. Lightman, *Radiative processes in astrophysics*, Wiley, 1979.

Saini, L., and R. Bradley, The Sinuous Antenna - a Dual Polarized Element for Wideband Phased Array Feed Application, *Internal Technical Memo Electronic Division Internal Report-No. 31*, National Radio Astronomy Observatory, Green Bank, W. Va, USA, 1996.

Sarpeshkar, R., R. Lyon, and C. Mead, *A Low-Power Wide-Dynamic-Range Analog VLSI Cochlea*, vol. 447, pp. 49–103, Springer, doi:10.1007/b102308, 2007.

Simons, R., *Coplanar Waveguide Circuits Components and Systems*, Wiley-IEEE Press, 2001.

Smoot, G. F., M. V. Gorenstein, and R. A. Muller, Detection of anisotropy in the cosmic blackbody radiation, *Physical Review Letters*, *39*, 898–901, doi:10.1103/PhysRevLett.39.898, 1977.

Smoot, G. F., et al., Structure in the COBE differential microwave radiometer first-year maps, *apjl*, *396*, L1–L5, doi:10.1086/186504, 1992.

Staniszewski, Z., et al., Galaxy Clusters Discovered with a Sunyaev-Zel'dovich Effect Survey, *apj*, *701*, 32–41, doi:10.1088/0004-637X/701/1/32, 2009.

Swanson, D., Thin-film lumped-element microwave filters, in *Microwave Symposium Digest, 1989., IEEE MTT-S International*, pp. 671 –674 vol.2, doi:10.1109/MWSYM.1989.38814, 1989.

Takahashi, Y., personal communication, 2008.

Van Duzer, T., *Principles of Superconducting Devices and Circuits*, Prentice Hall, 1998.

Vieira, J. D., et al., Extragalactic millimeter-wave sources in South Pole Telescope survey data: source counts, catalog, and statistics for an 87 square-degree field, *ArXiv e-prints*, 2009.

Watts, L., Cochlear Mechanics, Analysis and Analog VLSI, Ph.D. thesis, California Institute of Technology, 1993.

Weisend, J., *The Handbook Of Cryogenic Engineering*, CRC Press, 1998.

Werthamer, N. R., Theory of the Superconducting Transition Temperature and Energy Gap Function of Superposed Metal Films, *Phys. Rev.*, *132*(6), 2440–2445, doi:10.1103/PhysRev.132.2440, 1963.

Woodcraft, A. L., and A. Gray, A low temperature thermal conductivity database, in *A low temperature thermal conductivity database*, vol. 1185, edited by B. Young, B. Cabrera, and A. Miller, pp. 681–684, AIP, doi:10.1063/1.3292433, 2009.

Woody, D. P., and P. L. Richards, Spectrum of the cosmic background radiation, *Physical Review Letters*, *42*, 925–929, doi:10.1103/PhysRevLett.42.925, 1979.

Yassin, G., and S. Withington, Loss In Normal And Superconducting Millimetre-Wave And Submillimetre Wave Microstrip Transmission Line, in *Computation in Electromagnetics, Third International Conference on (Conf. Publ. No. 420)*, pp. 149 –154, 1996.

Yoon, K. W., et al., Feedhorn-Coupled TES Polarimeters for Next-Generation CMB Instruments, in *American Institute of Physics Conference Series*, *American Institute of Physics Conference Series*, vol. 1185, edited by B. Young, B. Cabrera, & A. Miller, pp. 515–518, doi:10.1063/1.3292392, 2009.

Zmuidzinas, J., Cramér-Rao sensitivity limits for astronomical instruments: implications for interferometer design, *Journal of the Optical Society of America A*, *20*, 218–233, doi:10.1364/JOSAA.20.000218, 2003a.

Zmuidzinas, J., Thermal noise and correlations in photon detection, *ao*, *42*, 4989–5008, doi:10.1364/AO.42.004989, 2003b.

Zmuidzinas, J., personal communication, 2010.

Appendix A

MATLAB raytracing software

A.1 Overview

This appendix contains a hardcopy of the raytracing script and all functions. This code is included here as a reference and to ensure that it is not lost. It was written with Matlab v 7.0. The function progmeter.m is need as well, but was written by another author and is available for download from http://www.mathworks.com/matlabcentral/fileexchange.

A.2 Main script

```
%BEAMSCRIPT
%
%This script modifies the far-field antenna patterns from ADS-momentum to
%account for a contacting extended hemispherical lens.  It accounts for
%refraction at the lens surface as well as diffraction.  The user should
%modify the *non-indented* variables at the begining of the script between
%the BEGIN and END USER DEFINED INPUT
%
%This script uses the following functions which must be present in the same
%directory for it to function properly: build_lens.m, raytrace.m,
%readfff.m, normalize.m, rect2plane_incidence.m, plane_incidence2rect.m,
%rect2sphere.m, sphere2rect.m, refraction_nocoat.m, refraction_1coat.m,
%refraction_3coat.m, matrix_mult4d.m, surfacecurrents.m, Diffraction.m,
%progmeter.m, writefff.m
%
%Because the program was developed on a laptop with 512MB RAM, there was
%insufficient memory to store all variables at once, so a series of loops
%are used instead, with a timer so the user can watch progress.  If all
%discritization is done at 3 degrees, then the integral takes 30 sec to
%finish.
%Special thanks to Jen Edwards for help troubleshooting this code, pointing
%out that Matlab's dot function conjugates it's first argument, and
%suggesting the use of image currents.
%Roger O'Brient         Jan 2010

home;
```

```
clear all;

c=3*10^8;%[m/s] speed of light free space
eta=377;%[Ohms] impedance free space

f_GHz=150; %[GHz] Frequency
f=f_GHz*10^9; %[Hz]
f_str=[num2str(round(f_GHz))];

%Lens Properties
er=11.7; % rel permativity of lens material (silicon)
%er=10.5;%rel permativity if lens material (sintered alumina)
    nlens=sqrt(er); %index refraction of lens material
R=13.7/2; %[mm] Lens Radius
    R=R/1000; %[m] Lens Radius
%Lext=.2767*R; %[mm] Hyperhemisphere for er=11.7
Lext=.3876*R; %[mm] Synth ellipse for er=11.7

%Change coating-flag for the three posible coatings:
%coatingflag='no coating';
coatingflag='single layer';
%coatingflag='three layers';

%Single Layer AR-coating properites
thickAR=0.30/2; %[mm] Currently lambda/4 for 300GHz
    thickAR=thickAR/1000; %[m]
nAR=2; %Index of stycast-2850, Lamb compendium data, 4.8K, 100GHz

%Multi-layer AR properites.  I've set all thicknesses to lambda/4 for
%160GHz center frequency
thick1=0.19; %[mm] TMM6
thick2=0.27; %[mm] TMM3
thick3=0.3906; %[mm] Zitex
    thick1=thick1/1000; %[m]
    thick2=thick2/1000; %[m]
    thick3=thick3/1000; %[m]
n1=2.45; %index refraction of TMM6, from Erin Quealy
n2=1.73; %index refraction of TMM3, from Erin Quealy
n3=1.2; %%index refraction of Zitex, from Dominec Benford et all.

%antenna location relative to hemispherical center
centerx=0; %[mm]
centery=0; %[mm]
centerz=-Lext; %[mm]
    ant_loc=[centerx;centery;centerz] ;

%To include image currents, set inc_img=1.  To exclude, set it to 0
inc_img=1 ;

%Angular steps for integration and far field pattern display
%Code takes 30-40 sec with all set to 3 deg.
hemthetastep=3; %[deg]
hemphistep=3; %[deg]
    hemthetastep=pi/180*hemthetastep; %[rad]
    hemphistep=pi/180*hemphistep; %[rad]
% PATTERN THETA/PHI
ffthetastep=3; %[deg]
ffphistep=3; %[deg]
    ffthetastep=pi/180*ffthetastep; %[rad]
```

```
    ffphistep=pi/180*ffphistep; %[rad]

%Input file from ADS momentum
pathin='TestResults\';
fnamein=[ 'Momentum_input.fff' ] ;

%Output file to write to.
pathout=pathin;
fnameout=['Sample_output_', f_str, 'GHz.txt'];

commentary = { [ 'Frequency = ' num2str(f_GHz), ' GHz' ];
               [ 'er = ', num2str(er,'%2.2f') ] ;
               [ 'Lens Radius = ' , num2str(R*1e3,'%2.4f'), ' mm, ' ,...
                 'Extension Length = ' , num2str(Lext*1e3,'%2.4f'),' mm '];
               [ 'antenna at x = ', num2str(centerx*1e3,'%2.6f'),' mm, '...
                 ' y = ', num2str(centery*1e3,'%2.6f'),...
                 ' mm relative to lens central axis' ] ;
                 [ 'Antireflection model: ', coatingflag]; }   ;



disp('Performing Raytracing inside the lens') ;
tic ;

%Diffraction happens at the outer-most surface, so we need to adjust the
%radius of the lens surface according to the number of layers in the
%AR-coating.
switch coatingflag
    case {'no coating'}
        Rsurf=R;
    case {'single layer'}
        Rsurf=R+thickAR;
    case {'three layers'}
        Rsurf=R+thick1+thick2+thick3;
end
%Calculate lens geometry:
%hemtheta,hemphi: angular postions of surface patches to hemispherical
%       center
%normal=unit vector normal to surface.
%anttheta,antphi: angular poistions of surface patches to antenna position
%dA, dA_img: patch area & image patch areas
%dist: distance to patch from antenna
%patch_pos img_pos: vectorial positions of patches relative to antenna.
%khat= unit wavevector incident to each patch
[hemphi hemtheta antphi anttheta normal dA dA_img patch_pos img_pos...
    distance khat]=build_lens(hemthetastep, hemphistep, Rsurf, ant_loc);

%Calculate the fields internal to the lens surface.  Use data from the
%provided momentum file as well as geometry calculated above.
%antE & antH are the fields radiated from the antenna just inside the lens
%surface patches.
lambda=c/nlens/f; %[m] wavelength inside lens
[antE antH]=raytrace([pathin,fnamein],anttheta,antphi,patch_pos,...
            lambda,nlens);

%Convert the internal fields to the basis wrt to the plane of incidence in
%preparation for refraction.
%TE_hat & TM_hat are unit vectors perpendicular to & within the plane of
%       incidence, both normal to k_hat
```

```
[TM_hat,TE_hat,Etransverse,Htransverse]=rect2transverse(normal,khat,...
                                          antE,antH);

%refractErect & refractHrect are electric and magnetic fields just outside
%the lens surface, in a rectangular basis
%The transmission coefficients are different depending on the style of
%AR-coating.  The three cases are:
switch coatingflag
    case {'no coating'}
        [refractErect,refractHrect] =refraction_nocoat(Etransverse,...
            Htransverse,khat,TM_hat,TE_hat,normal,nlens,1);
        disp('Refraction through an uncoated surface');
    case {'single layer'}
        [refractErect,refractHrect] =refraction_1coat(Etransverse,...
            Htransverse,khat,TM_hat,TE_hat,normal,thickAR,nlens,nAR,1,f);
        disp('Refraction through a single layer AR-coating');
    case {'three layers'}
        [refractErect,refractHrect]=refraction_3coat(Etransverse,...
         Htransverse,khat,TM_hat,TE_hat,normal,nlens,n1,n2,n3,1,thick1,...
         thick2,thick3,f);
        disp('Refraction through a triple-layer AR-coating');
end

%Calculate surface currents (J,M) and their images (J_img,M_img).
[J,M,J_img,M_img]=surfacecurrents(refractErect,refractHrect,normal,Lext);
disp(['Finished after: ',num2str(toc),' sec']);

%Do the Diffraction Integral to calculate far-fields (Efarfield, Hfarfield)
%at the angular positions (fftheta,ffphi)
[fftheta ffphi Efarfield Hfarfield]=Diffraction(ffthetastep,ffphistep,...
    J,M,J_img,M_img,dA,dA_img,patch_pos,img_pos,inc_img,Lext,f,...
                                                hemtheta,hemphi);

writefff(180/pi*ffphi,180/pi*fftheta,Efarfield,[pathout,fnameout],...
                                                    commentary);
```

A.3 Construct Lens Geometry

```
function [hemphi hemtheta antphi anttheta normal dA dA_img patch_pos...
    img_pos distance khat]=build_lens(hemthetastep, hemphistep, R, ant_loc)

%BUILD_LENS      build_lens(hem_theta_step, hem_phi_step, R, ant_loc)
%
%build_lens calculates lens geometry before any physics.
%This function accepts as arguments the angular step sizes for meshing the
%surface (hemthetastep & hemphistep) as well as lens radius (R) and the
%vectorial offset of the hemisphere's center from the antenna (ant_loc).
%It returns the folling in meshgrid format:
%HEMPHI & HEMTHETA: patch angular positions wrt center
%NORMAL: unit normal vectors to each patch
%dA: area if each patch, repeated for all 3-dimensions
%dA_img: area of image patchs
%PATCH_POS: vector position of each patch wrt antenna
%img_pos: location of image patches
```

```
%DISTANCE: distance to each patch from antenna
%KHAT: unit angle of incidence
%ANTPHI & ANTTHETA: patch angular positions wrt antenna
%All output vectors are in rectangular basis.
%Roger O'Brient              Oct 2009
%                            updated for image currents Jan 2010


%construct phi&theta coords on the hemisphere.  Exclude theta=0 (tip) and
%phi=360 (duplicate points).
[hemphi,hemtheta] = meshgrid(0:hemphistep:(2*pi-hemphistep),...
    hemthetastep:hemthetastep:pi/2);
numtheta=size(hemtheta,1);
numphi=size(hemphi,2);

%unit normal
normal=cat(3,sin(hemtheta).*cos(hemphi),...
             sin(hemtheta).*sin(hemphi),...
             cos(hemtheta));

Lext=ant_loc(3);
%area of each patch & of image patches
dA=R^2.*sin(hemtheta);
dA=repmat(dA,[1 1 3]);
dA_img=dA;
%location of each patch
patch_pos=R*normal-...
            repmat(permute(ant_loc,[3 2 1]),[numtheta,numphi,1]);

%img_pos = patch_pos(1:end-(Lext==0),:,:) ;
img_pos=patch_pos;
img_pos(:,:,3)=-img_pos(:,:,3);

distance=repmat(sqrt(dot(patch_pos,patch_pos,3)),[1 1 3]);
khat = patch_pos ./ distance ;

%atan is defined on [-90,90], but we need it over the full [0,360]
antphi=atan(khat(:,:,2)./khat(:,:,1))+...
    pi*((khat(:,:,1)<0)&(khat(:,:,2)>0))+...
    pi*((khat(:,:,1)<0)&(khat(:,:,2)<0))+...
    2*pi*((khat(:,:,1)>0)&(khat(:,:,2)<0));
anttheta=acos((khat(:,:,3)));
```

A.4 Construct Fields just inside lens

```
function [antE antH]=raytrace(fff_file,anttheta,antphi,patch_pos,lambda,n)

%RAYTRACE raytrace(fff_file,anttheta,antphi,patch_pos,normal,lambda,khat,n)
%
%This fucntion calculates the internal fields of the lens just inside the
%surface.  It reads an ADS momentum generated file fff_file='*.fff' and
%interpolates electric field values at patches at (ANTTHETA,ANTPHI).  It
%also accepts as input the rectangular location of each patch PATCH_POS,
%the wavelength in the material LAMBDA, and the wavespeed n to construct a
```

```
%propagator (greens function) that accounts for phase delays and 1/R field
%decay between the antenna and surface patches.  It returns NxMx3 arrays of
%field antE and antH in rectangular coords.  Note that the field must be
%the 1st argument of any cross product since Matlab conjugates the
%2nd argument.
%This function uses other functions NORMALIZE and SPHERE2RECT.
%
%Roger O'Brient     Jan 2010

eta=377; %[ohms]
%construct normalized wavevector
khat=cat(3,sin(anttheta).*cos(antphi),...
           sin(anttheta).*sin(antphi),...
           cos(anttheta));
ki=2*pi/lambda*khat;%[1/m] wavevector

%Read simulation file, interpolate field @ lens, convert to rect coords.
[simtheta,simphi,simEtheta,simEphi] = readfff(fff_file) ;
interpEphi = interp2(simphi,simtheta,simEphi,antphi,anttheta) ;
interpEtheta = interp2(simphi,simtheta,simEtheta,antphi,anttheta) ;
interpEsphere=cat(3,zeros(size(anttheta)),interpEtheta,interpEphi);
interpErect=sphere2rect(interpEsphere,anttheta,antphi);

%Construct propagator to account for phase delays to lens and 1/R field
%decay
R=repmat(sqrt(dot(patch_pos,patch_pos,3)), [1 1 3]);
propagator = repmat( exp( -j* dot( ki,patch_pos, 3 ) ), [ 1 1 3 ] ) ./R ;

%Now consctruct E and H fields at lens.
antE=interpErect.*propagator;
antH=-n*cross(antE,khat,3)/eta;
```

```
function [B]=normalize(A)
%Accepts an array of vectors (mxnx3), calculates the magnitude
%of each vector, and then divides that out to return an array of
%vectors that each have unit magnitude.  The vectors can be in
%any basis.
%Roger O'Brient Oct 07
Amag=repmat(sqrt(dot(A,A,3)),[1 1 3]);
B=A./Amag;
```

A.5 File reading & writing

```
function [theta phi Etheta Ephi] = readfff(fname)

fid=fopen( fname ) ;
if fid==-1
    error(['error: cannot find file ',fname]);
end

data=[];

%fget1 reads a line, ignores new line character
```

```
line=fgetl(fid);


%feof=1 if at end of file, 0 otherwise.
while ¬feof(fid)
    %igonre if the line is empty or begins with '#', otherwise,
    %concatinate with the data array as the next row.
    if ¬isempty( line ) && ¬strcmp( line(1), '#')
        %convert line string into a vector of floating point variables
        data = cat( 1, data, (sscanf( line, '%f' ))' ) ;
    end

    %read next line before repeat
    line=fgetl(fid);
end

%Data format is columns of:
%theta phi real(E_theta) imag(E_theta) real(E_phi) imag(E_phi)

%Now search the 1st two columns & ignore all the repeats
theta=unique(data(:,1))*pi/180 ;
phi=unique(data(:,2))*pi/180 ;

%Combine the real and imag components & put in meshgrid form
Etheta=reshape(complex(data(:,3),data(:,4)),...
                    length(theta),length(phi));
Ephi=reshape(complex(data(:,5),data(:,6)),...
                    length(theta),length(phi));
fclose(fid);
```

```
function wr=writefff(phi,theta,Efarfield,fname,commentary)
if nargin==5
    commentary={};
end

%put the data in *.fff format so it could be fed back into ADS momentum
ffEtheta=Efarfield(:,:,2);
ffEphi=Efarfield(:,:,3);
dataout=permute(cat(3,theta,phi,...
                    real(ffEtheta),imag(ffEtheta),...
                    real(ffEphi),imag(ffEphi)),...
                                                [3 1 2]);
fid=fopen(fname,'wt');
%first write comments, each line proceeded by a '#'
for i=1:length(commentary) ;
    fprintf(fid,'# %s \n',commentary{i});
end

%Write data.  Speparate each theta cut with 'Begin Cut' & 'End Cut' as
%Momentum does.
for i=1:size(phi,2)
    fprintf(fid,'# %s \n','Begin cut');
        fprintf(fid,'%2.8f  %2.8f  %2.8e  %2.8e  %2.8e  %2.8e  \n', ...
                dataout(:,:,i));
    fprintf(fid,'# %s \n\n','End cut');
end
fclose(fid);
```

A.6 Convert to & from spherical coordinates

```
function v_sphere=rect2sphere(v_rect,theta, phi)
%This converts an array of 3-d vectors in a rectangualr basis to a
%spherical basis.  All angles are in RADIANS.  The theta and
%phi matrices should have been generated by meshgrid of
%dimensions mxn, while v_sphere should be mxnx3.  The program
%constructs |r><x|+|r><y|+|r><z| etc and dots this against the
%vectors in an xyz basis: V_r|r> (|r><x|+|r><y|+|r><z|)|v_rect>
%etc.
%Roger O'Brient Oct 07

rhat=cat(3, sin(theta).*cos(phi), sin(theta).*sin(phi)...
    ,cos(theta));  %|r><x|+|r><y|+|r><z|
thetahat=cat(3, cos(theta).*cos(phi), cos(theta).*sin(phi)...
    ,-sin(theta)); %|theta><x|+|theta><y|+|theta><z|
phihat=cat(3, -sin(phi), cos(phi),0*phi);
                        %|phi><x|+|phi><y|+|phi><z|

v_sphere=cat(3,...
    dot(rhat,v_rect,3),... %V_r|r> (|r><x|+|r><y|+|r><z|)|v_rect>
    dot(thetahat,v_rect,3),...%V_th|th> (|th><x|+|th><y|+|th><z|)|v_rect>
    dot(phihat,v_rect,3)); %V_ph|ph> (|ph><x|+|ph><y|+|ph><z|)|v_rect>
```

```
function vrect=sphere2rect(vsphere,theta, phi)
%This converts an array of 3-d vectors in a spherical basis to a
%rectangular basis.  All angles are in RADIANS.  The theta and
%phi matrices should have been generated by meshgrid of
%dimensions mxn, while v_sphere should be mxnx3.  The program
%constructs |x><r|+|x><th|+|x><ph| etc and dots this against the
%vectors in an xyz basis: V_x|x> (|x><r|+|x><th|+|x><ph|)|v_sph>
%etc.
%Roger O'Brient Oct 07

xhat=cat(3, sin(theta).*cos(phi), cos(theta).*cos(phi)...
    ,-sin(phi));  %|x><r|+|x><th|+|x><ph|
yhat=cat(3, sin(theta).*sin(phi), cos(theta).*sin(phi)...
    ,cos(phi)); %|y><r|+|y><th|+|y><ph|
zhat=cat(3, cos(theta), -sin(theta),zeros(size(phi)));
                        %|z><r|+|z><th|+|z><ph|

vrect=cat(3,...
          dot(xhat,vsphere,3),... %V_x|x> (|x><r|+|x><th|+|x><ph|)|v_sph>
          dot(yhat,vsphere,3),...%V_y|y> (|y><r|+|y><th|+|y><ph|)|v_sph>
          dot(zhat,vsphere,3)); %V_z|z> (|z><r|+|z><th|+|z><ph|)|v_sph>
```

A.7 Convert to & from POI coordinates

```
function [TM_hat,TE_hat,Eplane,Hplane]=rect2transverse(normal,k_hat,...
                                                       Erect,Hrect)
%           This function accepts unit normal (NORMAL) and unit incident
```

```
%           (KHAT) vectors and constructs a basis perpendicular (TE_HAT)
%           and within the plane of incidence (TM_HAT).  The basis is
%               TM_HAT=TE_HAT X KHAT
%
%           TE stands for Transverse-Electric component while TM for
%           Transvere-Magnetic component.
%           It then resolves the provided E and H vectors into components
%           parallel (E_TM) and perpendicular (E_TE), where the output
%           format is an mxnx3 matrix.  The mxn columns refer to specific
%           angles of the lens surface patchs and the components on the
%           3-element dimension are:
%               1. along K_HAT (which will be zero)
%               2. along TM_HAT
%               3. along TE_HAT
%           The function returns the two new basis vectors as well as the
%           fields in that basis.
%           This function calls the custom function NORMALIZE which forces a
%           matrix of 3-vectors to be normal.
%           WARNING: Matlab's native "dot" function takes the conjugate of
%           it's first argument, and "cross" conjugates the second!
%           Roger O'Brient Oct 07

%set up the new basis.
normal=normalize(normal);
k_hat=normalize(k_hat);
TE_hat=cross(normal,k_hat,3);
TE_hat=normalize(TE_hat);
TM_hat=cross(TE_hat,k_hat,3);
TM_hat=normalize(TM_hat);

%Find components in new basis.  Basis vectors must be the first argument
%since they are real and Matlab will automatically conjugate those.
E_k=dot(k_hat,Erect,3);
E_tm=dot(TM_hat,Erect,3);
E_te=dot(TE_hat,Erect,3);

H_k=dot(k_hat,Hrect,3);
H_te=dot(TM_hat,Hrect,3);
H_tm=dot(TE_hat,Hrect,3);

%construct vectors in new basis as described in header
Eplane=cat(3,E_k,E_tm,E_te);
Hplane=cat(3,H_k,H_te,H_tm);
```

```
function [Erect,Hrect]=transverse2rect(normal,k_hat,...
                                        Etransverse,Htransverse)
%This function accepts unit normal (NORMAL) and unit incident
%(KHAT) vectors and constructs a basis perpendicular (TE_HAT)
%and within the plane of incidence (TM_HAT).  These names are in reference
%to the orientation of the electric fields of those componenents; e.g the
%electric field of the TM-component resides in the plane of incidence.
%The basis is
%       TM_HAT=TE_HAT x K_HAT
%and all vectors are ordered:
%       1.k_hat
%       2.TM_hat
%       3.TE_hat
```

```
%It then resolves the E and H vectors provided by the user in
%that basis back into a rectangular basis, where the output
%format is an mxnx3 matrix.  The mxn columns refer to specific
%anglular positions of the lens surface patchs and the components on the
%3-element dimension are:
%       1. x_hat
%       2. y_hat
%       3. z_hat
%This function calls the custom function NORMALIZE which forces a
%matrix of 3-vectors each be of unit length.
%WARNING: Matlab's native "dot" function takes the conjugate of
%it's first argument, and "cross" conjugates the second!
%Roger O'Brient Oct 2009

%Set up the new basis.  These are in cartesian coordinates.
normal=normalize(normal);
k_hat=normalize(k_hat);
TE_hat=cross(normal,k_hat,3);
TE_hat=normalize(TE_hat);
TM_hat=cross(TE_hat,k_hat,3);
TM_hat=normalize(TM_hat);

%extract components in the transverse-basis.
E_k=repmat(Etransverse(:,:,1),[1 1 3]);
E_tm=repmat(Etransverse(:,:,2),[1 1 3]);
E_te=repmat(Etransverse(:,:,3),[1 1 3]);

H_k=repmat(Htransverse(:,:,1),[1 1 3]);
H_te=repmat(Htransverse(:,:,2),[1 1 3]);
H_tm=repmat(Htransverse(:,:,3),[1 1 3]);

%Assemble vectors in rectangular coordinates.
Erect=E_k.*k_hat+E_tm.*TM_hat+E_te.*TE_hat;
Hrect=H_k.*k_hat+H_te.*TM_hat+H_tm.*TE_hat;
```

A.8 Refraction

There are three options: no coating, one-layer coating, and three layers. For brevity's sake (too late...), I have excluded the one-layer function which is similar to the three-layer.

```
function [transErect,transHrect] =refraction_nocoat(Etransverse,Hplane,...
    k_hat,TM_hat,TE_hat,normal,nlens,noutside)
%REFRACTION_NOCOAT refraction_nocoat(Etransverse,Hplane,...
%           k_hat,TE_hat,TM_hat,normal,nlens,noutside)
%This function reftacts the incident fields (EPLANE,HPLANE) in
%Plane-Of-Incidence (POI) coords into refracted fields
%(TRANSERECT,TRANSHRECT), rectangular coords.  All are mxnx3 arrays.
%It accepts the POI basis vectors (KHAT,TM_hat,TE_hat) as well as the
%surface normals NORMAL and the indicies inside (N1) and outside (N2) the
%lens.
%This function invokes Snell's law to calculate the new unit wavevector
%khatprime.  It calculates Fressnel Coefficients, and then the trnsmitted
%fields.  The TE component of the E-fields remains in the same
%positon, as does the TM component of the H-fields.  The others rotate
```

```
%about the basis vectors TE_hat.   HTRANS is calculated from ETRANS and
%khatprime.
%Roger O'Brient Jan 2010

eta=377; %[Ohms] Impedance Free Space

%Snell's law rotates pointing vector in khat-TM_hat plane by
%angleDelta:
angle_inc=acos(dot(k_hat,normal,3)); %[radians]
angle_trans=asin(nlens/noutside*sin(angle_inc)); %[radians]
angleDelta=angle_trans-angle_inc; %[radians]
%The wavevector for the transmitted ray is just a rotation of the incident
%wavevector by angle_Delta about the TE_hat axis.  transk_hat will be part
%of a new basis-set for the fields.
transk_hat=repmat(cos(angleDelta),[1 1 3]).*k_hat+...
    repmat(sin(angleDelta),[1 1 3]).*TM_hat;

%Fresnel Coefficients (unitless):
R_te=(nlens*cos(angle_inc)-noutside*cos(angle_trans))./...
    (nlens*cos(angle_inc)+noutside*cos(angle_trans));
T_te=1+R_te;
R_tm=(-noutside*cos(angle_inc)+nlens*cos(angle_trans))./...
    (noutside*cos(angle_inc)+nlens*cos(angle_trans));
T_tm=nlens/noutside*(1-R_tm);

%Transmitted E-field perpendicular to POI (Etransverse(:,:,3)) points in
%same direction before and after refraction.  The E-field within the POI
%Etransverse(:,:,2) rotates like khat by angleDelta

transEplane=cat(3,-T_tm.*Etransverse(:,:,2).*sin(angleDelta),...
                  T_tm.*Etransverse(:,:,2).*cos(angleDelta),...
                  T_te.*Etransverse(:,:,3));

%covert to rectangular coords
[transErect,transHrect]=transverse2rect(normal,k_hat,transEplane,...
                                        transEplane);

%Construct Magnetic-field
transHrect=1/eta*cross(transk_hat,transErect,3);
```

```
function [transErect,transHrect] =refraction_3coat(Etransverse,...
    Htransverse,k_hat,TM_hat,TE_hat,normal,nlens,n1,n2,n3,noutside,...
    thick1,thick2,thick3,f)
%REFRACTION_3COAT refraction_3coat(Etransverse,Htransverse,k_hat,TE_hat,...
%TM_hat,normal,nlens,n1,n2,n3,noutside,thick1,thick2,thick3,f)
%This function refracts the incident fields (ETRANSVERSE,HTRANSVERSE) in
%Plane-Of-Incidence (POI_ coords into refracted fields
%(TRANSERECT,TRANSHRECT).  All are mxnx3 arrays.  It accepts
%the basis vectors (KHAT,TM_HAT,TE_HAT) as well as the surface
%normals NORMAL and the indicies inside (NLEN) and outside (NOUTSIDE) the
%lens.  It also accepts the thicknesses of the 3 layers THICK1-THICK3 and
%their indices N1-N3.  Layer 1 is the inner-most, Layer 3 the outer-most.
%This function invokes Snell's law to calculate the new unit wavevector
%khatprime, which is just a rotation about the TE_hat basis.
%It calculates Fressnel Coefficients for a three layer AR-coating by
%forcing the fields to be continuous at the boundaries between the media,
%and then calculates transmitted fields.  The TE component of the E-fields
```

```
%remains in the same positon, as does the TM component of the H-fields.
%The others rotate about the basis vectors TE_hat just like the wavevector.
%TRANSHRECT is calculated from TRANSERECT and khatprime.
%This function uses the function matrix_mult4d, since matlab cannot
%natively do matrix multiplication on arrays of rank>2.
%Roger O'Brient         Jan 2010

c=3*10^8; %[m/s] Speed light free space
eta=377; %[Ohms] Impedance Free Space

lambda_o=c/f; %[m] wavelength outside lens
ko=(2*pi/lambda_o); %[1/m] wavenumber outside lens

%Snell's law rotates pointing vector in khat-TM_hat plane at every coating
%interface.  The net rotation is angleDelta, which is as if there never was
%no intermediate layers.  But we need the intermediate angles for
%calculating the transmission coefficients.
angle_inc=acos(dot(k_hat,normal,3)); %[radians]

angle1=asin(nlens/n1*sin(angle_inc)); %[radians]
angle2=asin(n1/n2*sin(angle1)); %[radians]
angle3=asin(n2/n3*sin(angle2)); %[radians]

angle_trans=asin(nlens/noutside*sin(angle_inc)); %[radians]
angleDelta=angle_trans-angle_inc; %[radians]
%The wavevector for the transmitted ray is just a rotation of the incident
%wavevector by angle_Delta about the TE_hat axis.  transk_hat can be part
%of a new basis-set for the fields, although I keep all vectors in the
%original incident basis
transk_hat=repmat(cos(angleDelta),[1 1 3]).*k_hat+...
    repmat(sin(angleDelta),[1 1 3]).*TM_hat;

%Construct Transmission coefficients using the well known algorithm
%discussed in section 9.7.1 of Hect's Optics using transfer matrices.
%Construct transfer matrics: [E1;H1]=M*[E2;H2] for each layer and then
%multiply them

Y_lens=nlens/eta*cos(angle_inc);

Y_1_te=n1/eta*cos(angle1);
Y_1_tm=n1/eta*sec(angle1);
Y_2_te=n2/eta*cos(angle2);
Y_2_tm=n2/eta*sec(angle2);
Y_3_te=n3/eta*cos(angle3);
Y_3_tm=n3/eta*sec(angle3);

Y_out=noutside/eta*cos(angle_trans);

h1=n1*thick1*cos(angle1);
h2=n2*thick1*cos(angle2);
h3=n3*thick3*cos(angle3);

M1_te=cat(3,cat(4,cos(ko*h1),              i*sin(ko*h1)./Y_1_te),...
           cat(4,i*sin(ko*h1).*Y_1_te,   cos(ko*h1)));
M1_tm=cat(3,cat(4,cos(ko*h1),              i*sin(ko*h1)./Y_1_tm),...
           cat(4,i*sin(ko*h1).*Y_1_tm,   cos(ko*h1)));

M2_te=cat(3,cat(4,cos(ko*h2),              i*sin(ko*h2)./Y_2_te),...
           cat(4,i*sin(ko*h2).*Y_2_te,   cos(ko*h2)));
```

```
77 M2_tm=cat(3,cat(4,cos(ko*h2),              i*sin(ko*h2)./Y_2_tm),...
78            cat(4,i*sin(ko*h2).*Y_2_tm,   cos(ko*h2)));
79
80 M3_te=cat(3,cat(4,cos(ko*h3),              i*sin(ko*h3)./Y_3_te),...
81            cat(4,i*sin(ko*h3).*Y_3_te,   cos(ko*h3)));
82 M3_tm=cat(3,cat(4,cos(ko*h3),              i*sin(ko*h3)./Y_3_tm),...
83            cat(4,i*sin(ko*h3).*Y_3_tm,   cos(ko*h3)));
84
85 %Multiply the transfer matrices.
86 Mtot_te=matrix_mult4d(M1_te,matrix_mult4d(M2_te,M3_te));
87 Mtot_tm=matrix_mult4d(M1_tm,matrix_mult4d(M2_tm,M3_tm));
88
89 %Construct transmission coefficients for the E-fields
90 T_te=2*Y_out./(Y_out.*Mtot_te(:,:,1,1)+...
91                Y_out.*Y_lens.*Mtot_te(:,:,1,2)+...
92                Mtot_te(:,:,2,1)+...
93                Y_lens.*Mtot_te(:,:,2,2));
94
95 T_tm=2*Y_out./(Y_out.*Mtot_tm(:,:,1,1)+...
96                Y_out.*Y_lens.*Mtot_tm(:,:,1,2)+...
97                Mtot_tm(:,:,2,1)+...
98                Y_lens.*Mtot_tm(:,:,2,2));
99
100 %Transmitted E-field perpendicular to POI (Etransverse(:,:,3)) points in
101 %same direction before and after refraction.  The E-field within the POI
102 %(Etransverse(:,:,2))rotates by angleDelta like khat.
103
104 transEplane=cat(3,-T_tm.*Etransverse(:,:,2).*sin(angleDelta),...
105                   T_tm.*Etransverse(:,:,2).*cos(angleDelta),...
106                   T_te.*Etransverse(:,:,3));
107
108 %covert to rectangular coords
109 [transErect,transHrect]=transverse2rect(normal,k_hat,transEplane, ...
110                                         transEplane);
111
112 %Construct Magnetic-field
113 transHrect=1/eta*cross(transk_hat,transErect,3);
```

```
1  function [C]=matrix_mult4d(A,B)
2  %4DMATRIX_MULT C=matrix_mult4d(A,B)
3  %This function multiplies two mxnx2x2 arrays A and B in the last two
4  %indices according to standard matrix multiplication definition.  It
5  %returns a mxnx2x2 array where each of the mth,nth 2x2 array is the matrix
6  %product of the corresponding ones from A and B.  Matlab
7  %does not have a native way of doing this, but this is needed for 2x2
8  %multiplication in the AR-coating algoerithm in our ray-tracing code.
9  %
10 %Roger O'Brient     Feb 2010
11
12 C11=A(:,:,1,1).*B(:,:,1,1)+A(:,:,1,2).*B(:,:,2,1);
13 C12=A(:,:,1,1).*B(:,:,1,2)+A(:,:,1,2).*B(:,:,2,2);
14 C21=A(:,:,2,1).*B(:,:,1,1)+A(:,:,2,2).*B(:,:,2,1);
15 C22=A(:,:,2,1).*B(:,:,1,2)+A(:,:,2,2).*B(:,:,2,2);
16
17 Ccol1=cat(4,C11,C12);
18 Ccol2=cat(4,C21,C22);
19 C=cat(3,Ccol1,Ccol2);
```

A.9 diffraction

```
function [J,M,J_img,M_img]=surfacecurrents(E,H,normal,Lext)
%           Function takes as input mxnx3 arrays of 3-D vectors in
%           rectangualr basis correspondong to Electric Fields E, Magnetic
%           Fields H, and unit normal vectors NORMAL at the lens sruface.
%           It constructs fictitious electrinc J and magnetic currents M on
%           the surface to assist with the Huygens Integral.  These vectors
%           are also in a rectangular coordinate basis.  It also returns
%           the image currents J_IMG & M_IMG, but reflects them to ensure
%           that the electric fields at the ground plane are normal and
%           magnetic fields are tangential.
%           Roger O'Brient          October 2009
%                                   updated for image currents Jan 2010

J= cross(normal,H,3);
M= -cross(normal,E,3);

J_img=J;
J_img(:,:,1:2)=-J_img(:,:,1:2);

M_img=M;
M_img(:,:,3)=-M_img(:,:,3) ;
```

```
function [fftheta ffphi Efarfield Hfarfield]=Diffrcation(ffthetastep,...
    ffphistep,J,M,J_img,M_img,dA,dA_img,patch_pos,img_pos,inc_img,Lext,...
    f,hemtheta,hemphi)
%DIFFRACTION
%This function returns the far-fields (EFARFIELD,HFARFIELD) at angular
%positions (FFTHETA,FFPHI).  It's arguments are theta and phi steps for
%the far field, surface currents and their images, the locations of those
%curretns, patch surface areas, a flag to include the images, and the
%extension length LEXT.
%The code uses a common Fourier Transform algorithm outline in most
%antenna textbooks for radiation through an aperature.  This was developed
%on a laptop with 0.5Gb RAM, which was insuffient to store 5-index arrays
%needed for the difffaction calculations.  So it uses a loop instead and it
%reports progress to the user with the function PROGMETER.  If all angles
%steps are 3deg, then the code takes 30-40sec to execute on my laptop with
%1.8GHz processor.
%Roger O'Brient    Aug2009

c=3*10^8; %[m/s]
eta=377; %[Ohms]
if Lext==0
    remove=1;
else
    remove=0;
end
tic ;
[ffphi,fftheta]=meshgrid(0:ffphistep:(2*pi),0:ffthetastep:(pi/2));
Efarfield=zeros(cat(2,size(ffphi),3));
Hfarfield=zeros(cat(2,size(ffphi),3));
progmeter(0, 'Performing Diffraction Integral')

```

```
for p=1:size(ffphi,2)
    for t=1:size(fftheta,1)
        %Construct the wavevector of the total wave at the far-field
        %angular positon (fftheta,ffphi
        theta=fftheta(t,p);
        phi=ffphi(t,p);
        ffk=2*pi*f/c*cat(3,...
      repmat(sin(theta).*cos(phi),[size(hemtheta,1) size(hemphi,2) 1]),...
      repmat(sin(theta).*sin(phi),[size(hemtheta,1) size(hemphi,2) 1]),...
      repmat(cos(theta),[size(hemtheta,1) size(hemphi,2) 1]));
        %Construct Propagator to far field.  This only accounts for phase
        %difference since intensity decay is roughly the same at all
        %points.  The Propagator for the images is almost the same, except
        %excludes equator points if Lext=0.
        Propagator = repmat(exp(i*sum(ffk.*patch_pos,3)),[1 1 3]) ;
        if inc_img
            Propagator_img=repmat(exp(i*sum(ffk(1:end-remove,:,:).*...
                                            img_pos,3)),[ 1 1 3 ]);
        end
        %Construct Far-field Magnetic (N) and Electric (L) Vector
        %potentials.  These exclude common factors of phase delay and 1/r
        %field decay.
        Nrect=sum(sum(J.*Propagator.*dA,1),2)+...
            inc_img*sum(sum(J_img.*Propagator_img.*dA_img,1),2);
        Lrect=sum(sum(M.*Propagator.*dA,1),2)+...
            inc_img*sum(sum(M_img.*Propagator_img.*dA_img,1),2);
        N=rect2sphere(Nrect,theta,phi);
        L=rect2sphere(Lrect,theta,phi);

        %Fields are deivatives of the potentials:
        Efarfield(t,p,2)=-(L(:,:,3)+eta*N(:,:,2));
        Efarfield(t,p,3)=(L(:,:,2)-eta*N(:,:,3));
        Hfarfield(t,p,2)=(N(:,:,3)-L(:,:,2)/eta);
        Hfarfield(t,p,3)=-(N(:,:,2)+L(:,:,3)/eta);
    end
    progmeter(phi/(2*pi));
end

%normalize beams to peak
EPower=dot(Efarfield,Efarfield,3);
HPower=dot(Hfarfield,Hfarfield,3);
Efarfield=Efarfield/sqrt(max(max(EPower)));
Hfarfield=Efarfield/sqrt(max(max(HPower)));
% ffEtheta=Efarfield(:,:,2);
% ffEphi=Efarfield(:,:,3);
% ffHtheta=Hfarfield(:,:,2);
% ffHphi=Hfarfield(:,:,3);
progmeter done
disp(['Diffraction Calculation finished after ',num2str(toc),' sec']);
```